Electromagnetic and Thermal Design of Axial Flux Permanent Magnet Synchronous Machines

Elektromagnetisch en thermisch ontwerp van permanentemagneetbekrachtigde synchrone machines met axiale flux

Ahmed Mohammed Abdelmoneam Hemeida

Promotoren: prof. dr. ir. P. Sergeant, prof. dr. ir. J. Vierendeels
Proefschrift ingediend tot het behalen van de graad van
Doctor in de ingenieurswetenschappen: werktuigkunde-elektrotechniek

UNIVERSITEIT
GENT

Vakgroep Elektrische Energie, Metalen, Mechanische Constructies en Systemen
Voorzitter: prof. dr. ir. L. Dupré
Faculteit Ingenieurswetenschappen en Architectuur
Academiejaar 2016 - 2017

ISBN 978-94-6355-011-6
NUR 950, 959
Wettelijk depot: D/2017/10.500/46

Electromagnetic and Thermal Design of Axial Flux Permanent Magnet Synchronous Machines

Ahmed Mohammed Abdelmoneam Hemeida

Dissertation submitted to obtain the academic degree of
Doctor of Electromechanical Engineering

Publicly defended at Ghent University on 7 June 2017

Supervisors:

prof. dr. ir. Peter Sergeant
Electrical Energy Laboratory (EELAB)
Department of Electrical Energy, Metals, Mechanical Constructions and Systems (EEMMeCS)
Faculty of Engineering and Architecture
Ghent University
Technologiepark 913
B-9052 Zwijnaarde, Belgium
http://www.ugent.be/ea/eemmecs/en

prof. dr. ir. Jan Vierendeels
Department of Flow, Heat and Combustion Mechanics (FloHeaCom)
Faculty of Engineering and Architecture
Ghent University
Sint-Pietersnieuwstraat 41
B-9000, Gent, Belgium
http://www.floheacom.UGent.be/

Members of the examining board:

Prof. dr. ir. Patrick de Baets (Chairman)	EEMMeCS, University of Ghent
Prof. dr. ir. Peter Sergeant (Supervisor)	EEMMeCS, University of Ghent
Prof. dr. ir. Jan Vierendeels (Supervisor)	FloHeaCom, University of Ghent
Prof. dr. ir. Amr Adly	University of Cairo
Prof. dr. ir. Ruth Vazquez Sabariego	KU Leuven
dr. ir. Ahmed Abouelyazied Abdallh	Flanders Make
Prof. dr. ir. Hendrik Rogier	IBCN, University of Ghent
Prof. dr. ir. Jan Desmet	EEMMeCS, University of Ghent
dr. ir. Hendrik Vansompel (Secretary)	EEMMeCS, University of Ghent

FACULTY OF ENGINEERING AND ARCHITECTURE

GHENT UNIVERSITY

Preface

I would like to express my sincere thanks and gratitude to my supervisors, prof. Peter Sergeant and prof. Jan Vierendeels for their guidance and help throughout the accomplishment of this work. Thank you very much for the countless hours spent on discussions, debugging and proofreading. I would like also to express my gratitude and appreciation for their efforts in finding the financial resources to fund this research. I gratefully acknowledge the financial support of the project FWO-G.0110.13 of the Fund of Scientific Research-Flanders of Ghent University.

I would like to thank all the members of the examination board: prof. Patrick de Baets, prof. Amr Adly, prof. Ruth Vazquez Sabariego, prof. Jan Desmet, prof. Hendrik Rogier, dr. Ahmed Abouelyazied Abdallh, and dr. Hendrik Vansompel for spending their valuable time to judge my thesis. Their comments were valuable to enhance the quality of the thesis

I would like to offer my thanks to all the colleagues in EELAB for the great team work, we had together. In particular thanks to my office mates: dr. Ahmed Abouelyazied Adballh, dr. Setareh Gorji Ghalamestani, dr. Damian Kowal, ir. Mohamed Nabil and dr. Mohamed Taha for the brilliant working atmosphere, the help every time needed and permanent support. I am grateful to prof. Luc Dupré, prof. Alex Van Den Bossche, dr. Hendrik Vansompel, dr. Aboubakr Salem, dr. Alireza Rasekh, ir. Bart Wymeersch, ir. Mariem Harabech, ir. Mohannad Mnati and ir. Bert Hannon for their help and great discussion since my first days in Belgium.

Special thanks to dr. Ahmed Abouelyazied Abdallh and dr. Mohamed Taha. Together with them, I have been able to learn more about optimization of electric machines for electric vehicle applications. I would like also to thank ir. Baocheng Guo from southeast university of China. Throughout the co-operation with him, we were able to make different models for the machine in the eccentricity mode. I would like to acknowledge ir. Bert Hannon. Throughout the collaboration with Bert, we were capable to make different models for the machine. Together with dr. Alireza Rasekh, we were able to strongly collaborate in the project for four years. Thanks to ir. Mohamed Nabil and Aboubakr Salem. Through the discussions with them, we have made lots of progress in the research.

Special thanks to dr. Hendrik Vansompel. I continued the research of Hendrik in the axial flux machines. I was able through his continuous help in thermal mod-

eling and experimental setup during my stay in EELAB to produce lots of work together.

I would like to express my gratitude to Mrs. Ingrid Dubois and Mrs. Marilyn Vanden Bossche for their essential administrative work, Mr. Tony Boone and Mr. Stefaan Dhondt for setup preparations, and ir. Nic Vermeulen for his continuous help in solving computer problems.

Moreover, I am very grateful to my colleagues and staff members in Cairo University in the electrical power and machines department especially, prof. Amr Adly and prof. Osama Mahgoub for their support. The knowledge that I gained in Cairo University as an undergraduate and a master student was a foundation in the success of this research.

In Ghent, I met a lot of people from different countries. I cannot forget the fantastic time that I spent with them. Thanks to my real friends, they gave me the continuous support to continue my research.

Finally, I would like to thank my family. Mom and dad, I have no words to acknowledge the sacrifices you made and the dreams you had to let go, just to give me a shot at achieving mine. Special thanks to my sister, my brother, his wife, and their little daughter Mariam. Special thanks to my fiancee Eman and her family for their sincere encouragement and continuous support. She made my life full of colours and joy. Great thanks to my aunts and uncles. Thanks to everyone.

Ahmed Mohammed Abdelmoneam Hemeida,
June 2017

Contents

Preface **v**

Contents **x**

Summary **xi**

Samenvatting **xv**

List of Abbreviations **xix**

List of Symbols **xxi**

1 Introduction **1**
1.1 Motivation 1
1.2 Objectives 2
1.3 Outline 3
1.4 Scientific Publications 5
1.4.1 Articles in International SCI Journals 5
1.4.2 Publications in the Proceedings of International Conferences 6

2 The Yokeless and Segmented Armature (YASA) Machine **7**
2.1 Introduction 7
2.2 AFPMSMs Topologies 8
2.2.1 Single Stator Single Rotor (SSSR) 10
2.2.2 Double Stator Single Rotor (DSSR) 11
2.2.3 Single Stator Double Rotor (SSDR) 12
2.2.4 Multi Stator Multi Rotor (MSMR) 15
2.3 Why Yokeless and Segmented Armature (YASA) Machine? 16
2.4 Conclusions 17

3 Modeling of Axial Flux Permanent Magnet Synchronous Machines **19**
3.1 Introduction 19
3.2 Test Case Machine 20

3.3 Description of the Finite Element (FE) Models 21
3.3.1 3D FE Model 22
3.3.2 2D Multi-slice FE Model 22
3.4 Description of the Analytical Models 27
3.4.1 Lateral Force Method (LF Model) 28
3.4.2 Complex Schwarz Christoffel Transformation (SC Model) 36
3.4.3 Subdomain Model (SD Model) 46
3.5 Comparison between Different Models 54
3.5.1 Comparison of CPU Time 54
3.5.2 Comparison of Flux Densities 55
3.5.3 Comparison of Cogging Torque 55
3.5.4 Comparison of Torque Ripple at Full Load 58
3.5.5 Comparison of No Load and Full Load Voltages 60
3.6 Conclusions 61

4 Coupled Schwarz-Christoffel - Magnetic Equivalent Circuit Model 63
4.1 Introduction 63
4.2 FE Models Including Non-Linear Magnetic Material 64
4.2.1 Mathematical Modelling of Non-Linear Material 65
4.2.2 Core Loss Computation 66
4.3 Magnetic Equivalent Circuit Model 69
4.3.1 Magnetic Reluctance Values 71
4.3.2 Resultant Field From Maxwell's Equations 73
4.3.3 Flux Loop Equations 74
4.3.4 Voltage Computation 75
4.3.5 Torque Computation 75
4.3.6 Stator Core Loss Computation 75
4.4 Comparison of Test Results 75
4.4.1 Magnetic Flux Density 76
4.4.2 Voltage and Torque 79
4.4.3 Flux Density and Losses in Stator Core 83
4.4.4 CPU Time Comparison 85
4.4.5 Extreme Loading Study 87
4.4.6 Influence of Geometrical Parameters Study 90
4.4.7 Influence of the MEC Grid Refinement 91
4.5 Conclusions 93

5 Eddy Current Loss in the Permanent Magnets 99
5.1 Introduction 99
5.2 Electric Circuit Network for PM Eddy Current Loss Calculation . 101
5.2.1 Multi-Slice 2D Analytical Solution 101
5.2.2 PM Flux Density Reconstruction 102
5.2.3 Induced Voltage 104

5.2.4 Resistance Calculation 105
5.2.5 Inductance Calculation 105
5.3 PM Segmentation 108
5.4 2D Multi-Slice FE Model 108
5.4.1 FE Model Without the Consideration of the Reaction Field 109
5.4.2 FE Model With the Consideration of the Reaction Field . . 111
5.5 3D Time Stepping FE Model 111
5.6 Simulation Results 113
5.6.1 Sinusoidal Operating Conditions 113
5.6.2 Pulse Width Modulation (PWM) Operating Conditions . . 116
5.6.3 Skin Depth Effect 119
5.6.4 PM Segmentation 120
5.6.5 CPU Computation Time 121
5.7 Conclusions 122

6 An Electromagnetic Design Procedure for AFPMSMs 125
6.1 Introduction 125
6.2 Literature Review of Machines Working in the FW Region 126
6.3 AFPMSM Design Procedure 127
6.3.1 Set of Inputs Generation 129
6.3.2 Internal Parameters Evaluation 132
6.3.3 Machine Selection 138
6.4 Analytical Model Results and Discussions 141
6.4.1 The Effect of Different Combinations on Performance . . 142
6.4.2 Finite Speed Design 148
6.4.3 Infinite Speed Design 151
6.4.4 Comparison Between Finite and Infinite Speed Designs . . 152
6.4.5 Results of a 14-12, 3-phase machine 152
6.5 Finite Element Validation 154
6.6 d and q Current Effects on Torque Ripple 157
6.7 Conclusions 158

7 Thermal Modeling of Air Cooled YASA Machine 161
7.1 Introduction 161
7.2 Heat Transfer 163
7.2.1 Conduction 163
7.2.2 Convection 163
7.2.3 Radiation 164
7.3 Description of the Stator Heat Extraction System 165
7.4 Thermal Properties of Electromagnetic Materials 165
7.5 AFPMSM Thermal Models 168
7.5.1 3D FE Thermal Model 169
7.5.2 Lumped Parameter Thermal Network (LPTN) 173

7.6 Inward Heat Extraction System Evaluation 179
7.7 Conclusions 181

8 YASA Experimental Setup **183**
8.1 Introduction 183
8.2 Prototype Construction 183
8.2.1 Construction of the rotors 184
8.2.2 Construction of the modular stator element 185
8.2.3 Experimental Test Set-Up 186
8.3 Experimental Validations 188
8.3.1 Electromagnetic Models Validations 188
8.3.2 Thermal Models Validations 188
8.4 Machine Performance Over Entire Working Speed Range 194
8.5 Conclusions 199

9 Concluding Remarks **203**
9.1 Conclusions 203
9.2 Recommendations for Future Research 205

Appendices **207**
A Reluctance Evaluation of the MEC 209
B AFPMSM Modes of Operation and Lossless Equations 213
C Finite and Infinite Speed Design 215

Bibliography **217**

Summary

Nowadays, electric machines consume about half of the electrical energy worldwide[1]. A slight enhancement of the efficiency in electric machines would save a huge amount of energy, and hence money. Permanent magnet synchronous machines offer great opportunities compared to conventional DC and asynchronous machines. The high efficiency, power factor and power density of these machines has allowed the integration of permanent magnet (PM) machines into a wide range of applications that require a highly efficient drive system, such as applications in renewable energy (wind turbines), aerospace applications, electric vehicles (EVs), hybrid electric vehicles (HEVs), *etc.* In order to reduce the CO_2 emissions, the improvement of the electric drives in these vehicles has become an important research topic.

Because of the need of electric machines with high efficiency and power density, new topologies of electric motors are studied. One of these topologies is the axial flux permanent magnet synchronous machine (AFPMSM). Generally speaking, axial flux machines can have superior characteristics regarding the power to weight ratio compared to the traditional radial flux machines. Furthermore, thanks to the high ratio between the outer diameter and the axial length, axial flux machines can be integrated in several applications where the axial length must be small. Different topologies of AFPMSMs are described in literature.

In this PhD, the yokeless and segmented armature (YASA) machine has been chosen as a research subject. Thanks to the absence of the yoke, the YASA machine can provide a high power density combined with a great efficiency compared to other topologies. The usage of the double layer fractional slot concentrated winding facilitates an easy construction of the machine. The different stator core elements are manufactured individually, provided with a tooth coil winding, and finally arranged together into the stator.

Specifically for YASA machines, an electromagnetic analytical design tool has been developed to optimize the performance of the YASA machine for applications with any input power and speed. This tool is based upon validated analytical models that describe the electromagnetic and thermal characteristics of the machine.

[1]Waide, P. and C. Brunner (2011), "Energy-Efficiency Policy Opportunities for Electric Motor-Driven Systems", IEA Energy Papers, No. 2011/07, OECD Publishing, Paris.

Different electromagnetic analytical models for AFPMSMs are proposed for a complete study of the machine's electromagnetic performance. The models allow computing the terminal voltage, iron losses, eddy current losses in the permanent magnets, copper losses, torque ripple, and cogging torque. These models are 2D multi-slice modeling techniques. Like most analytical techniques, they neglect non-linear behavior. They are based on conformal mapping or on the subdomain principle. A comparison between these models is described and validated. Each modeling technique is parameterized and can be used to compute the above mentioned voltages, loss components and torque. The comparison has shown that the subdomain model is the only analytical model that can accurately compute the mean value of the torque and the torque ripple when compared to a 3D Finite Element model.

In addition, a novel analytical model, based on a combined solution of Maxwell's equations and a magnetic equivalent circuit (MEC), is developed. In contrast to the models in previous paragraph, this model takes into account the non-linear behavior of the magnetic material. This model can accurately compute the iron losses and terminal voltage. For validations, this model is compared to 3D and 2D finite element models.

The eddy current losses in the permanent magnets are computed based on different methods. The eddy currents result from the rather high electric conductivity of rare earth permanent magnets, which are widely used in permanent magnet machines. The eddy current loss leads to increased temperature of the permanent magnets and to a demagnetization risk. Therefore, modeling of the eddy currents is important. In this PhD, an electric circuit model is developed to compute the eddy current losses in the permanent magnets. This electric circuit is composed of resistances and inductances, and sources representing the time variant flux density in the magnets. A comparison is made between two variants: the first including the reaction field of the currents in the permanent magnets, and the second neglecting this reaction field. The electric circuit model is successfully verified amongst others through a complete 3D transient finite element model.

Based on the analytical models, a design tool is developed for YASA axial flux machines. This framework is intended to optimize the machine's geometry based on the required power and speed of the application. Thanks to the developed analytical models described before, the design tool gives the optimal geometrical machine parameters in a very short time and in an accurate way. Since AFPMSMs are currently used in HEV, it is important to check their applicability in the field weakening (FW) region. Therefore, a sensitivity analysis is done for different geometrical parameters to select the optimum values for machines operating in the FW region. Different slots/poles/phases combinations have been studied to reveal the optimum combination. It is also worth mentioning that this toolbox has been used to design a 100kW YASA machine for a low speed high torque (wind turbine) application. The prototype of this machine is still under construction.

Finally, thermal models are developed for the YASA AFPMSMs. These mod-

els are based on a finite element model and lumped parameter thermal network (LPTN). The main advantage of these models is the use of convection coefficient equations for the air gap. These equations are developed specifically for the YASA machines by the *Department of Flow, Heat and Combustion Mechanics* at Ghent University. By enforcing these convection equations to the air gap surfaces, the thermal models of the stator and rotor are decoupled. This decoupling allows a fast evaluation of two simple thermal models: the simulation time is about 1 second. Moreover, the LPTN gives an accurate solution of the temperature distribution in the stator, which is proven by comparison to the measured temperatures from the experimental setup of a 4 kW YASA machine. However, more research is still needed to model the shaft and the bearings in the LPTN to have an accurate estimation of the rotor temperature.

A 4 kW experimental research prototype has been developed in the Electrical Energy Laboratory together with several colleagues to validate the electromagnetic and thermal models described before. Furthermore, new conductive and convective cooling concepts of the stator and rotor has been developed. The conductive cooling concept is based on inward fins that are placed between the stator windings to better evacuate the heat to the outer circumference. The convective cooling concept is based on a specific shape of the permanent magnets, positioned on the rotor discs with air channels between them. During rotation, the magnets behave like ventilator fins, creating a radial air flow through the air gaps.

Samenvatting

Vandaag de dag verbruiken elektrische machines zowat de helft van de elektrische energie wereldwijd[2]. Een kleine rendementstoename in elektrische machines zou een grote hoeveelheid energie besparen. Permantemagneetbekrachtigde synchrone machines bieden veel mogelijkheden vergeleken met conventionele gelijkstroom-machines en asynchrone machines. Het hoge rendement, de hoge arbeidsfactor en de hoge vermogendichtheid van deze machines heeft ervoor gezorgd dat ze ontwikkeld worden voor een groot aantal applicaties die een zeer efficiënte aandrijving vereisen, zoals toepassingen in de hernieuwbare energie (windturbines), ruimtevaart, elektrische voertuigen (EV), hybride elektrische voertuigen (HEV), enzovoort. Om CO_2-emissies te verlagen, is er zeer veel onderzoek lopende om de elektrische aandrijvingen in deze voertuigen te verbeteren.

Wegens de nood aan elektrische machines met hoog rendement en vermogendichtheid worden nieuwe topologieën van elektrische motoren bestudeerd. Eén van de topologieën is de machine met axiale flux. In het algemeen kunnen machines met axiale flux superieure karakteristieken hebben wat betreft de verhouding van vermogen op gewicht, in vergelijking met de traditionele machines met radiale flux. Bovendien kunnen machines met axiale flux geïntegreerd worden in toepassingen waar de axiale lengte klein moet zijn, dankzij hun hoge verhouding van diameter tot axiale lengte. Verschillende topologieën van permanentemagneetbekrachtigde machines met axiale flux (AFPMSMs) zijn beschreven in de literatuur.

In dit doctoraat wordt de “yokeless and segmented armature” (YASA) machine gekozen als onderzoeksonderwerp. Dankzij de afwezigheid van een statorjuk kan de YASA machine een grote vermogendichtheid combineren met een hoog rendement in vergelijking met andere topologieën. Het gebruik van een tweelaags-breukgroefwikkeling vergemakkelijkt de constructie van de machine. De verschillende statorkernelementen worden eerst individueel vervaardigd, dan bewikkeld, en daarna geassembleerd tot een volledige stator.

Specifiek voor YASA machines werd een elektromagnetische en thermische ontwerpstool gebouwd om de performantie van de YASA machine te optimaliseren voor toepassingen met om het even welk vermogen en snelheid. Deze tool

[2]Waide, P. and C. Brunner (2011), ”Energy-Efficiency Policy Opportunities for Electric Motor-Driven Systems”, IEA Energy Papers, No. 2011/07, OECD Publishing, Paris.

is gebaseerd op gevalideerde analytische modellen die het elektromagnetisch en thermisch gedrag van de machine beschrijven.

Verschillende elektromagnetische analytische modellen van AFPMSMs worden gepresenteerd om een volledige studie van het elektromagnetisch gedrag mogelijk te maken. De modellen berekenen de klemspanning, ijzerverliezen, wervelstroomverliezen in de permanente magneten, koperverliezen, koppelrimpel en kleefkoppel. Deze modellen zijn 2D "multi-slice" modelleringstechnieken. Zoals de meeste analytische technieken verwaarlozen ze niet-lineair gedrag. Ze zijn gebaseerd op conforme afbeeldingen of op de subdomeintechniek. Een vergelijking tussen deze modellen is beschreven en gevalideerd. Elke techniek wordt geparametriseerd en kan gebruikt worden om bovenvermelde spanningen, verliestermen en koppel te berekenen. De vergelijking heeft getoond dat de subdomeintechniek de enige analytische techniek is die – bij vergelijking met een 3D Eindige-Elementenmodel – een nauwkeurige oplossing geeft van het gemiddeld koppel en van de koppelrimpel.

Daarnaast wordt in dit doctoraat een nieuwe analytische methode voorgesteld. Deze bestaat uit een gecombineerd oplossen van de Maxwellvergelijkingen en een magnetisch equivalent circuit (MEC). In tegenstelling met de modellen in vorige paragraaf houdt dit gecombineerd model rekening met het niet-lineair gedrag van het magnetisch materiaal. Dit model kan nauwkeurig ijzerverlies en klemspanning berekenen. Het model wordt vergeleken met 3D en 2D FE modellen om het te valideren.

De wervelstroomverliezen in de permanente magneten worden berekend op basis van verschillende methoden. De wervelstromen zijn een gevolg van de eerder hoge elektrische geleidbaarheid van de zeldzame-aarde magneten, die zeer vaak gebruikt worden in permanentemagneetbekrachtigde machines. De wervelstroomverliezen leiden tot verhoogde temperatuur van de permanente magneten. De hoge temperatuur houdt een risico in op demagnetizatie. Daarom is het belangrijk om de wervelstromen te modelleren. In het doctoraat wordt een elektrisch netwerkmodel ontwikkeld om de wervelstroomverliezen in de permanente magneten te berekenen. Dit elektrisch netwerk bestaat uit weerstanden en inductanties, en uit bronnen die de tijdsveranderlijke inductie in de magneten voorstellen. Een vergelijking wordt gemaakt tussen twee varianten: de eerste houdt rekening met het reactieveld van de stromen in de permanente magneten. Het tweede verwaarloost het reactieveld. Het elektrisch netwerkmodel wordt onder andere geverifieerd via een transiënt 3D Eindige-elementenmodel.

Op basis van de analytische modellen werd een ontwerpstool ontwikkeld voor YASA machines met axiale flux. De tool is bedoeld om de geometrie van de machine te optimaliseren op basis van het vereiste vermogen en de vereiste snelheid van de applicatie. Dankzij de eerder beschreven analytische modellen, kan de ontwerpstool de optimale geometrische parameters snel en nauwkeurig bepalen. Aangezien AFPMSMs momenteel ook gebruikt worden in hybride elektrische voertuigen, is het belangrijk om ook hun toepasbaarheid te bestuderen

in het fluxverzwakkingsgebied. Verschillende combinaties van aantallen gleuven, polen en fasen werden bestudeerd om de optimale combinatie te achterhalen. Het is nuttig te vermelden dat deze ontwerpstool ook gebruikt werd om een 100kW YASA machine te ontwerpen voor een windturbine-toepassing met lage snelheid en hoog koppel. Een prototype van deze machine is onder constructie.

Tenslotte werden thermische modellen ontwikkeld van YASA AFPMSMs. Deze modellen zijn gebaseerd op eindige-elementenmodellen en een thermisch netwerk. Het grootste voordeel van deze modellen is het gebruik van vergelijkingen met convectie-coëfficiënten voor de luchtspleet. Deze vergelijkingen werden ontwikkeld specifiek voor YASA machines, door de Vakgroep *Mechanica van Warmte, Stroming en Verbranding* van de Universiteit Gent. Door deze convectie-coëfficiënten op te dringen op de luchtspleetoppervlakken, worden de thermische modellen van de stator en de rotor ontkoppeld. Deze ontkoppeling maakt een snelle evaluatie mogelijk van twee simpele thermische modellen: de simulatietijd is ongeveer 1 seconde. Bovendien geeft het thermisch netwerk een nauwkeurige oplossing van de temperatuursverdeling in de stator, wat blijkt uit vergelijking met gemeten temperaturen op de experimentele opstelling van een 4kW YASA machine. Niettemin is er meer onderzoek vereist om de as en de lagers te modelleren in het thermisch netwerkmodel om een nauwkeurige schatting te hebben van de rotortemperatuur.

Een experimentele testopstelling van 4kW werd gebouwd in het Labo voor Elektrische Energietechniek, samen met andere collega's aan het labo. Met deze opstelling werden de hoger beschreven elektromagnetische en thermische modellen gevalideerd. Bovendien werden nieuwe koelingstechnieken voor stator en rotor ontwikkeld, gebaseerd op conductie en convectie. De koeling via conductie is gebaseerd op radiaal inwaarts gerichte vinnen die tussen de statorwikkelingen geplaatst zijn om de warmte beter te evacueren naar de buitenomtrek van de machine. De koeling via convectie is gebaseerd op een specifieke vorm van de permanente magneten, die op de rotorschijven gepositioneerd zijn met luchtkanalen ertussen. Bij rotatie gedragen de magneten zich als schoepen van een ventilator, en zorgen ze voor een radiaal gerichte luchtstroom doorheen de luchtspleten van de machine.

List of Abbreviations

AF	axial flux
AFIR	axial flux internal rotor
AFPMSM	axial flux permanent magnet synchronous machine
CFD	computational fluid dynamics
FE	finite element
FSCW	fractional slot concentrated winding
FW	field weakening
HFT	Maxwell stress harmonic filter
GO	grain oriented
IGBT	insulated-gate bipolar transistor
LF	lateral force
LPTN	lumped parameter thermal network
MEC	magnetic equivalent circuit
NdFeB	Neodymium Iron Boron
NN	north north
NO	non oriented
NS	north south
PM	permanent magnet
PMSM	permanent magnet synchronous machine
PWM	pulse width modulation
SC	schwarz christoffel
SD	subdomain
YASA	yokeless and segmented armature
2D	two dimensional space
3D	three dimensional space

List of Symbols

Torque, Speed, Power and Energy Efficiency

η	energy efficiency
f	frequency [Hz]
k_{c}	temperature coefficient electric conductivity
k_{Fe}	iron loss coefficient(s)
k_{R}	ac/dc-resistance ratio
Ω	rotational speed (mechanical) [rad/s]
ω	rotational speed (electric) [rad/s]
$_{\mathrm{MAX}}$	property calculated by Maxwell stress tensor
T	torque [Nm]
T_{cog}	cogging torque [Nm]
P	active power [W]
P_{c}	copper losses in the conductors [W]
P_{cl}	classical loss component [W]
P_{m}	mechanical power [W]
P_{e}	electric power [W]
P_{exc}	excess loss component [W]
P_{Fe}	iron losses [W]
P_{fr}	friction losses [W]
P_{hy}	hysteresis loss component [W]
P_{PM}	eddy current losses in the permanent magnets [W]
Q	reactive power [VAr]
R_{ac}	ac-resistance [Ω]
R_{dc}	dc-resistance [Ω]
R	reluctance
T	electromagnetic torque [Nm]
θ	angular rotor position [rad]
θ_m	angular mechanical position [rad]
Ψ_m	angular mechanical displacement [rad]
θ_e	angular electrical position [rad]
y	axial direction [m]

Electromagnetic Modelling

$\mathbf{A}$, A_r, A_z	magnetic vector potential [Vs/m]
φ	magnetic scalar potential [A]
$\mathbf{B}$, B	magnetic flux density [T]
B_{PM}	remanent magnetisation of the permanent magnet material [T]
$_{\mathrm{c}}$	property of conductor material / tooth coil winding
δ	skin depth [m]
∇	del operator
Δ	Laplace operator
$\mathbf{E}$, E	electric field [V/m]
$\mathbf{e}_{(x)}$	unit vector
$_{\mathrm{Fe}}$	stator core material property
$\mathbf{H}$, H	magnetic field [A/m]
H_{exc}	excess field [A/m]
$\mathbf{J}$, J	current density [A/m^2]
k	number of periods/layers
K	current sheet
λ	permeance function
n	number of computation planes
$\mathbf{M}$, M	magnetisation [A/m]
μ_0	vacuum permeability
$\mu_{(\mathrm{r})}$	relative permeability or harmonic number
$\mu_{(\mathrm{rec})}$	recoil permeability
ν	harmonic number (N_{p} pole representation)
$_{\mathrm{ph}}$	phase property
θ_{m}	azimuthal coordinate
Ψ	gauge factor
$_{\mathrm{r}}$	referred in the rotor reference frame
r	radial coordinate
r_{cp}	radius of computation plane [m]
ρ	electric resistivity [Ωm]
S	cross section area [m^2]
$_{\mathrm{s}}$	referred in the stator reference frame
σ	electric conductivity [Sm^{-1}]
t	time [s]
t_{cp}	computation plane thickness [m]
W_{em}	magnetic energy [J]

Flux Linkage, Voltage and Current

$V_{(x)}$	electromotive force corresponding to parameter x [V]
I	current [A]
I_{rated}	rated rms current [A]
I_{peak}	rated peak current [A]
V_{rated}	Rated rms voltage [V]
V_{peak}	Rated peak voltage [V]
k_{C}	Carter's factor
N_{t}	number of turns placed on one core element
m	number of phases
ψ	flux linkage [Vs]
ξ	winding factor
ξ_{p}	pitch factor
ξ_{d}	distribution factor

Geometrical Parameters

α_{PM}	permanent magnet span
b_{so}	width of the stator slot openings [m]
b_{s}	slot width [m]
D_{i}	inner diameter [m]
D_{o}	outer diameter [m]
R_{i}	inner radius [m]
R_{o}	outer radius [m]
g	air gap thickness [m]
h_{PM}	dimension of the permanent magnets in the magnetisation direction [m]
l_{c}	electric conductor length [m]
N_m	number of poles
p	number of pole pairs
N_{s}	number of stator slots
τ_{p}	pole pitch [m]
τ_{s}	slot pitch [m]

Chapter 1

Introduction

1.1 Motivation

The history of electric machines started at the beginning of the 18^{th} century. The idea started firstly by the British scientist Michael Faraday in 1821. Faraday constructed a vertically suspended wire that moved in a circular orbit around a magnet. Later in 1834, the German scientist Moritz Hermann, developed the first electric motor in history. His electric motor was capable to lift a weight of 5kg with an equivalent speed of 0.3m/s. This is equivalent to 15W. His second motor was powerful enough to drive a boat with 14 people across a wide river. Later on, the scientist Werner Siemens in 1856, developed the first DC machine. Later in 1885, the first two phase induction machine was developed by Nikola Tesla.

A century afterwards, the "magical irons" referring to the "permanent magnets (PM)" today were applied into actual electrical machines. Nowadays, permanent magnet synchronous machines are irreplaceable. Since then, a new era of electric machines started through this exploration.

Nowadays, about half[1] of the electrical energy is consumed by electric machines. Given this volume, a slight enhancement of the efficiency in electric machines would save a huge amount of energy. Permanent magnet synchronous machines offer great opportunities compared to conventional DC and asynchronous machines. The high efficiency, power factor and power density associated with these machines have allowed the integration of permanent magnet machines into a wide range of applications (renewable energy sources (wind turbines), aerospace applications, electric vehicles, *etc.*) that required a highly efficient drive system.

The evolution of electric machines led to the discovery of new challenging topologies of permanent magnet (radial flux, axial flux, transverse flux) machines.

These topologies have provided a great enhancements to the efficiency and the weight of the complete electric drive system. Moreover, deep investigations of

[1] Waide, P. and C. Brunner (2011), "Energy-Efficiency Policy Opportunities for Electric Motor-Driven Systems", IEA Energy Papers, No. 2011/07, OECD Publishing, Paris.

the topologies resulted in new variants like outer rotor radial flux machines, the yokeless and segmented armature axial flux machine, *etc.*

In this context, the yokeless and segmented armature (YASA) machine has provided a great enhancement to the electric machines technology. The high ratio of the outer diameter to the axial length allows the machine to be used for many vital applications. Moreover, thanks to the absence of the yoke, the YASA machine can provide a high power density with a great efficiency compared to other topologies. The usage of the double layer fractional slot concentrated winding facilitates an easy construction of the machine.

This research focusses on the YASA axial flux permanent magnet synchronous machine. Within the research scope of the YASA machine, an efficient design toolbox is missing for an optimal performance of the YASA machine. Such a toolbox needs to consider the electromagnetic, thermal, and mechanical properties of the YASA machine. Moreover, a geometrical parameterized toolbox can sufficiently design the machine for any application. In addition, fast appealing and accurate results should be the outcome of such toolbox.

1.2 Objectives

To distinguish this research among other scientific contributions on axial flux PM machines, the research topics were properly defined and the objectives were set:

- The main objective of the thesis is to develop precise models that are capable to accurately compute all the electromagnetic properties of the machine accurately and within a very short time. These models are geometrically parameterized to allow the design of axial flux machines for any input power and speed.
- A novel combined solution of Maxwell's equations and a magnetic equivalent circuit to precisely calculate the voltage output and stator iron core losses of the machine is developed.
- A comparison between different analytical and finite-element (FE) tools for the computation of cogging torque and torque ripple in the YASA machine is made. This allows the authors to directly choose the ideal model for computing these parameters.
- As the permanent magnet material has a good electric conductivity, eddy currents are induced in the permanent magnets when they are subjected to a magnetic flux density that varies in time. Therefore, models for permanent magnet eddy current losses are developed. These models are also based on Maxwell's equations and an electric network. All these models are geometrically parameterized and can give very accurate results compared to the finite element models.

- An electromagnetic design toolbox is also developed using the aforementioned analytical models. This toolbox is capable to optimally design the machine for any input power and speed. This can be used for any application to have very good results for the optimal geometry. A sensitivity analysis for the optimal selection of the slots, poles, and phase combinations is studied to operate the YASA machine in the field weakening region. Additionally, this toolbox is used to design a 100kW machine for wind turbine applications.
- For the thermal modeling of the YASA machine, a new lumped parameter thermal model that can be integrated with the design toolbox to have a complete multi-physical design for the YASA machine.
- A research prototype is developed during this research and number of experiments are carried out. The experimental test setup is used to validate all the developed models.

1.3 Outline

The structure of the thesis is composed of nine main chapters: introduction to the axial flux PM machine, electromagnetic modelling of the axial flux PM machine including cogging torque, torque ripple, stator iron core losses, terminal voltage and permanent magnet losses, an electromagnetic design toolbox for the axial flux PM machine, introduction of the experimental test setup, thermal modeling of the machine, and concluding remarks.

- An introduction to the axial flux permanent magnet (PM) machine is done. A comparison between different topologies is briefly investigated. The yokeless and segmented armature machine is selected to be studied in this research based on this comparison. The benefits of this machine are highlighted in chapter 2.
- Chapters 3, 4 and 5 are dedicated to the electromagnetic modeling of the axial flux permanent magnet (PM) machines. Accurate and fast modeling techniques are compulsory for a complete design of electric machines. In these chapters, a general analytical model for the study of the axial flux machine is proposed for a complete study of the machine's electromagnetic parameters including the terminal voltage, iron losses, eddy current losses in the permanent magnets, copper losses, torque ripple, and cogging torque of the machine. This part can be divided into: cogging torque and torque ripple calculations, iron losses and terminal voltage of the machines, and PM eddy current losses.
  - Different modeling techniques are introduced in chapter 3. These models are based on 3D and 2D multi-slice modeling techniques. Furthermore, different concepts of analytical models are developed. They are

based on conformal mapping models and the subdomain models. A comparison between these models is described and validated. Each modeling technique can be used to precisely compute certain parameters. These points are highlighted and deeply investigated. In this chapter, a 50kW machine is used to validate all the models. The number of poles and slots in this machine are 70 poles and 60 slots.

  - In addition, a novel analytical model, based on a combined solution of Maxwell's equations and a magnetic equivalent circuit (MEC), is developed in chapter 4. This model takes into account the non-linear behavior of the magnetic material. This model can accurately compute the iron losses and terminal voltage. This model is validated through 3D and 2D finite element models. In this chapter, a 5kW machine is used to validate all the models. The number of poles and slots in this machine are 16 poles and 15 slots.
  - In chapter 5, an electric circuit network is developed to compute the eddy current losses in the permanent magnets. The solution of Maxwell's equations is applied to this electric network. This network is verified through a complete 3D transient finite element model and different concepts of FE simulations. In this chapter, the same machine described in chapter 4 is used.

- An electromagnetic design toolbox is developed for the axial flux permanent magnet machines in chapter 6. This toolbox is developed to optimize the machine's geometry based on the required input power and speed of the application. Thanks to the developed analytical models described before, the design toolbox gives the geometrical machine parameters in a very short time and in an accurate way. In addition, a sensitivity analysis is done for different machine's geometrical parameters to select the optimum values for machines operating in the field weakening region. It is also worth-mentioning that this toolbox has been used to design a 100kW YASA machine for a wind turbine application. The prototype of this machine is still under construction.

- An experimental research prototype was developed in the laboratory together with several colleagues to validate the electromagnetic models described before. This experimental setup is described in chapter 8. Furthermore, an overview of the cooling concept of the stator core and winding is evaluated. This cooling concept is based on an inward fins that are placed behind the windings to provide a new path for evacuating the heat.

- Finally, chapter 7, thermal models are developed to evaluate the complete performance of the axial flux machine. These models are based on finite element and lumped parameter thermal network. The main advantage of these models is the introduction of convection coefficient equations that allow the separation of the stator and rotor models. These convection co-

efficient equations are developed by Alireza Rasekh in the department of Flow, Heat and Combustion Mechanics of Ghent University under the FWO project G.0110.13. This separation allows very accurate and fast results to be obtained. These models are provided in chapter 7. Experimental verifications ar provided in the end of the chapter.

- Chapter 9 concludes this work and makes some proposals for future research in the domain of axial flux PM machines with the focus on their applications.

1.4 Scientific Publications

1.4.1 Articles in International SCI Journals

An overview of journal papers published in peer-reviewed international journals at the time of publication of this thesis:

- A. Hemeida, M. Taha, A. A.−E. Abdallh, H. Vansompel, L. Dupré, P. Sergeant, "Applicability of Fractional Slot Axial Flux Permanent Magnet Synchronous Machines in the Field Weakening Region," *IEEE Transactions on Energy Conversion*, vol. 32, no. 1, pp. 111−121, 2017.

- Y. Huang, B. Guo, Y. Guo, J. Zhu, A. Hemeida, and P. Sergeant, "Analytical modeling of axial flux PM machines with eccentricities," *International Journal of Applied Electromagnetics and Mechanics*, vol. 53, no. 4, pp. 757−777, Apr. 2017.

- Y. Huang, B. Guo, A. Hemeida, and P. Sergeant, "Analytical Modeling of Static Eccentricities in Axial Flux Permanent-Magnet Machines with Concentrated Windings," *Energies*, vol. 9, no. 12, p. 892, Oct. 2016.

- A. Hemeida, B. Hannon, H. Vansompel, and P. Sergeant, "Comparison of Three Analytical Methods For The Precise Calculation of Cogging Torque and Torque Ripple in Axial Flux PM Machines," *Mathematical Problems in Engineering*, Art. 2171547, 2016.

- H. Vansompel, A. Rasekh, A. Hemeida, J. Vierendeels, and P. Sergeant, "Coupled Electromagnetic and Thermal Analysis of an Axial Flux PM Machine," *in IEEE Transactions on Magnetics*, vol. 51, no. 11, pp. 1−4, Nov. 2015.

- A. Hemeida, P. Sergeant, and H. Vansompel, "Comparison of Methods for Permanent Magnet Eddy Current Loss Computations With and Without Reaction Field Considerations in Axial Flux PMSM," *IEEE Transactions on Magnetics*, vol. 51, Art. 8107511, Sep. 2015.

- A. Hemeida and P. Sergeant, "Analytical Modeling of Surface PMSM Using a Combined Solution of Maxwell's Equations and Magnetic Equivalent Circuit," *IEEE Transactions on Magnetics*, vol. 50, no. 12, Art. 7027913, 2014.

- P. Sergeant, H. Vansompel, A. Hemeida, A. Van den Bossche, and L. Dupré, "A computationally efficient method to determine iron and magnet losses in VSI-PWM fed axial flux permanent magnet synchronous machines," *IEEE Transactions on Magnetics*, vol. 50, no. 8, Art. 8101710, 2014.

1.4.2 Publications in the Proceedings of International Conferences

An overview of conference papers:

- A. Hemeida and P. Sergeant, "Impact of single layer, double layer and four layer windings on the performance of AFPMSMs," *2016 19th International Conference on Electrical Machines and Systems (ICEMS)*, Chiba, Japan, 2016, pp. 1−6.

- A. Hemeida, P. Sergeant, A. Rasekh, H. Vansompel and J. Vierendeels, "An optimal design of a 5MW AFPMSM for wind turbine applications using analytical model," *2016 XXII International Conference on Electrical Machines (ICEM)*, Lausanne, Switzerland, 2016, pp. 1290−1297.

- A. Hemeida, M. Taha and P. Sergeant, "High speed operation design considerations for fractional slot axial flux PMSM," *2015 IEEE Workshop on Electrical Machines Design, Control and Diagnosis (WEMDCD)*, Torino, Italy, 2015, pp. 97−103.

- A. Hemeida and P. Sergeant, "Analytical modeling of eddy current losses in Axial Flux PMSM using resistance network," *2014 International Conference on Electrical Machines (ICEM)*, Berlin, Germany, 2014, pp. 2688−2694.

Chapter 2

The Yokeless and Segmented Armature (YASA) Machine

2.1 Introduction

Axial flux permanent magnet synchronous machines (AFPMSMs) have been the subject of significant, worldwide research efforts for the past 20 years and can now be considered as mature technology. The proof is their use in a wide variety of applications, from renewable energy systems in [1–6] to electric vehicle applications in [7–10].

Wherever extreme axial compactness, high torque density and high efficiency are necessary, AFPMSMs can provide great opportunities. AFPMSM topologies have been extensively investigated in the literature. The authors in [11] reviewed the literature for the most recent development of AFPMSM electromagnetic modeling, thermal modeling, mechanical modeling, and assembling enhancements.

The basic operation principle of a surface AFPMSM is – similar to conventional radial flux permanent magnet machines – based on the interaction between two sources of rotating magnetic fields. One rotating magnetic field is produced by the permanent magnets (PMs). These PMs are mounted on the surface of the rotor. As adjacent permanent magnets are alternately magnetized, they produce a pulsating magnetic field that crosses the air gap to the stator and returns back again to the rotor in a stationary mode. This field rotates in the space while the rotor is rotating.

In the stator, a time varying magnetic flux is generated in the stator teeth by the currents induced in the windings. The interaction between the two fields produces a force. This force produces the required torque. Like most electric machines, the AFPMSM can be motor or generator. In motor mode, electric power is transferred into mechanical power, available at the shaft of the machine. In generator mode, the rotating magnetic field produced by the PMs induces a back electromotive force (EMF) in the stator windings. This back EMF produces a current in the

connected load. Therefore, the power is transferred from the mechanical source to the connected electric load.

The operation principles of both the radial flux permanent magnet synchronous machine (RFPMSMS) and the AFPMSM are the the same. However, they differ in the orientation of the magnetic field produced by the PMs with respect to the rotation direction. The magnetic field in the RFPMSM is produced in the radial direction. In the AFPMSM, the magnetic field is produced in the axial direction.

Many authors reviewed the differences between different configurations of RFPMSMs and AFPMSMs. They are summarized in [11, 12]. They are briefly summarized in this chapter.

There are several types of AFPMSMs technologies described in literature. The hierarchy of the division is summarized in Fig. 2.1 and explained in more details in the next section. They are subdivided according to the following criterion. [11].

- The structure configuration: number of stators and rotors.
- Iron cored or coreless stator.
- The core configuration: slotted or slot-less stator.
- The winding configuration: drum winding or ring winding. Fig. 2.2 (a) shows an example of a drum winding. When the stator is slotted, drum windings are used. They are also known as tooth-wound windings. These windings can be a distributed or a fractional slot concentrated winding (FSCW). On the other hand, ring windings, also known as back to back, toroidal or core-wound windings have end connections placed axially on the outer and inner radius of the machine; this type of winding is always a FSCW, and an example is shown in Fig. 2.2 (b).
- The permanent magnet (PM) configuration. The two PMs opposing each other can have either the same polarities or opposite polarities. Different machines concepts with different polarities are described in Figs. 2.3 (a), (b), (c) and (d).

2.2 AFPMSMs Topologies

AFPMSMs can be classified into four general types. They are described in Fig. 2.1 in the first column of the figure. The AFPM machine is a structure with either surface mounted or interior PMs, with or without armature slots, with or without armature core, with ring winding or drum winding, and single or multi-stage.

The AFPM machines are classified as single-stator single-rotor (SSSR), single-stator double-rotor (SSDR), double-stator single-rotor (DSSR), or multi-stator multi-rotor (MSMR). All mentioned design configurations are briefly described in the following sections [12].

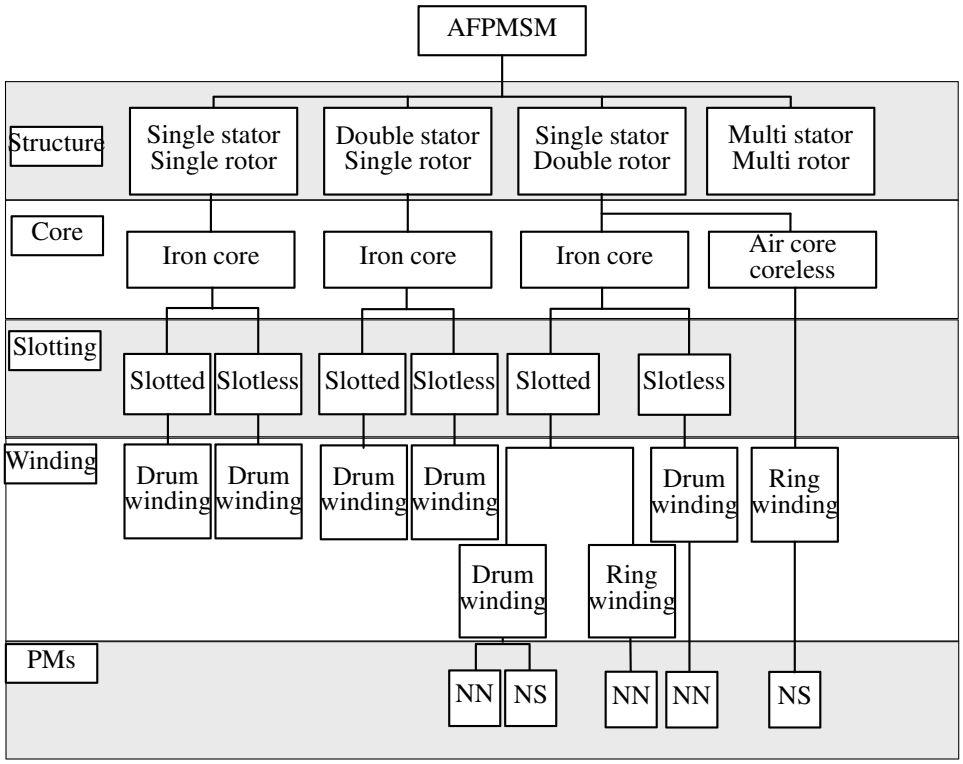

Figure 2.1: AFPMSM topologies. [12]

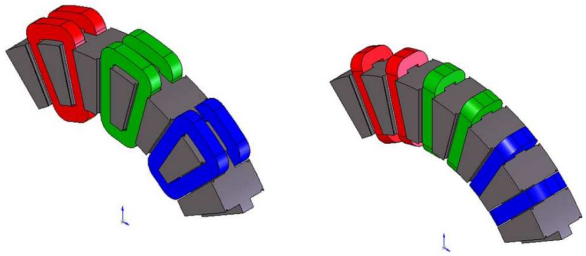

(a) (b)

Figure 2.2: AFPMSM winding types: (a) drum (tooth wound) and (b) ring (core wound). [11]

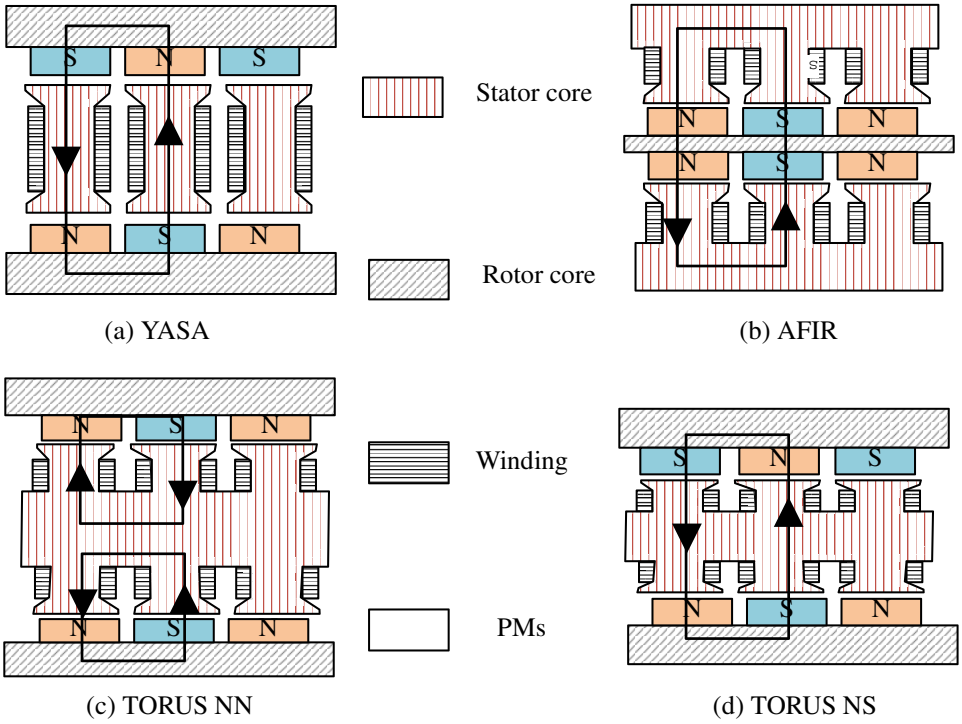

Figure 2.3: Schematic representation of different configurations of the AF-PMSM.

2.2.1 Single Stator Single Rotor (SSSR)

The most basic version of an axial flux machine is composed of only a single stator and a single rotor (SSSR) on which the permanent magnets are mounted [13, 14]. This configuration is shown in Fig. 2.4.

In the SSSR topology, the stator iron core is composed of a yoke and teeth as shown in Fig. 2.4. The teeth carry the windings that are placed in the slots between the teeth. The yoke is used as a return path for the flux density inside the machine. In addition, it is used as a mechanical fixation of the stator to the structure of the machine. The PMs are mounted on the rotor surface and are magnetized in the axial direction.

The magnetic flux is produced by the PMs and the currents in the windings. The flux lines flow axially in the PMs and the teeth. In addition, they flow circumferentially in the rotor and the stator yoke.

The major disadvantage of this machine is the unbalanced axial force between the stator and the rotor, which may twist the structure easily [13]. Therefore, the bearings must be dimensioned to handle a greater axial force.

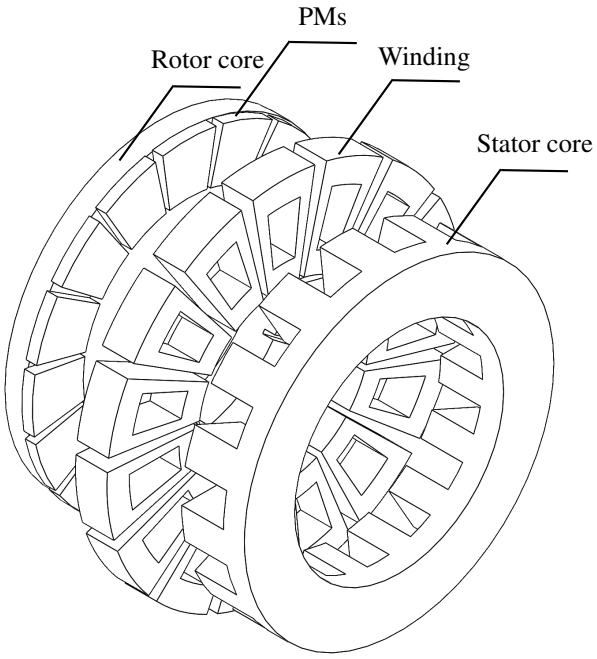

Figure 2.4: Schematic representation of the basic version of AFPMSM: Single stator single rotor.

2.2.2 Double Stator Single Rotor (DSSR)

The second topology is the double stator single rotor (DSSR) topology, known as the axial flux internal rotor (AFIR) [15, 16]. The construction of the machine is shown in Fig. 2.5. Fig. 2.3 (b) shows the simplified geometry of this topology, in a 2D plane at constant radius.

The cored version of the DSSR topology is shown in Fig. 2.5 and offers some extra reliability since it is able to operate with only one stator if the stators are connected in parallel [17]. The stator losses are distributed between the two stators and because of the large surface of the stators, it is rather easy to cool them by air. Theoretically, no rotor core is needed for this topology, as the magnetic flux path is only in the axial direction through the rotor. The magnetic path for this configuration is shown in Fig. 2.3 (b).

In this topology, many authors investigated the opportunity for gluing the PMs on the surface of the rotor or buried inside the rotor [16].

In case of slotted windings, the stator is made of a material with high permeability (laminated silicon steel, soft magnetic composite, amorphous iron) and the winding is placed in the stator slots. The main disadvantage of using a slotted winding is the so called cogging torque: a ripple in the torque at no-load. This

cogging torque is caused by the stator slot openings near the air gap. These slot openings result in a rotor position dependent torque as a result of the interaction (change in permeance) of the permanent magnets and the stator slots. The absence or at least minimization of these cogging torques is crucial in distinct applications. For example, the cogging torque can prevent generators in wind turbines to start up at low wind speeds and therefore decrease the annual energy yield of the wind turbine.

In wind turbine applications, usually coreless (air cored) windings are introduced. In coreless DSSR axial flux PM machines, the winding is mostly embedded in an epoxy resin having unit permeability. Despite the absence of cogging, the lower mass of the machine and the absence of core losses, the high equivalent air gap thickness requires relatively high permanent magnet volumes to obtain sufficiently high magnetic fluxes in the windings. The permanent magnets very often contain rare earth materials such as Neodymium, Samarium, Dysprosium. The rare-earth PMs are costly compared to silicon steel and copper. Therefore, the reduction of cogging torque in axial flux PM machines with slotted windings is a topic of much recent scientific research.

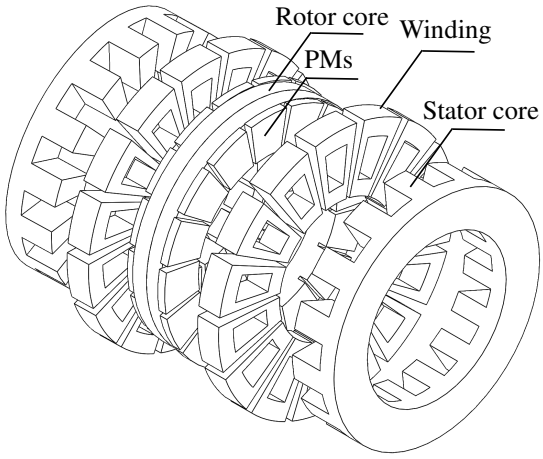

Figure 2.5: Schematic representation of the double stator single rotor topology.

2.2.3 Single Stator Double Rotor (SSDR)

In the SSDR topology, the stator is located between two rotors [18]. Three main classes in the stator construction can be distinguished: a stator with slotted windings, a slot-less stator and a coreless stator [19–21].

The cored versions of the stator cores are shown in Figs. 2.6 and 2.7. These

topologies are called the toroidally wound internal stator (TORUS) machine [17]. Figs. 2.3 (c) and (d) show the simplified geometry of two different types of of the TORUS topology, in a 2D plane at constant radius.

The TORUS machine consists of a stator in the middle between the two rotors. The stator consists of double sided teeth on both axial sides and a stator yoke in the middle between them. In the rotor, the arrangement of the magnets has an effect on the main flux path in the machine rotor and stator [22]. As a consequence, there are two types of the TORUS machine studied in literature. Both types are shown in Figs. 2.6 and 2.7. They are described below.

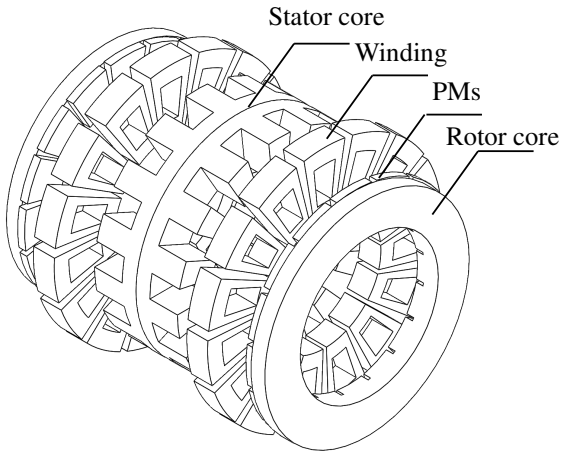

Figure 2.6: Schematic representation of the single stator double rotor topology of the NS type (TORUS NS).

- Figure 2.6 shows the north-south (NS) type of the TORUS machine. If a north pole (N) of the PM on one rotor is facing a south pole (S) on the other rotor, then the flux lines flow axially in the stator yoke and return through the rotors circumferentially. This configuration is the so called the NS TORUS configuration. In this configuration, the winding is toroidally wound around the stator tooth as shown in Fig. 2.6. The flux lines flow is shown in Fig. 2.3 (d).

- On the other hand, in the north-north (NN) TORUS configuration shown in Fig. 2.7, if the two rotors have the PMs of the same polarity facing each other, then the flux lines flow circumferentially in the stator yoke. In this configuration, the winding is toroidally wound around the stator yoke as shown in Fig. 2.7. The flux lines flow is shown in Fig. 2.3 (c).

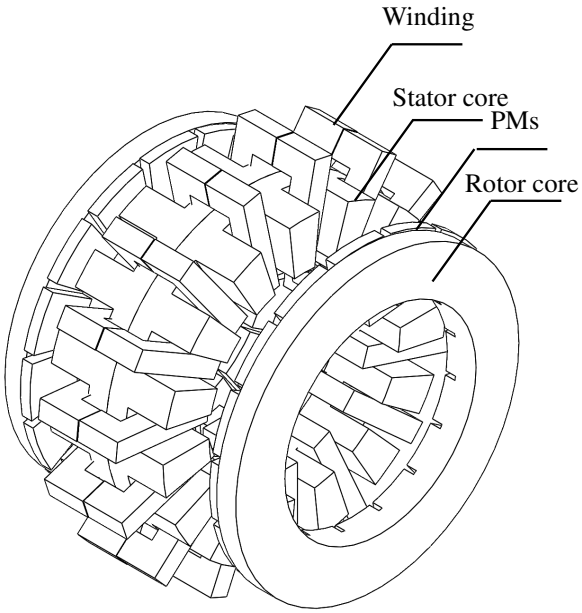

Figure 2.7: Schematic representation of the single stator double rotor topology of the NN type (TORUS NN).

For the north-north (NN) TORUS machine, shown in Fig. 2.7, the phase winding is wound around the stator yoke giving short end windings in both the axial and radial directions of the machine. In this structure, the copper losses are reduced due to the very short end windings. However, a thicker stator yoke is needed to attain the magnetic flux passing through it. Therefore, the mass and iron losses of the stator core are larger than in the NS configuration.

The yokeless and segmented armature (YASA) topology, shown in Fig. 2.8, was introduced in [7] to combine the advantages of both the shorter end windings of the NN type and the short stator yoke of the NS type. Fig. 2.3 (a) shows the simplified geometry of the YASA topology, in a 2D plane at constant radius.

Starting from the original NS TORUS topology, the following manipulations are performed:

- In the NS TORUS configuration, from electromagnetic point of view, there is no need for the stator yoke. This is clearly illustrated by the flux line paths in Fig. 2.3 (a). Therefore, the stator yoke is removed entirely in the YASA machine. This increases the power density and the efficiency of the machine. This results in the existence of individually segmented armature elements.

- By enlarging the pitch of the teeth so that their arc is similar to the PMs, fractional slot concentrated windings (FSCW) [23] can be used. Therefore,

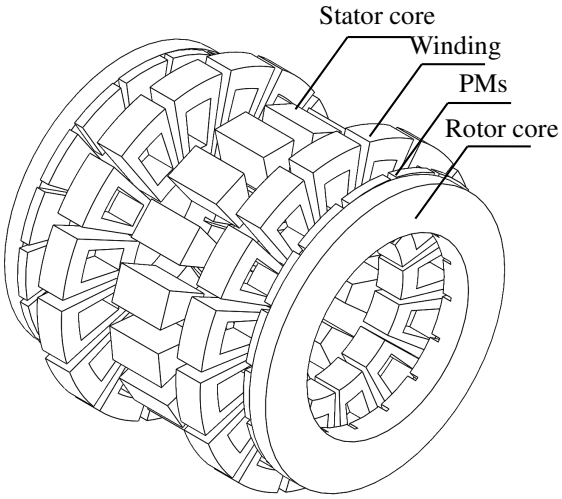

Figure 2.8: Schematic presentation of the single stator double rotor scheme (YASA).

each coil can be wound around one tooth. This makes the manufacturing process much easier.

- Using a double layer FSCW, the winding arrangement complexity is reduced. This winding arrangement allows the winding to be toroidally wound around the tooth. This is often called a tooth coil winding.

Therefore, the YASA machine has proven a great opportunity to be used for several applications instead of the TORUS machine. The absence of the stator yoke provides a better power density and a better efficiency due to the shorter axial length of the stator iron core.

2.2.4 Multi Stator Multi Rotor (MSMR)

A multistage AFPM machine can be constructed from either DSSR or SSDR configurations [24]. This machine includes the N stators and $N + 1$ rotors that have the same mechanical shaft. The stator windings can be connected either in parallel or in series. The multistage configuration enhances the torque and power density without increasing the machine diameter.

Multi-stack machines described in [25, 26], can be used in wind energy applications to reduce the outer diameter of the total machine and hence reduce the total structural mass. On the other hand, the axial length of the machine is increased.

2.3 Why Yokeless and Segmented Armature (YASA) Machine?

Many authors compared AFPMSMs with other synchronous machines topologies such as radial and transverse flux machines.

In [27], the authors designed and evaluated a radial flux permanent magnet synchronous machines (RFPMSMs) and four AFPMSMs configurations: a SSSR slotted axial field machine, a DSSR slotted axial field machine, a SSSR slot-less axial field machine, and a DSSR slot-less axial field machine. Designs were done for five power levels, ranging from 0.25 kW to 10 kW. Key conclusions are: the AFPMSMs designs have the highest power densities for a given amount of permanent magnet material and a given air-gap flux density.

In [28], the authors compared the DSSR AFPM motor performance with the RFPM machine in terms of provided electromagnetic torque and torque density, when the overall motor volume, losses per surface, and the air-gap flux density are kept constant. The results indicated that AFPMSM configuration had a better performance in terms of electromagnetic torque and torque density if the number of poles is high (more than 10) and the axial length is short.

From these studies, the AFPMSMs provided a great performance to be used for a wide range of applications. Therefore, the AFPMSM is used in this thesis to be deeply investigated.

In [29], a comparative study between different types of radial and axial flux machine types till 200 kW for wind turbine applications was done. The comparison was done for the same voltage, power factor and the same current density. It was shown that the axial machine has a smaller mass for a given power, *i.e.* higher power density. It was also proven in [29] that the yokeless and segmented armature (YASA) type machine has the highest power density. Therefore, in this thesis, we focus only on the YASA topology of the surface AFPMSM. This topology has proven great robustness in terms of power density and efficiency.

For further improvement of the research in the topic area of the YASA machine, some further research aspects are done for the modeling and design of this machine. A design toolbox has been developed in this thesis to optimally design the AFPMSM for any geometrical parameters including the slots, poles and phases. This design toolbox is based on analytical models that are developed in this thesis. These analytical models are capable of estimating all electromagnetic parameters of the machine. All analytical models are verified by 2D and 3D finite element (FE) models. In addition, a lumped parameter thermal network is also developed to have a complete multi-physical optimal design of the AFPMSM.

2.4 Conclusions

In this chapter, a brief review of the most developed AFPMSM topologies existing in literature is done. Based on literature, a comparison between these topologies is done afterwards. This comparison revealed that the YASA type is the optimum selection compared to the other topologies. Thanks to the absence of the yoke, the YASA machine provides the greatest power density and efficiency compared to other machines. Several comparative studies between the YASA and other machines have been addressed. They show that the YASA machine would be the optimum selection. Therefore, in this thesis, the YASA machine is selected to be further studied.

Chapter 3

Modeling of Axial Flux Permanent Magnet Synchronous Machines

3.1 Introduction

Accurate and fast modeling techniques are indispensable for a complete design of electric machines. A multi-physical design is mandatory *i.e.* for involving thermal, electromagnetic, and mechanical modeling. This chapter studies only the electromagnetic behaviour of the machine. The thermal behaviour is studied in Chapter 7. The mechanical design is out of the scope.

This chapter describes various electromagnetic modeling techniques to describe the air gap flux density inside the machine as well as performance indicators.

Cogging torque and torque ripple are one of the most important performance indicators in the design of electrical machines. It is important in almost all machines to keep these values as low as possible. Therefore, a large number of finite element (FE) and analytical models have been developed to analyze these parameters. the aforementioned authors have reported good accordance with FE calculations.

Different techniques like permanent magnet (PM) skewing, pole arc shifting, and optimized PM shapes are used to reduce the cogging torque and the torque ripple [30]. In addition, a proper selection of the slot opening might give an optimum performance in terms of cogging torque and the torque ripple [31]. The scope of this chapter is to compare different modeling techniques based on their computational efficiency and accuracy.

Numerous modeling techniques were used in the past few decades for these types of machines. Two types of models are mainly used in electric machines *i.e.* the finite element (FE) models and the analytical models. Multi-slice technique uses 2D FE models.

A 3D FE model is considered to be the most accurate model to predict the cogging torque and torque ripple [32]. However, such a model is very time consuming.

Faster 2D FE based techniques are developed in [33–35]. These techniques consist of three steps. Firstly, the AFPMSM is divided in a number of slices in the radial direction. Secondly, the solution is obtained by a 2D FE model for each slice and finally the obtained solutions are combined using superposition. This type of models neglects the radial flux, which results in a less accurate solution. Although these quasi-3D models require less computational time than classic 3D models, their computational time consumption is still quite large.

Therefore, analytical models are developed to obtain fast and accurate results. Analytical tools are important for the sake of fast and accurate design and optimization of electric machines. Therefore, analytical models are used in AFPMSM optimization in many articles in [22, 36].

Another comparative study between these different concepts for AFPMSMs has been applied by Hemeida *et al* in [37]. The conclusion is that for the calculation of the no load voltages, the result is satisfactory for the all methods. However, for torque ripple and cogging torque calculation, the subdomain (SD) model is the most accurate technique to predict them. In addition, the impact of number of slices is studied on the performance of the result.

In this chapter, a comparison between different analytical and finite-element (FE) tools for the computation of cogging torque and torque ripple in axial-flux permanent-magnet synchronous machines is made. 2D and 3D FE models are the most accurate for the computation of cogging torque and torque ripple. However, they are too time consuming to be used for optimization studies. Therefore, analytical tools are also used to obtain the cogging torque and torque ripple. Three types of analytical models are considered and validated. They are all based on dividing the machine into many slices in the radial direction. One model computes the lateral force based on the magnetic field distribution in the air gap area. Another model is based on conformal mapping and uses complex Schwarz-Christoffel (SC) transformations. The last model is based on the subdomain technique, which divides the studied geometry into a number of separate domains. The different types of models are compared for different slot openings and permanent-magnet widths. One of the main conclusions is that the subdomain model is best suited to compute the cogging torque and torque ripple with a much higher accuracy than the SC model.

3.2 Test Case Machine

In order to validate the model, an axial flux machine with fractional slot concentrated winding (FSCW) of 70 poles and 60 tooth coil windings has been studied. The geometrical properties of the machine are described in Table 3.1.

Table 3.1: Experimental setup geometrical parameters. [37]

Parameter	Symbol	Value
Rated Power	P_{n}	50kW
Number of pole pairs	$p = N_{\mathrm{m}}/2$	35
Number of stator slots	N_{s}	60
Rated speed	n_{rated}	60 rpm
Rated Torque	T_{em}	8 kNm
Outer diameter	D_{o}	1.1 m
Inner diameter	D_{i}	0.9 m
Axial length core element	$2(Y_{\mathrm{c1}} + Y_{\mathrm{c2}} + Y_{\mathrm{c3}})$	114 mm
Axial length slot	$2Y_{\mathrm{c1}}$	100 mm
Tooth width	T_{w}	25 mm
Slot opening width	b_{so}	8 mm
Air gap axial length	g	1 mm
PM axial length	Y_{m}	5 mm

A test case machine of 50kW that is designed for wind turbine application is simulated to validate the results. The number of poles and slots are multipliers of 14 poles and 12 slots combination. The star of the slot is developed by the author and can generate any combination of slots, poles, and phases. The star of the slot for this combination is shown in Fig. 3.1.

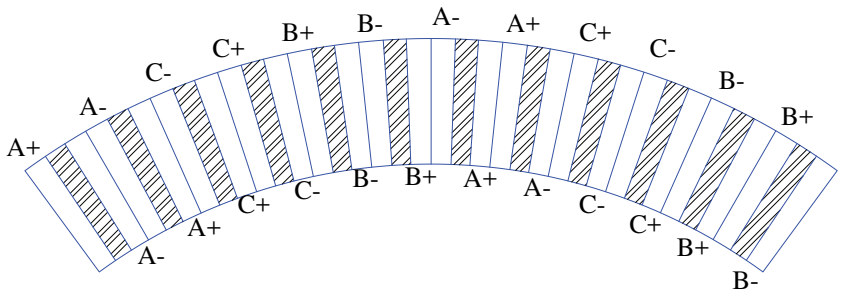

Figure 3.1: Phases distribution across the circumference for the 60 slot 70 pole combination.

3.3 Description of the Finite Element (FE) Models

In the 3D and 2D multi-slice FE models, described in Figs. 3.2 (a) and (c) respectively, Only half of the machine is modeled and symmetry boundary condition is imposed at half of the tooth. In this chapter and chapter 4, the 3D, and 2D FE models and analytical models are solved for static solutions. The rotor disc is rotated

manually by a certain step assuming no solution from the previous steps. In these static simulations, time dependent eddy currents in electric conductive materials such as the neodymium permanent magnets, cannot be calculated simultaneously. However, eddy currents are calculated *a posteriori* using the data retrieved from static simulations. In addition, a complete transient 3D solution is introduced in chapter 5. However, a complete transient 3D FE solution can consume weeks to obtain a good result without a significance benefit as will be shown in Chapter 5. Within the scope of this chapter, it is assumed that the influence of the magnetic field produced by the induced eddy currents is minor to the magnetic fields obtained through static simulations. This is the so called resistance limited approach.

3.3.1 3D FE Model

In this section, the 3D and 2D FE models are described, and analyzed. The 3D FE model will serve as the reference solution to evaluate the accuracy of the other FE and analytical models. The 3D FE is shown in Fig. 3.2 (a).

Half of the machine is modeled in Fig. 3.2 (a). An even symmetry plane is placed in half of the machine to let the flux lines flows in the perpendicular plane to the stator surface. The no-load flux density distribution of the machine is shown in Fig. 3.3 for the 3D FE model.

3.3.2 2D Multi-slice FE Model

The idea of this method is to stretch the machine over the the radial length of the machine to n_s slices. Each slice has an average radius of R^i_av in (3.1) and a radial length t_cp in (3.1). The 3D to 2D transformation is shown in Fig. 3.2 (b). In all the 2D FE models, the radial component of the magnetic flux density is neglected. Each slice represents a 2D FE model shown in Fig. 3.2 (c). The axis definition in Fig. 3.2 (b) is R for the radial direction, and θ_m for circumferential direction. The y-axis in Fig. 3.2 (c) presents the axial direction. This method will lack the ability to compute the radial flux component.

$$\begin{aligned} R^\mathrm{i}_\mathrm{av} = R_\mathrm{i} + \frac{R_\mathrm{o} - R_\mathrm{i}}{n_\mathrm{s}} \left(i - \frac{1}{2} \right), \quad i = 1, 2, ..., n, \\ t_\mathrm{cp} = \frac{R_\mathrm{o} - R_\mathrm{i}}{n_\mathrm{s}}, \end{aligned} \tag{3.1}$$

where R_o is the outer radius of the machine, R_i is the inner radius, and n_s is the number of slices. By applying Maxwell's equations on each slice and by summing the air gap flux due to the armature current and the PMs, it is possible to obtain any quantity like torque.

On the surface, shown in Fig. 3.2 (c), a 2D FE solver is applied in the cartesian coordinate system. This FE solver calculates the magnetic vector potential

over the defined geometries. The magnetic vector potential has only a component perpendicular to the computation plane, *i.e.* the z-direction.

$$\mathbf{A} = A_z \mathbf{e}_z. \tag{3.2}$$

and the magnetic flux density can be expressed by:

$$\mathbf{B} = B_x \mathbf{e}_x + B_y \mathbf{e}_y, \tag{3.3}$$

where $\mathbf{e}_x$ and $\mathbf{e}_y$ are the unit vectors in the x and y directions.

The x- and y-directions are defined in Figs. 3.4 (a) and (b). The flux densities are calculated afterwards from the magnetic vector potential.

$$B_{\mathrm{x}} = \frac{\partial A_z}{\partial y}, \tag{3.4}$$

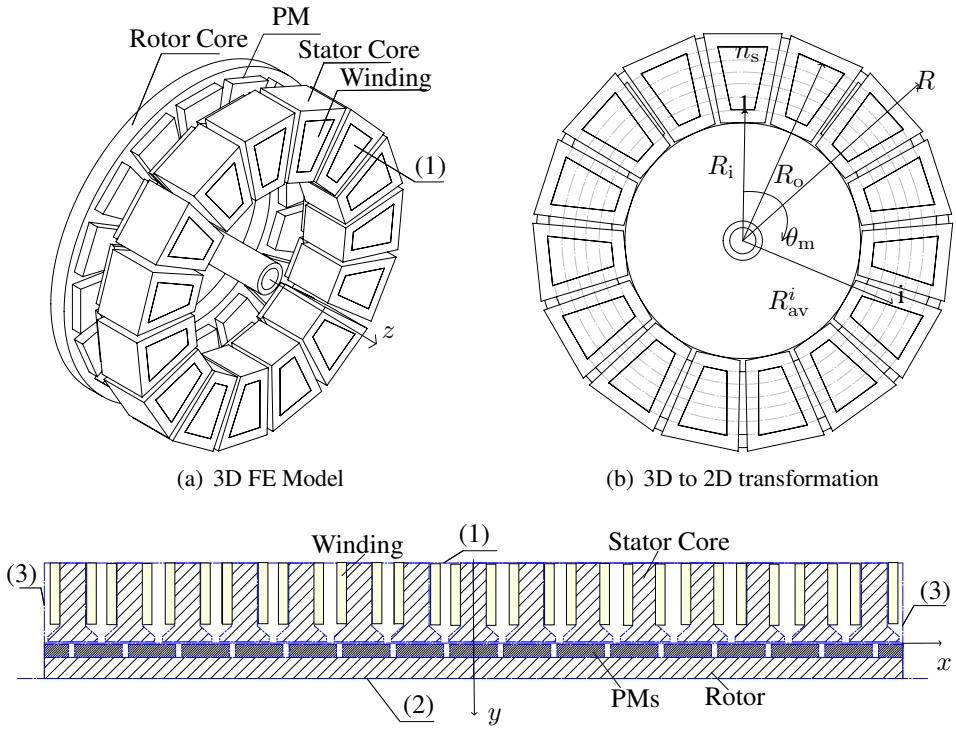

Figure 3.2: 3D and 2D FE models. (1) Neumann boundary condition. (2) Dirichlet boundary condition. (3) Periodic boundary condition.

and

$$B_y = -\frac{\partial A_z}{\partial x}. \tag{3.5}$$

The 2D FE analysis requires the correct imposition of the boundary conditions. An illustrative overview of the finite element model is suggested in Fig. 3.2 (c). The boundary conditions are described as follows [35]:

- Only half of the machine is modeled, therefore, axial symmetry (1) is presented at half of the stator tooth (Neumann boundary conditions). The tangential magnetic field equals zero on this surface:

$$\mathbf{n} \times \mathbf{H} = 0. \tag{3.6}$$

- Furthermore it is assumed that the magnetic field lines do not exit the outer side of the rotor disc. Therefore, the Dirichlet boundary condition is expressed at the edge indicated by (2). The Dirichlet boundary condition imposes that the normal component to the boundary vanishes and is expressed through:

$$A_z = 0. \tag{3.7}$$

- A continuity in the solution for the magnetic vector potential along this edge, indicated by (3), should be included in the finite element model. This is done

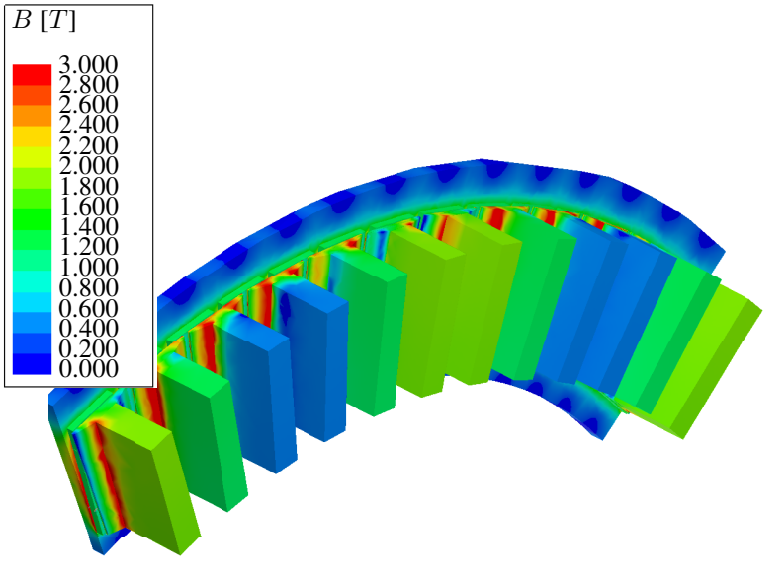

Figure 3.3: 3D field distribution of the machine at no load.

by introducing a periodic boundary condition. If $\mathbf{A}_{z1}$ and $\mathbf{A}_{z2}$ are the magnetic vector potentials at both sides of the model, then the periodic boundary condition requires that:

$$A_{z1} = A_{z2}. \tag{3.8}$$

The number of model symmetries (sym) is calculated as the greatest common divisor (gcd) between the number of slots N_s and the number of pole pairs $p = N_\mathrm{m}/2$. Therefore, only part of the machine is modeled depending on the symmetry value.

$$sym = \gcd(N_\mathrm{s}, p). \tag{3.9}$$

Different material properties are assigned to the defined subdomains.

- In the air gap region, the equation for the magnetic vector potential is defined by;

$$\nabla \times \left(\frac{1}{\mu_0} \nabla \times \mathbf{A} \right) = 0. \tag{3.10}$$

- In the permanent magnet region, the magnetic remanence B_rem (estimated as 1.26T for NdFeB) as well as the relative permeability μ_r (estimated as 1.05 for NdFeB) are taken into account when defining the magnetic vector potential;

$$\nabla \times \left(\frac{1}{\mu_0 \mu_\mathrm{r}} \nabla \times \mathbf{A} - \mathbf{B}_\mathrm{rem} \right) = 0. \tag{3.11}$$

- As the winding sections carry a current density **J**, the equation for the magnetic vector potential in this region becomes:

$$\nabla \times \left(\frac{1}{\mu_0} \nabla \times \mathbf{A} \right) = \mathbf{J}. \tag{3.12}$$

- Finally, there are the subdomains defining the stator cores and the rotor disc. As both parts are made of a steel grade with a good relative permeability μ_r, the magnetic vector potential in these subdomains is expressed by:

$$\nabla \times \left(\frac{1}{\mu_0 \mu_\mathrm{r}} \nabla \times \mathbf{A} \right) = 0. \tag{3.13}$$

The relative permeability is modelled by a constant value μ_r, when linear behaviour of the material is sufficient. In this chapter, the iron core relative magnetic permeability of both the 3D and the 2D FE models of the stator and rotor cores is set to 10000.

For the rotor disks, a constant permeability is assumed. While this model is still isotropic, all magnetic properties are the same in all directions which is a good assumption for non-oriented steel grades.

All analytical models are based on defining open slots without tooth tips. Of course, an important fraction of the electric machines does have tooth tips. Therefore, two versions of the 2D FE model are considered, one with and without tooth tips. Both 2D finite element models are shown in Figs. 3.4 (a) and (b).

The x-axis represents the circumferential distance which equals $x = \theta_{\mathrm{m}} R^i_{\mathrm{av}}$, where θ_{m} is the circumferential angle shown in Fig. 3.2 (b). The y-axis represents the axial direction of the machine measured from the stator tooth surface.

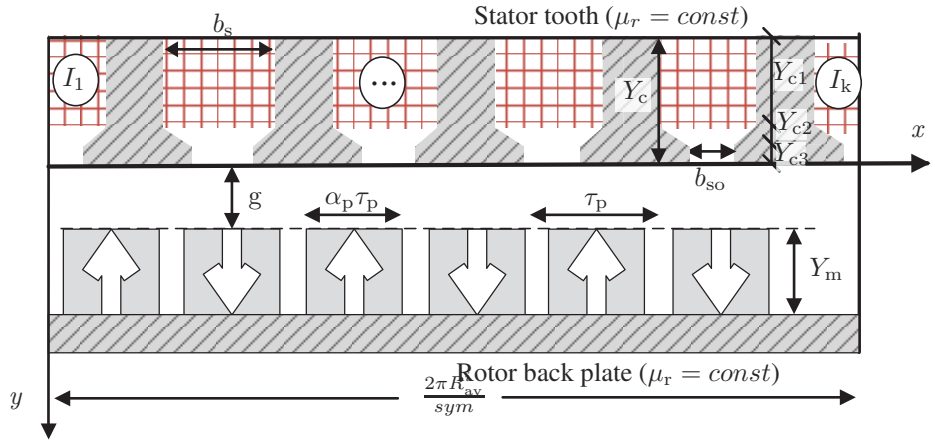

(a) 2D FE Model including tooth tips

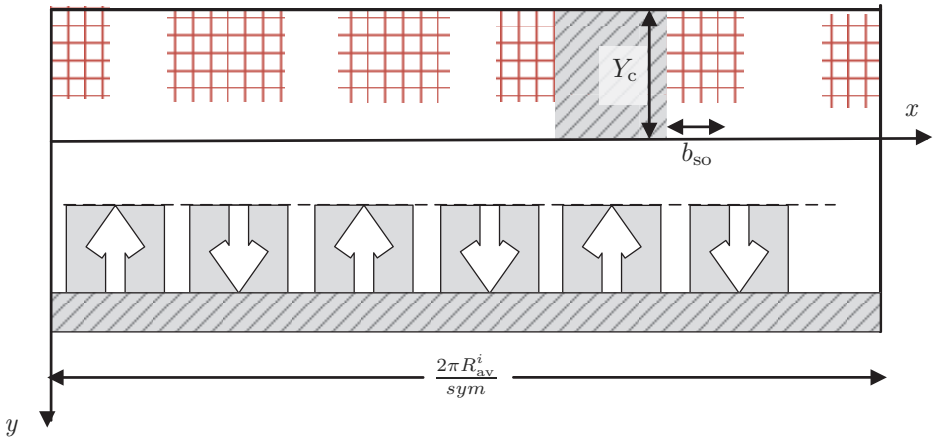

(b) 2D FE Model without tooth tips

Figure 3.4: Different 2D FE models geometries and assumptions.

To summarize, the assumptions taken into account for all FE models and all analytical models in this chapter are;

- The permeability of the rotor and stator tooth is assumed to be constant for

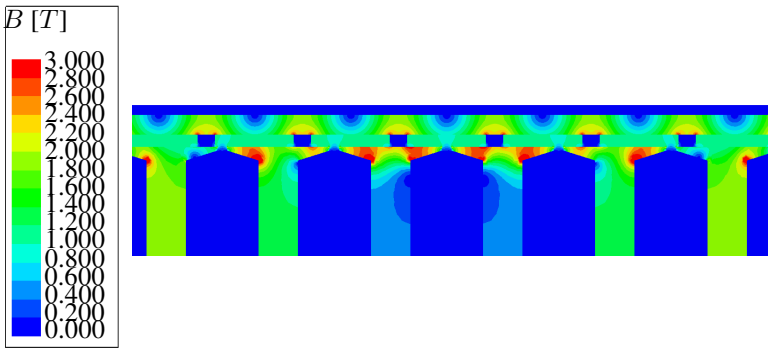

Figure 3.5: The 2D FE model flux distribution at no load at slice number 8.

the FE models and equals 10000 and infinite for the analytical model.

- The eddy current in the PMs are neglected. The eddy currents can be reduced by segmenting the PMs as described in [38].
- The PMs have a constant recoil permeability of μ_{rec}.

The no-load flux distribution of the 2D FE model is shown in Fig. 3.5 for the geometry with tooth tips. Both 2D FE models use an extremely fine mesh in the air gap area, which results in a reliable solution for the torque ripple and cogging torque. The 2D FE model without tooth tips will be used as reference solution to compare the different analytical models. The comparisons between different models are illustrated in section 3.5.

3.4 Description of the Analytical Models

The models that are introduced in this section calculate the flux density in the air gap area using the analytical tools.

There are different concepts of analytical models, each of which requires an accurate computation of the flux density to calculate the electromagnetic parameters. An overview of different analytical model concepts is described in [39]. These concepts can be divided in two main categories *i.e.* Maxwell's equations and magnetic equivalent circuit (MEC). The MEC is discussed in details in Chapter 4.

Maxwell's equations solve the problem in 2D. They divide the 3D structure of the AFPMSMs into 2D slices in the radial direction. A superposition of the solution of different slices is done afterwards to obtain the complete solution.

The first category is based on obtaining the flux density due to permanent magnets and armature reaction currents assuming a smooth, i.e. slot-less, half plane with infinite permeability, as in [40]. Afterwards, the slots are taken into account by introducing a permeance function of the slots. In [41], the slots are taken into

account using a simple conformal-mapping technique in radial-flux permanent-magnet synchronous machines (RFPMSMs). However, this method only computes the radial field component. It cannot predict the circumferential (tangential) field component and is therefore less accurate. This method, called the lateral force (LF) method, assumes that the force acting on the tooth surface is caused by the flux density variations beneath the surface of the slot opening.

In [42, 43], the authors developed another permeance function based on complex conformal mapping. The mapping is done via a more complex Schwarz-Christoffel (SC) transformation that is capable of obtaining both the radial and tangential component of the flux density of the machine in both directions. The technique has been adopted by Hemeida *et al* in [44] to be used for AFPMSMs. This class of models is called SC models. Its most important disadvantage is that it neglects the interaction between neighboring slots.

The third category is based on the subdomain (SD) technique. The SD technique divides the geometry into a number of regions, called subdomains. In this technique, the slots are directly taken into account. In [45–50], the authors developed subdomain models for RFPMSMs. These models define the magnetic vector potential separately in the following domains: each slot, the air gap and the PMs. The obtained vector potentials are linked to each other via suitable boundary conditions. The authors in [33, 51], updated the model to be used for AFPMSMs with semi-closed slots. In [52], the authors developed a subdomain model of one slot and two PMs and made a superposition of all PMs and slots in the machine. All of the aforementioned literatures have reported a good accordance with FE calculations. In [53], a general formulation for the calculation of the flux density using the subdomain model is developed.

3.4.1 Lateral Force Method (LF Model)

This model is based on the conformal transformation discussed in [41]. It uses a simple SC transformation to predict the slotting effect. However, it only accounts for the axial component of the resulting permeance function. This method results in an accurate solution for the predicted axial flux density. It is very simple compared to the other methods. This technique solves the problem assuming a smooth surface of stator iron without including the slots effect as shown in Fig. 3.6 (a). Afterwards, the slots are introduced by a simple SC transformation.

Model of PMs Using Maxwell's Equations

In a first step, the LF technique assumes smooth iron surfaces, as shown in Fig. 3.6 (a). The magnetization vector $\mathbf{M}$ in Fig. 3.6 (b) represents the magnetization vector along the x-direction. The x-axis represents the distance in the circumferential direction. The y-axis denotes the distance in the axial direction, measured from the surface of the stator tooth.

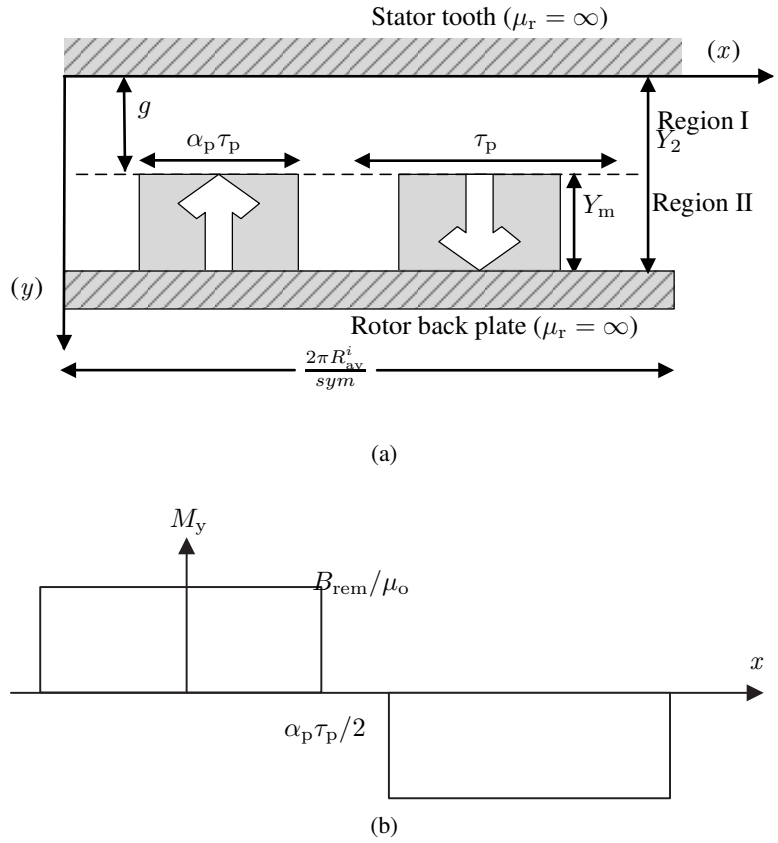

Figure 3.6: The LF model assuming infinitely permeable half planes with a smooth surface.

The magnetic induction in the PM is expressed by:

$$\mathbf{B} = \mathbf{B}_{\mathrm{rem}} + \mu_{\mathrm{rec}}\mathbf{H} = \mu_{\mathrm{o}}\mathbf{M} + \mu_{\mathrm{rec}}\mathbf{H}, \tag{3.14}$$

where $\mathbf{B}_{\mathrm{rem}} = B_{\mathrm{rem_x}}\mathbf{e}_{\mathrm{x}} + B_{\mathrm{rem_y}}\mathbf{e}_{\mathrm{y}} = B_{\mathrm{rem}}\mathbf{e}_{\mathrm{y}}$ is the remanent flux density of the PM, μ_{o} is the permeability of free space, $\mu_{\mathrm{rec}} = \mu_{\mathrm{o}}\mu_{\mathrm{r}}$ is the recoil permeability, and $\mathbf{H} = H_{\mathrm{x}}\mathbf{e}_{\mathrm{x}} + H_{\mathrm{y}}\mathbf{e}_{\mathrm{y}}$ is the magnetic induction.

The amplitude of the Fourier-series expansion of the magnetization vector shown in Fig. 3.6 (b) can be obtained as:

$$M_{\mathrm{n_i}} = \frac{4B_{\mathrm{rem}}}{n\pi\mu_{\mathrm{o}}} \sin\left(\frac{n\pi\alpha_{\mathrm{p_i}}}{2}\right), \tag{3.15}$$

where n is the harmonic order, and $\alpha_{p_{\mathrm{i}}}$ is the PM angle ratio of PM width over pole pitch $\tau_{\mathrm{p_i}}$ at a slice number i.

We use Laplace equation shown in (3.16), which is valid in both the magnets and the air space [40, 54]:

$$\nabla \cdot \nabla \varphi = \frac{\partial^2 \varphi}{\partial x^2} + \frac{\partial^2 \varphi}{\partial y^2} + \frac{\partial^2 \varphi}{\partial z^2} = 0, \tag{3.16}$$

where φ is the magnetic scalar potential.

The magnetic field strength related to φ is

$$H_{\mathrm{x}} = -\frac{\partial \varphi}{\partial x}, H_{\mathrm{y}} = -\frac{\partial \varphi}{\partial y}. \tag{3.17}$$

The following boundary conditions are applied to the solution of the Laplace equations. Fig. 3.6 shows the axis used for these boundary conditions:

$$\begin{cases} \begin{cases} H_{\mathrm{xII}}(x,y)\,|_{y=Y_2} = 0 \\ H_{\mathrm{xI}}(x,y)\,|_{y=0} = 0 \end{cases} \\ \begin{cases} B_{\mathrm{yI}}(x,y)\,|_{y=g} = B_{\mathrm{yII}}(x,y)\,|_{y=g} \\ H_{\mathrm{xI}}(x,y)\,|_{y=g} = H_{\mathrm{xII}}(x,y)\,|_{y=g} \end{cases} \end{cases}, \tag{3.18}$$

This results in two field components, i.e. $B_{\mathrm{xI_i}}$ in the x-direction and $B_{\mathrm{yI_i}}$ in the y-direction. This results in a two region solution of the PMs and the air gap.

In region I, the results for the circumferential and axial components of the flux density are [44]:

$$B_{\mathrm{xI_i}}(x,y) = \mu_{\mathrm{o}} \sum_{n=1,3,5,\ldots}^{\infty} M_{\mathrm{n_i}} \frac{\sinh(U_{\mathrm{n_i}} Y_{\mathrm{m}})}{\Delta} \sinh(U_{\mathrm{n_i}} y) \sin(U_{\mathrm{n_i}} x), \tag{3.19}$$

$$B_{\mathrm{yI_i}}(x,y) = \mu_{\mathrm{o}} \sum_{\mathrm{n}=1,3,5,\ldots}^{\infty} M_{\mathrm{n_i}} \frac{\sinh(U_{\mathrm{n_i}} Y_{\mathrm{m}})}{\Delta} \cosh(U_{\mathrm{n_i}} y) \cos(U_{\mathrm{n_i}} x). \tag{3.20}$$

In region II, the results for the circumferential and axial components of the flux density are [44]:

$$B_{\mathrm{xII_i}}(x,y) = \mu_{\mathrm{o}} \sum_{\mathrm{n}=1,3,5,\ldots}^{\infty} M_{\mathrm{n_i}} \frac{\mu_{\mathrm{r}} \sinh[U_{\mathrm{n_i}}(Y_2 - Y_{\mathrm{m}})]}{\Delta} \sinh(U_{\mathrm{n_i}}(Y_2 - y)) \sin(U_{\mathrm{n_i}} x), \tag{3.21}$$

$$B_{\mathrm{yII_i}}(x,y) = \mu_{\mathrm{o}} \sum_{\mathrm{n}=1,3,5,\ldots}^{\infty} M_{\mathrm{n_i}} \left(1 - \frac{\mu_{\mathrm{r}} \sinh[U_{\mathrm{n_i}}(Y_2 - Y_{\mathrm{m}})]}{\Delta} \cosh(U_{\mathrm{n_i}} y)\right) \cos(U_{\mathrm{n_i}} x), \tag{3.22}$$

where $U_{\mathrm{n_i}} = n\pi/\tau_{\mathrm{p_i}}$, and Δ is calculated as in (3.23):

$$\Delta = \mu_r \cosh\left(U_{\mathrm{n_i}} Y_{\mathrm{m}}\right) \sinh\left[U_{\mathrm{n_i}}\left(Y_2 - Y_{\mathrm{m}}\right)\right] + \cosh\left[U_{\mathrm{n_i}}\left(Y_2 - Y_{\mathrm{m}}\right)\right] \sinh\left(U_{\mathrm{n_i}} Y_{\mathrm{m}}\right). \tag{3.23}$$

The axial and circumferential flux densities caused by the PMs assuming a smooth surface of iron in space are shown in Figs. 3.7 and 3.8 respectively. The circumferential angle θ_{m} equals x/R^i_{av}.

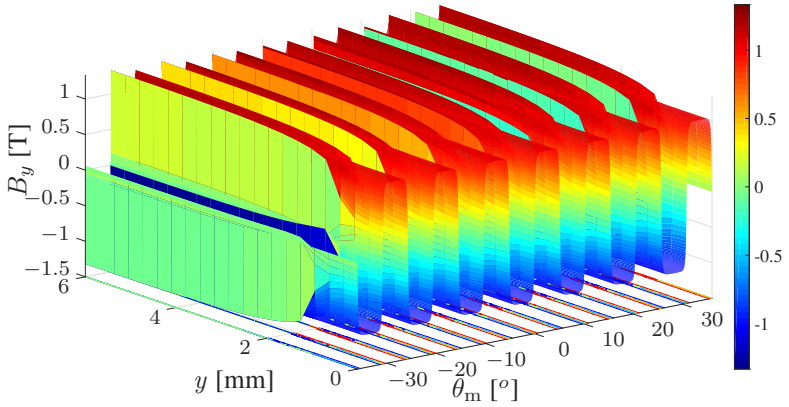

Figure 3.7: Axial flux density distribution of the PM flux in space.

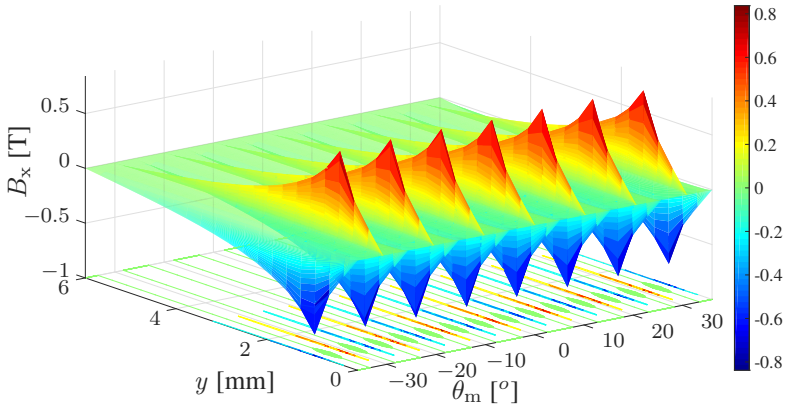

Figure 3.8: Circumferential flux density distribution of the PM flux in space.

The axial PM flux density is almost constant over the axial direction. However, the circumferential flux density reaches a peak on the PM surface $y = g$. On this surface, the leakage flux is peak. The flux density starts to decrease until reaching the rotor surface at $y = Y_2$. On this surface it becomes zero again.

Stator Slotting Effect

In a second step, the effect of the slot opening is included using a simple conformal mapping technique described in [41]. This technique introduces a permeance function $\lambda_{\mathrm{LF_i}}(x, y)$ which can be multiplied with the axial flux density in (3.20) and (3.32), resulting in a total axial flux density $B_{\mathrm{y_{LF_i}}}$ for slice number i.

$$B_{y_{\mathrm{LF_i}}}(x, y) = B_{\mathrm{y}}(x, y)\lambda_{\mathrm{LF_i}}(x, y). \tag{3.24}$$

This function neglects the effect of neighbouring slots on each slot opening. Therefore, each slot can be modeled individually. This assumption is not valid for open slot machines. However, it is still acceptable for PM machines in which the ratio of the air gap to the slot opening is high [41].

This permeance function can be obtained as follows;

For PM machines, due to the fact that the relative permeability of the PM is slightly higher than air, the effective air gap area g' equals:

$$g' = g + \frac{Y_{\mathrm{m}}}{\mu_{\mathrm{r}}}. \tag{3.25}$$

An additional factor k_{C} is introduced representing the reduction of the average air gap flux density . This factor is called the Carter coefficient $k_{\mathrm{C}} > 1$. This coefficient has a value close to 1 and can be neglected.

$$k_{\mathrm{C}} = \frac{\tau_{\mathrm{s_i}}}{\tau_{\mathrm{s_i}} - \gamma g'}, \tag{3.26}$$

where $\tau_{\mathrm{s_i}}$ is the slot pitch at slice number i and γ equals:

$$\gamma = \frac{4}{\pi}\left[\frac{b_{\mathrm{so}}}{2g'}\tan^{-1}\left(\frac{b_{\mathrm{so}}}{2g'}\right) - \ln\sqrt{1 + \left(\frac{b_{so}}{2g'}\right)^2}\right]. \tag{3.27}$$

A Fourier series expansion over the azimuthal coordinate $\theta_{\mathrm{m}} = x/R^i_{\mathrm{av}}$ is done to obtain the permeance function. The relative permeance function is periodic with the azimuthal width corresponding to the slot pitch. Therefore in case of N_{s} slots the equation for the relative permeance function becomes:

$$\tilde{\lambda_{LF_i}}(\theta_m, y) = \tilde{\Lambda}_0(y) + \sum_{\nu=1,2,....}^{\infty} \tilde{\Lambda}_\nu(y)\cos\left(\nu N_{\mathrm{s}}\theta_m\right), \tag{3.28}$$

where $\theta_{\mathrm{m}} = x/R^i_{\mathrm{av}}$ is the azimuth angle. The coefficients are determined in [41]:

$$\begin{aligned}\tilde{\Lambda}_0(z) =& 1 - 1.6\beta(y)\frac{b_{\mathrm{so}}}{\tau_{\mathrm{s_i}}},\\ \tilde{\Lambda}_\nu(z) =& -\beta(y)\frac{4}{\nu\pi}\left[0.5 + \frac{\left(\nu\frac{b_{\mathrm{so}}}{\tau_{\mathrm{s}}}\right)^2}{0.78125 - 2\left(\nu\frac{b_{\mathrm{so}}}{\tau_{\mathrm{s_i}}}\right)^2}\right]\\ & \sin\left(1.6\nu\pi\frac{b_{\mathrm{so}}}{\tau_{\mathrm{s_i}}}\right),\end{aligned} \tag{3.29}$$

where

$$\beta(y) = \frac{1}{2}\left[1 - \frac{1}{\sqrt{1 + \left(\frac{b_{\mathrm{so}}}{2g'}\right)^2(1+v^2)}}\right]', \tag{3.30}$$

where v also can be determined by solving the non-linear equation for each axial length y:

$$(g' - y)\frac{\pi}{b_{\mathrm{so}}} = \frac{1}{2}\ln\left(\frac{\sqrt{a^2+v^2}+v}{\sqrt{a^2+v^2}-v}\right) + \frac{2g'}{b_{\mathrm{so}}}\arctan\left(\frac{2g'}{b_{\mathrm{so}}}\frac{v}{\sqrt{a^2+v^2}}\right), \tag{3.31}$$

and

$$a^2 = 1 + \left(\frac{2g'}{b_{\mathrm{so}}}\right)^2. \tag{3.32}$$

In Fig. 3.9 (a) and (b), $\lambda_{\mathrm{LF_i}}$ is shown as a function of the axial length of the machine y and the circumferential angle $\theta_m = x/R^i_{\mathrm{av}}$. These coordinates are shown in Figs. 3.6 (b) and (c). Due to the presence of the slot, a dip below the opening of the slot occurs. The dip has a behaviour as shown in Fig. 3.9 (b). It is clear also that while the axial length increases, the effect of the permeance function until reaching the rotor surface. Due to this effect, the average air gap flux density reduces. Therefore, this leads to a reduction to the total torque production and other concerning points that will be discussed later. Therefore, accurate modeling of this parameter is important.

Torque Ripple Causes

Torque pulsations occur due to the following reasons [16].

- Cogging torque is one of the main reasons for torque pulsation. It occurs because of the interaction between permanent magnets (PMs) and slot openings in the stator core. Therefore, at no load, the machine will not be able

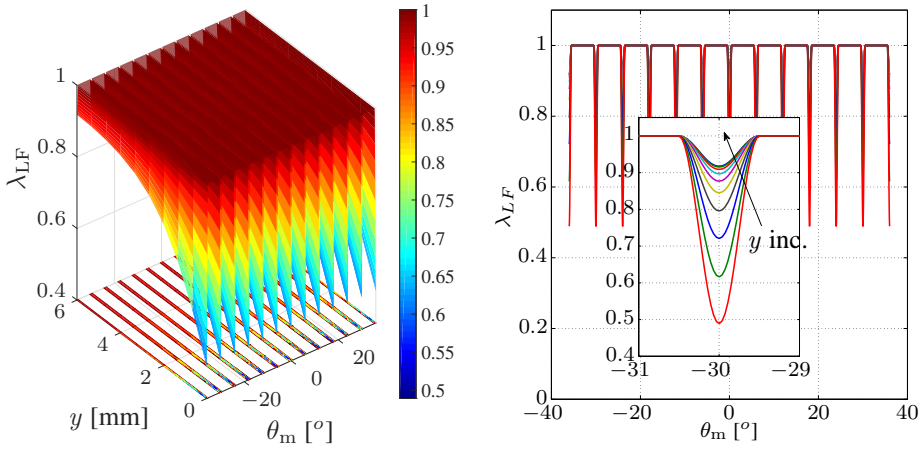

(a) (b)

Figure 3.9: The permeance function of the axial length of the machine and the circumference.

to start until the torque produced is much higher than the cogging torque. In wind energy applications, it is an important issue to keep this value as low as possible to reduce the start up wind speed to a low value.

Figure 3.10 shows the force interactions between the slots and PMs for different positions of PMs with respect to the position of the slot opening. It is clear that the forces produced depend greatly on this position. Therefore, the cogging torque depends greatly on the combinations of slots and poles.

The frequency of the cogging torque equals the lowest common multiple of the number of slots and poles ($lcm(N_s, N_m)$) [55]. It is important to keep the lowest common multiple as high as possible to keep the cogging torque as minimum as possible. Additional PM skewing can be used to reduce the cogging torque [30].

- Another cause of the torque ripple is the interaction between the magnetomotive force (MMF) of the stator currents and MMF of the rotor PMs. The concentrated windings impose additional air gap harmonics than the distributed windings.

  From mathematical point of view, if the inductances and the resistances of the machine are neglected, the electromagnetic torque ripple occurs due to the harmonic contents existing in the no load voltage and currents. The frequency of the harmonic contents equals multiples of six times the fundamental frequency [16].

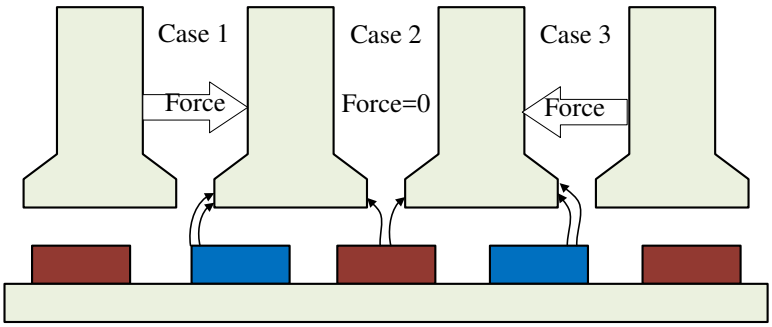

Figure 3.10: Forces resulting from interaction between slot openings and PMs.

The harmonic contents in the voltage occur due to the two aforementioned reasons of interaction of slot opening and the distribution of slots with poles.

Validation: Flux Densities Comparison for 50kW Reference Machine

The axial flux density for this method is shown in Fig. 3.11. It shows that the predicted axial flux density using this method is comparable to the 2D FE model[1]. The horizontal axis in Fig. 3.11 ($\theta_m = x/R^i_{av}$) represents the already defined circumferential angle in degrees.

The force is now computed by assuming that the flux density computed by (3.24) is circular near the slot opening, as shown in Fig. 3.12. Fig. 3.12 divides the slot opening regions in two parts. One part results in a positive force, while the other part results in a negative one. The radius of the flux path is r_{so}. The actual torque computation is done by integrating along the entire flux path under half of the slot opening [56]:

$$T_{\mathrm{c}} = \sum_{i=1}^{N_s} t_{\mathrm{cp}} \int_0^{b_{\mathrm{so}}/2} \left({B_{y_{\mathrm{LF_{b2_i}}}}}^2 - {B_{y_{\mathrm{LF_{b1_i}}}}}^2 \right) / \left(2\mu_o\right) R^i_{\mathrm{av}} \mathrm{dr_{so}}, \tag{3.33}$$

where $B_{\mathrm{y_{LF_{b1_i}}}}(x, y)$ is the flux density beneath the slot opening at the left side of Fig. 3.12. While $B_{\mathrm{y_{LF_{b2_i}}}}(x, y)$ is the flux density on the right side of Fig. 3.12. b_{so} is the slot opening width. The flux density is computed using (3.24).

The LF method can only compute the cogging torque because it neglects the energy variations in the part of the air gap that does not lie below the slot opening. Therefore, it is not used for the calculation of the total torque.

[1]The percentage error of the second norm of the error divided by the second norm of the 2D FE model flux densities of the y and x components are shown in Table 3.3. It shows a percentage error of 5.2%

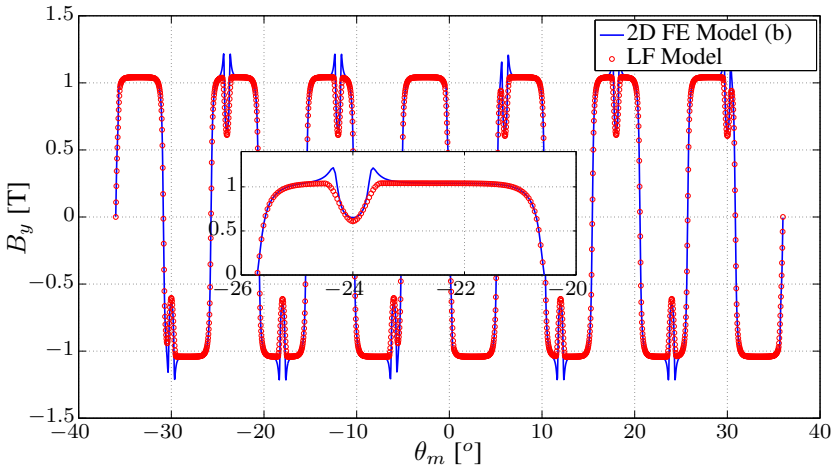

Figure 3.11: The axial flux density for 5mm slot opening: comparison between the LF model and the 2D FE model at the center of the air gap area.

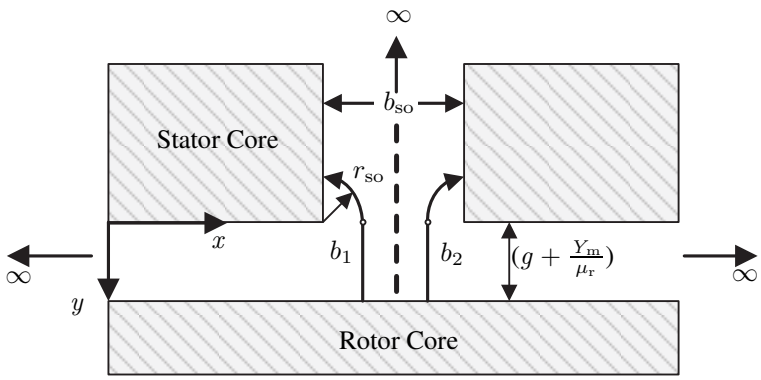

Figure 3.12: The cogging torque model using LF model [56].

3.4.2 Complex Schwarz Christoffel Transformation (SC Model)

SC models use a conformal mapping technique, introduced by Zarko *et al.* in [42], to account for the slotting effect. This technique transforms the complex shapes of the slots into a smooth surface. Again, the PM and armature current fluxes are obtained firstly and then the transformation is introduced.

Model of PMs Using Maxwell's Equations

In this section, the solution of the PM is obtained using the same technique described in the LF model in section 3.4.1.

Model of Armature Reaction Current

To account for the armature winding current effect, one should solve the Laplace equation again. This time, the armature windings, which are fractional slot concentrated windings (FSCWs) will be assumed as thin wires. This type of windings has lots of advantages over many other types that are described in [23]. The current sheet due to the distribution in space of slots in the stator in per unit (K_{m}) of each phase m is plotted in Fig. 3.13.

Afterwards, to obtain the total current sheet (K) in space, the current sheet for each phase m in per unit (K_{m}) is generated according to the star of the slot. Afterwards, they are multiplied by the values of the instantaneous currents of each phase over the thickness of the slot opening b_{so}. To obtain the total current sheet distribution, summations for all phases are done:

$$\begin{aligned} K = \Bigg(& K_{\mathrm{a}} I_{\mathrm{a}} \sin\left(\omega_{\mathrm{e}} t\right) + K_{\mathrm{b}} I_{\mathrm{b}} \sin\left(\omega_{\mathrm{e}} t - \frac{2\pi}{3}\right) \\ & + K_{\mathrm{c}} I_{\mathrm{c}} \sin\left(\omega_{\mathrm{e}} t + \frac{2\pi}{3}\right) \Bigg) \frac{1}{b_{\mathrm{so}}}, \end{aligned} \tag{3.34}$$

where ω_{e} is the electrical angular frequency in rad/sec. In addition, Fourier series is needed for this current sheet per phase, to obtain the spatial distribution of the current in space in the following form.

$$K = \sum_{\mathrm{n}=1,2,3}^{\infty} \left(A_{\mathrm{n}} \cos\left(U_{\mathrm{n}2} x\right) + B_{\mathrm{n}} \sin\left(U_{n2} x\right) \right), \tag{3.35}$$

where $U_{\mathrm{n}2} = 2n\pi/(2p\tau_p)$.

By using the same Laplace equation shown in equations (3.16) and (3.17) and by applying the boundary equations in (3.36) to Fig. 3.14, the solution can be obtained:

$$\begin{cases} \begin{cases} H_{\mathrm{xIII}}(x,y)\,|_{y=0} = 0 \\ H_{\mathrm{xIV}}(x,y)\,|_{y=Y_2} = 0 \end{cases} \\ \begin{cases} H_{\mathrm{xIV}}(x,y)\,|_{y=Y_3} - H_{\mathrm{xIII}}(x,y)\,|_{y=Y_3} = K \\ H_{\mathrm{yIII}}(x,y)\,|_{y=Y_3} = H_{\mathrm{yIV}}(x,y)\,|_{y=Y_3} \end{cases} \end{cases}. \tag{3.36}$$

The results of the circumferential and axial flux densities are for region III:

$$B_{\mathrm{xIII}}(x,y) = \sum_{\mathrm{n}=1,2,3,....}^{\infty} \Delta'' \sinh\left(U_{\mathrm{n}2} y\right) \left(\mathrm{A}_{\mathrm{n}} \cos\left(U_{\mathrm{n}2} x\right) + \mathrm{B}_{\mathrm{n}} \sin\left(U_{\mathrm{n}2} x\right) \right), \tag{3.37}$$

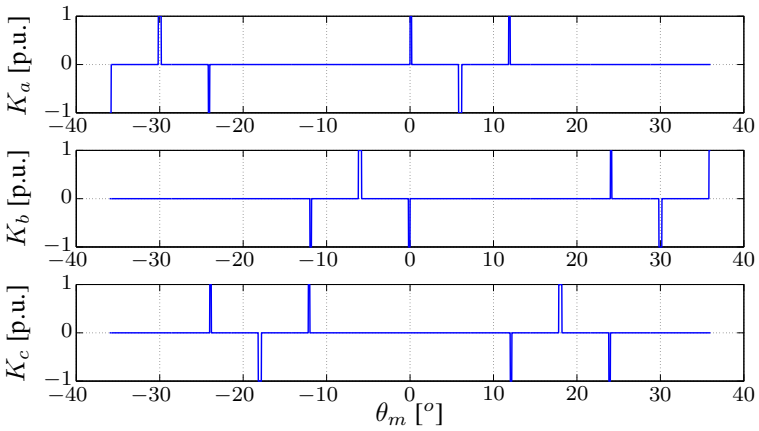

Figure 3.13: Current sheet spatial distribution in space for each phase in per unit for an axial flux machine.

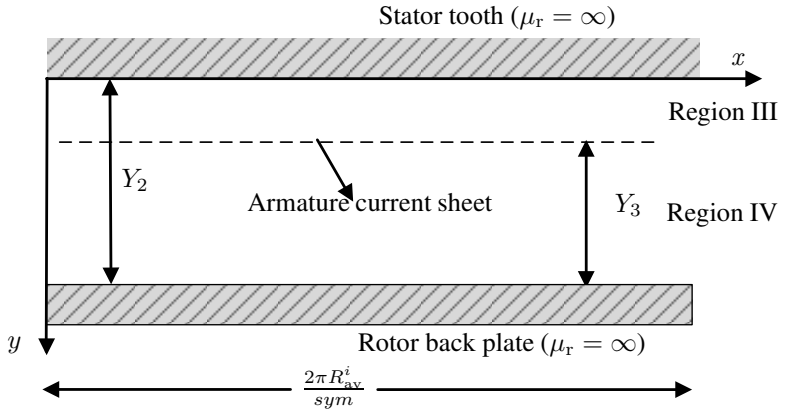

Figure 3.14: The model assuming infinitely permeable half planes with a smooth surface for current sheet solution.

$$B_{\mathrm{yIII}}(x,y) = \sum_{\mathrm{n}=1,2,3,\ldots.}^{\infty} -\Delta'' \cosh(U_{\mathrm{n}2} y)\left(\mathrm{A_n}\sin(U_{\mathrm{n}2}x) - \mathrm{B_n}\cos(U_{\mathrm{n}2}x)\right) . \tag{3.38}$$

Region IV:

$$B_{\mathrm{xIV}}(x,y) = \sum_{\mathrm{n}=1,2,3,\ldots.}^{\infty} -\Delta' \sinh(U_{\mathrm{n}2}(Y_2 - y))\left(\mathrm{A_n}\cos(\mathrm{U_{n2}x}) + \mathrm{B_n}\sin(U_{\mathrm{n}2}x)\right) , \tag{3.39}$$

$$B_{\mathrm{yIV}}(x,y) = \sum_{n=1,2,3,\ldots}^{\infty} -\Delta^{'}\cosh\left(U_{\mathrm{n2}}(Y_2-y\right)\left(\mathrm{A_n}\sin\left(U_{\mathrm{n2}}x\right) - \mathrm{B_n}\cos\left(U_{\mathrm{n2}}x\right)\right), \tag{3.40}$$

where

$$\Delta^{'} = \frac{\mu_{\mathrm{o}}\cosh\left(U_{\mathrm{n2}}(Y_2-Y_3)\right)}{\sinh\left(U_{\mathrm{n2}}Y_2\right)}, \tag{3.41}$$

$$\Delta^{''} = \frac{\mu_{\mathrm{o}}\cosh\left(U_{\mathrm{n2}}Y_3\right)}{\sinh\left(U_{\mathrm{n2}}Y_2\right)}. \tag{3.42}$$

Figures 3.15 and 3.16 show the flux density distribution in space for the armature reaction effect at time instant zero. Both fluxes start with a high value of flux density on the stator surface bore. The axial flux density keeps a constant value on the PM surface. However, the circumferential part decays to zero while reaching the rotor surface.

Stator Slotting Effect

The flux was calculated for a smooth stator having an infinite permeability. The effect of stator slotting can be included by defining a vector potential in each of the stator slots and by linking them to the solution in the air gap region [33, 57, 58]. As this set of partial differential equations increases the complexity of the analytical model, the permeance function using conformal mapping techniques was introduced in [41, 42]. This technique was used firstly by Zhu *et al.* in [41], but it was not accurate enough to calculate the effect of stator slotting on the circumferential induction as illustrated in section 3.4.1. Then it was improved to take into account the effect of stator slotting on the circumferential induction in [42]. Both techniques were used with radial flux machines. In this work, the second technique was adapted to be used with axial flux machines to be able to calculate the circumferential part. There are three conformal mappings used in this chapter to convert the Z_n-plane to the T-plane, where calculation could be the easiest. This is done through passing by the W-plane which is deduced through a Schwarz-Christoffel transformation as described in Fig. 3.17 (a), (b), and (c).

The first transformation used is to transform the Z_n-plane to the W-plane using Schwarz-Christoffel:

$$\frac{\mathrm{d}z_n}{\mathrm{d}w} = j\frac{Y_2}{\pi}\frac{(w-a)^{0.5}(w-b)^{0.5}}{(w-1)\,w}. \tag{3.43}$$

The coefficients a and b are described as:

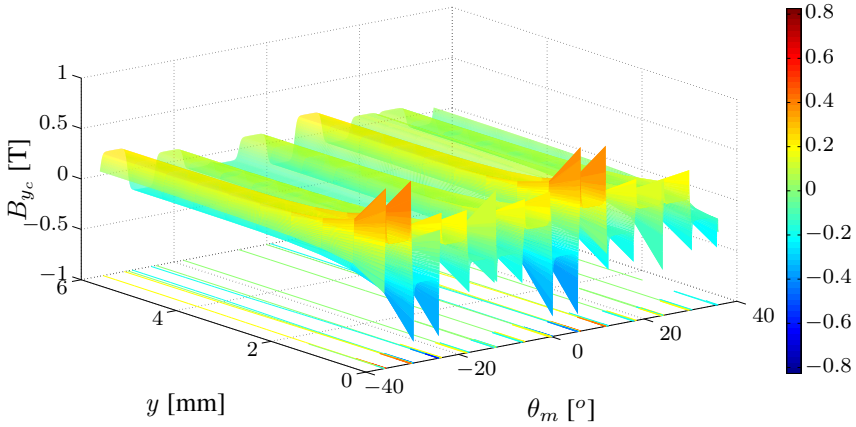

Figure 3.15: Axial flux density distribution of the armature reaction current flux density in space assuming zero remanent flux.

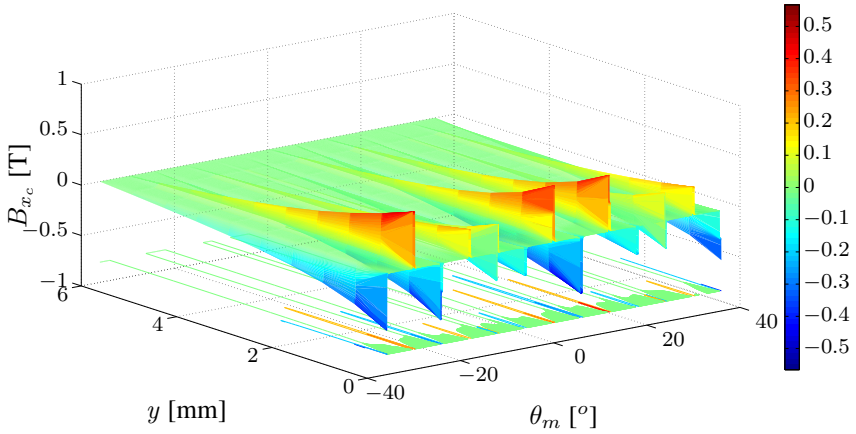

Figure 3.16: Circumferential flux density distribution of the armature reaction current flux density in space assuming zero remanent flux.

$$b = \left[\frac{b_{\text{so}}}{2Y_2} + \sqrt{\left(\frac{b_{\text{so}}}{2Y_2} \right)^2 + 1} \right]^2, \tag{3.44}$$

$$a = \frac{1}{b}. \tag{3.45}$$

The second transformation is to transform the W-plane into the T-plane using following equation

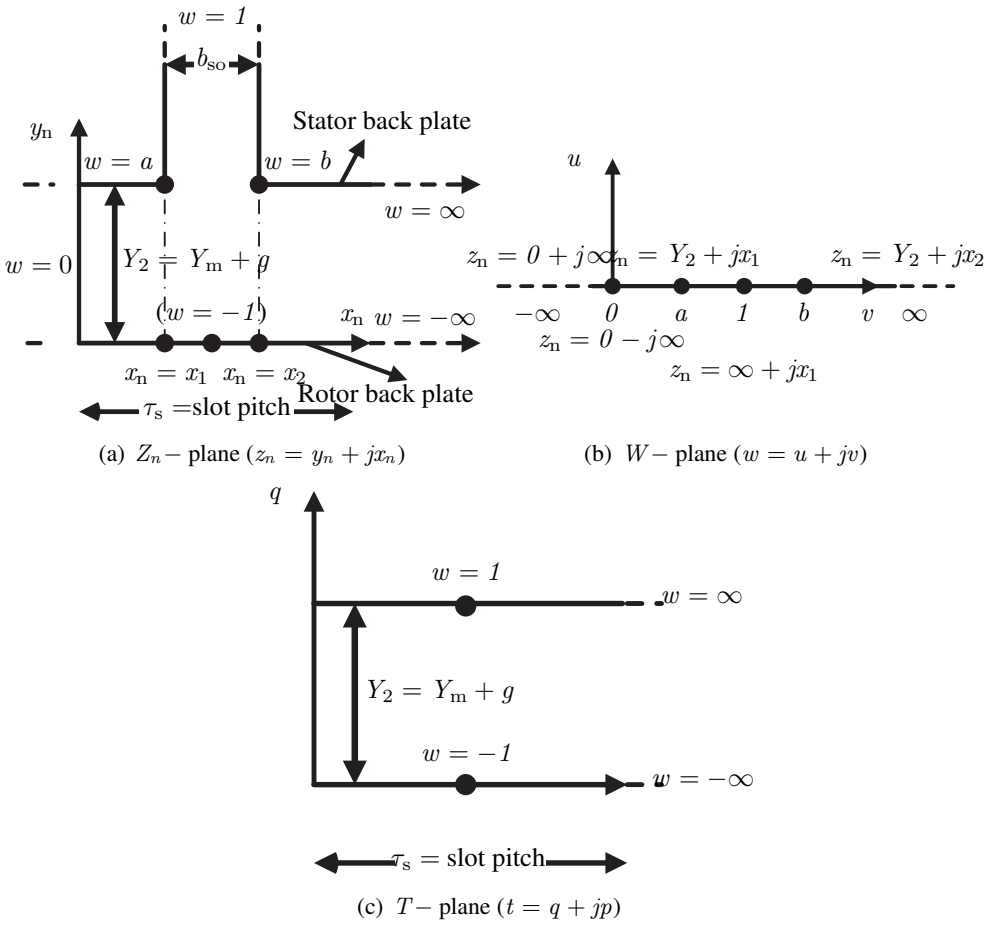

Figure 3.17: The model assuming infinitely permeable half planes with a smooth surface [44].

$$t = j\frac{Y_2}{\pi}\ln w + Y_2 + j\frac{\tau_{\mathrm{s}}}{2} = q + jp. \tag{3.46}$$

After some derivations which are described in more details in [42], it was deduced that

$$B_{\mathrm{z_n}} = B_{\mathrm{t}}\lambda^{*}_{\mathrm{SC_i}} = B_{\mathrm{y_n}}\mathrm{Re}\left\{\lambda_{\mathrm{SC_i}}\right\} - jB_{\mathrm{x_n}}\mathrm{Im}\left\{\lambda_{\mathrm{SC_i}}\right\}, \tag{3.47}$$

where $\lambda_{\mathrm{SC_i}}(x, y)$ equals:

$$\lambda_{\mathrm{SC_i}}(x, y) = \frac{w - 1}{(w - a)^{0.5}(w - b)^{0.5}}, \tag{3.48}$$

where the real part represents the axial component of the field and the imaginary part is the circumferential part.

To obtain the value of w, which corresponds to a certain dimensions in the Z_n-plane, (3.43) will be integrated using the limits shown in Fig. 3.17 (a), and it will results in

$$z_{\mathrm{n}} = j\frac{Y_2}{\pi}\left(\ln\left[\frac{1+p_{\mathrm{c}}}{1-p_{\mathrm{c}}}\right] - \ln\left[\frac{b+p_{\mathrm{c}}}{b-p_{\mathrm{c}}}\right] - \frac{2\,(b-1)}{\sqrt{b}}\tan^{-1}\frac{p_{\mathrm{c}}}{\sqrt{b}}\right) + C,\, z_{\mathrm{n}} = y_{\mathrm{n}} + jx_{\mathrm{n}}, \tag{3.49}$$

where

$$p_{\mathrm{c}} = \sqrt{\frac{w-b}{w-a}}, \tag{3.50}$$

$$C = Y_2 + jX_2, \tag{3.51}$$

In order to obtain the resultant field, the value of the resultant y-component of PM in (3.20) or (3.22) according to the studied region and armature reaction fields in (3.40) should be added together. In addition, the same for the x-component of both fields in (3.19), (3.21), and (3.39). Afterwards, the resultant field should be multiplied by the permeance function to obtain the resultant field after taking into account the slotting effect as shown in (3.47).

Figures 3.18 (a) and (b) show the real part of the permeance function as a function of the axial and circumferential angle. The effect of slotting diminishes while reaching the rotor surface. The same conclusion could be observed for the imaginary part of the permeance function shown in Figs. 3.19 (a) and (b).

Validation: Flux Densities Comparison for 50kW Reference Machine

The comparison of the axial flux density B_{ySC} and the circumferential flux density B_{xSC} with the 2D FE model (a) is shown in Figs. 3.20 and 3.21 respectively. The comparison is done for a slot opening of 5mm. Fig. 3.20 shows that the axial flux density is in a good agreement with the 2D FE model. Comparing Fig. 3.20 and Fig. 3.11 shows that the SC model is more accurate than the LF model[2].

However, at a time instant of zero, the correspondence in Fig. 3.21 shows that the x-component of the field does not correspond to the 2D FE model. This results in an error in the calculation of the cogging torque as will be shown later. The deviation between the 2D FE model and the analytical models is discussed in more detail in section 3.5.

[2]The percentage error of the second norm of the error divided by the second norm of the 2D FE model flux densities of the y and x components are shown in Table 3.3. It shows percentage errors for the y and x components of 2% and 30% respectively

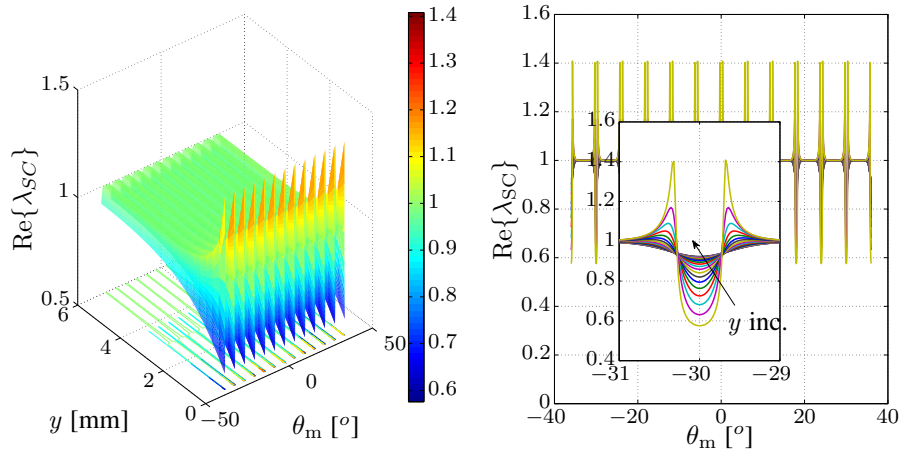

Figure 3.18: The real part of the permeance function as a function of the axial length of the machine and the circumference.

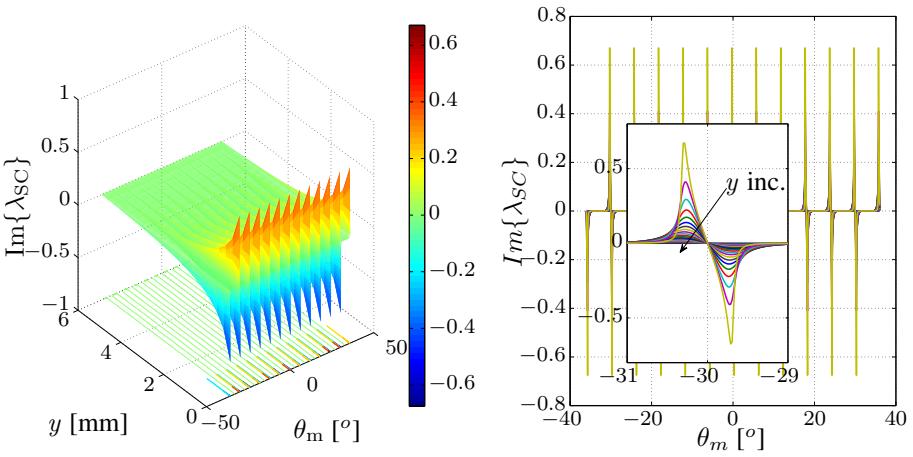

Figure 3.19: The imaginary part of the permeance function as a function of the axial length of the machine and the circumference.

Figures 3.22 and 3.23 show the axial and circumferential flux densities under armature-reaction conditions. The currents are injected into the current sheets taking into account the slotting effect. It is clear that there is a small error between the

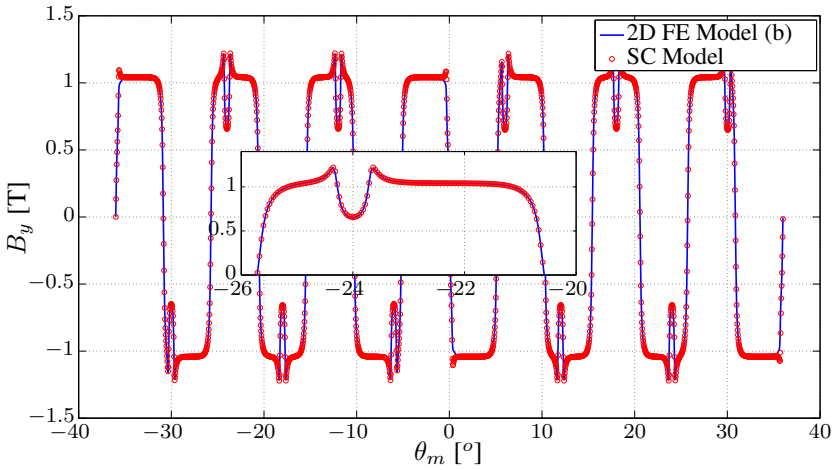

Figure 3.20: Axial flux density component B_y of the SC model compared with the 2D FE model at no load at the center of the air gap area.

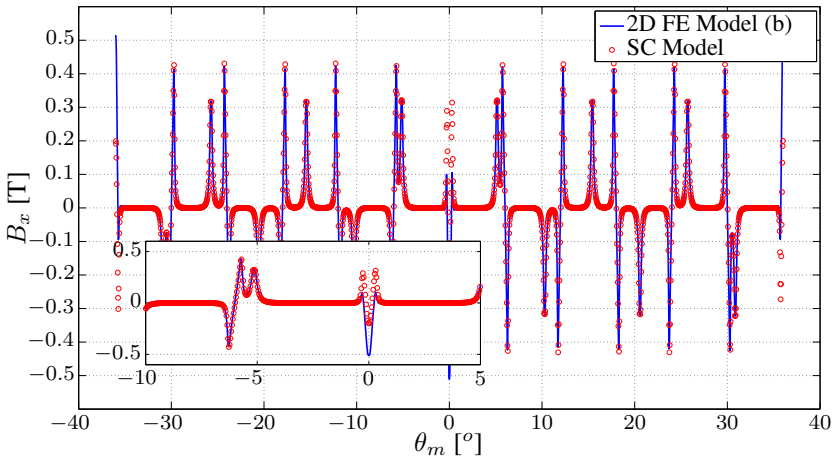

Figure 3.21: Circumferential flux density component B_x of the SC model compared with the 2D FE model at no load at the center of the air gap area.

analytical and the FE model[3].

It is true that the surface becomes smooth when transforming from the Z-plane to the T-plane and the calculation of the flux density is much easier in the T-plane.

[3]The percentage error of the second norm of the error divided by the second norm of the 2D FE model flux densities of the y and x components are shown in Tables 3.4. It shows percentage errors for the y and x components of 14.2% and 33% respectively

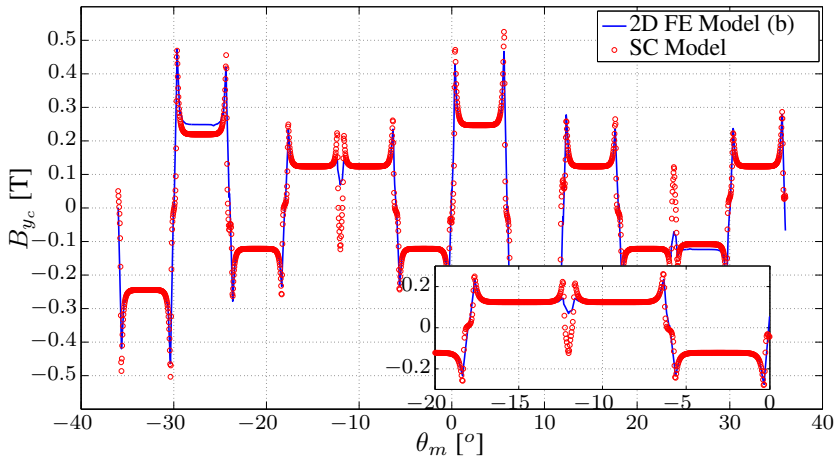

Figure 3.22: Axial flux density component B_y of the SC model compared with the 2D FE model considering only armature current at the center of the air gap.

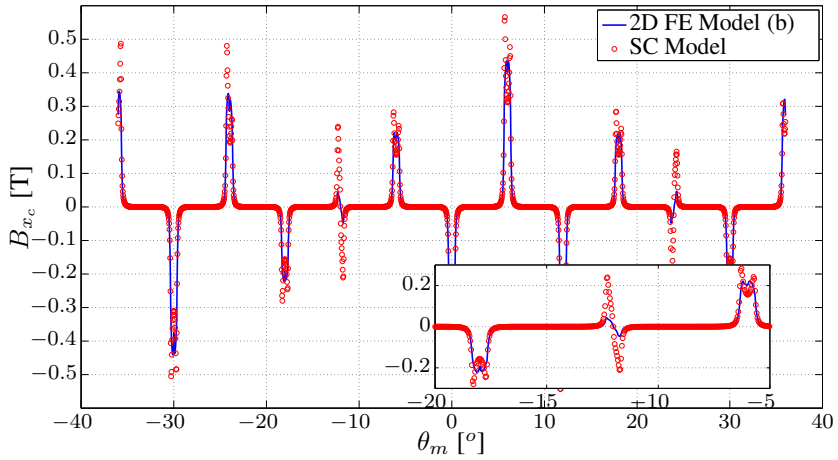

Figure 3.23: Circumferential flux density component B_x of the SC model compared with the 2D FE model considering only armature current at the center of the air gap.

However, the transformation introduces a deformation of the PM, causing errors in the calculation of the flux densities which, in turn, lead to a major error in the calculation of cogging torque and the torque ripple [44].

3.4.3 Subdomain Model (SD Model)

In the SD model, the slots are assumed to be infinitely deep, as shown in Fig. 3.24. In this model, the interdependence of different slots is considered.

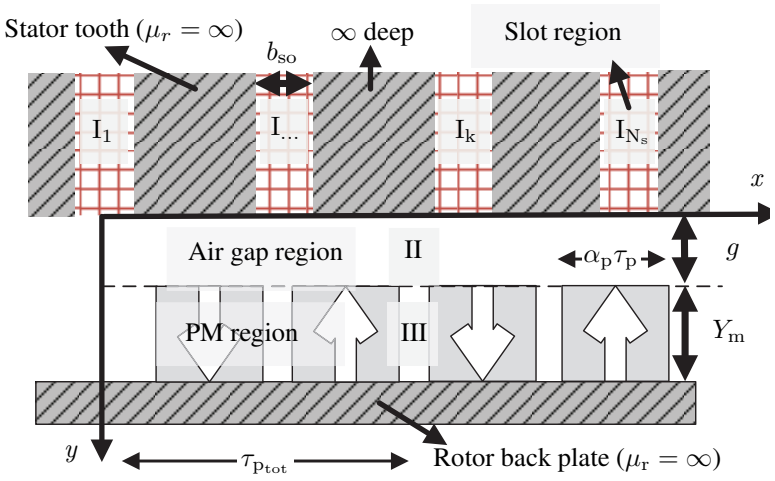

Figure 3.24: The subdomain model.

The machine's geometry, consisting of N_s slots and N_m PMs, is divided into three main regions.

1- Region (I_k). The slotting region consists of several subdomains (1,2,..,k,..,N_s), where the variable k indicates the number of the studied slot. The current I_k with a current density $J_k = \frac{N_t I_k}{b_{so}}$ is imposed to each slot, as shown in Fig. 3.24. Where N_t is the number of turns per slot shown in Fig. 3.24.

For regions with soft magnetic material boundaries, *i.e.* the slot subdomain region, Neumann boundary condition has to be applied on these surfaces [53]. The tangential component of the flux density is forced to be zero on these surfaces. Therefore, in this region, the periodicity of the solution (W_s) is determined by the width of the slot opening (b_{so}):

$$W_s = \frac{s\pi}{b_{so}}, \quad s = 1, 2, 3, ..., \infty, \tag{3.52}$$

where s represents the harmonic orders in the slot region.

2- Region (II). This region covers the air gap area.

3- Region (III). This region contains the PMs. The PMs are assumed to be tangentially and axially magnetized in both directions. In fact, Fig. 3.24 shows that the PMs are only magnetized in axial direction. However, to make the model more generalized and could be used for other application like the Hallbach array AFPMSMs [59], it has been modeled in such a way.

The x and y components of the magnetization vectors can be described as shown below:

$$\begin{aligned} M_{\mathrm{y}} &= \sum_{m=1,2,..}^{\infty} M_{\mathrm{c_y}} \cos(W_{\mathrm{m}} x) + M_{\mathrm{s_y}} \sin(W_{\mathrm{m}} x), \\ M_{\mathrm{x}} &= \sum_{m=1,2,..}^{\infty} M_{\mathrm{c_x}} \cos(W_{\mathrm{m}} x) + M_{\mathrm{s_x}} \sin(W_{\mathrm{m}} x), \\ \overrightarrow{M} &= M_{\mathrm{x}} \mathbf{e_x} + M_{\mathrm{y}} \mathbf{e_y}. \end{aligned} \tag{3.53}$$

In region (II) and (III), the periodicity is defined by the pole pitch multiplied with the number of pole pairs of the machine divided by the number of symmetries in the machine (sym) described in (3.9).

The periodicity of this region is determined by:

$$W_{\mathrm{m}} = \frac{m\pi}{\tau_{\mathrm{p_{tot_i}}}}, \quad m = 1, 2, 3, ..., \infty, \tag{3.54}$$

where m represents the harmonics in the air gap and the PM region. $\tau_{\mathrm{p_{tot_i}}}$ equals:

$$\tau_{\mathrm{p_{tot_i}}} = \frac{\mathrm{p}\tau_{\mathrm{p_i}}}{sym}, \tag{3.55}$$

where $\tau_{p_i} = \frac{2\pi R_{av_i}}{N_m}$ is the pole pitch at slice i.

Using the magnetic vector potential $(\overrightarrow{A})$, Maxwell's equations can be rewritten in the form of a second-order differential equation in each of the subdomains:

$$\begin{aligned} \nabla^2 \overrightarrow{A_{\mathrm{I_k}}} &= -\mu_{\mathrm{o}} J_{\mathrm{k}}, & Region \quad \mathrm{I_k} \\ \nabla^2 \overrightarrow{A_{\mathrm{II}}} &= 0, & Region \quad \mathrm{II} \\ \nabla^2 \overrightarrow{A_{\mathrm{III}}} &= -\mu_o (\nabla \times \overrightarrow{M}). & Region \quad \mathrm{III} \end{aligned} \tag{3.56}$$

This results in the following equation for the magnetic vector potential for each

region:

$$\begin{aligned}
A_{\mathrm{zI_k}} &= \sum_{s=1,2,..}^{\infty} \frac{1}{W_s}\Big[\left(A_{\mathrm{I}_k} e^{W_{\mathrm{s}} y} + B_{\mathrm{I}_k} e^{-W_{\mathrm{s}} y}\right) \cos(W_{\mathrm{s}} x) \\
&+ \left(C_{\mathrm{I}_k} e^{W_{\mathrm{s}} y} + D_{\mathrm{I}_k} e^{-W_{\mathrm{s}} y}\right) \sin(W_{\mathrm{s}} x)\Big] - \mu_{\mathrm{o}} J_{\mathrm{k}} y, \\
A_{\mathrm{zII}} &= \sum_{m=1,2,..}^{\infty} \frac{1}{W_{\mathrm{m}}}\Big[\left(A_{\mathrm{II}} e^{W_{\mathrm{m}} y} + B_{II} e^{-W_{\mathrm{m}} y}\right) \cos(W_{\mathrm{m}} x) \\
&+ \left(C_{\mathrm{II}} e^{W_{\mathrm{m}} y} + D_{\mathrm{II}} e^{-W_{\mathrm{m}} y}\right) \sin(\mathrm{W_m x})\Big], \\
A_{\mathrm{zIII}} &= \sum_{m=1,2,..}^{\infty} \frac{1}{W_{\mathrm{m}}}\Big[\left(A_{\mathrm{III}} e^{W_{\mathrm{m}} y} + B_{\mathrm{III}} e^{-W_{\mathrm{m}} y}\right) \cos(W_{\mathrm{m}} x) \\
&+ \left(C_{\mathrm{III}} e^{W_{\mathrm{m}} y} + D_{\mathrm{III}} e^{-W_{\mathrm{m}} y}\right) \sin(W_{\mathrm{m}} x)\Big].
\end{aligned} \tag{3.57}$$

where the current density in each slot is defined by J_k by A/m.

The flux densities at slice number i can now be obtained by:

$$B_{\mathrm{y_{SD_i}}} = -\frac{\partial A_{\mathrm{z}}}{\partial x}, B_{\mathrm{x_{SD_i}}} = \frac{\partial A_{\mathrm{z}}}{\partial y}. \tag{3.58}$$

The integration constants, introduced in the solutions of the different subdomains (3.57), are then defined by imposing the correct boundary conditions. A more detailed discussion on the SD technique, including the boundaries are described below [52].

Region I: Slots Region

In this region, there are five boundary conditions to apply. Two Neumann boundary condition on the two interface parts between the tooth and slots. Additional boundary condition at $-\infty$ for zero circumferential field. These are described below.

$$\begin{aligned}
&B_{\mathrm{y_{I_k}}} = 0 \quad \text{at} \quad x = x_{1\mathrm{k}} \quad \text{and} \quad x = x_{1\mathrm{k}} + b_{\mathrm{so}}, \\
&B_{\mathrm{x_{I_k}}} = 0 \quad \text{at} \quad y = -\infty,
\end{aligned} \tag{3.59}$$

where $x_{1\mathrm{k}} = (k-1)\tau_{\mathrm{s_i}} - \frac{b_{\mathrm{so}}}{2}$. $\tau_{\mathrm{s_i}} = \frac{2\pi R^i_{\mathrm{av}}}{N_{\mathrm{s}}}$ is the slot pitch at average radius i.

Substituting by these boundaries will lead to the following equation:

$$A_{\mathrm{zI_k}} = \sum_{s=1,2,..}^{\infty} \frac{1}{W_{\mathrm{s}}} A_{\mathrm{I}_k} e^{W_{\mathrm{s}} y} \cos\left(W_{\mathrm{s}}(x - x_{1\mathrm{k}})\right) - \mu_{\mathrm{o}} J_{\mathrm{k}} y, \tag{3.60}$$

The x and y components of the flux densities:

$$\begin{aligned} B_{\mathrm{x}} &= \sum_{s=1,2,..}^{\infty} A_{\mathrm{I_k}} e^{W_{\mathrm{s}} y} \cos\left(W_{\mathrm{s}}(x - x_{1\mathrm{k}})\right) - \mu_{\mathrm{o}} J_{\mathrm{k}}, \\ B_{\mathrm{y}} &= \sum_{s=1,2,..}^{\infty} A_{\mathrm{I_k}} e^{W_{\mathrm{s}}(y)} \sin\left(W_{\mathrm{s}}(x - x_{1\mathrm{k}})\right). \end{aligned} \tag{3.61}$$

The x and y flux densities at the interface boundaries between the slots and air gap are.

$$\begin{aligned} B_{\mathrm{x}}(y=0) &= \sum_{s=1,2,..}^{\infty} A_{\mathrm{I_k}} \cos\left(W_{\mathrm{s}}(x - x_{1\mathrm{k}})\right) - \mu_{\mathrm{o}} J_{\mathrm{k}}, \\ B_{\mathrm{y}}(y=0) &= \sum_{s=1,2,..}^{\infty} A_{\mathrm{I_k}} \sin\left(W_{\mathrm{s}}(x - x_{1\mathrm{k}})\right). \end{aligned} \tag{3.62}$$

There are other two boundary conditions related to the interface between regions I and II.

Equalizing the x-component of the flux density of region I and II. Because of the two components have different frequencies, an equivalent Fourier series is obtained for the flux density of region I.

$$B_{\mathrm{x_{I_{eq}}}}(y=0) = \sum_{m=1,2,..}^{\infty} \zeta_1 \cos(W_m x) + \eta_1 \sin(W_{\mathrm{m}} x), \tag{3.63}$$

where

$$\begin{aligned} \zeta_1 &= \sum_{k=1,2,..}^{N_{\mathrm{s}}} \frac{1}{\tau_{\mathrm{p_{tot_i}}}} \int_{x_{1\mathrm{k}}}^{x_{1\mathrm{k}}+b_{\mathrm{so}}} \left(\sum_{s=1,2,..}^{\infty} A_{\mathrm{I_k}} e^{W_{\mathrm{s}} y} \cos\left(W_{\mathrm{s}}(x - x_{1\mathrm{k}})\right) - \mu_{\mathrm{o}} J_{\mathrm{k}} \right) \cos(W_{\mathrm{m}} x), \\ \eta_1 &= \sum_{k=1,2,..}^{N_{\mathrm{s}}} \frac{1}{\tau_{\mathrm{p_{tot_i}}}} \int_{x_{1\mathrm{k}}}^{x_{1\mathrm{k}}+b_{\mathrm{so}}} \left(\sum_{s=1,2,..}^{\infty} A_{\mathrm{I_k}} e^{W_{\mathrm{s}} y} \cos\left(W_{\mathrm{s}}(x - x_{1\mathrm{k}})\right) - \mu_o J_{\mathrm{k}} \right) \sin(W_{\mathrm{m}} x). \end{aligned} \tag{3.64}$$

The x-axis flux density of region II at $y = 0$:

$$B_{\mathrm{x_{II}}}(y=0) = \sum_{m=1,2,..}^{\infty} \left(\Big(A_{\mathrm{II}} - B_{\mathrm{II}}\Big) \cos(k_{\mathrm{n}} x) + \Big(C_{\mathrm{II}} - D_{\mathrm{II}}\Big) \sin(k_{\mathrm{n}} x) \right). \tag{3.65}$$

Equalizing both the cosine and sine components of both (3.64) and (3.65). This results in two equations.

$$\begin{aligned} A_{\mathrm{II}} - B_{\mathrm{II}} &= \zeta_1, \\ C_{\mathrm{II}} - D_{\mathrm{II}} &= \eta_1. \end{aligned} \tag{3.66}$$

Equalizing the y-component of the flux density of region II to region I. The y-axis flux density of region II equals.

$$B_{\mathrm{y_{II}}}(y=0) = \sum_{m=1,2,..}^{\infty} \Big(-(A_{\mathrm{II}} + B_{\mathrm{II}}) \sin(W_{\mathrm{m}} x) + (C_{\mathrm{II}} + D_{\mathrm{II}}) \cos(W_{\mathrm{m}} x) \Big). \tag{3.67}$$

By obtaining an equivalent fourier series of this flux density in region I. Therefore, only a $\sin$-component exists in the fourier spectrum of the axial component in region I_{k} of the flux density shown in (3.62).

$$B_{\mathrm{y_{II_{eq}}}}(y=0) = \sum_{s=1,2,..}^{\infty} \sigma_1 \mathrm{sin}(\mathrm{W_s}(\mathrm{x} - \mathrm{x_{1t}})), \tag{3.68}$$

where σ_1 equals:

$$\begin{aligned} \sigma_1 = \frac{1}{W_{\mathrm{s}}} \int_{x_{1\mathrm{k}}}^{x_{1\mathrm{k}}+b_{\mathrm{so}}} \sum_{m=1,2,..}^{\infty} \Big(&-(A_{\mathrm{II}} + B_{\mathrm{II}}) \sin(W_{\mathrm{m}} x) \\ &+ (C_{\mathrm{II}} + D_{\mathrm{II}}) \cos(W_{\mathrm{m}} x) \Big) \mathrm{sin}(\mathrm{W_s}(\mathrm{x} - \mathrm{x_{1t}})). \end{aligned} \tag{3.69}$$

By equalizing (3.62) by the flux density of region I_{k} in the y-component in (3.69) at $y = 0$.

$$\sigma_1 = A_{\mathrm{I_k}}. \tag{3.70}$$

This results in N_s equations.

Region III; PM Region

The y and x components of the flux densities in region III are:

$$
\begin{aligned}
B_{\mathrm{y}} = \sum_{m=1,2,..}^{\infty} & \big(- C_{\mathrm{III}} e^{W_{\mathrm{m}} y} - D_{\mathrm{III}} e^{-W_{\mathrm{m}} y} + \mu_{\mathrm{o}} M_{\mathrm{c_y}} \big) \cos(W_{\mathrm{m}} x) \\
& + \big(A_{\mathrm{III}} e^{W_{\mathrm{m}} y} + B_{\mathrm{III}} e^{-W_{\mathrm{m}} y} + \mu_{\mathrm{o}} M_{\mathrm{s_y}} \big) \sin(W_m x), \\
B_{\mathrm{x}} = \sum_{m=1,2,..}^{\infty} & \big(A_{\mathrm{III}} e^{W_{\mathrm{m}} y} - B_{\mathrm{III}} e^{-W_{\mathrm{m}} y} - \mu_{\mathrm{o}} M_{\mathrm{c_x}} \big) \cos(W_{\mathrm{m}} x) \\
& + \big(C_{\mathrm{III}} e^{W_{\mathrm{m}} y} - D_{\mathrm{III}} e^{-W_{\mathrm{m}} y} - \mu_{\mathrm{o}} M_{\mathrm{s_x}} \big) \sin(W_{\mathrm{m}} x).
\end{aligned}
\tag{3.71}
$$

At $y = g + Y_{\mathrm{m}}$ the x-component of the magnetic field equals zero resulting in the following equations:

$$
\begin{aligned}
A_{\mathrm{III}} e^{W_{\mathrm{m}}(g+Y_{\mathrm{m}})} - B_{\mathrm{III}} e^{-W_{\mathrm{m}}(g+Y_{\mathrm{m}})} - \mu_o M_{\mathrm{c_x}} = 0, \\
C_{\mathrm{III}} e^{W_{\mathrm{m}}(g+Y_{\mathrm{m}})} - D_{\mathrm{III}} e^{-W_{\mathrm{m}}(g+Y_{\mathrm{m}})} - \mu_o M_{\mathrm{s_x}} = 0.
\end{aligned}
\tag{3.72}
$$

At $y = g$ the x-component of the magnetic field of region III equals the magnetic field of region II, resulting in the following equations:

$$
\begin{aligned}
\mu_{\mathrm{r}} \left(A_{\mathrm{II}} e^{W_{\mathrm{m}} g} - B_{\mathrm{II}} e^{-W_{\mathrm{m}} g} \right) - \left(A_{\mathrm{III}} e^{W_{\mathrm{m}} g} - B_{\mathrm{III}} e^{-W_{\mathrm{m}} g} - \mu_{\mathrm{o}} M_{\mathrm{c_x}} \right) = 0, \\
\mu_{\mathrm{r}} \left(C_{\mathrm{II}} e^{W_{\mathrm{m}} g} - D_{\mathrm{II}} e^{-W_{\mathrm{m}} g} \right) - \left(C_{\mathrm{III}} e^{W_{\mathrm{m}} g} - D_{\mathrm{III}} e^{-W_{\mathrm{m}} g} - \mu_{\mathrm{o}} M_{\mathrm{s_x}} \right) = 0.
\end{aligned}
\tag{3.73}
$$

In addition, at $y = g$ the y-component of the magnetic flux density of region III equals the magnetic field of region II, resulting in the following equations:

$$
\begin{aligned}
\left(A_{\mathrm{II}} e^{W_{\mathrm{m}} g} + B_{\mathrm{II}} e^{-W_{\mathrm{m}} g} \right) - \left(A_{\mathrm{III}} e^{W_{\mathrm{m}} g} + B_{\mathrm{III}} e^{-W_{\mathrm{m}} g} + \mu_{\mathrm{o}} M_{\mathrm{s_y}} \right) = 0, \\
\left(-C_{\mathrm{II}} e^{W_{\mathrm{m}} g} - D_{\mathrm{II}} e^{-W_{\mathrm{m}} g} \right) - \left(-C_{\mathrm{III}} e^{W_{\mathrm{m}} g} - D_{\mathrm{III}} e^{-W_{\mathrm{m}} g} + \mu_{\mathrm{o}} M_{\mathrm{c_y}} \right) = 0.
\end{aligned}
\tag{3.74}
$$

There are 6 equations in (3.72), (3.73), and (3.74). In addition, there are N_{s} equations in (3.70), and additional two equations in (3.66).

There are eight variables in region II and III, and additional N_{s} variables in region I.

Therefore, a matrix is constructed with all the subsequent equations and all variables are solved.

Validation: Flux Densities Comparison for 50kW Reference Machine

The comparisons of the no-load axial and circumferential flux densities, i.e. B_y and B_x, with the results from the 2D FE model are shown in Figs. 3.25 and 3.26 respectively. The flux densities are compared with the 2D FE model shown in Fig.

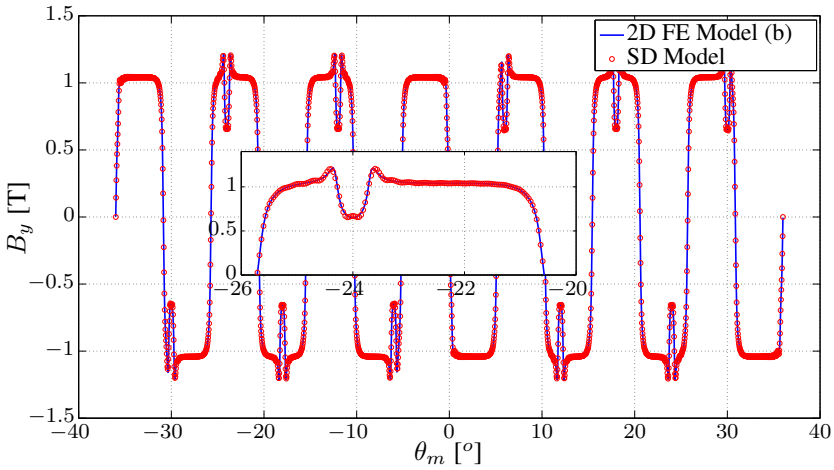

Figure 3.25: Axial flux density component B_y of the SD model compared with the 2D FE model at no load in the center of the air gap area.

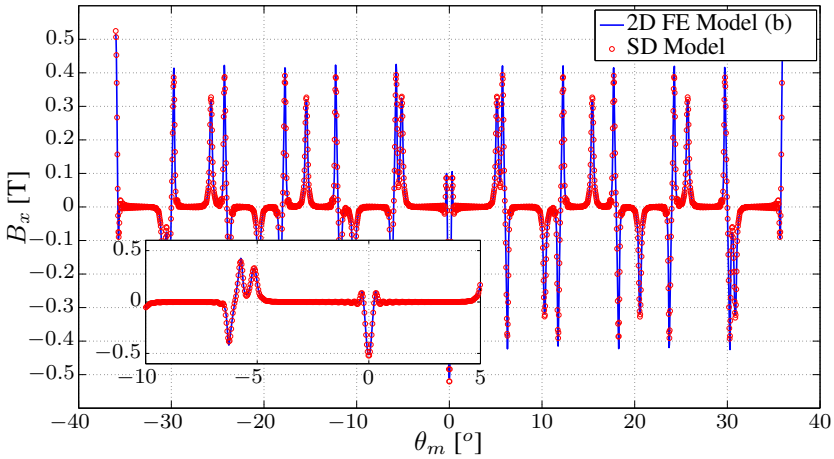

Figure 3.26: Circumferential flux density component B_x of the SD model compared with the 2D FE model at no load in the center of the air gap area.

3.4. (b) without the tooth tips at a slot opening of 5mm. It clearly shows that the correspondence is very good[4].

Figures 3.27, and 3.28 show the axial and tangential flux density respectively

[4]The percentage error of the second norm of the error divided by the second norm of the 2D FE model flux densities of the y and x components are shown in Tables 3.3. It shows percentage errors for the y and x components of 1.1% and 8.4% respectively

of the armature-reaction field. They show a good correspondence with the 2D FE model[5].

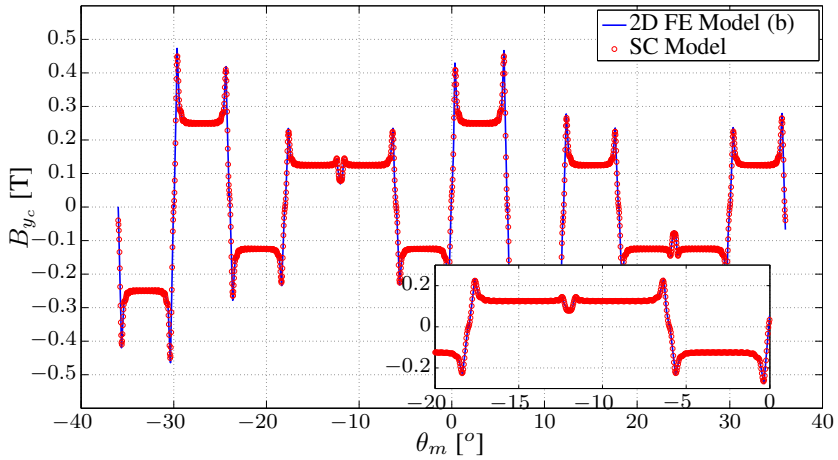

Figure 3.27: Axial flux density component B_y of the SD model compared with the 2D FE model considering only the armature current in the center of the air gap area.

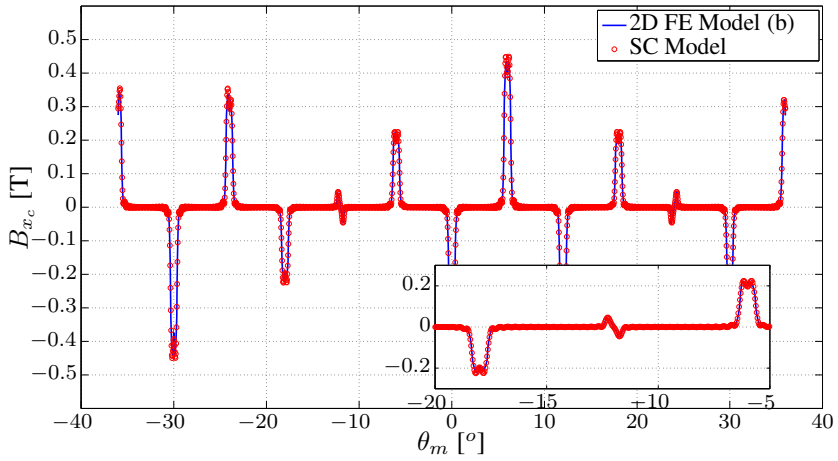

Figure 3.28: Circumferential flux density component B_x of the SD model compared with the 2D FE model considering only the armature current in the center of the air gap area.

[5]The percentage error of the second norm of the error divided by the second norm of the 2D FE model flux densities of the y and x components are shown in Tables 3.4. It shows percentage errors for the y and x components of 3% and 5.7% respectively

Figures 3.29 (a) and (b) show the distribution of the norm of the flux density and the magnetic vector potential at no load for 5mm slot opening and slice number 8. Fig. 3.29 (a) shows that the flux density reaches a minimum under the slot opening. Over the axial length, the effect of slot opening reduces. This is revealed also by the contour plot of the magnetic vector potential in Fig. 3.29 (b).

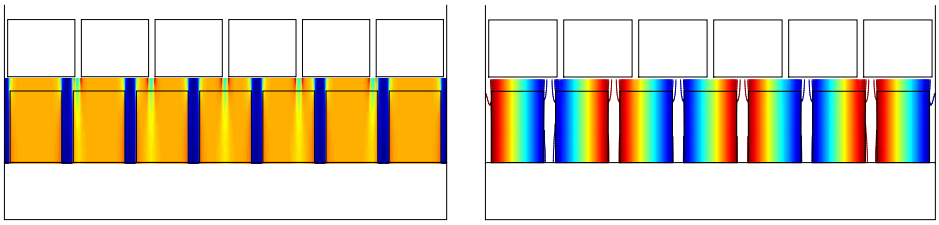

(a) $\sqrt{B_x^2 + B_y^2}$ (b) A_z

Figure 3.29: Surface plot of the flux density and contour plot of the magnetic vector potential at the no load.

Figures 3.30 (a) and (b) show the distribution of the norm of the flux density and the magnetic vector potential due to the armature reaction current with zero remanent flux for 5mm slot opening and slice number 8. Fig. 3.30 (a) shows that the flux density reaches a minimum under the slot opening. Over the axial length, the effect of slot opening reduces. This is revealed also by the contour plot of the magnetic vector potential in Fig. 3.30 (b).

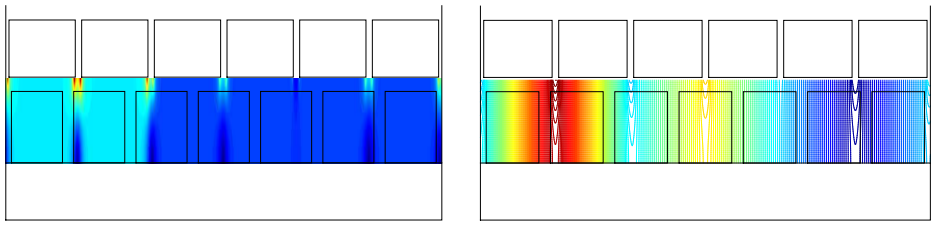

(a) $\sqrt{B_x^2 + B_y^2}$ (b) A_z

Figure 3.30: Surface plot of the flux density and contour plot of the magnetic vector potential considering only the armature current.

3.5 Comparison between Different Models

3.5.1 Comparison of CPU Time

Table 3.2 summarizes the CPU time for each of the tested models. All calculations were done on a PC operating a 64 bit version of Windows 7, the PC has a core i7 processor, and a memory of 8 GB. Both the 2D FE and analytical models divide

the machine in eight slices. All models were computed for 50 positions of the rotor, equally divided over one cycle. The comparison shows that the 3D FE model is very time consuming compared to the other models. In addition, both 2D FE models required one hour of computation which is still very time consuming. The comparison also shows the superiority of analytical models compared to the FE models. Moreover, the LF and the SC models are much faster than the SD model, this is due to the more complex equations that have to be solved in the SD model. The LF and SC models use 300 harmonic orders for the calculation of the PM flux density, while the SD model uses 280 in the air gap and PM area and 35 harmonics in each slot.

Table 3.2: Comparison of the CPU time between the analytical and the FE models.

	Model Type	CPU Time
FE Models	3D FE Model (Section 3.3.1)	10hrs
	2D FE Model (a) (Section 3.3.2)	1hr
	2D FE Model (b) (Section 3.3.2)	1hr
Analytical Models	LF Model (Section 3.4.1)	13s
	SC Model (Section 3.4.2)	15s
	SD Model (Section 3.4.3)	40s

3.5.2 Comparison of Flux Densities

Tables 3.3 and 3.4 show the second vector norm of the error between the circumferential (x) and axial (y) flux densities of the different analytical models and the 2D FE model, shown in Fig. 3.4 (a), in percentage from the second vector norm of the flux density of the same 2D FE model. Table 3.3 shows the error for no-load condition and Table 3.4 shows it for armature-reaction conditions. It can be seen that the SD model is the most accurate model in all circumstances. In addition, the SC model is more accurate than the LF model for the calculation of the axial component. The norm of the error in the circumferential flux density for the SC model is very high compared to the SD model.

3.5.3 Comparison of Cogging Torque

The torque is calculated for the complex SC and the SD models using the Maxwell's stress tensor by obtaining the circumferential and axial components of

Table 3.3: Comparison of the no load flux density between the analytical and the 2D FE models.

Analytical Model type	$\frac{\left\|\mathbf{B}_{\mathrm{y_{ana}}}-\mathbf{B}_{\mathrm{y_{FE}}}\right\|_2}{\left\|\mathbf{B}_{\mathrm{y_{FE}}}\right\|_2} * 100\ [\%]$	$\frac{\left\|\mathbf{B}_{\mathrm{x_{ana}}}-\mathbf{B}_{\mathrm{x_{FE}}}\right\|_2}{\left\|\mathbf{B}_{\mathrm{x_{FE}}}\right\|_2} * 100\ [\%]$
LF Model	5.2	-
SC Model	2.0	30.0
SD Model	1.1	8.4

Table 3.4: Comparison of the armature reaction flux density between the analytical and the 2D FE models considering only armature current.

Analytical Model type	$\frac{\left\|\mathbf{B}_{\mathrm{y_{ana}}}-\mathbf{B}_{\mathrm{y_{FE}}}\right\|_2}{\left\|\mathbf{B}_{\mathrm{y_{FE}}}\right\|_2} * 100\ [\%]$	$\frac{\left\|\mathbf{B}_{\mathrm{x_{ana}}}-\mathbf{B}_{\mathrm{x_{FE}}}\right\|_2}{\left\|\mathbf{B}_{\mathrm{x_{FE}}}\right\|_2} * 100\ [\%]$
SC Model	14.2	33.0
SD Model	3.0	5.7

the flux densities in half of the air gap area and using (3.75) [44]:

$$T = \frac{1}{\mu_o} \sum_{i=1,2,..}^{N_s} \int_0^{2\pi R^i_{\mathrm{av}}} R^i_{\mathrm{av}} B_{\mathrm{x_i}}(x,y) B_{\mathrm{y_i}}(x,y)\ t_{\mathrm{cp}}\ \mathrm{d}x \tag{3.75}$$

Figure 3.31 shows the difference between the three FE models described in the chapter for cogging torque computation at 5mm slot opening. The horizontal axis in Fig. 3.31 indicates the rotor position (Φ_m). Fig. 3.31 shows that the 2D FE models may indeed be used as a reference solution. Their deviation with regard to the 3D FE model is negligible. Fig. 3.31 also confirms that the usage of the geometry without tooth tips is sufficient to describe the cogging torque for all other geometries.

The cogging torque for the analytical models and the FE model without tooth tips is shown in Fig. 3.32. It is clear that the subdomain model is the most accurate one. It is clear also that the models based on lateral force (LF) and complex Schwarz Christoffel (SC) models can not accurately predict the cogging torque.

Figure 3.33 depicts the peak-to-peak value of the cogging torque as a function of the slot opening. The PM is a rectangular shape of 40mm width. The x-axis in this figure indicates the slot opening over the tooth pitch at minimum radius. It is obvious that at a certain slot opening, the cogging torque is minimized. The SD model is the most accurate analytical tool to predict both the value of the cogging torque and the locus of minimum cogging torque. The models based on LF and SC can not exactly determine the value of the cogging torque, nor the locus of the minimal cogging torque.

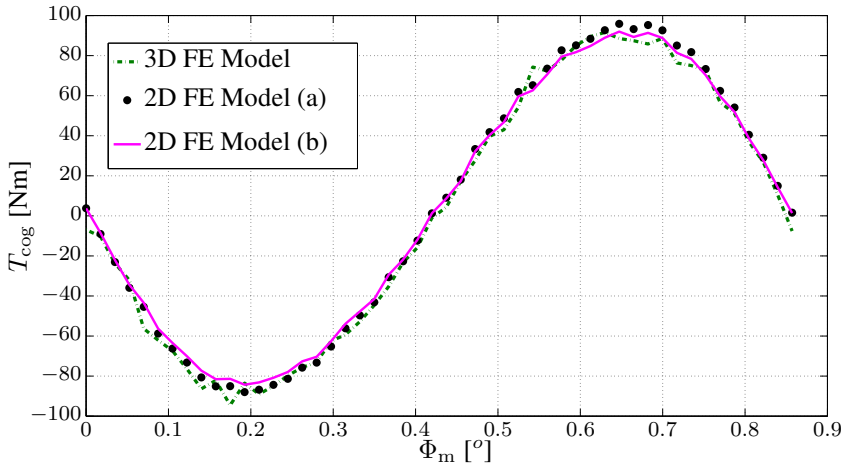

Figure 3.31: Cogging torque variations for different rotor positions Φ_m for the three FE models only.

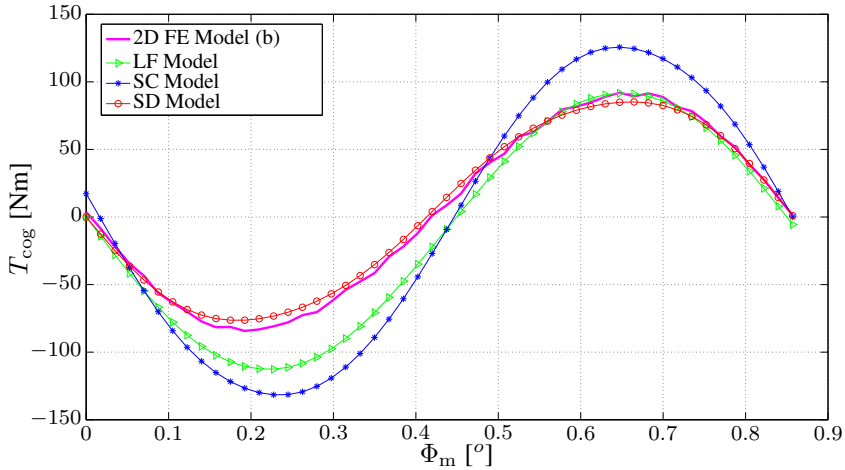

Figure 3.32: Cogging torque variations for different rotor positions Φ_m for the FE model (b) and the analytical models.

Figure 3.34 describes the variations of the peak-to-peak cogging torque with respect to the ratio between PM width and pole arc at minimum radius. A similar observation can be noticed. In this figure, the most accurate model is the SD one.

In addition, the SC model succeeded to obtain the locus of minimum cogging torque. However, it could not obtain the same peak-to-peak value as the 2D FE model.

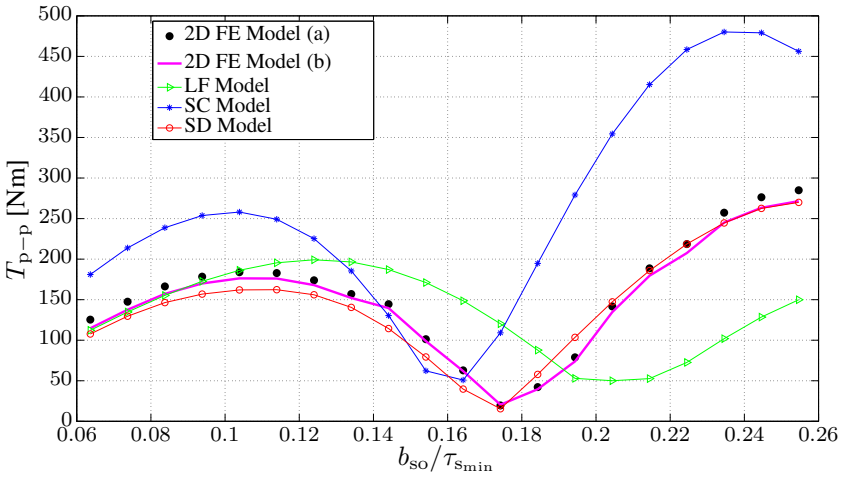

Figure 3.33: Impact of slot opening on the peak-to-peak cogging torque.

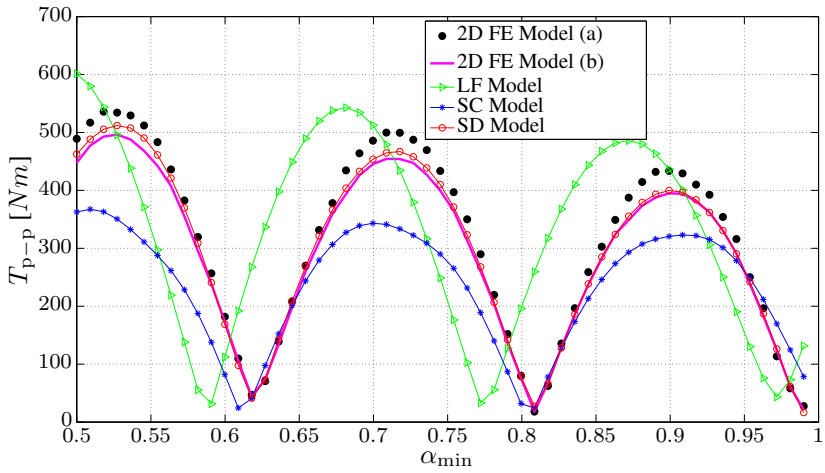

Figure 3.34: Impact of pole arc to pole pitch ratio at minimum radius on the peak-to-peak cogging torque.

3.5.4 Comparison of Torque Ripple at Full Load

The full load torque of the complex SC and SD model is calculated by inducing the currents and calculating the fluxes in the center of the air gap area. Afterwards, using (3.75) to obtain the full load torque.

The torque waveform at full load is studied in Fig. 3.35. It shows that the 2D FE model can accurately predict the mean value of torque and torque ripple, giving almost the same results as the 3D FE model. Both versions of the 2D FE models can accurately predict the torque and its ripple. However, the SD model resulted in a

less accurate solution compared to the 3D FE models. The error occurs because the FE model calculates the torque using the magnetic co-energy while the analytical models calculate it using Maxwell's stress tensor. The SD model can track the results in comparison with the 2D FE model (b) without tooth tips. Moreover, the SD model can predict almost the same value of torque ripple. The SC model is less accurate for the calculation of torque ripple and mean value of torque.

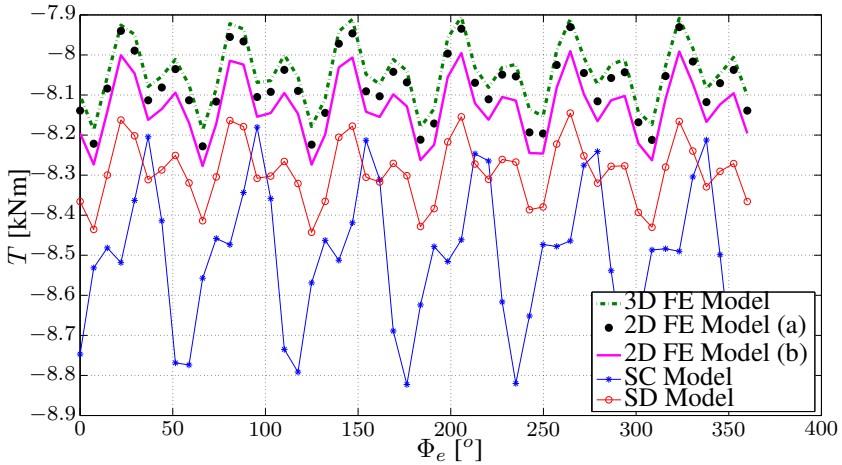

Figure 3.35: Electromagnetic torque variations output for different models with respect to the electrical angle Φ_e.

Table 3.5 summarizes the results. It shows the mean torque values for each method and the error relative to the mean torque of the 3D FE models. It also shows the peak-to-peak torque error relative to the peak-to-peak torque of the 3D FE model. It clearly states that the SC model can not accurately predict the torque ripple. It can predict the mean value of torque with a 6 % error. In addition, the SD model is robust enough to predict both the torque ripple and mean torque. It clearly states that the both 2D FE models can predict the torque ripple and mean torque accurately.

Table 3.5: Comparison of the mean torque, torque ripple, and relative error compared to the 3D FE model.

	Model Type				
	FE Models			Analytical Models	
	3D FE Model	2D FE Model (a)	2D FE Model (b)	SC Model	SD Model
T_{mean} (kNm)	-8.04	-8.07	-8.13	-8.5	-8.3
Error$_{T_{\text{m}}}$ (%)	-	0.4	1	6	3
$T_{\text{p-p}}$ (Nm)	282	297	286	642	297
Error$_{T_{\text{r}}}$ (%)	-	5	1.5	128	5

3.5.5 Comparison of No Load and Full Load Voltages

The voltage is calculated based on the winding function generated according to the star of the slot of the machine described in Fig. 3.37.

$$\begin{aligned} \phi_{\mathrm{a}} &= t_{\mathrm{cp}} \int_0^{2\pi R_{\mathrm{av}}^i} B_{\mathrm{y}} N_{\mathrm{a}} \mathrm{d}x, \\ V_{\mathrm{a}} &= -\frac{\phi_{\mathrm{a}}(t) - \phi_{\mathrm{a}}(t-1)}{\Delta t}, \end{aligned} \tag{3.76}$$

where $\theta_e = 2\pi f t$ is the time in seconds.

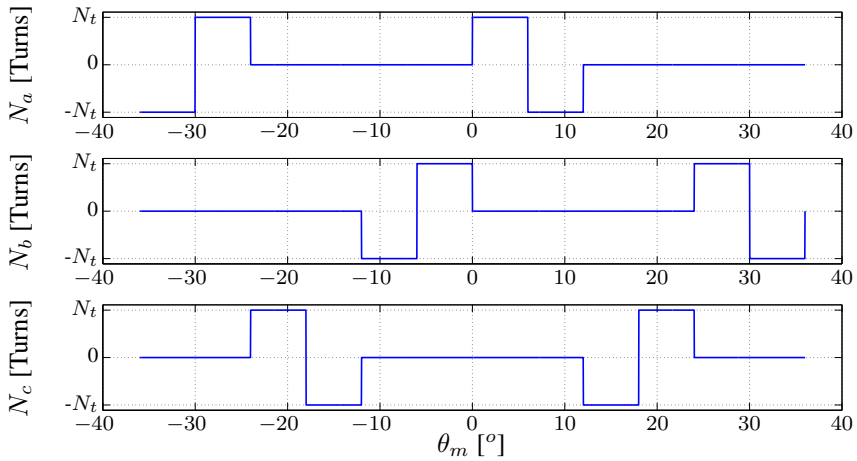

Figure 3.36: Winding function distribution of the three phases. N_t is the number of turns per slot.

Figure 3.37 shows the no load voltage comparison between all methods. All methods can predict the same no load voltage without significant error. Table 3.6 summarizes the no load rms voltage difference between all methods. The SD model is the best predicting analytical model for the no load voltage. The 2D FE model with tooth tips gives also the lowest error compared to the other model without tips. In conclusion, the error in the axial component of the flux density does not really cause a significant error in the no load voltage.

At the full load conditions, the shape of the slot plays an important role for the amplitude of the voltage. As the slot width decreases, it results in more voltage rms values. Therefore, the 2D FE model without tooth tips results in a higher voltage amplitudes as shown in Fig. 3.38 because of the reduced slot width. The accuracy of the 2D FE model with tooth tips is comparable with the 3D FE model as shown in Table 3.6. The analytical models predict only the air gap inductances without any prediction of the slot leakage inductance. Therefore, all analytical models result in lower voltage amplitudes as described in Table 3.6.

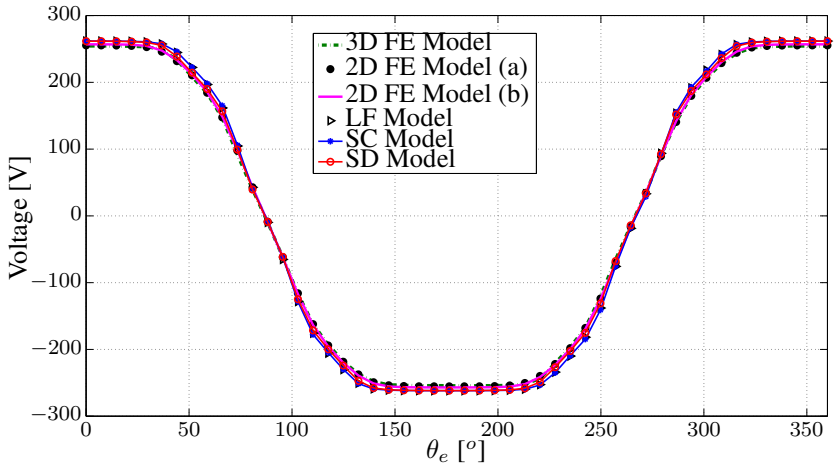

Figure 3.37: No load voltage output for different models with respect to the electrical angle θ_e.

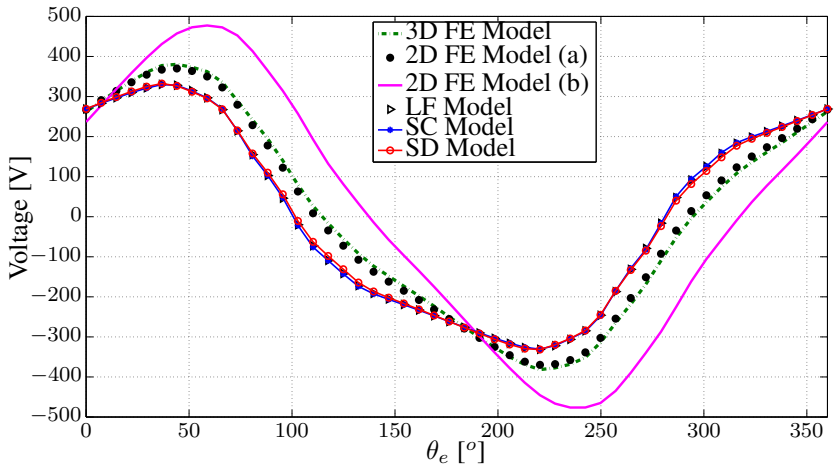

Figure 3.38: Full load voltage output for different models with respect to the electrical angle θ_e.

3.6 Conclusions

This chapter investigated the effect of different modeling techniques on the prediction of the cogging torque, and torque ripple at full load. A comparison between a 3D FE model, 2D FE models, and the analytical models has been done. Two

Table 3.6: Comparison of the no load, full load voltage, and relative error compared to the 3D FE model.

	Model Type					
	FE Models			Analytical Models		
	3D FE Model	2D FE Model (a)	2D FE Model (b)	LF Model	SC Model	SD Model
No load voltage (V)	211.3	211.9	213.3	220.3	220.59	218.1
$\text{Error}_{V_{\text{no}_{\text{rms}}}}$ (%)	-	0.28	0.95	4.3	4.35	3.2
Full load voltage (V)	253.3	250.2	312.2	235	235	234.1
$\text{Error}_{V_{\text{full}_{\text{rms}}}}$ (%)	-	0.83	23	7.1	7.1	7.4

types of FE models are studied in this chapter, i.e. a model with and one without tooth tips. The 2D FE model without tooth tips is used as reference solution to compare the different analytical models. Three analytical models are studied in this comparison. One is based on the lateral force model using a simple Schwarz Christoffel transformation. Another model is based on a more complex Schwarz Christoffel transformation that can account for both the axial and circumferential flux densities. The third model is based on the subdomain model (SD).

The comparison shows that both versions of the 2D FE models are capable of obtaining almost the same value for the cogging torque as the 3D model, which models the tooth tips. This proves that neglecting the tooth tips results in a good solution for the cogging torque and torque ripple.

The comparison has clearly shown that the subdomain model is the only analytical model that can accurately compute the mean value of the torque and the torque ripple when compared to the 3D FE model.

Additional studies concerning slot opening variations, and permanent magnet pole arc width variations were done. They have clearly shown that the only method that is capable of obtaining the locus of minimum cogging torque and its value is the subdomain model. Therefore, it is well recommended for studies concerning optimization of cogging torque and torque ripple for the axial flux permanent magnet synchronous machines to model the machine with this technique.

The no load and full load voltage waveforms have been compared together. They have shown that all models can accurately predict the no load voltages without a significant error. However, the full load voltage can only be predicted by the 2D FE model without tooth tips. All analytical models can only obtain the voltage taking into account the air gap inductance without any details about the slot leakage inductance.

Chapter 4

Coupled Schwarz-Christoffel - Magnetic Equivalent Circuit Model

4.1 Introduction

Modeling of non-linear properties of magnetic materials is essential for a proper behaviour estimation of any electromagnetic device, especially electric machines (EMs). To this end, several numerical as well as analytical techniques were developed and used over last decades [7, 9, 34–36, 60]. Although numerical techniques, such as finite element (FE) analysis, are the most accurate techniques to model EMs, they are not preferable in early design stages due to their expensive computational burden.

Therefore, different analytical modeling concepts, with different accuracy levels, were developed [33,40–42,51,53,56]. In chapter 3, analytical models based on solving Maxwell's equations under the assumption of infinite permeability of the magnetic materials of the electric machine, are presented and discussed. Although these models are very useful to accurately obtain the cogging torque and torque ripple, they can't be used to calculate either the losses or the inductances. This is due to not considering the non-linear behaviour of the magnetic material.

An alternative analytical modeling concept is to use the magnetic equivalent circuit (MEC), which is based on representing the EM with a magnetic reluctance network that depends on machine geometrical parameters and non-linear magnetic material properties. In such a technique, the modeling accuracy highly depends on the used discretization level. Additionally, it is important to model the air gap by reasonable reluctance paths, that change continuously with the rotation of the EM. This means that at each rotor position, all rotor and stator nodes need to be aligned

with the air gap nodes[1] [61–64], which increases the complexity of the MEC.

In [61], the MEC was developed for an interior radial flux fractional slot permanent magnet synchronous machine. Although a huge reluctance network size was utilized, cogging torque and torque ripple results were not validated.

In order to simplify the air gap reluctance representation, the alignment between the rotor and stator is divided into three states in [63]; a state when a little part of the magnet contributes to the MMF in the stator, a state when a higher part contributes and a state when it totally contributes. However, a very large matrix is obtained and the problem becomes more complex.

Other attempts have been made to simplify the air gap reluctance representation, such as the refined mesh approach, that was proposed in [64]. In the refined mesh approach, each magnet is subdivided into a high number of elements, i.e. 15, which allows the demagnetization effect investigation. The reluctances connecting a stator tooth and a rotor element are obtained by integrating the product of their window functions and the inverse of the air gap length function. Although the MEC accuracy is highly improved using this refined mesh approach the complexity dramatically increases. Very recently, a hybrid subdomain-MEC model of radial flux permanent magnet synchronous machines that includes saturation effects has been developed in [65].

When axial flux EMs are being modeled using MEC, the machine is divided into a number of radial slices, where the magnetic equivalent model is applied in each slice, [62]. In [62], the developed MEC model of the AFPMSM was nicely validated with FE model, but only for the mean value of the torque and the terminal voltage.

As has been mentioned earlier, the alignment between rotor and stator reluctances is the most challenging aspect in MEC-based models. In order to tackle this issue, we have proposed in this thesis to combine the SC model, that was described in section 3.4.2, with the MEC considering the non-linear properties of the magnetic material, see [44].

In this chapter, this combined solution is described in details. A solution of Maxwell's equations based on the SC technique, described in section 3.4.2, is used with the developed MEC to obtain all the magnetic induction values everywhere inside the stator tooth including the non-linear behaviour of the material. Other quantities like torque, terminal voltage, and losses are then obtained a posteriori.

4.2 FE Models Including Non-Linear Magnetic Material

For both 3D and 2D FE models, described in Figs. 3.2 (a) and (c), the relative magnetic permeability in (3.13) of the stator core is modelled by a saturation dependent relative permeability $\mu_{\mathrm{r}}(B)$, see section 4.2.1.

[1] Nodes are the terminals of each magnetic reluctance

Saturation of the magnetic material results in additional harmonics in the air gap flux density that lower the electromagnetic torque produced by the machine. Therefore, the use of a non-linear material model in the stator cores is necessary. For the rotor disks, a constant relative magnetic permeability is assumed of 10000.

The norm of the flux densities distribution of different loading conditions for the stator core material considering non-linear permeability are shown in Figs. 4.1 (a), (b), and (c) for no load, rated loading and double the rated loading conditions. The peak flux density distribution on all the teeth increases as shown in Figs. 4.1 (a), (b), and (c) from no load to double the rated load.

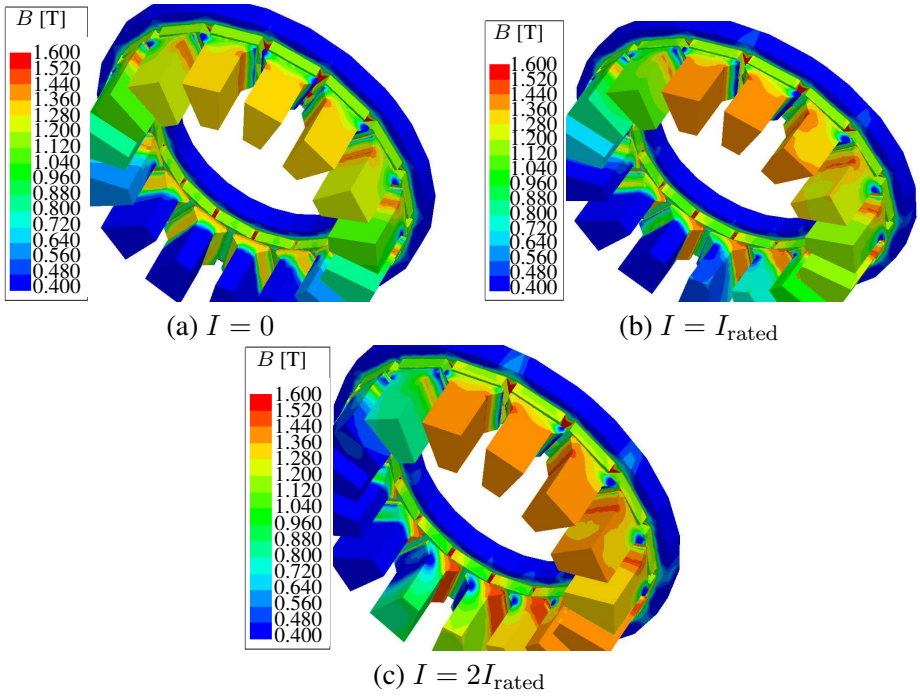

(a) $I = 0$ (b) $I = I_{\text{rated}}$

(c) $I = 2I_{\text{rated}}$

Figure 4.1: 3D absolute flux density distribution of the machine for different loading conditions.

4.2.1 Mathematical Modelling of Non-Linear Material

To express the nonlinearity and saturation feature of the magnetic material in the stator cores, the magnetic field H and the magnetic flux density B are linked through:

$$H(B) = \frac{1}{\mu_{\text{o}}\mu_{\text{r}}(B)}B, \tag{4.1}$$

in which the relative magnetic permeability μ_r depends on the actual value of the magnetic flux density. For numerical stability reasons, the mathematical expression for the magnetic permeability $\mu_\mathrm{r}(B)$ as well as its first derivative $\frac{\mathrm{d}\mu_\mathrm{r}(B)}{\mathrm{d}B}$ need to be continuous functions.

In literature, many analytical approximations for the single value magnetisation curve are found [66–69]. The single valued non-linear constitutive relation of the soft magnetic material is modelled by three material dependent parameters H_0, B_0 and ν [70]. The expression for the relative magnetic permeability of the soft magnetic material μ_r is given by:

$$\mu_\mathrm{r}(B) = \frac{B_\mathrm{o}}{\left[H_\mathrm{o}\mu_\mathrm{o}\left(1+\left(\frac{B}{B_\mathrm{o}}\right)^{\nu-1}\right)\right]}. \tag{4.2}$$

The parameters H_o and B_o determine the initial value of the relative permeability of the material $\mu_\mathrm{r,ini}$:

$$\mu_\mathrm{r,ini} = \frac{B_\mathrm{o}}{H_\mathrm{o}\mu_\mathrm{o}}. \tag{4.3}$$

When $B = B_\mathrm{o}$, the magnetic permeability reaches half of its maximum value.

The third parameter ν defines the slope of the variation of the relative magnetic permeability as a function of the magnetic flux density B. The higher the value of ν, the steeper the slope [71].

The material used in the simulations in both the FE and the combined SC-MEC model is M600-50A. The fitted parameter values are $H_\mathrm{o} = 230.98$ A/m, $B_\mathrm{o} = 1.46$ T, and $\nu = 20.4$. The non-linear permeability μ_r with respect to the magnetic flux density of the measured $\mu_\mathrm{r} - B$ characteristics at 50Hz and equation (4.2) are shown in Fig. 4.2.

Equation (4.2) is used for both the FE models and the combined SC-MEC model. The $B - H$ curve is shown in Fig. 4.3. Machines are normally designed to operate at the knee point. For the material M600-50A, the knee point in the $B - H$ curve exists at almost 1.4 T. Therefore, the design point is at 1.45T-1.5T.

4.2.2 Core Loss Computation

The flux densities are calculated at the grid points for the 3D and 2D FE models shown in Figs. 4.4 and 4.5 respectively. These flux densities are used to *a posteriori* calculate the iron losses. For the 3D FE model, the three coordinates are recorded to calculate the losses; for the 2D FE model, only the x-y flux densities are recorded.

Here, the principle of loss separation is introduced in [72]. The total stator losses for different grid points, shown in Figs. 4.4 and 4.5 are calculated using the radial, axial and tangential flux densities obtained from the FE models.

Here, the total stator core loss is composed of a hysteresis loss, a classical loss and an excess loss component:

$$P_\mathrm{Fe} = P_\mathrm{hy} + P_\mathrm{cl} + P_\mathrm{exc}. \tag{4.4}$$

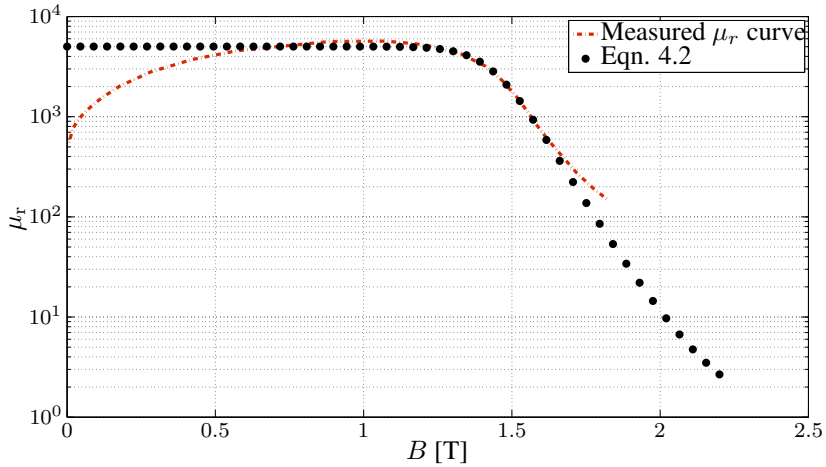

Figure 4.2: μ_r-B curve of the used stator material in the studied models.

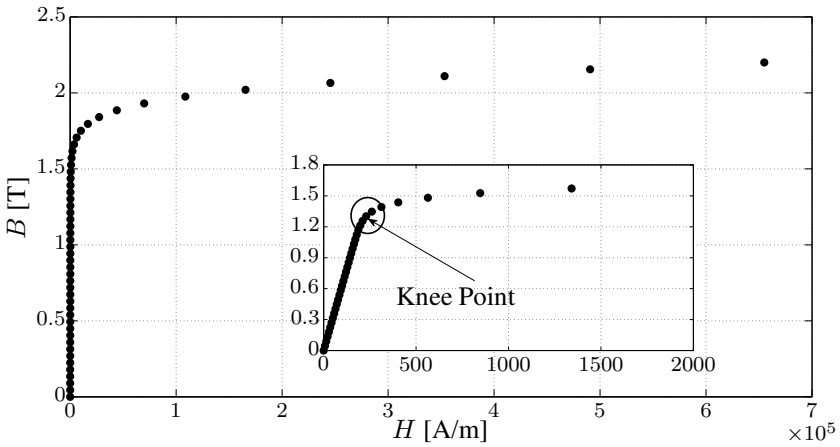

Figure 4.3: B-H curve of the used stator material in the studied models.

The hysteresis loss p_{hy} is determined by the peak value of the magnetic flux density B_{p}:

$$< p_{\mathrm{hy}} >= k_{\mathrm{Fe},1} B_{\mathrm{p}}^{k_{\mathrm{Fe},2}} f, \tag{4.5}$$

where f is the frequency corresponding with the fundamental component. $k_{\mathrm{Fe},1}$ and $k_{\mathrm{Fe},2}$ are fitting parameters for the hysteresis losses for the selected iron material. $< p_{\mathrm{hy}} >$ indicates the time average value of the hysteresis loss per kilogram over the fundamental period.

The instantaneous classical power losses per kilogram depends on the time

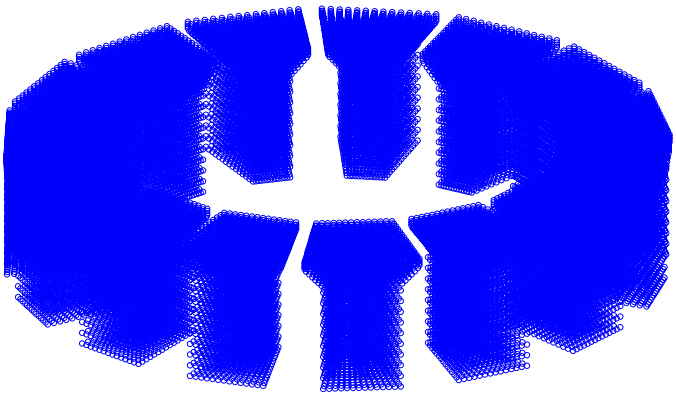

Figure 4.4: Grid points in 3D FE Model recorded to calculate losses.

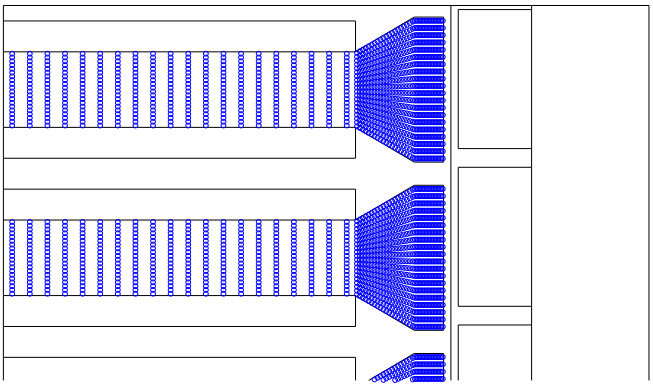

Figure 4.5: Grid points in 2D FE Model of two teeth recorded to calculate losses.

derivative of the magnetic flux density $B(t)$:

$$p_{\mathrm{cl}}(t) = k_{\mathrm{Fe},3} \left(\frac{\mathrm{d}B}{\mathrm{d}t} \right)^2 , \tag{4.6}$$

where the constant $k_{\mathrm{Fe},3}$ is determined by the conductivity and the thickness of the laminated silicon steel material.

In [73], an expression of the instantaneous excess loss per kilogram was introduced:

$$p_{\mathrm{exc}}(t) = k_{\mathrm{Fe},4} \left(\sqrt{1 + k_{\mathrm{Fe},5} \left| \frac{\mathrm{d}B}{\mathrm{d}t} \right|} - 1 \right) \left| \frac{\mathrm{d}B}{\mathrm{d}t} \right| . \tag{4.7}$$

The grid point are recorded in the 3D FE model (Fig. 4.4) or in the 2D FE model (Fig. 4.5) as a function of time. Later, the loss value is evaluated in each

grid point in the stator core geometry. Finally, summation of the losses of all grid points is done after multiplication by the volume of each grid point V_{i}.

$$P_{\mathrm{hy}} = \sum_{i}^{n} < p_{\mathrm{hy}} > \rho V_i, \tag{4.8}$$

$$P_{\mathrm{cl}} = \sum_{i}^{n} \left\{ \frac{1}{T} \int_{0}^{T} p_{\mathrm{cl}}(t) \mathrm{d}t \right\} \rho V_i, \tag{4.9}$$

$$P_{\mathrm{exc}} = \sum_{i}^{n} \left\{ \frac{1}{T} \int_{0}^{T} p_{\mathrm{exc}}(t) \mathrm{d}t \right\} \rho V_i, \tag{4.10}$$

where ρ is the iron material density which equals 8760 kg/m^3 and n is the number of grid points.

The total classical losses P_{cl} and excess losses P_{exc} are obtained by averaging of (4.6) and (4.7) respectively. This is shown as an integration over the studied time period T in (4.9) and (4.10). The hysteresis losses (4.8) are only dependent on the peak value of the flux density. The total loss value P_{Fe} in Watts can be obtained then by (4.4).

The losses distribution per unit volume in W/m^3 is shown in Figs. 4.6 (a) and (b) for 3D and 2D FE models, respectively. For the 2D FE model, the losses per unit volume for different layers are added together to compute the total W/m^3 for all computed slices described in chapter 3. It is clear that the W/m^3 for both models are quite similar. They preserve the same average losses per unit volume of 6.5$\times 10^5$ W/m^3.

4.3 Magnetic Equivalent Circuit Model

A magnetic equivalent circuit (MEC) is based on the re-presentation of major flux sources and lumped reluctance elements. The flux sources are the magneto-motive force (MMF) sources, which represent the injected electric currents in the windings. On the other hand, the PM is usually modeled by a flux source in parallel to a self reluctance. The lumped reluctance elements consist of linear and non-linear reluctances of the stator and rotor cores. They are dependent on the relative permeability of the used material. The stator core relative permeability is a function of the flux passing through the element itself. The PM and air gap permeability in this case are constant.

As previously outlined, in this section, a novel approach is proposed to avoid the alignment between the rotor and stator reluctances. In this technique, the solution of Maxwell's equations are obtained firstly for the combined effects of the electric currents and PMs. This is done through the axial component of the flux

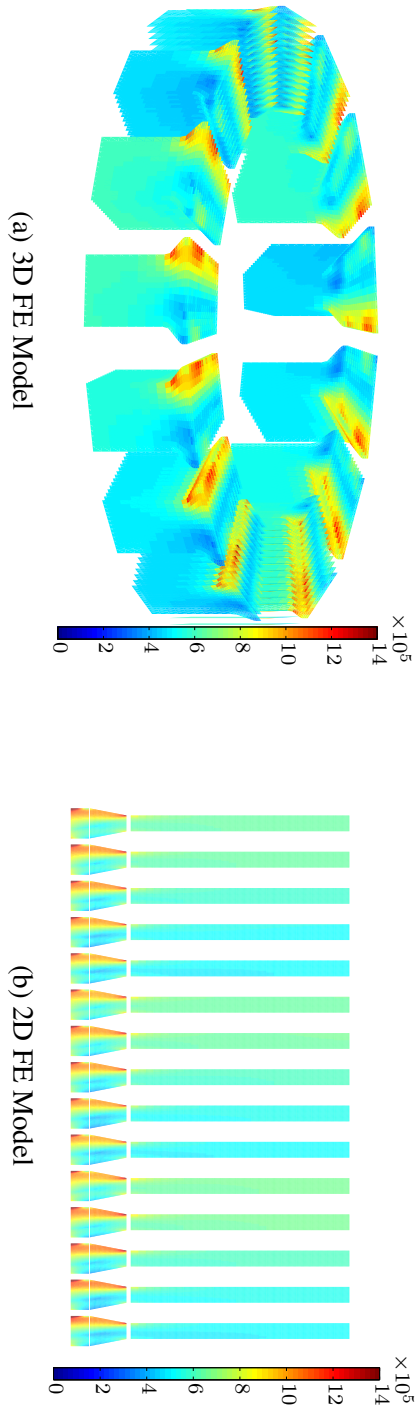

Figure 4.6: Loss distribution in W/m^3 for the 3D and the 2D FE models.

density of the complex SC model described in section 3.4.2. Afterwards, the flux densities, obtained from the complex SC model, are applied to the MEC. Through this technique, the solution for the terminal voltage and iron losses are obtained accurately without any alignment problem between the rotor and stator reluctances.

This technique neglects the effect of saturation of the stator core on the air gap flux density. However, as will be shown in the results section, this effect under rated loading and double the loading condition can be neglected.

The proposed combined solution of SC-MEC model is shown in Fig. 4.7. It consists of four main components shown on the right part of the figure. The non-linear reluctances are associated with the iron core of the tooth. The air between the teeth is represented by a linear reluctance. The flux sources are the fluxes obtained from the solution of the SC model described in section 3.4.2. The MMF sources are the currents multiplied by the number of turns. Thanks to the symmetry, only half of the stator tooth is modeled as shown in Fig. 4.7.

Each tooth is divided into five regions as shown in Fig. 4.8. According to the flux direction flows in each region, the reluctance model division of each region, shown in Figs. 4.9 (a), (b), and (c) is determined. In the next subsections, the reluctance network of each region is determined. Moreover, the resultant flux sources of Maxwell's equations are then deduced. Finally, the non-linear set of equations is solved.

In the subsequent sections, the reluctance network is derived in section 4.3.1. The flux sources from Maxwell's equations are then deduced in section 4.3.2. The solution of the MEC is obtained in section 4.3.3. Finally the voltage and torque computations using the SC-MEC model are described in sections 4.3.4 and 4.3.5.

4.3.1 Magnetic Reluctance Values

The flux has to flow in certain paths in the reluctance network. The paths are determined for each part of the tooth such as described in [74, 75]. The tooth is modeled as shown in Fig. A.1 by reluctances in the x and z directions only.

For each region, described in Fig. 4.8, the flux has to flow in certain directions.

In regions 1 and 2, the flux lines flow mainly in the axial direction and less lines flow in the circumferential direction. Therefore, it is only useful to use the T type reluctance described in Fig. 4.9 (a). The derivations of these reluctances are described in Appendix A.

In region 3, where the flux starts to deviate and divide into more regions, the modeled flux lines are divided into three paths. The shape of the reluctance is changed as shown in Fig. 4.9 (c). The derivations of these reluctances are described in Appendix A.

In fractional slot concentrated winding (FSCW) machines, the number of stator slots is often not much different from the number of rotor poles. Consequently, there is typically a significant amount of leakage flux that crosses the stator slots. As a result, both radial and circumferential flux paths in the stator tooth-tips must

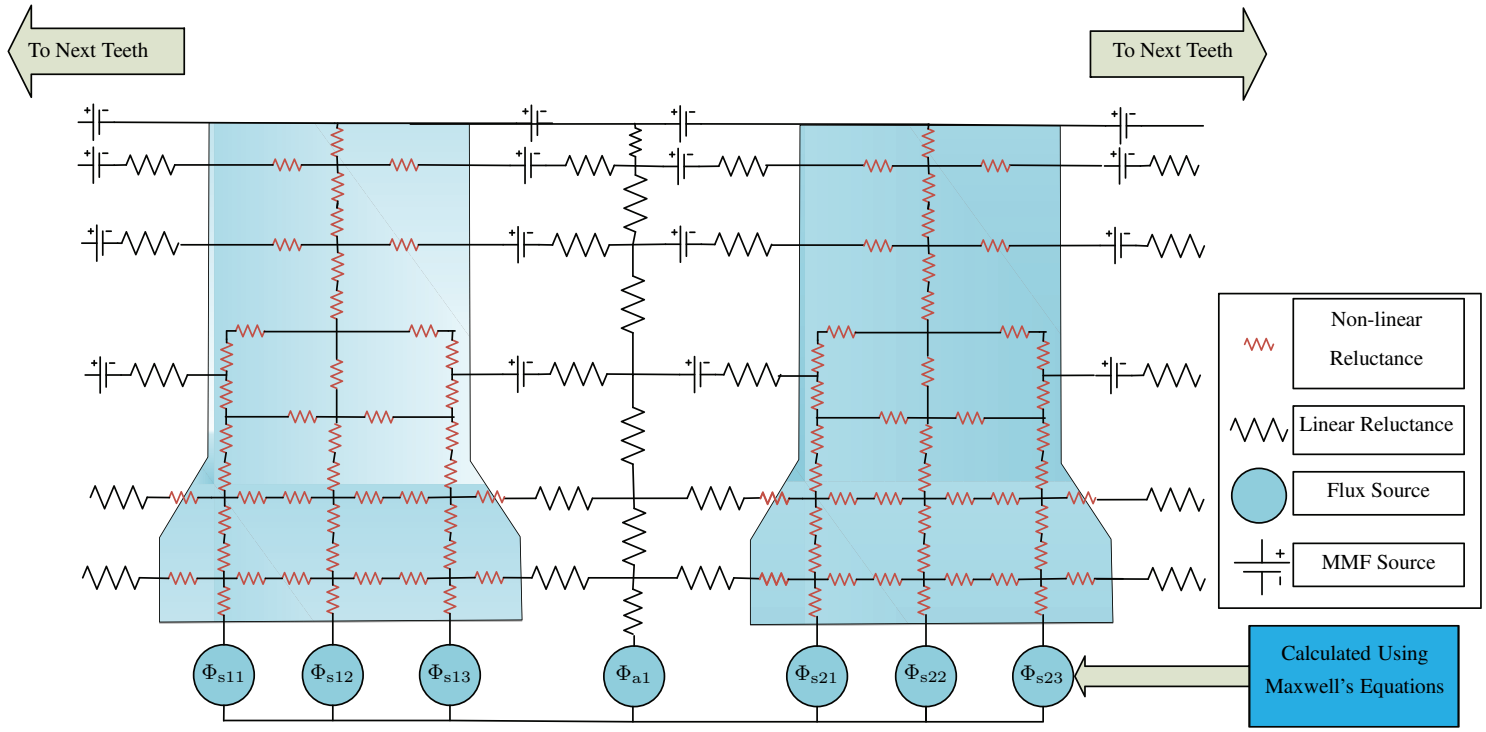

Figure 4.7: Combined SC-MEC model.

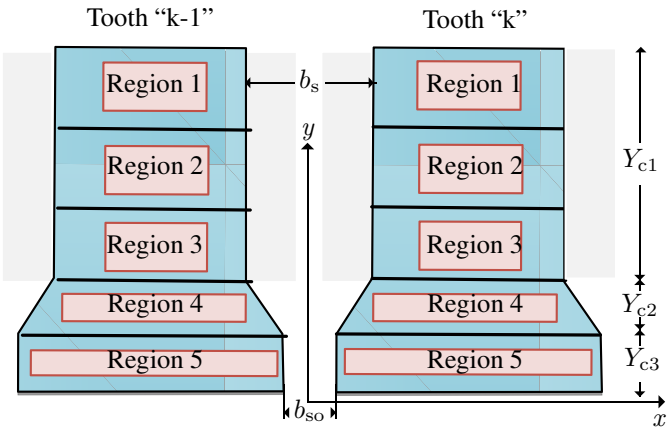

Figure 4.8: Regions dividing the tooth.

be captured by the model.

It is worth mentioning that the tooth-tip regions (regions 4 and 5 in Figs. 4.8) need to be modelled by a relatively high number of reluctances, as shown in Fig. 4.9 (b), due to the complex flux density patterns in such regions. The divisions of the reluctances R_{y2} and R_{y3} depend on a value D. The value of D and all the derivations of the reluctances are described in Appendix A.

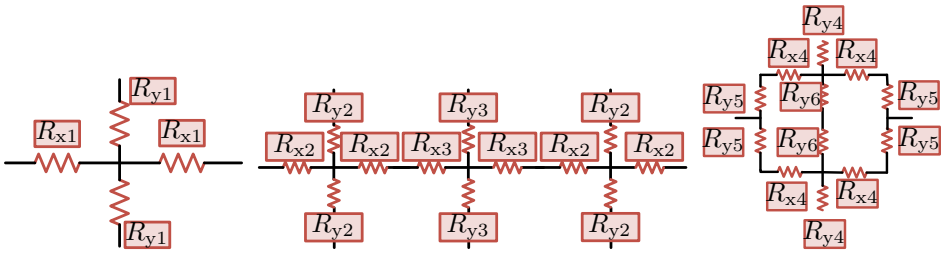

(a) Model (a) (b) Model (b) (c) Model (c)

Figure 4.9: Models of reluctance network used for each region.

4.3.2 Resultant Field From Maxwell's Equations

In this part, the resultant flux linkage sources (Φ_{a1}, Φ_{s11}, Φ_{s12}, and Φ_{s13}) are calculated using the SC model described in section 3.4.2, and then imposed to the MEC, as shown in Fig. 4.7.

Here, the first subscript corresponds to the tooth number k and the second one corresponds to the section at which the induced flux is calculated, N_s represents the number of teeth, b_s is the slot width, b_{so} is the slot opening, and t_{cp} is the slice width described in (3.1).

The total flux induced is obtained by integrating the flux density on the area at each slice. Summation of all slices is done at the end to obtain the total induced flux.

The tooth tip circumferential length for an average radius R^i_{av} equals:

$$L^i_{\mathrm{tip}} = \frac{2\pi R^i_{\mathrm{av}}}{N_{\mathrm{s}}} - b_{\mathrm{so}}. \tag{4.11}$$

Each flux Φ_{s11}, Φ_{s12}, and Φ_{s13} is computed by integrating the flux density over the area under the tooth tip.

$$\Phi_{\mathrm{a1}} = \int\int B_{\mathrm{ytot}_i}\mathrm{dS} = \sum_{i=1}^{n_{\mathrm{s}}} \int_{(k-1)\frac{2\pi R^i_{\mathrm{av}}}{N_{\mathrm{s}}} - \frac{b_{\mathrm{so}}}{2}}^{(k-1)\frac{2\pi R^i_{\mathrm{av}}}{N_{\mathrm{s}}} + \frac{b_{\mathrm{so}}}{2}} B_{\mathrm{ytot}_i} t_{\mathrm{cp}} \mathrm{d}x, \tag{4.12}$$

$$\Phi_{\mathrm{sk1}} = \int\int B_{ytot_i}\mathrm{dS} = \sum_{i=1}^{n_{\mathrm{s}}} \int_{(k-1)\frac{2\pi R^i_{\mathrm{av}}}{N_{\mathrm{s}}} + \frac{b_{\mathrm{so}}}{2}}^{(k-1)\frac{2\pi R^i_{\mathrm{av}}}{N_{\mathrm{s}}} + \frac{b_{\mathrm{so}}}{2} + \frac{1-D}{2} L^i_{\mathrm{tip}}} B_{\mathrm{ytot}_i} t_{\mathrm{cp}} \mathrm{d}x, \tag{4.13}$$

$$\Phi_{\mathrm{sk2}} = \int\int B_{\mathrm{ytot}_i}\mathrm{dS} = \sum_{i=1}^{n_s} \int_{(k-1)\frac{2\pi R^i_{\mathrm{av}}}{N_{\mathrm{s}}} + \frac{b_{\mathrm{so}}}{2} + \frac{1-D}{2} L^i_{\mathrm{tip}}}^{(k)\frac{2\pi R^i_{\mathrm{av}}}{N_{\mathrm{s}}} - \frac{b_{\mathrm{so}}}{2} - \frac{1-D}{2} L^i_{\mathrm{tip}}} B_{\mathrm{ytot}_i} t_{\mathrm{cp}} \mathrm{d}x, \tag{4.14}$$

$$\Phi_{\mathrm{sk3}} = \int\int B_{\mathrm{ytot}_i}\mathrm{dS} = \sum_{i=1}^{n_s} \int_{(k)\frac{2\pi R^i_{\mathrm{av}}}{N_{\mathrm{s}}} - \frac{b_{\mathrm{so}}}{2} - \frac{1-D}{2} L^i_{\mathrm{tip}}}^{k\frac{2\pi R^i_{\mathrm{av}}}{N_{\mathrm{s}}} - \frac{b_{\mathrm{so}}}{2}} B_{\mathrm{ytot}_i} t_{\mathrm{cp}} \mathrm{d}x, \tag{4.15}$$

where $B_{\mathrm{ytot_i}}$ is the total axial flux density component which is deduced by the real part of (3.47), R^i_{av} is the average radius at slice i.

After obtaining the overall air gap induced flux in the stator tooth tip, the reluctance network in the tooth can be solved in order to calculate the magnetic induction in all grid points to calculate the iron losses.

4.3.3 Flux Loop Equations

After obtaining all the reluctance values and calculating all the magneto-motive force (MMF) sources for the armature windings, it is possible to solve the main system equation[2] to estimate the induced flux in each individual loop ϕ_{loop}:

[2] It is similar to solving an electric circuit using a mesh analysis [76].

$$MMF = R(\mu_r(B))\phi_{loop}, \tag{4.16}$$

where MMF represents the matrix of magneto-motive sources, *i.e.* in all loops. R is the reluctance matrix representing the reluctances values, which are non-linear permeability dependent, as expressed in (4.2). To solve this non-linear problem, Newton-Raphson (N-R) technique is used with an error norm of 1e-5.

4.3.4 Voltage Computation

The flux induced in each coil is calculated by summation of the appropriate induced fluxes from the MEC in each tooth in regions 1, 2, and 3 shown in Fig. 4.8. The induced voltage per phase is then calculated using the voltage equation described in (3.76).

4.3.5 Torque Computation

The torque is calculated from the output power, obtained from the coupled SC-MEC model, divided by the rotational speed ω_m. The instantaneous output power can be obtained by summation over all phases $j = 1, .., m$ the instantaneous no load voltage V_j multiplied by the instantaneous input currents I_j for each phase j.

$$T = \frac{1}{\omega_m} \sum_{j=1}^{m} V_j(t) I_j(t). \tag{4.17}$$

The calculated torque is compared to the FE results as well as to the ones obtained using the subdomain model as described in (3.75).

4.3.6 Stator Core Loss Computation

The total stator losses for different grid points, introduced in Fig. 4.8 are calculated through the axial and tangential flux density from each grid point in the MEC.

4.4 Comparison of Test Results

In order to validate the combined SC-MEC model, an AFPMSM with 16 poles and 15 tooth coil windings is studied. The geometrical and electromagnetic properties of the machine are described in Table 4.1.

Table 4.1: Geometrical parameters of the studied machine. [32]

Parameter	Symbol	Value
Rated Power	P_{n}	5 kW
Number of pole pairs	$p = N_{\mathrm{m}}/2$	8
Number of stator slots	N_{s}	15
Rated speed	n_{r}	2500 rpm
Rated Torque	T_{em}	19.1 Nm
Outer diameter	D_{o}	148 mm
Inner diameter	D_{i}	100 mm
Axial length core element	$2(Y_{\mathrm{c1}} + Y_{\mathrm{c2}} + Y_{\mathrm{c3}})$	60 mm
Axial length slot	$2Y_{\mathrm{c1}}$	48 mm
Slot width	b_{s}	12 mm
Slot opening width	b_{so}	3 mm

The star of the slot[3] is generated for any combination. The star of the slot for the studied combination is shown in Fig. 4.10.

The validation scenario of the SC-MEC model is conducted as follows:

- The air gap axial (y) and circumferential (x) flux densities in the SC and SD model are compared with the 2D and 3D FE models. The comparison is conducted for different loading conditions.
- The terminal voltage and torque of the SC-MEC model are compared with the 2D and 3D FE models at different loading conditions.
- The local induction in each region described in Fig. 4.8 and the losses in the teeth are compared with the results from 2D and 3D FE models.
- At a final stage, the model is excited by extreme loading and geometrical conditions and compared with other models.

4.4.1 Magnetic Flux Density

No Load Conditions

The normal component of the no-load magnetic field on the surface of the PMs is shown in Fig. 4.11. Additionally, the flux densities in the center of the air gap for the axial and circumferential components, are depicted in Figs. 4.12 and 4.13 respectively. The curves in the figures show a very good agreement between the 3D, 2D FE models as well the analytical models of the SC and SD models.

[3] Refers to the winding connection [77]

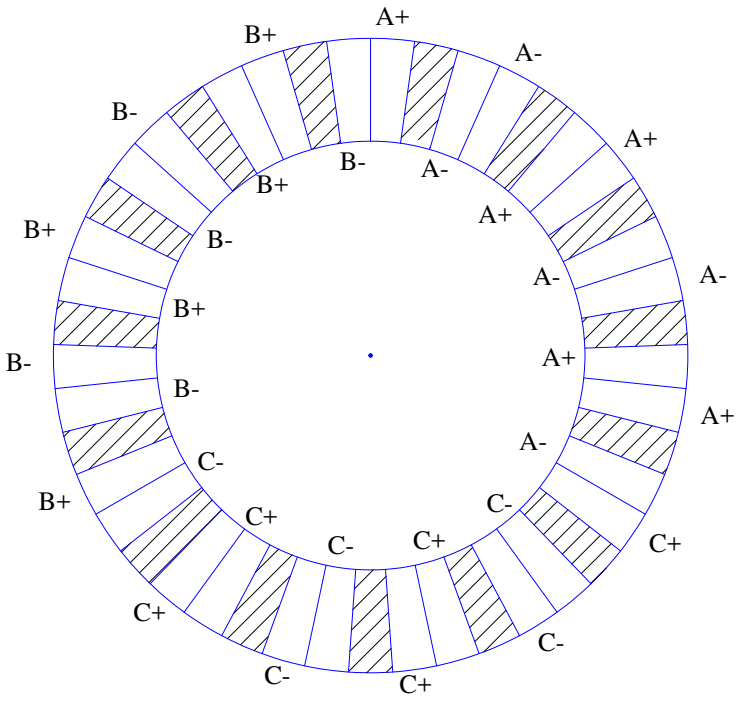

Figure 4.10: Phases distribution across the circumference for the 15 slot 16 pole combination.

The circumferential component shows a very good agreement with the SD model described in section 3.4.3. The SC model can not obtain the circumferential flux density as proven in chapter 3. The accuracy of these comparisons are summarized in Table 4.2.

Loading Conditions

The curves of analytical and FE models in Figs. 4.14 and 4.15 show good correspondence for the normal and circumferential components of the air gap flux densities when loading the machine with the rated current I_{rated}. The circumferential component shows very good agreement with the results of the SC model. The accuracy of these comparisons is summarized in Table 4.2.

Table 4.2 summarizes the second vector norm of the error between the circumferential x and axial y flux densities of the different analytical models and 2D FE model with respect to the 3D FE model shown in Fig. 3.4. (a) considering the non-linear behaviour of the material.

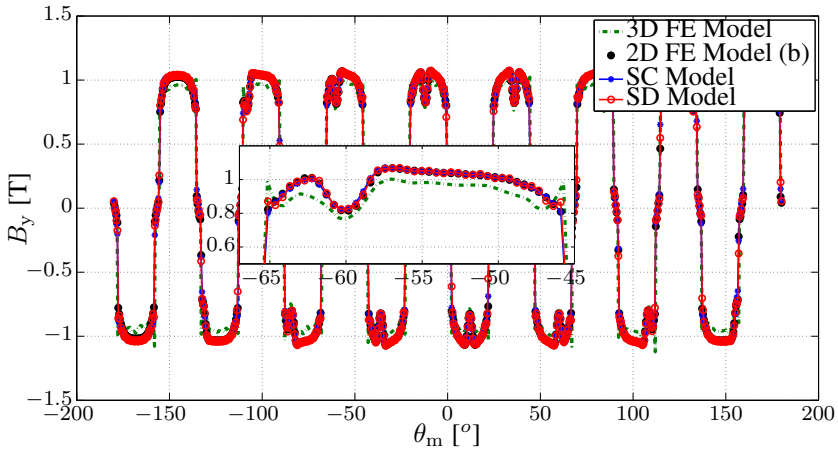

Figure 4.11: Axial component B_y at the surface of the PM at no-load.

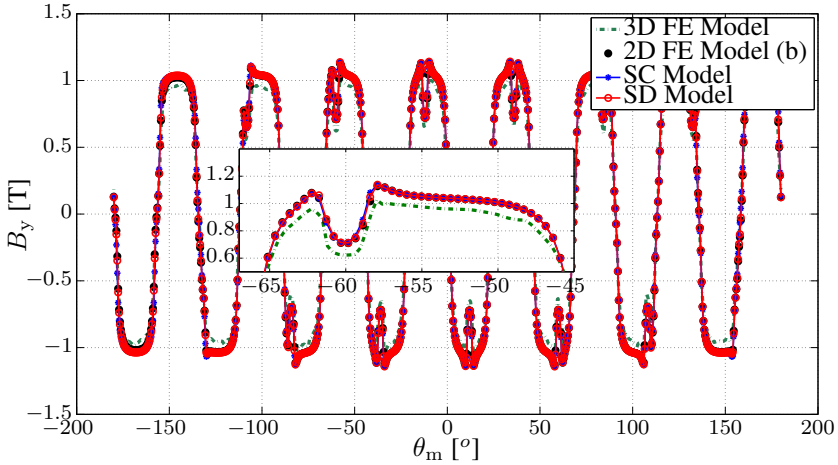

Figure 4.12: Axial component B_y at the center of the air gap at no-load.

The error difference between the SD model and the 3D FE model is very low[4]. In addition, the circumferential component corresponds accurately with the 2D and 3D FE models[5].

In addition, the SC model axial component is accurate enough to be used instead of the SD model to obtain all the required electromagnetic parameters with

[4]The maximum second norm percentage error difference in the axial flux density between the SD and the 3D FE model at double rated conditions is 11.2%.

[5]The maximum second norm percentage error difference in the circumferential flux density between the SD and the 3D FE model is 18.5%.

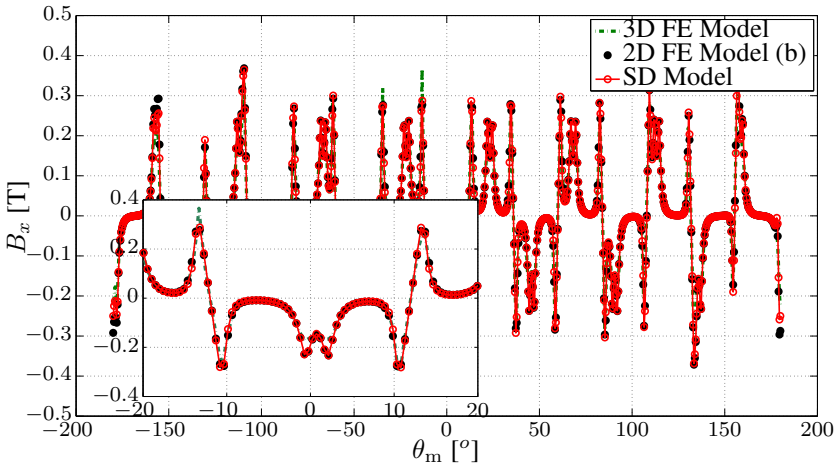

Figure 4.13: Circumferential component B_{x} at the center of the air gap at no-load.

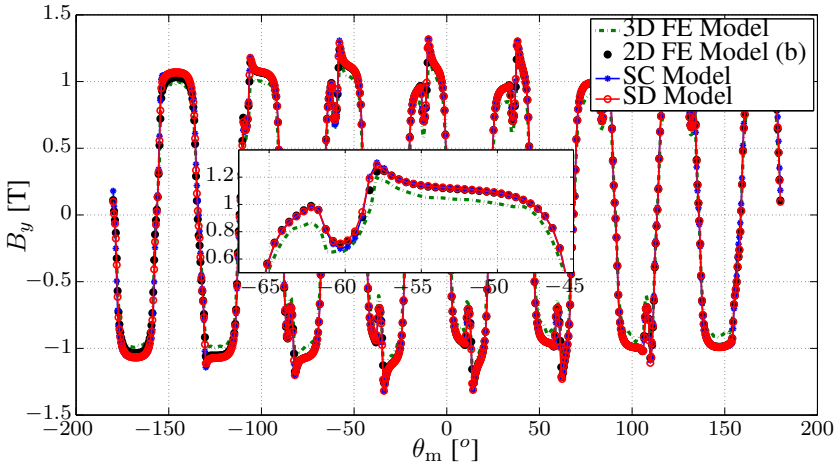

Figure 4.14: Axial component B_{y} at the center of the air gap at no-load.

faster results[6].

4.4.2 Voltage and Torque

The voltage and torque are calculated at no load and different loading conditions. Fig. 4.16 shows the voltage for phase a at no load, rated load, and double the rated

[6]The maximum second norm percentage error difference in the axial flux density between the SC and the 3D FE model is 11.9%.

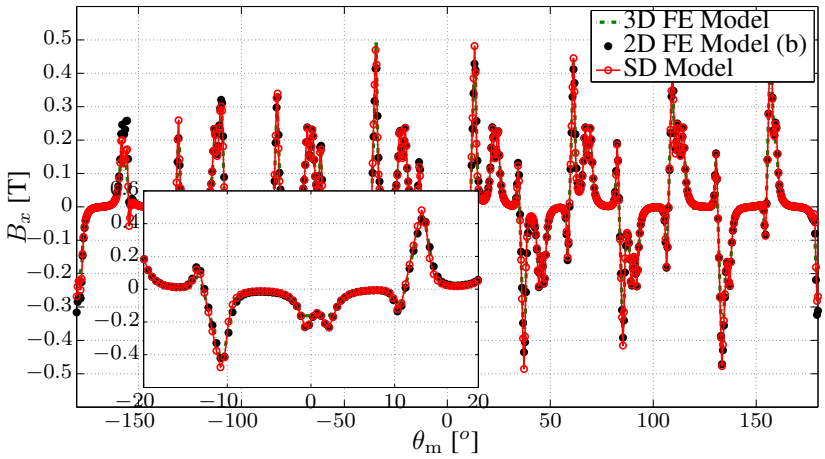

Figure 4.15: Circumferential component B_x at the center of the air gap at no-load.

Table 4.2: Comparison of the flux densities between the analytical and the FE models.

I	Model Type	$\frac{\|\mathbf{B}_{y_{\text{Model}}}-\mathbf{B}_{y_{\text{3DFE}}}\|_2}{\|\mathbf{B}_{y_{\text{3DFE}}}\|_2} * 100$ [%]	$\frac{\|\mathbf{B}_{x_{\text{Model}}}-\mathbf{B}_{x_{\text{3DFE}}}\|_2}{\|\mathbf{B}_{x_{\text{3DFE}}}\|_2} * 100$ [%]
0	2D FE Model	10.2	20.5
	SD Model	10.6	18.5
	SC Model	11.1	-
I_{rated}	2D FE Model	9.8	21.3
	SD Model	10.5	18.2
	SC Model	11.1	-
$2I_{\text{rated}}$	2D FE Model	9.7	21.4
	SD Model	11.2	16.3
	SC Model	11.9	-

load. The voltage curves show a good correspondence between the results of the FEs and the SC-MEC model. The 3D FE model has a higher voltage amplitude because of the 3D leakage flux, which is not considered in the SC-MEC model.

Table 4.3 depicts the root mean square (rms) values for the voltage for different loading conditions. The errors between both 3D FE, 2D FE model and SC-MEC model are observed.

This figure clearly shows that SC-MEC model can predict the voltage of the 3D FE model with a maximum percentage of error of 3% for the rated loading condition. However, for double the rated loading condition, where the material is heavily saturated, more leakage flux occurs leading to more deviation of maximum 11%. For normal machines, operating at rated loading conditions, the 2D FE and the SC-MEC models are sufficient to give good and accurate results.

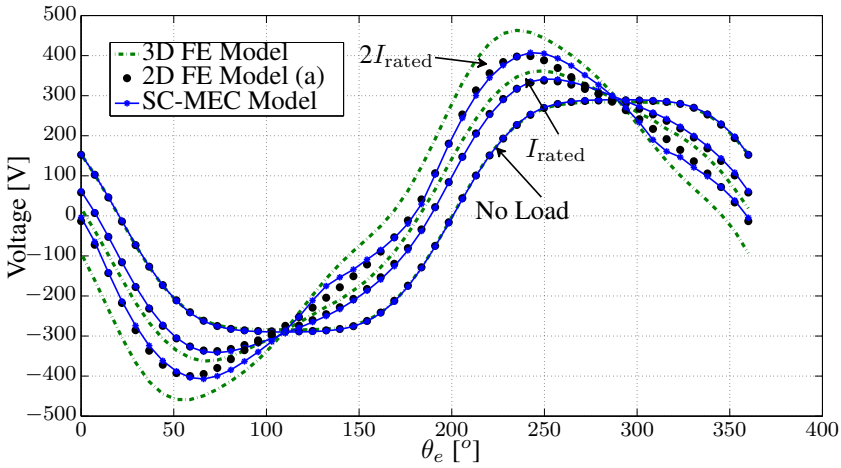

Figure 4.16: Voltage output for different loading conditions.

Table 4.3: rms Values for the voltage for different loading conditions.

I	Parameter	3D FE Model	2D FE Model	SC-MEC Model
0	V_{rms} [V]	230	232	233
	$\text{Error}_{V_{\text{rms}}}$ [%]	-	0.9	1.3
I_{rated}	V_{rms} [V]	251	242	245
	$\text{Error}_{V_{\text{rms}}}$ [%]	-	3.6	2
$2I_{\text{rated}}$	V_{rms} [V]	302	265	268
	$\text{Error}_{V_{\text{rms}}}$ [%]	-	12.2	11.4

Figs. 4.17 and 4.18 compare different calculation methods for torque at rated loading and double the rated loading conditions, respectively. This is done using 2D and 3D FE models and different analytical models described in section 4.3.5.

The analytical models are based on the SD model and the summation of the instantaneous voltages and currents divided by the rotational speed. Both figures show that all techniques can track the same shape of the torque of the 3D FE model. However, for the calculation of the mean value of the torque, a noticeable difference is observed.

Table 4.4 summarizes the deviation of the mean torque between different models. The maximum percentage of mean torque error, as well as the torque ripple error, are 2.9% and 28% respectively observed compared to the 3D FE model.

The analytical model described in (4.17) gives more accurate result than the SD model for the mean torque values. However, for the torque ripple the result is in favour for the SD model.

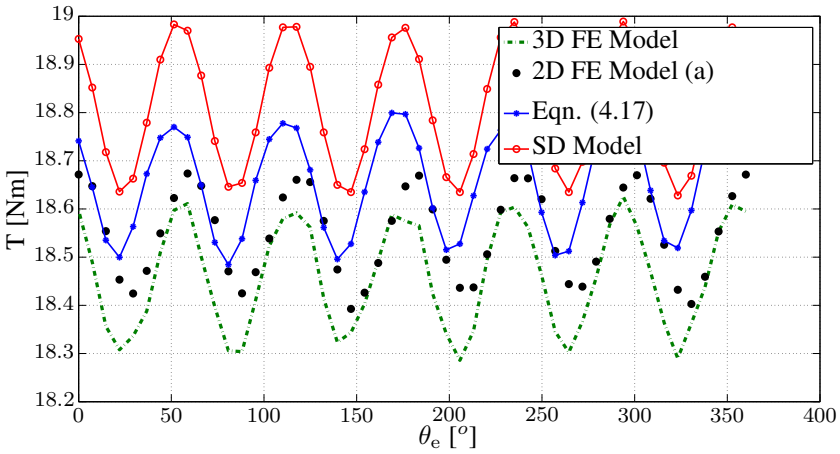

Figure 4.17: Torque output for rated loading conditions for different calculation techniques.

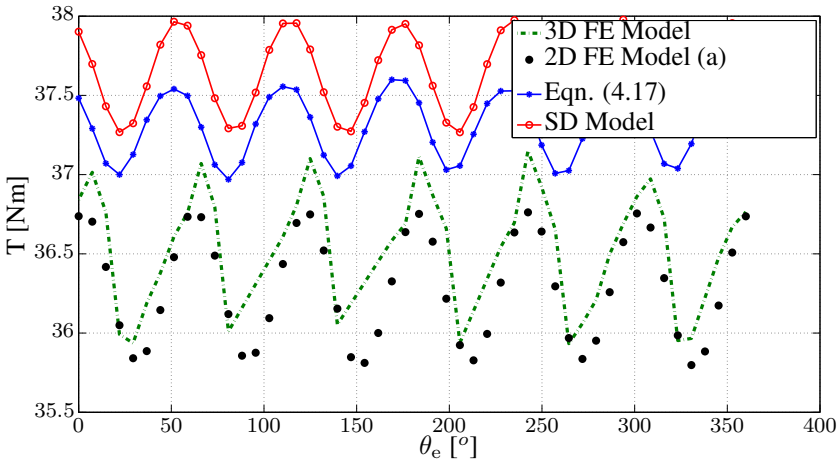

Figure 4.18: Torque output for double the rated loading conditions for different calculation techniques.

Table 4.4: Mean torque and torque ripple comparison between different models.

I	Parameter	3D FE Model	2D FE Model	Eqn. (4.17)	SD Model
I_{rated}	T_{m} [Nm]	18.46	18.55	18.66	18.82
	$\text{Error}_{T_{\text{m}}}$ [%]	-	0.4	1	2
	$T_{\text{p-p}}$ [Nm]	0.34	0.28	0.36	0.36
	$\text{Error}_{T_{\text{p-p}}}$ [%]	-	17	5.8	5.8
$2I_{\text{rated}}$	T_{m} [Nm]	36.56	36.29	37.32	37.63
	$\text{Error}_{T_{\text{m}}}$ [%]	-	0.7	2	2.9
	$T_{\text{p-p}}$ [Nm]	1	0.97	0.72	0.72
	$Error_{T_{p-p}}$ [%]	-	3	28	28

4.4.3 Flux Density and Losses in Stator Core

The flux densities for the SC-MEC model for different regions, shown in Fig. 4.8, are compared with the 2D FE model. The results of the comparison are shown in Figs. 4.19, and 4.20 for the rated load for different regions. In addition, they are also compared in Figs. 4.21 and 4.22 for double the rated current. As a conclusion from these figures, the flux densities correspond very well in regions 1 to 4 with the results of the 2D FE model. Region 5 needs more discretization to be well comparable to the 2D FE model. However, as the volume of region 5 is small, it does not affect the accuracy of the total losses computation. The flux densities, recorded in many points, are averaged in each region to obtain the avarage flux density in each region.

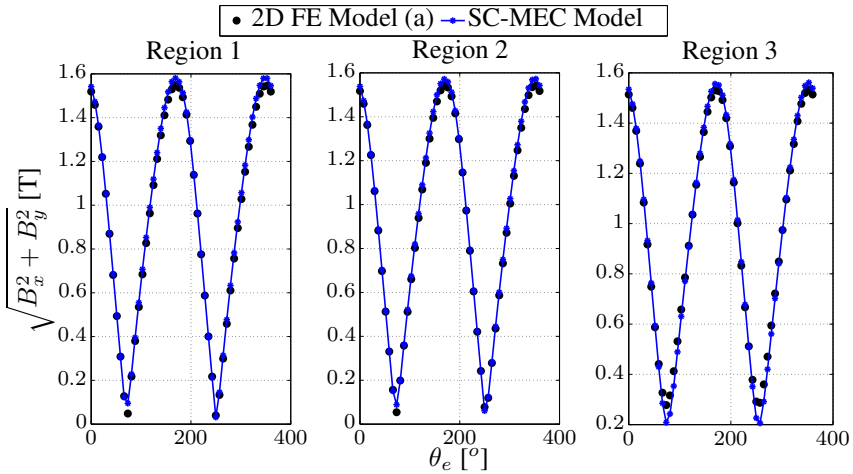

Figure 4.19: Norm of the flux density in different regions for rated current.

Figs. 4.23 and 4.24 show the losses in different regions for rated and double the rated loading conditions. It is clear from these figures that the losses correspond very well with the results of the 2D FE model, which validate the proposed SC-MEC model. In regions 1, 2, 3 and 4, the maximum error is less than 5%. For region 5, the maximum error is about 20%. However, as stated earlier, region 5 volume is small compared to the total volume. Therefore, the effect of this volume on the total iron losses is not significant.

Table 4.5 summarizes the total losses in case of the 3D FE, 2D FE, and the SC-MEC models. The total error is noted for different models compared to the 3D FE model. The maximum error of the SC-MEC model at no load and rated loading is only 1.25% from the 3D FE model. At double the rated load conditions, the error deviates around 10%.

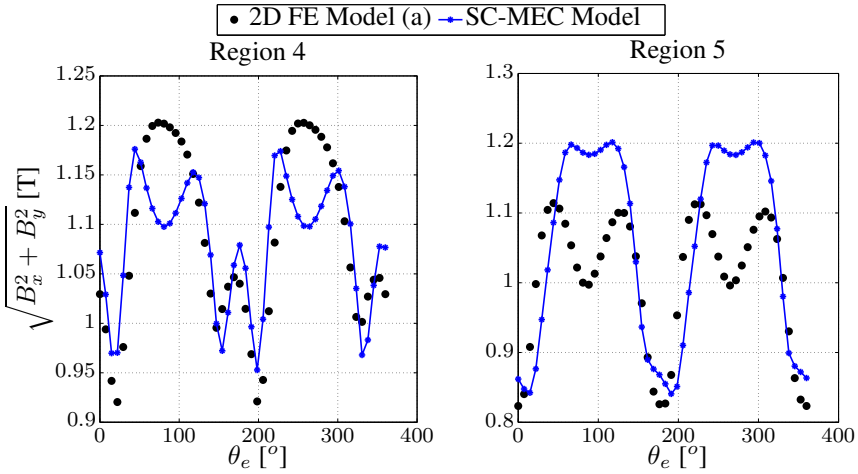

Figure 4.20: Norm of the flux density in different regions for rated current.

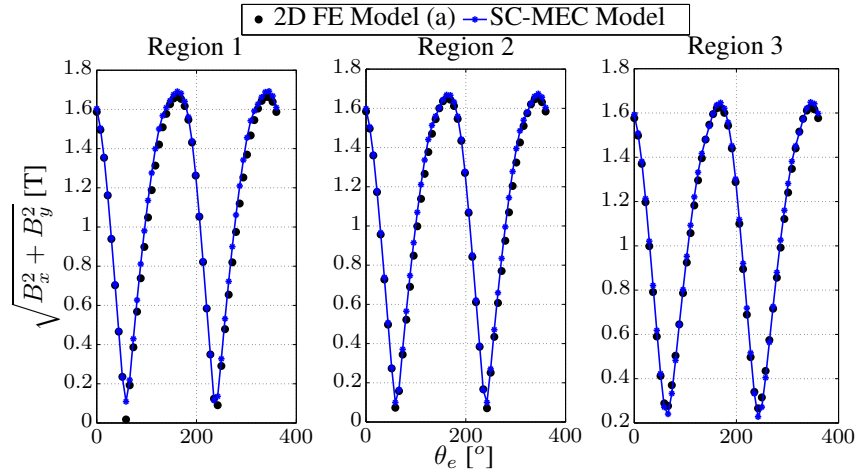

Figure 4.21: Norm of the flux density in different regions for double the rated current.

Table 4.5: Total stator core losses.

I	Parameter	3D FE Model	2D FE Model	SC-MEC Model
0	Losses [W]	168	168.74	170.4
	$\text{Error}_{\text{Losses}}$ [%]	-	0.4	1.4
I_{rated}	Losses [W]	180.3	182.4	182.2
	$\text{Error}_{\text{Losses}}$ [%]	-	1.2	1
$2I_{\text{rated}}$	Losses [W]	231	208.45	208.24
	$\text{Error}_{\text{Losses}}$ [%]	-	9.7	9.7

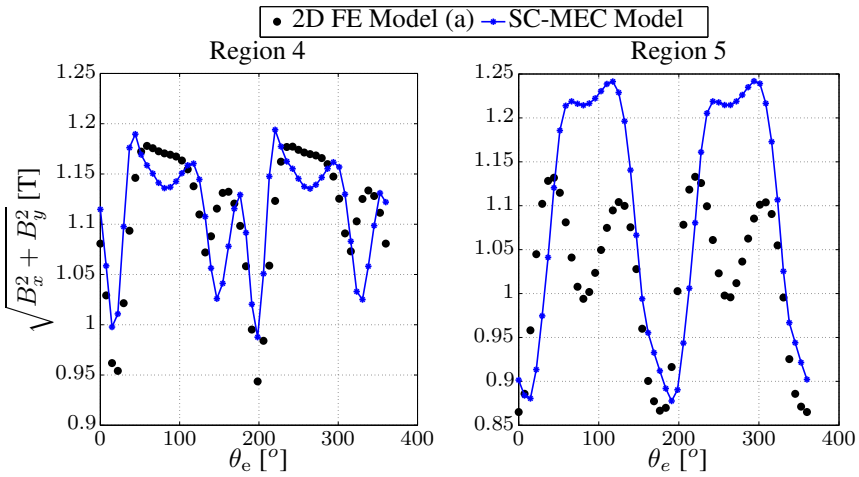

Figure 4.22: Norm of the flux density in different regions for double the rated current.

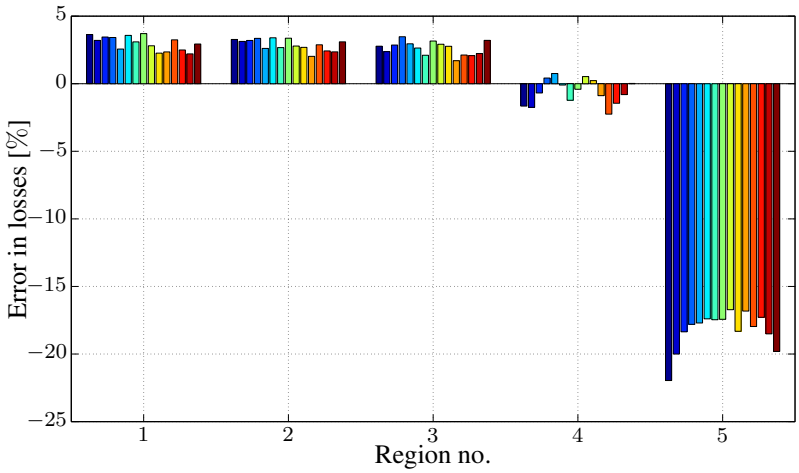

Figure 4.23: Error in losses in different regions for the rated current.

4.4.4 CPU Time Comparison

The CPU time is compared between the FE models with a non-linear permeability and the SC-MEC model. This is done on a core i5 processor, and 8 GB installed memory with 64 bit operating system Windows 8.

Table 4.6 summarizes the CPU time between the FE models and the SC-MEC model. The SC-MEC model is very fast compared to the FE models. It is also

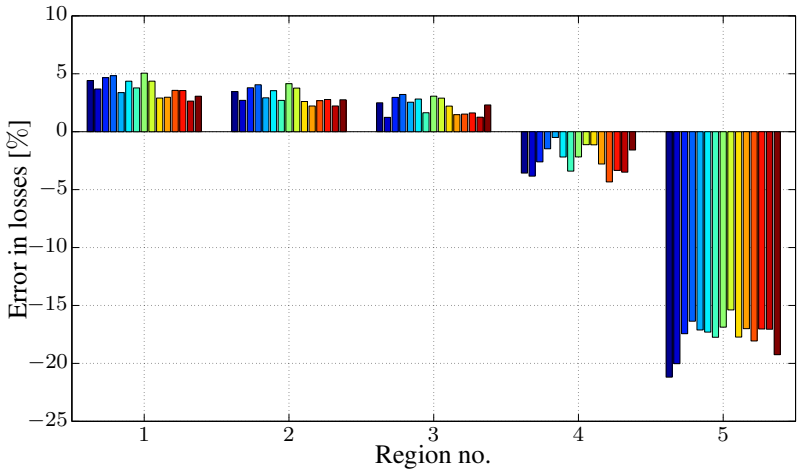

Figure 4.24: Error in losses in different regions for double the rated current.

noted that as the current increases, the simulation time increases. This is due to the fact that the non-linear solver takes more iterations to reach the same accuracy due to the nature of the non-linear problem.

The SC-MEC is about 200 times faster than the 2D FE model and about 500 times faster than the 3D FE model. In addition, the SC-MEC model gives a maximum percentage of error of 2% in the rms value of the voltage at rated loading conditions. Moreover, the SC-MEC model can also estimate the average torque with an error of 2%. For the iron core losses, only 1% error compared to the 3D FE model is observed.

To conclude, the model can predict all the electromagnetic parameters of the machine in a very fast way, with an error of only 2% at the rated loading conditions.

Table 4.6: Comparison of the CPU time between the FE 'approximate time' and analytical models 'exact time'.

	Model Type	CPU Time
FE Models	3D FE Model	15 hrs
	2D FE Model (b) ($I = 0$)	5.5 hrs
	2D FE Model (b) ($I = I_{\text{rated}}$)	5.7 hrs
	2D FE Model (b) ($I = 2_{\text{rated}}$)	6.5 hrs
Analytical Model	SC-MEC Model ($I = 0$)	117 s
	SC-MEC Model ($I = I_{\text{rated}}$)	143 s
	SC-MEC Model ($I = 2I_{\text{rated}}$)	326 s

4.4.5 Extreme Loading Study

The machine is loaded with four times the rated currents keeping all other parameters constant. Comparisons are conducted with the developed FE models in this condition.

The axial flux densities for the 3D FE model, 2D FE model, the SC model, and the SD model are shown in Fig. 4.25. The peak flux density of the 3D FE model, 2D FE model, SC model, and SD model are 1.29T, 1.34T, 1.87T, and 1.84T. The SC and the SD models differ from the 3D FE model at its peak by about 0.5T. This difference influences the losses, voltage, and torque.

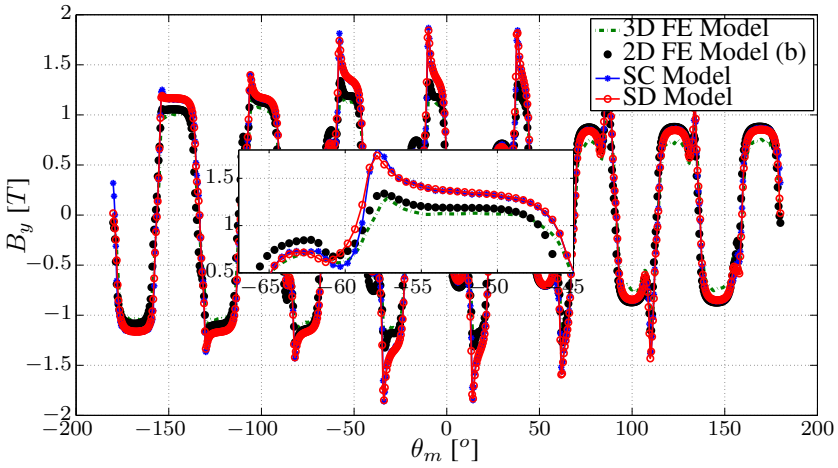

Figure 4.25: Axial component B_y at the center of the air gap at four times the rated load.

Figure 4.31 depicts the terminal voltage waveforms for the 3D FE model, 2D FE model, and the SC-MEC model. Compared to the 2D FE model, the SC-MEC model is still capable of obtaining the same amplitudes. However, due to the extreme loading conditions, the peak flux density inside the tooth reaches 1.8T in the center of the tooth as shown in Fig. 4.27 for four the rated current. The material chosen saturates at 1.6T as shown from the material B-H curve in Fig. 4.3. This means that the stator iron core is heavily saturated. This causes the difference between the different models compared to the 3D FE model.

Table 4.7 summarizes the difference between both the SC-MEC model, the 3D FE model and the 2D FE model for the rms value of the terminal voltage and the stator iron losses for the same condition. It can be observed that the difference between the SC-MEC and the 3D FE model is increased due to the leakage 3D fluxes. However, comparing the SC-MEC model with the 2D FE model, the results are still satisfactory. The error between the SC-MEC model and the 2D FE model is less than 1% for the voltage and 3.5% for the stator iron losses.

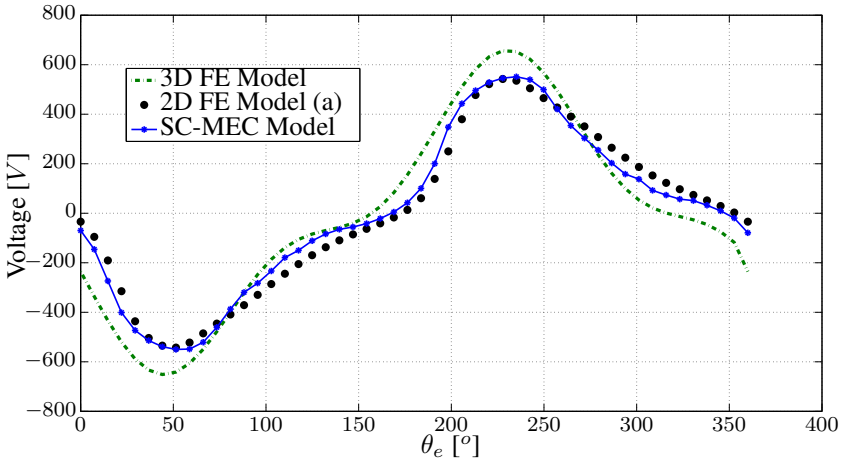

Figure 4.26: Output terminal voltage for four times the rated current.

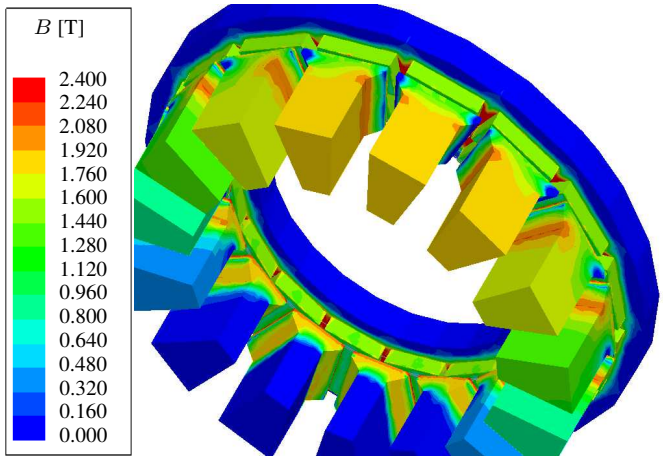

Figure 4.27: 3D absolute flux density distribution of the stator for four times the rated current.

Figure 4.28 depicts the torque variations for different calculation techniques for the 3D FE model 2D FE model and the analytical models discussed in section 4.3.5. All models can track the same shape of the 3D FE model torque waveform. However, the accuracy of the mean torque and torque ripple differ with respect to the 3D FE model.

The mean value of the torque and the torque ripple are summarized in Table

Table 4.7: rms value of the voltage and the stator iron losses differences for four times the rated current.

Parameter	3D FE Model	2D FE Model	SC-MEC Model
V_{rms} [V]	378	319	322
$\text{Error}_{V_{\text{rms}}}$ [%]	-	15.6	14.81
Losses [W]	340	284.7	274.8
Error_{Losses} [%]	-	16.18	19.12

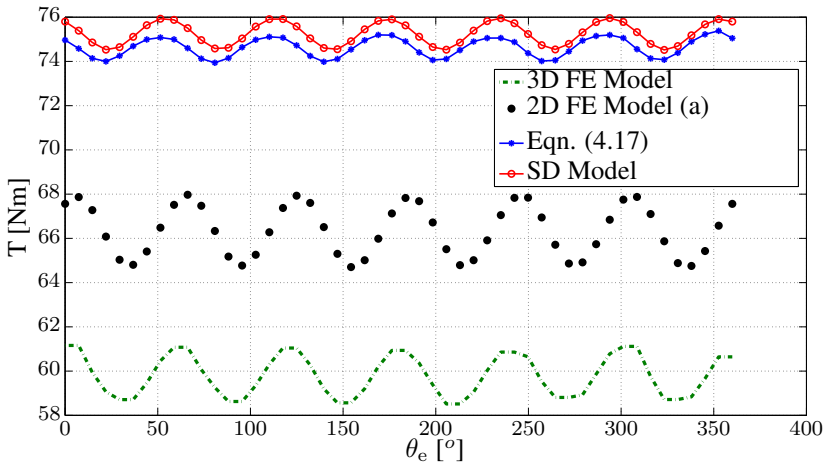

Figure 4.28: Torque waveforms for four times the rated current.

4.8. The errors of the mean torque and the torque ripple are calculated with respect to the 3D FE model.

The 2D FE model gives the best results with a percentage error of 11% for the mean torque and 25% in the torque ripple with respect to the 3D FE model. Both analytical models, based on the SD model and no load voltage, give a 25% error in the mean torque and 45% with respect to the 3D FE model. In this heavy loading conditions, neither the mean torque or torque ripple can be accurately computed.

To conclude, under four times the rated loading conditions, the stator iron material becomes heavily saturated. This causes additional leakage flux that is not presented in the 2D FE model and the SC-MEC model. Therefore, the error between the SC-Model and the 3D FE model increases to 15% in the rms value of the voltage and 19% in the iron losses. In addition, the error in the mean value of the torque is 25% and 45% of the torque ripple.

Table 4.8: Mean value of the torque and torque ripple differences for four times the rated current.

Parameter	3D FE Model	2D FE Model	Eqn. (4.17)	SD Model
T_{m} [Nm]	59.82	66.36	74.64	75.27
$\mathrm{Error}_{T_{\mathrm{m}}}$ [%]	-	10.9	25	25.82
T_{p-p} [Nm]	2.64	3.3	1.44	1.44
$\mathrm{Error}_{T_{\mathrm{p-p}}}$ [%]	-	25	45	45

4.4.6 Influence of Geometrical Parameters Study

To study the applicability of the model with different geometrical conditions, the slot opening is chosen to be close enough to the slot width (12mm). The slot opening is changed to be 10mm. The model is excited by the rated loading conditions. This condition is almost similar to an open slot machine.

The difference for the axial component of the flux density in the air gap area between the 3D FE model, 2D FE model and the analytical models are observed in Fig. 4.29. All models correspond very well with the 3D FE model. The 3D flux density distribution for the 3D FE model is shown in Fig. 4.30. The flux density distribution shows that the peak flux density at the center of the tooth equals about 1.35T. This means that the material is not saturated to affect the air gap flux density. Therefore, it is expected that the air gap flux density of all models will be similar.

Figure 4.31 depicts the terminal voltage waveforms for the 3D FE model, 2D FE model, and the SC-MEC model. The SC-MEC model is capable to obtain the same amplitudes as the 3D FE model and the 2D FE model. The error difference between the rms value of the SC-MEC model and the 3D FE model is only 6%. The stator core iron losses error is only 7% different compared to the 3D FE model.

Comparing the results of the torque waveforms for all models are shown in Fig. 4.32. It is clear that all models can track the same mean voltage with a maximum percentage of error of 3% compared to the 3D FE model as described in Table 4.10.

Table 4.9: rms value of the voltage and the stator iron losses differences for the machine with a slot opening of 10mm and the rated loading conditions.

Parameter	3D FE Model	2D FE Model	SC-MEC Model
V_{rms} [V]	224	220	211
$\mathrm{Error}_{V_{\mathrm{rms}}}$ [%]	-	1.7	5.8
Losses [W]	150	145.9	139
Error_{Losses} [%]	-	2.7	7.3

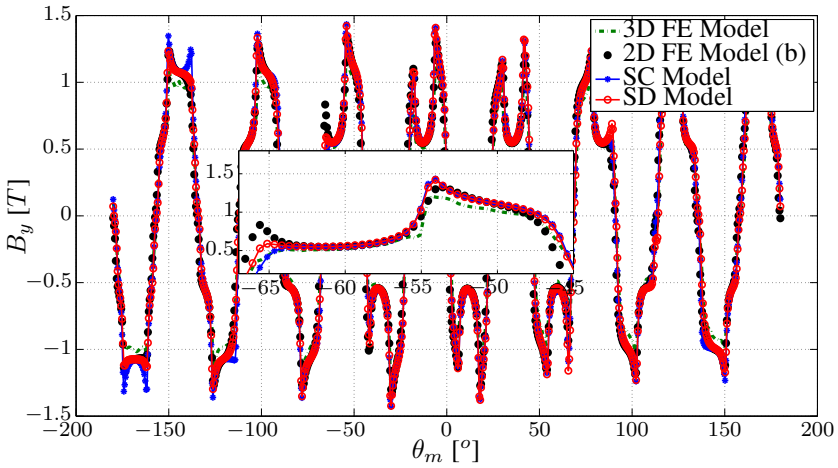

Figure 4.29: Axial component B_y at the center of the air gap at rated load for slot opening of 10 mm.

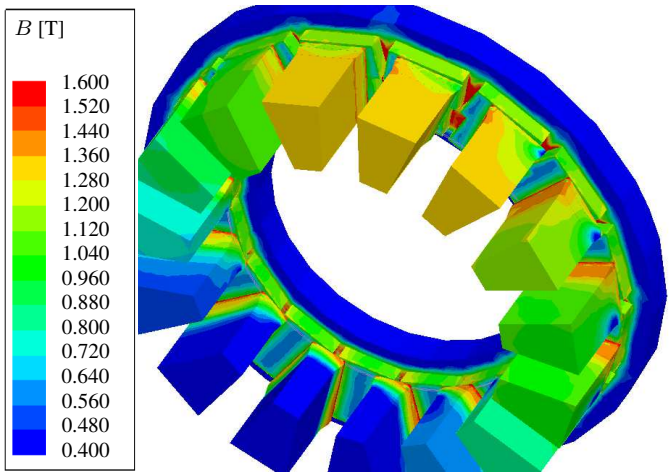

Figure 4.30: 3D absolute flux density distribution of the stator for 10mm slot opening and the rated loading conditions.

4.4.7 Influence of the MEC Grid Refinement

The refinement of the reluctance grid in Fig. 4.7 is an compromise between on the one hand solution accuracy and on the other hand the complexity.

In this section, the relation between the network refinement and the accuracy of the flux density, terminal voltage and losses is illustrated. We compare three models with different refinement levels:

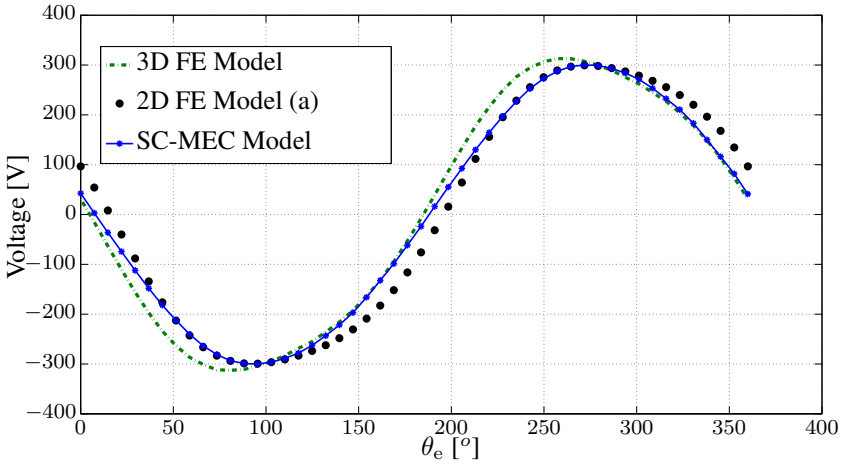

Figure 4.31: Terminal voltage variations for 10 mm slot opening case.

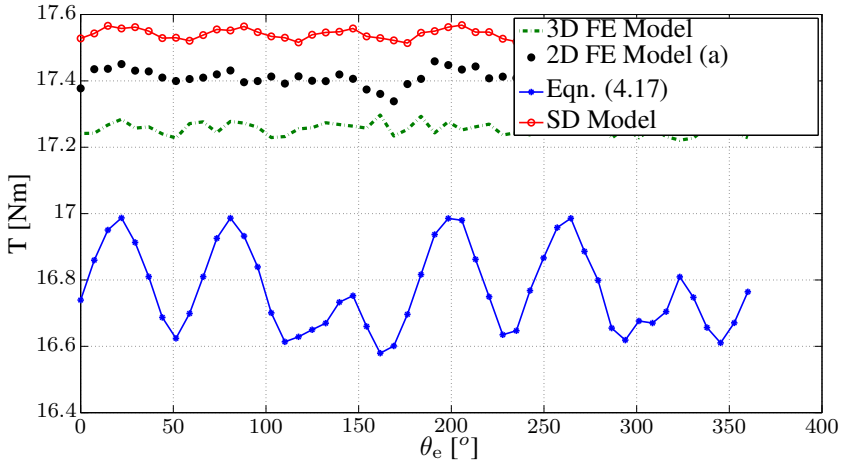

Figure 4.32: Torque output for rated loading conditions at slot opening of 10 mm for different calculation techniques.

- The coarse model (Model 1), shown in Fig. 4.33.
- The intermediate model (Model 2), shown in Fig. 4.34.
- The fine model (Model 3), shown in Fig. 4.7.

In the coarse model of Fig. 4.33, in all the five regions, the coarse discretization of Fig. 4.9 (a) is used. The air gap area between the slots is refined in a similar way as the fine model. This results in a good calculation of the voltage as described in Fig. 4.35. This shows a good correspondence with the 2D FE model. On the other

Table 4.10: Mean value of the torque and torque ripple differences for the machine with a slot opening of 10mm and the rated loading conditions.

Parameter	3D FE Model	2D FE Model	Eqn. (4.17)	SD Model
T_{m} [Nm]	17.26	17.41	16.77	17.54
$\mathrm{Error}_{T_{\mathrm{m}}}$ [%]	-	0.9	2.8	1.6
$T_{\mathrm{p-p}}$ [Nm]	0.076	0.12	0.4	0.054
$\mathrm{Error}_{T_{\mathrm{p-p}}}$ [%]	-	58	426	29

hand, due to the bad representation of the regions 3, 4, and 5, the total losses of the complete machine will deviate more from the result of the final model (Model 3) as shown in Table 4.11. This is because when the PM is not in the center of the tooth there are some flux lines that flow circumferentially in the tooth itself and not in the air gap area. Then, this theory is not well represented in this version.

The second model, shown in Fig. 4.34, uses the finer discretization of Fig. 4.9 (b) to represent regions 4 and 5. Regions 1, 2, and 3 were represented by the coarse discretization of Fig. 4.9 (a) and the air gap was assumed to have only fluxes that flow in the horizontal direction and no flow in the vertical directions. As a conclusion, it can be found that the losses are a little bit higher due to the fact that region 3 is not well represented in this scheme. However, in total, the loss compared to 2D FE model has less error than model 1. The terminal voltage error is higher in this case, because the air gap is not well divided in the area between different teeth as shown in Table 4.11 and described in Fig. 4.35. Fig. 4.35 shows that this is the only model that does not correspond well with FE models.

Table 4.11 summarizes the effect of different models on the losses and terminal voltage values. Concerning the grid refinement, we can conclude that:

- The coarse model (model 1, Fig. 4.33) is accurate for the voltage, but not for the iron losses.
- The fine model (model 3, Fig. 4.7) is almost as accurate as 2D FE model for both voltage and iron losses.
- The coarse model is about $1/3$ faster than the fine model, and about 200 times faster than 2D FE model.

4.5 Conclusions

This chapter presents a complete analytical model for AFPMSMs. A simple and fast technique is developed to obtain accurate results for the calculation of ma-

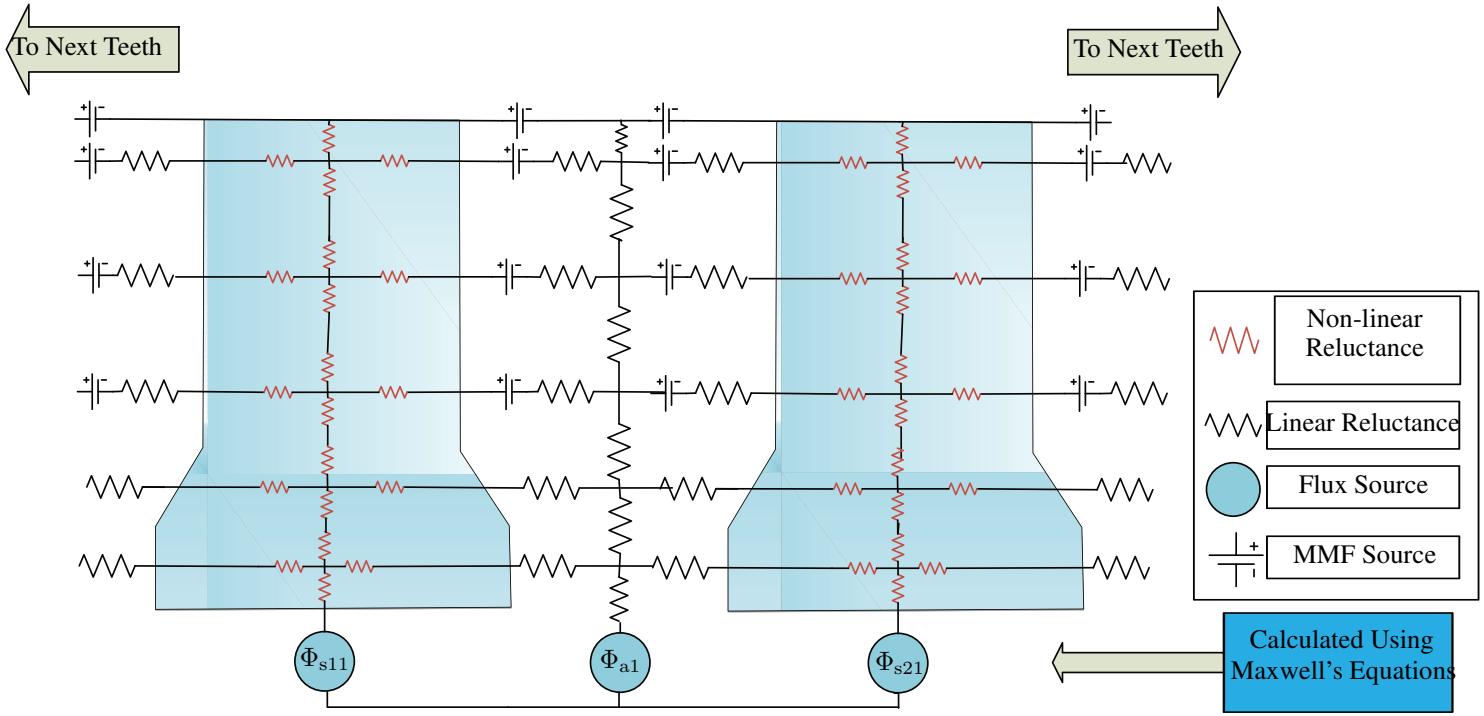

Figure 4.33: SC-MEC coarse model (Model 1).

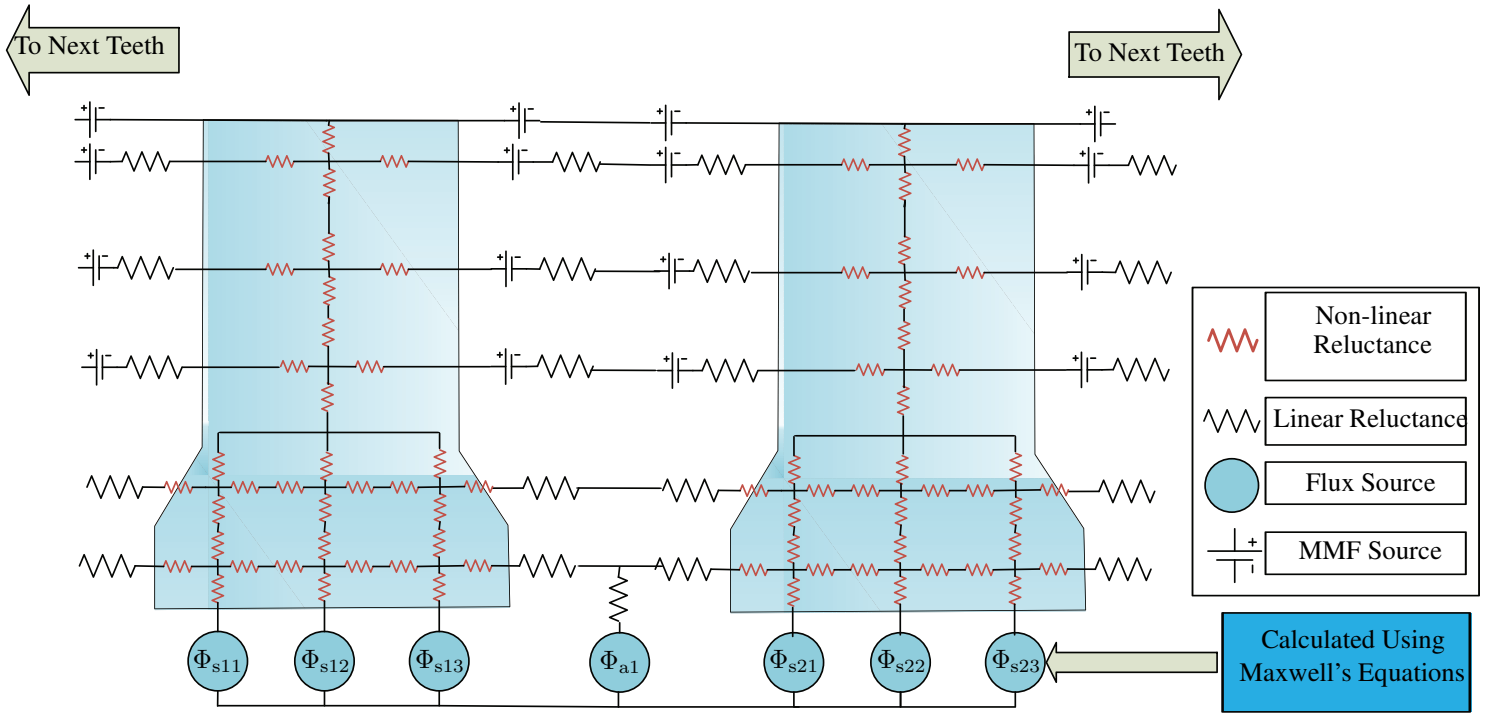

Figure 4.34: SC-MEC intermediate model (Model 2).

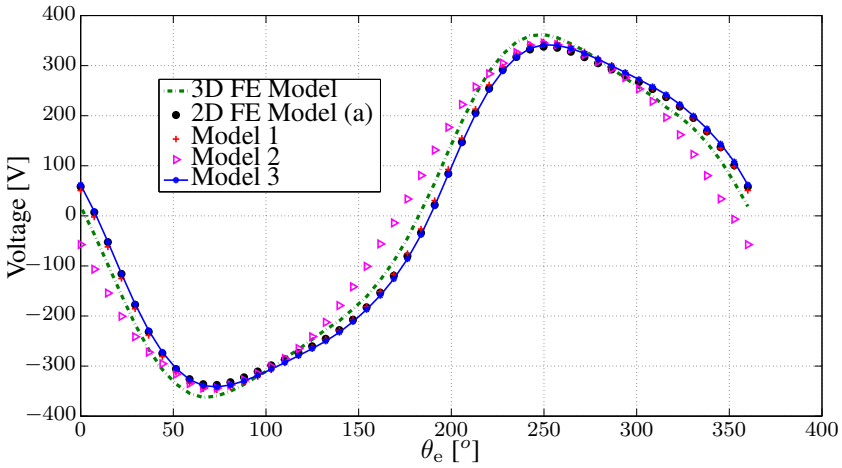

Figure 4.35: EMF comparison between the three models.

Table 4.11: Comparison of terminal voltage, total core losses, and CPU time for the studied models.

Parameter	3D FE Model	2D FE Model	Model 1	Model 2	Model 3
V_{rms} [V]	251	242	247	243	245
$\text{Error}_{V_{\text{rms}}}$ [%]	-	3.6	1.6	3.19	2.4
Losses [W]	180.3	182.4	168	176	182.2
$\text{Error}_{\text{Losses}}$ [%]	-	1.2	7.9	2.4	1.1
CPU Time	15hrs	5.7hrs	96 secs	136 secs	143secs

chine parameters (terminal voltage, torque, and iron losses). This technique is based upon a combined solution of two models. The first model generates an exact solution of Maxwell's equations in the air gap area applied to a very simple geometry using conformal mapping technique. The second model gives an accurate solution in the detailed parts with complex geometry, based on a magnetic equivalent circuit to obtain fast and accurate results in a simple way. The MEC considers the non-linear behaviour of the magnetic material. This combined model is called SC-MEC model. The machine's global quantities are then obtained and validated by the results of 3D and 2D finite element (FE) models for different loading conditions. In addition, the models are excited by extreme loading and geometrical conditions to estimate the accuracy of the developed SC-MEC model under these conditions.

Compared to 3D FE model, the proposed combined solution has the advantage of flexibility in the geometrical machine parameters change, a significantly less CPU time (500 times faster compared to the 3D FE model and 200 times faster than the 2D FE model) and an accuracy for the considered AFPMSM up to 2%

in the rms value of the terminal voltage at rated loading conditions, 2% in the mean value of the torque and 1% in the stator core iron losses. Finally, the relation between grid refinement in the MEC (coarse or fine reluctance grid) and accuracy is pointed out, showing that the terminal voltage can be accurately computed with a rather coarse grid, while accurate loss computation requires a fine grid.

Chapter 5

Eddy Current Loss in the Permanent Magnets

5.1 Introduction

This chapter presents an analytical solution of the eddy currents in the PMs in the AFPMSMs using a coupled solution of Maxwell's equations and an electric circuit network.

It is necessary for high-speed applications to decrease the eddy current losses in the PMs to avoid their demagnetization. In a design procedure, it is necessary to have a fast and an accurate calculation method to obtain the PM losses in the PMs.

In the literature, several computational techniques are described for computing magnet losses. A first method is based on finite element (FE) models. It was developed to obtain accurate results for eddy current losses [78]. A full 3D time stepping FE model would be one solution. This method is accurate and very time consuming. Another less time consuming and nevertheless accurate model is the 2D FE model described in [79]. In that article, the authors divided the machine into slices. Then, the field solution is reconstructed and applied to a simple geometry of one PM in the 2D FE model.

There are several analytical tools for the calculation of eddy current losses for radial flux permanent magnet synchronous machines (RFPMSMs). The differences among many techniques were investigated in this review article [80]. In this review paper, the eddy current losses were subdivided into two types depending on the main sources. The sources are the armature field described in [81–83], and the slotting described in [84]. The power losses formula, developed in [81, 82], was based on obtaining the current sheet distribution formula in space. Then, the magnetic vector potential is deduced using Maxwell's equations. The solution in this case neglects the slotting and skin effect. The skin effect has a major impact at high speeds and also when connecting the machine to a frequency converter. [83] introduced simple mathematical formulations for eddy-current loss calculations due to

the time harmonics in the stator current which neglected the spatial distribution of this field on the surface of the PMs and also neglected the slotting and skin effect. The comparison in [80] showed that the computation of the eddy-current loss due to slotting introduced in [84] should be more investigated for more precise results.

Another technique was introduced in [85,86]. In this technique, the flux density was deduced in the PM by using the Magnetic Equivalent Circuit (MEC) in RF-PMSM. The eddy losses were calculated in post processing by assuming a certain resistance limited path for the current that was assumed to be frequency independent. Also the skin effect was neglected. This was proven to be inaccurate in a later article [87]. For each harmonic, in the magneto-motive force (MMF), a different wavelength of the eddy losses is obtained. In [87], four different cases were suggested according to the wavelength of the applied MMF and the width of the magnet to define a certain path for the current. The slotting effect is neglected. This may be a major part of the losses at low rotational speed.

In [88], simpler techniques were proposed for the calculation of losses at no load due to the slotting effect. This is based on calculating the flux density on the surface of the PM by using a Carter coefficient and the permeance function developed in [41]. The resistance path also was assumed to be constant. In [89], the authors also assumed a certain path without considering the spatial distribution of MMF in space. In [90], the authors proposed an analytical and FE model for radial flux machines that includes the effect of magnet segmentation in axial and circumferential directions. Both models include the effect of the reaction field. In [91], a very accurate technique based on the subdomain model for calculation of magnet eddy losses is proposed. However, the model is complex from the mathematical point of view. In [92], a 2D analytical method for PM eddy current losses calculation with the reaction field effect for slot-less machines with surface inset PMs is proposed.

In radial flux machines, the flux density is constant over the axial length of the machine. In axial flux machines, the width of the PMs is changing over the radial length. Because of this, it was required to develop a model that is able to calculate the eddy losses in AFPMSM. Under this varying width, the analytical model described in this chapter could be used for this study.

In [93], the authors developed a combined solution of magnetic equivalent circuit (MEC) and en electric network to compute the eddy current losses in the PMs for RFPMSMs. In this chapter, the authors adapted the electric network to be used for AFPMSMs. This technique has an important advantage: it is able to calculate the distribution of the induced currents in the PMs.

In this chapter, in spite of using the MEC, Maxwell's equations are used to obtain the flux densities on the surface of the PMs, including the effect of armature current and the slotting as derived in [44]. This solution is applied to the electric network to obtain the total current flowing through the PMs. The inductances are added to describe the skin effect on the total losses in the PMs.

In this chapter, an analytical method based on Maxwell's equations and electric

network model is used. This model is based on resistances and inductances that are used to derive the PM losses in AFPMSMs. Maxwell's equations are solved firstly to obtain the flux density on the surface and inside the PM. This flux density distribution is then used as a source term for the network for calculation of eddy current losses.

5.2 Electric Circuit Network for PM Eddy Current Loss Calculation

5.2.1 Multi-Slice 2D Analytical Solution

The flux density, calculated in section 3.4.2 using the complex Schwarz-Christoffel transformation, is recorded on the PM volume shown in Fig. 5.1 (a) for different slices in the radial direction.

There are mainly three contributions of the total magnetic flux density described in section 3.4.2.

- The PM flux density assuming a smooth iron surface.
- The armature reaction current assuming a smooth surface of iron.
- The slotting effect described by conformal mapping.

The total flux density is obtained afterwards by considering the three contributions using (3.47). In all these equations a stationary coordinate system (x and y) is used. These axis are described in Fig. 3.2 (c).

Because of the rotor motion, another coordinate system is considered. This system is described by axis (x_r and y_r) shown in Fig. 5.1 (a). This system is moving with the rotor.

The differences between these coordinates are described below:

$$x = x_\mathrm{r} + \omega_\mathrm{m} R^\mathrm{i}_\mathrm{av} t, \tag{5.1}$$

where ω_m is the mechanical rotational speed in rad/s, R^i_av is the average radius at a slice i described in Fig. 3.2 (b), and t is the time.

For each new rotor position, the solution is obtained using Maxwell's equations on the PM volume for each slice in the radial direction. Each radial slice, described in Fig. 5.1 (a), has a new flux density denoted by $B_1, B_2, B_3, ...$

Figures 5.1 (a) and (b) show the difference between AFPMSMs and RFPMSMs. The difference occurs because of the changing perimeter and the changing PM width in the AFPMSMs. Therefore, for every radial plane, there is a new flux density value. However, for RFPMSMs, the flux density is constant at all over the PM length in the axial direction neglecting the end effects at the two axial ends of the machine.

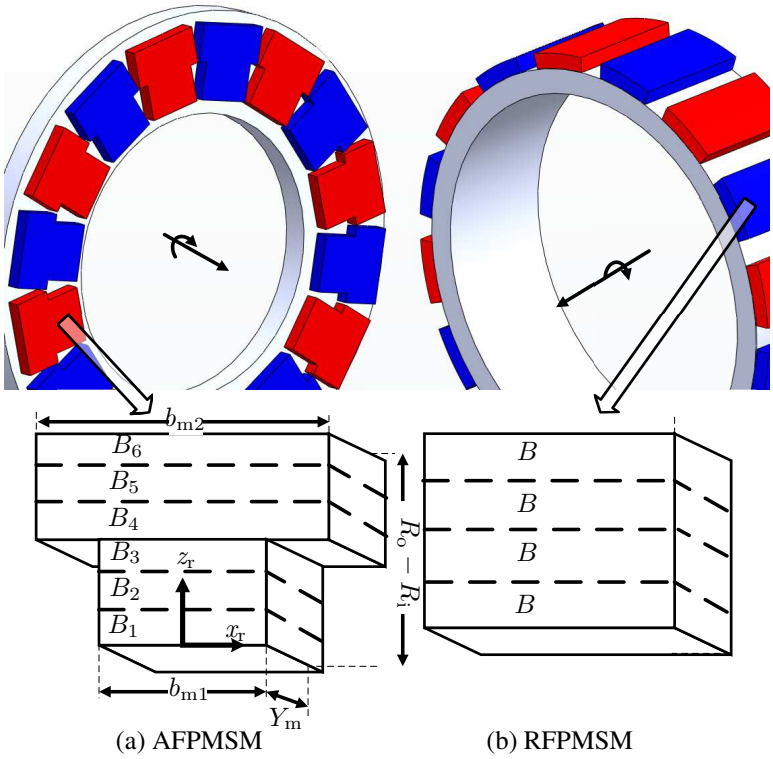

Figure 5.1: Magnified version of the PM for the axial and radial flux machines.

5.2.2 PM Flux Density Reconstruction

Using the analytical model with the conformal mapping method, the resulting axial flux density on each slice is reconstructed on the total surface of the PM and over the axial length of the PM. The reconstructed flux density, on the front and back surfaces of the PM, is shown in Figs. 5.2 (a) and (b). It is clear that the slotting effect has completely decayed on the PM back surface. Additionally, the magnetic flux density caused by the armature currents changes over the axial length of the PM as described in Fig. 3.15.

Therefore, the solution is repeated for n_{ym} slices in the axial direction as shown in Fig. 5.3 (b). Each slice s in the axial direction has a width of Δ_{y}.

Subsequently, the rotor positions dependent magnetic flux density is transformed to the frequency domain by means of a Fourier series. For each point on the PM volume, each harmonic order n of the axial component of the magnetic flux density B_{n} is used to excite the developed electric network.

Additionally, the electric network is solved for each slice s and the total losses

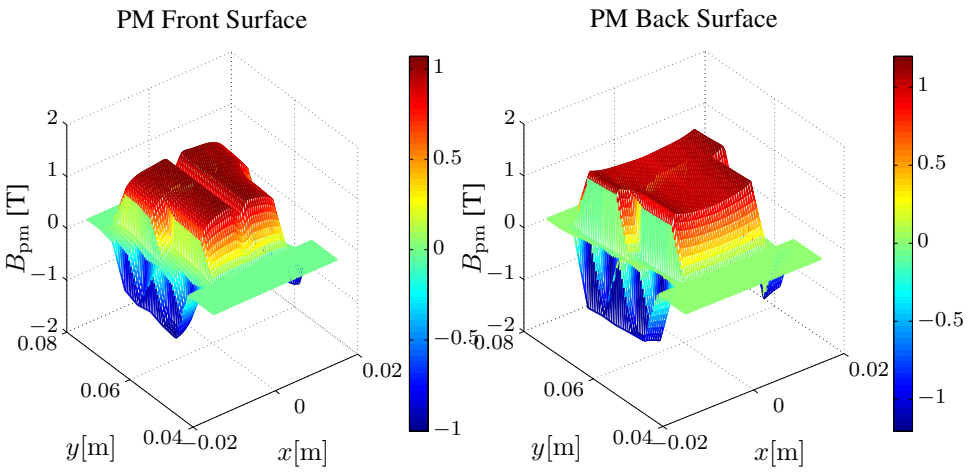

Figure 5.2: Reconstructed flux density on the front and back surfaces of the PM from the Analytical Model.

are computed for the complete slices multiplied by the width of each slice. The varying term on each slice is the flux density obtained by Maxwell's equations. The number of radial slices used in this thesis is 6.

The flux density computed on the center of each slice s, shown in Fig. 5.3 (b), is the source term of the network as described in [94]. In [94], this network was composed only of resistances without taking into account the effect of reaction

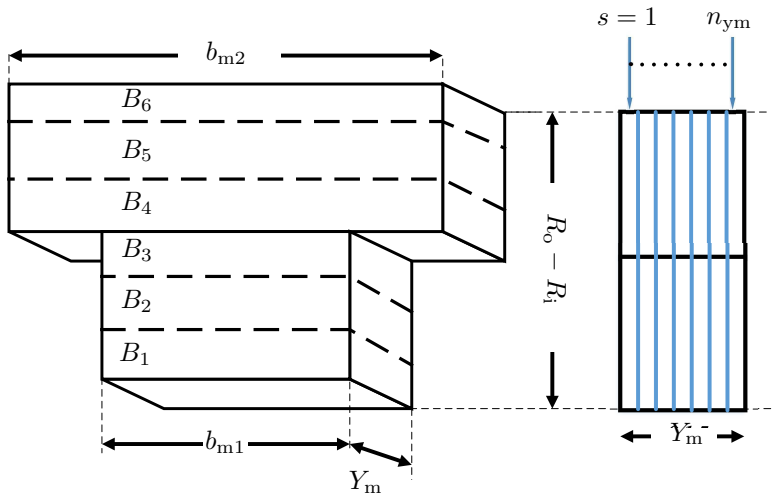

(a) Front View of PM. (b) Side View of PM.

Figure 5.3: Axial slices of the PM model.

field of induced currents in the PMs on the applied field and without considering PM segmentations.

This electric network is shown in Fig. 5.4 (a). It is composed of a number of nodes n_{node} and branches n_{branch}. Each node bounds four branches around it. Each node affects all other branches existing in the whole geometry.

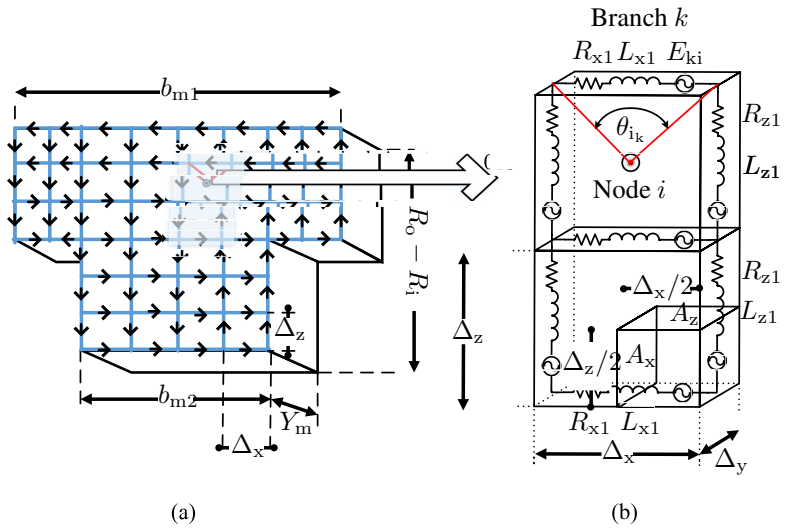

Figure 5.4: Electric network distribution consisting of induced voltage, resistances and inductances (self and mutual inductances).

Figure 5.4 (b) shows the main components of the electric network to be studied. It consists of three main components: the induced voltage E_{ki}, the resistance (R_{xi}, R_{zi}) and the inductance (L_{xi}, L_{zi}). In next sub-sections, these main components are described.

5.2.3 Induced Voltage

The induced voltage E_{ki} is calculated based on the reconstructed flux density. This flux density is integrated over the enclosed area bounded by Δ_x Δ_z shown in Fig. 5.4 (b) to obtain the total flux in this area for slice 's' in the axial direction.

$$\phi_{\text{i}_\text{s}} = \iint B_{\text{y}_\text{s}} \text{d}x\text{d}z. \tag{5.2}$$

In each branch, the induced voltage is calculated for each harmonic order n individually. Fourier analysis is done to the induced flux ϕ_{i_s} to obtain the coefficients $a_{\text{n}_{\text{i}_\text{s}}}$ and $b_{\text{n}_{\text{i}_\text{s}}}$.

$$a_{\text{n}_{\text{i}_\text{s}}} = \frac{1}{\pi} \int_0^{2\pi} \phi_{\text{i}_\text{s}} \cos(n\omega_\text{e} t) \text{d}(\omega_\text{e} t), \tag{5.3}$$

$$b_{\mathrm{n_i s}} = \frac{1}{\pi} \int_{0}^{2\pi} \phi_{\mathrm{i_s}} \sin(n\omega_{\mathrm{e}} t) \mathrm{d}(\omega_{\mathrm{e}} t), \tag{5.4}$$

where ω_{e} is the electrical speed in rad/s.

The voltage in each branch $E_{\mathrm{k_n}}$ at a harmonic order n is calculated based on the Fourier coefficients of the applied field ϕ_{i}. For each branch k, the fourier coefficients of the applied field are multiplied by the angle $\theta_{\mathrm{i_k}}$ shown in Fig. 5.4 (b). $\theta_{\mathrm{i_k}}$ is the angle bounding both ends of branch k and node i where the applied field $\phi_{\mathrm{i_s}}$ exists. This procedure is repeated for all nodes, to obtain the effect of all nodes on this branch.

$$E_{\mathrm{k_n}} = \sum_{i=1}^{n_{\mathrm{nodes}}} -jn \frac{2\pi n_{\mathrm{m}}}{60} \frac{(a_{\mathrm{n_i}} + j b_{\mathrm{n_i}})}{\sqrt{2}} \frac{\theta_{\mathrm{i_k}}}{2\pi}, \tag{5.5}$$

where $E_{\mathrm{k_{n_s}}}$ is the voltage at branch k due to a harmonic n for slice s, $\theta_{\mathrm{i_k}}$ is the intersecting angle between each node i and both ends of each branch k shown in Fig. 5.4, and n_{m} is the rotational speed in rpm. The equation is divided by $\sqrt{2}$ to obtain the root mean square (rms) value.

5.2.4 Resistance Calculation

In each branch, the resistance is calculated based as follows.

$$R_{\mathrm{x}} = \frac{\Delta_{\mathrm{x}}}{\sigma(\Delta_{\mathrm{z}}/2)\Delta_{\mathrm{y}}}, \tag{5.6}$$

$$R_{\mathrm{z}} = \frac{\Delta_{\mathrm{z}}}{\sigma(\Delta_{\mathrm{x}}/2)\Delta_{\mathrm{y}}}, \tag{5.7}$$

where σ is the electrical conductivity.

5.2.5 Inductance Calculation

The inductances are introduced to describe the reaction field of the eddy currents flowing through the PM. These inductances in Fig. 5.5 are divided into two categories: one is the self inductance of each element $L_{11}\&L_{22}$, and the other one is the mutual inductance between this element and the other elements $L_{12}\&L_{21}$ existing in the system. The PM is divided into number of branches. Each branch, e.g. 1 in Fig. 5.5, links the other branches, e.g. 2 in Fig. 5.5, by the mutual inductances $L_{12}\&L_{21}$. The total inductance at each branch equals the self inductance of this branch and the summation of the mutual inductances between this branch and the other branches. The final forms of the mutual and self inductances are shown in Fig. 5.5. The derivation of these forms can be found in [95]. The boundaries shown in (5.8) are substituted in the summation form shown also in (5.8).

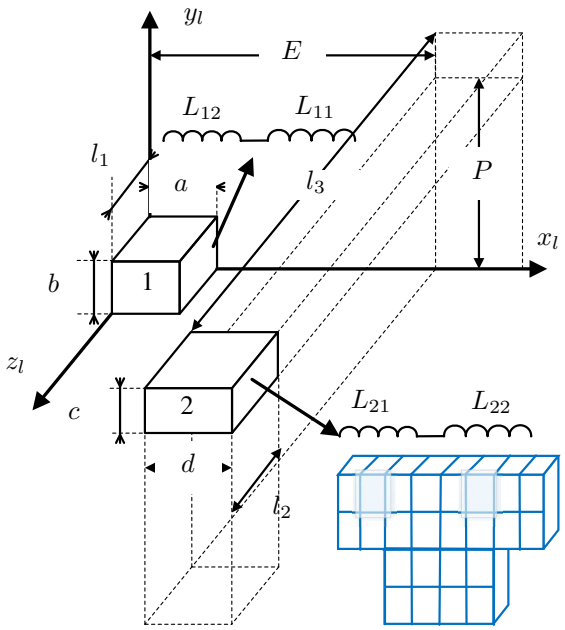

Figure 5.5: Self and mutual inductances. (1) and (2) denote small blocks inside the PM.

$$L_{12} = L_{21} = \frac{\mu_o \mu_r}{4\pi} \frac{1}{abcd} \left[\left[\left[f\left(x_l, y_l, z_l\right) \right] \begin{matrix} E-a, E+d \\ (x_l) \\ E+d-a, E \end{matrix} \right] \begin{matrix} P-b, P+c \\ (y_l) \\ P+c-b, P \end{matrix} \right] \begin{matrix} l_3-l_1, l_3+l_2 \\ (z_l) \\ l_3+l_2-l_1, l_3 \end{matrix}, \tag{5.8}$$

where

$$\left[\left[\left[f\left(x_l, y_l, z_l\right) \right] \begin{matrix} q_1, q_3 \\ (x_l) \\ q_2, q_4 \end{matrix} \right] \begin{matrix} r_1, r_3 \\ (y_l) \\ r_2, r_4 \end{matrix} \right] \begin{matrix} s_1, s_3 \\ (z_l) \\ s_2, s_4 \end{matrix} = \sum_{i=1}^{4} \sum_{j=1}^{4} \sum_{k=1}^{4} (-1)^{(i+j+k+1)} f(q_{\mathrm{i}}, r_{\mathrm{j}}, s_{\mathrm{k}}), \tag{5.9}$$

where i corresponds to the boundary number. For example, if the x_{l} and $i = 1$ are considered, then $q_{\mathrm{i}} = E - a$.

$$L_{11} = 8\frac{\mu_{\mathrm{o}}\mu_{\mathrm{r}}}{4\pi}\frac{1}{a^2b^2}\left[\left[\left[f\left(x_{\mathrm{l}},y_{\mathrm{l}},z_{\mathrm{l}}\right)\right]\begin{matrix}a\\(x_{\mathrm{l}})\\0\end{matrix}\right]\begin{matrix}b\\(y_{\mathrm{l}})\\0\end{matrix}\right]\begin{matrix}l_1\\(z_{\mathrm{l}})\\0\end{matrix}, \tag{5.10}$$

where

$$\left[\left[\left[f\left(x_{\mathrm{l}},y_{\mathrm{l}},z_{\mathrm{l}}\right)\right]\begin{matrix}q_1\\(x_{\mathrm{l}})\\q_2\end{matrix}\right]\begin{matrix}r_1\\(y_{\mathrm{l}})\\r_2\end{matrix}\right]\begin{matrix}s_1\\(z_{\mathrm{l}})\\s_2\end{matrix} = \sum_{i=1}^{2}\sum_{j=1}^{2}\sum_{k=1}^{2}(-1)^{(i+j+k+1)}f(q_{\mathrm{i}},r_{\mathrm{j}},s_{\mathrm{k}}), \tag{5.11}$$

where i corresponds to the boundary number. For example, if the x_{l} and $i = 1$ are considered, then $q_{\mathrm{i}} = a$.
where also $f(x_l, y_l, z_l)$ equals

$$\begin{aligned}
f(x_{\mathrm{l}},y_{\mathrm{l}},z_{\mathrm{l}}) &= \left(\frac{y_{\mathrm{l}}^2z_{\mathrm{l}}^2}{4}-\frac{y_{\mathrm{l}}^4}{24}-\frac{z_{\mathrm{l}}^4}{24}\right)x_{\mathrm{l}}\ln\left(\frac{x_{\mathrm{l}}+\sqrt{x_{\mathrm{l}}^2+y_{\mathrm{l}}^2+z_{\mathrm{l}}^2}}{\sqrt{y_{\mathrm{l}}^2+z_{\mathrm{l}}^2}}\right)\\
&+\left(\frac{x_{\mathrm{l}}^2z_{\mathrm{l}}^2}{4}-\frac{x_{\mathrm{l}}^4}{24}-\frac{z_{\mathrm{l}}^4}{24}\right)y_{\mathrm{l}}\ln\left(\frac{y_{\mathrm{l}}+\sqrt{y_{\mathrm{l}}^2+z_{\mathrm{l}}^2+x_{\mathrm{l}}^2}}{\sqrt{z_{\mathrm{l}}^2+x_{\mathrm{l}}^2}}\right)\\
&+\left(\frac{x_{\mathrm{l}}^2y_{\mathrm{l}}^2}{4}-\frac{x_{\mathrm{l}}^4}{24}-\frac{y_{\mathrm{l}}^4}{24}\right)z_{\mathrm{l}}\ln\left(\frac{z_{\mathrm{l}}+\sqrt{z_{\mathrm{l}}^2+x_{\mathrm{l}}^2+y_{\mathrm{l}}^2}}{\sqrt{x_{\mathrm{l}}^2+y_{\mathrm{l}}^2}}\right)\\
&+\frac{1}{60}(x_{\mathrm{l}}^4+y_{\mathrm{l}}^4+z_{\mathrm{l}}^4-3x_{\mathrm{l}}^2y_{\mathrm{l}}^2-3y_{\mathrm{l}}^2z_{\mathrm{l}}^2-3z_{\mathrm{l}}^2x_{\mathrm{l}}^2)\sqrt{x_{\mathrm{l}}^2+y_{\mathrm{l}}^2+z_{\mathrm{l}}^2}\\
&-\frac{x_{\mathrm{l}}y_{\mathrm{l}}z_{\mathrm{l}}^3}{6}\arctan\frac{x_{\mathrm{l}}y_{\mathrm{l}}}{z_{\mathrm{l}}\sqrt{x_{\mathrm{l}}^2+y_{\mathrm{l}}^2+z_{\mathrm{l}}^2}}-\frac{x_{\mathrm{l}}y_{\mathrm{l}}^3z_{\mathrm{l}}}{6}\arctan\frac{x_{\mathrm{l}}z_{\mathrm{l}}}{y_{\mathrm{l}}\sqrt{x_{\mathrm{l}}^2+y_{\mathrm{l}}^2+z_{\mathrm{l}}^2}}\\
&-\frac{x_{\mathrm{l}}^3y_{\mathrm{l}}z_{\mathrm{l}}}{6}\arctan\frac{y_{\mathrm{l}}z_{\mathrm{l}}}{x_{\mathrm{l}}\sqrt{x_{\mathrm{l}}^2+y_{\mathrm{l}}^2+z_{\mathrm{l}}^2}}.
\end{aligned} \tag{5.12}$$

It should also be noted that if either x_{l}, y_{l} or z_{l} approaches zero, all inverse tangents in (5.12) will equal zero. If any of x_{l}, y_{l} and z_{l} approach zero, all terms go to zero except the square root term.

Finally, the matrices for the resistances A_{r} and inductances A_{l} for the whole network are constructed. The sources for a harmonic order n also are combined together in a vector $E_{\mathrm{n_s}}$. Where 's' corresponds to the slice number in the axial direction. Finally, it is possible to apply Kirchhoff Current Law (KCL), to obtain the current flow for each harmonic order.

$$(A_{\mathrm{r}} + j\omega_{\mathrm{m}} n A_{\mathrm{l}}) I_{\mathrm{n_s}} = E_{\mathrm{n_s}}, \tag{5.13}$$

where ω_{m} is the mechanical rotational speed in rad/s and subscript n describes the harmonic order. The power losses are calculated by summing the squares of the norm of the current densities for all nodes n_{nodes}. Another summation for all harmonic orders is then applied to obtain the total time average losses. Finally, a summation of the power losses is done for each slice 's' in the axial direction of the PM.

$$\begin{aligned} P_{\mathrm{pm}} = 4pP_{\mathrm{pm_{np}}} &= 4p \sum_{n=1,2,..}^{\infty} \frac{1}{\sigma} \int_{S_{\mathrm{pm}}} \int_{0}^{Y_m} {J_{\mathrm{n_i}}}^2 \mathrm{d}z \mathrm{d}S_{\mathrm{pm}} \\ &= \frac{4p}{\sigma} \sum_{s=1,2,..}^{n_{ym}} \sum_{n=1,2,..}^{\infty} \sum_{i=1}^{n_{\mathrm{nodes}}} {J_{\mathrm{n_{i_s}}}}^2 \Delta_{\mathrm{x}} \Delta_{\mathrm{z}} \Delta_{\mathrm{y}}, \end{aligned} \tag{5.14}$$

where $J_{\mathrm{n_{i_s}}}$ is the norm of the current density at node i and slice s, Δ_{y} is the axial length of each slice in the PM area, and p is the number of pole pairs. This equation is multiplied by $4p$ to represent the total number of magnets existing in the machine. If the model is used only with resistances it is considered to model the losses without the reaction field effect.

5.3 PM Segmentation

Segmentation for the PMs in AFPMSMs is introduced to reduce the total eddy losses in [78]. The circuit model has the effectiveness to calculate the losses for different numbers of segments. The electric network is used to calculate the losses for one, two and four segments. The electric network results are validated by the 3D and 2D FE model results in two cases. The first case takes into account the reaction field effect, and the second case does not take into account this effect. The segments are shown in Fig. 5.6. The number of nodes in the one segment is 240 nodes, while in the two segments and four segments, they are 240 nodes for each segment.

5.4 2D Multi-Slice FE Model

The finite element (FE) models are used to obtain the eddy current losses in the PMs. Steps similar to sections 5.2.1 and 5.2.2 are used to obtain the PM flux density in the frequency domain. They are briefly described below.

- Firstly, the 2D multi-slice FE model, shown in Fig. 3.2 (c) and described in chapter 3, is solved. The rotor disc is rotated manually by sufficiently small

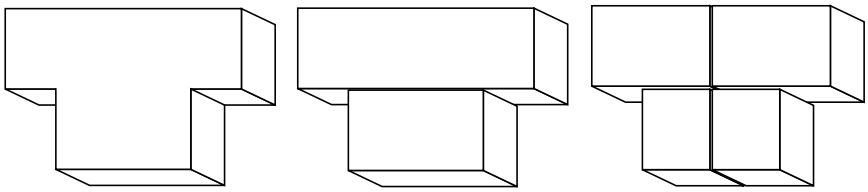

(a) One Segment (b) Two Segments (c) Four Segments

Figure 5.6: Permanent magnet segmentation.

rotor steps. Therefore, the solution assumes a resistance limited PM. Thus, the reaction fields of the eddy currents in the PMs are not considered in this phase.

Eddy currents are solved *a posteriori* by means of frequency domain FE models.

- The flux density distributions on a number of slices n_{ym}, shown in Fig. 5.3 (b), are recorded for each radial length i, described in Fig. 3.2 (b).

  On each slice s in the axial direction, shown in Fig. 5.3 (b), the flux density is reconstructed on the complete surface of the PM for all slices n_{ym}.

- For each point in the reconstructed magnetic flux density, the harmonic with order n of the scalar magnetic flux density B_{n} is obtained by means of a Fourier series.

- These harmonic magnetic flux density patterns will be imposed to the permanent magnet FE models described in sections 5.4.1 and 5.4.2. These are also shown in Figs 5.7 (a) and (b) respectively. The model described in section 5.4.1 does not consider the reaction field effect, while, the model described in section 5.4.2 considers it.

5.4.1 FE Model Without the Consideration of the Reaction Field

In this part, the FE model shown in Fig. 5.7 (a) is modeled in 2D. This model does not take into account the effect of reaction field of the eddy currents. In this solution, a time harmonic analysis is used. A similar model was presented in [79]. The principle operation of this model is to convert the time series axial component of the flux density into the frequency domain. This results in the flux density amplitude $B_{\mathrm{n}}(x, z)$ for each harmonic order n. Afterwards, it is possible to apply Maxwell's equations for each harmonic order n.

$$\nabla \times \mathbf{E} = -jn\omega_{\mathrm{m}}\mathbf{B}_{\mathrm{n}}, \tag{5.15}$$

$$\nabla \cdot \mathbf{E} = 0, \tag{5.16}$$

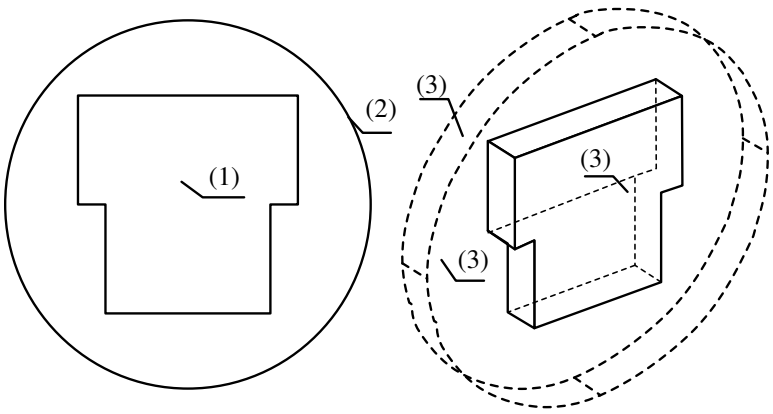

Figure 5.7: PM FE Model. (1) Imposition of the air gap magnetic field over the PM area. (2) Dirichlet Boundary Condition. (3) Neumann Boundary Condition. (a) FE model without considering reaction field effect. (b) FE model considering reaction field effect.

where $\mathbf{E} = \left(\frac{1}{\sigma}\right)\mathbf{J}$ and n is the harmonic order. For each harmonic order, (5.17) is solved for Fig. 5.3 (a).

$$\nabla \times \left(\frac{1}{\sigma}\nabla \times \mathbf{F}\right) = -jn\omega_{\mathrm{m}}\mathbf{B}_{\mathrm{n}}, \tag{5.17}$$

where $\mathbf{J} = \nabla \times \mathbf{F}$.

$\mathbf{F}$ is a new electric vector potential which is used instead of the magnetic vector potential $\mathbf{A}$ in the electromagnetic problems.

For each harmonic order n, (5.17) is solved to obtain the vector potential $\mathbf{F}$. The current density is then obtained. To compute the total losses, the current density is integrated over the complete surface of the PM and summation of the complete harmonics is done to obtain the total losses. Another summation is done to obtain the power losses for all slices s, shown in Fig. 5.3, in the axial direction.

$$\begin{aligned} P_{\mathrm{pm}} &= 4p \sum_{n=1,2,..}^{\infty} \frac{1}{\sigma} \int_{S_{\mathrm{pm}}} \int_{0}^{Y_{\mathrm{m}}} {J_{\mathrm{n}}}^2 \mathrm{d}z \mathrm{d}S_{\mathrm{pm}} \\ &= 4p \sum_{s=1,2,..}^{n_{ym}} \sum_{n=1,2,..}^{\infty} \frac{1}{\sigma} \int_{S_{\mathrm{pm}}} {J_{\mathrm{n_s}}}^2 \mathrm{d}S_{\mathrm{pm}} \Delta_{\mathrm{y}}, \end{aligned} \tag{5.18}$$

To obtain Maxwell's equation as a function of the magnetic vector potential $\mathbf{A}$, $\mathbf{E}$ is substituted in (5.15) by $-jn\omega_{\mathrm{m}}\mathbf{A}$ and applying the curl to it. This would

result in:

$$\nabla \times (\nabla \times \mathbf{A}) = \nabla \times \mathbf{B}_{\mathrm{n}}, \tag{5.19}$$

5.4.2 FE Model With the Consideration of the Reaction Field

The 3D FE Model shown in Fig. 5.7 (b) is used to model the eddy currents including the effect of the reaction field. In this solution, a time harmonic analysis is used.

In the PM region, shown in Fig. 5.7 (b), the PM is defined by a magnetic remanence flux density $\mathbf{B}_{\mathrm{rem}}$ for each harmonic order n, a relative permeability μ_{r} (estimated at 1.05 for NdFeB) as well as a conductivity σ. Therefore, the PM flux density is computed as:

$$\mathbf{B} = \mu_{\mathrm{o}}\mu_{\mathrm{r}}\mathbf{H} + \mathbf{B}_{\mathrm{rem}}, \tag{5.20}$$

where $\mathbf{H}$ corresponds to the reaction field of the eddy currents flowing through the PM.

It is worth mentioning that the remanent flux desnity $\mathbf{B}_{\mathrm{rem}}$ imposed to the PM is obtained based on the solution of the Fourier series of the reconstructed flux density in the PM volume computed from the multi-slice 2D FE model.

Afterwards, it is possible to apply the time harmonic Maxwell's equations to the FE model shown in Fig. 5.3 (b) using the constitutive law in (5.20). This results in:

$$\nabla \times (\nabla \times \mathbf{A}) = \nabla \times (\mathbf{B}_{\mathrm{rem}}) - j\mu_{\mathrm{o}}\mu_{\mathrm{r}}\omega_{\mathrm{m}}n\sigma\mathbf{A}, \tag{5.21}$$

This FE model is solved for each harmonic and then summation for the complete harmonic orders is done to obtain the total eddy loss in the PM using (5.18).

Comparing the two models without the reaction field effect in (5.19) and with the reaction field effect in (5.21), it is clear that the term $-j\mu_{\mathrm{o}}\mu_{\mathrm{r}}\omega_{\mathrm{m}}n\sigma\mathbf{A}$ in (5.21) corresponds to the effect of reaction field.

5.5 3D Time Stepping FE Model

Another 3D FE transient time stepping model is developed. The mesh of this model is shown in Fig. 5.8. Only half of the machine is modeled and a symmetry plane is taken in the middle half of the machine. This 3D FE model is programmed in Ansys Maxwell 3D software to validate the results for all FE models and the circuit model. A high mesh quality of the 3D FE model, shown in Fig. 5.8, is used to obtain an accurate solution.

The eddy losses at no load condition at a certain time instant is shown in Fig. 5.9 for the complete PMs. This figure shows that the main component affecting the eddy losses is caused by the slot opening in the stator core. The regions where the eddy current losses in the PMs are higher, correspond to the position of the slot openings.

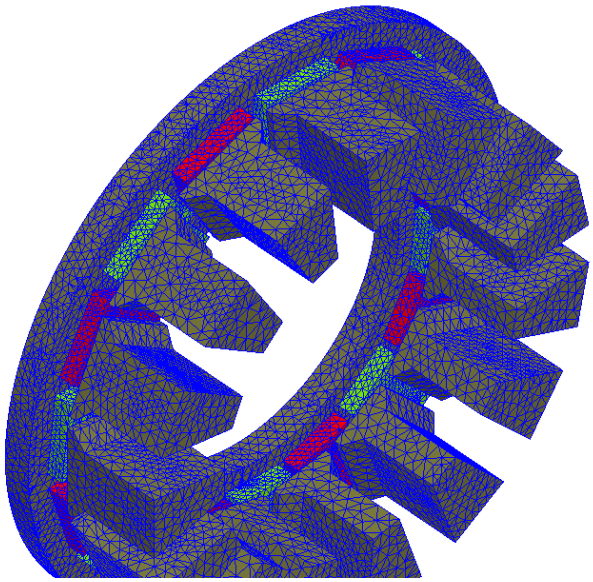

Figure 5.8: Compete 3D FE Model in Ansys Maxwell software and the mesh quality.

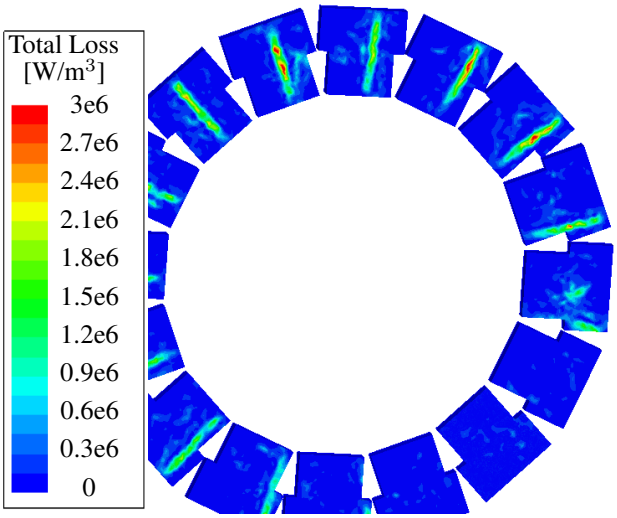

Figure 5.9: Eddy Current Losses in the PM at no load computed using the 3D time stepping FE model.

It will be shown later from the harmonic spectrum that the main component affecting eddy losses is caused by the slot numbers. Due to the time limitation of such a model, the simulations are only conducted for no load and rated loading conditions. The time required for a completely verified simulation is about 5 days.

5.6 Simulation Results

The simulations are implemented for an AFPMSM of 16 poles and 15 tooth fractional slot winding machine. The geometrical and electromagnetic properties of the machine are summarized in Table 4.1.

There are five models to be studied.

- A circuit model that neglects the effect of the reaction field. This model considers only the resistances in the circuit. This is illustrated in section 5.2.
- A circuit model that considers the reaction field effect. The circuit model in this case is composed of resistances and inductances. This is illustrated in section 5.2.
- A FE model that neglects the reaction field effect described in section 5.4.1.
- A FE model that considers the reaction field effect described in section 5.4.2.
- A full 3D time stepping FE model described in section 5.5.

The simulation is conducted for different loading conditions and rotational speeds and for different PM segmentations to have a full validity of the model. To show also the effectiveness of the model, a pulse width modulated (PWM) current is injected to the machine to have a deep understanding of the effect of this reaction field.

The simulation results are organized as follows. The first subsection will study the models for sinusoidal currents for different loading conditions. In the second subsection, injection of PWM will be studied for different carrier frequencies and speeds. In a third subsection, PM segmentations will be studied also for the four models in the third part.

5.6.1 Sinusoidal Operating Conditions

The models are excited by a sinusoidal supply at different operating conditions. It is mandatory to demonstrate the ability of the model to obtain the power losses at different harmonic orders.

Figure 5.10 shows the difference between circuit and FE model for different harmonic orders at no load conditions. [79].

The circuit model shows a good correspondence with the FE model. Fig. 5.10 also shows that there is no observable difference between taking into account the reaction effect and without it. It is shown that the main orders affecting the eddy current losses are caused by multiples of the slot numbers ($N_{\mathrm{s}} = 15$). This was proven analytically in [79].

Figure 5.11 shows the eddy current paths for different harmonic orders at rated loading conditions.

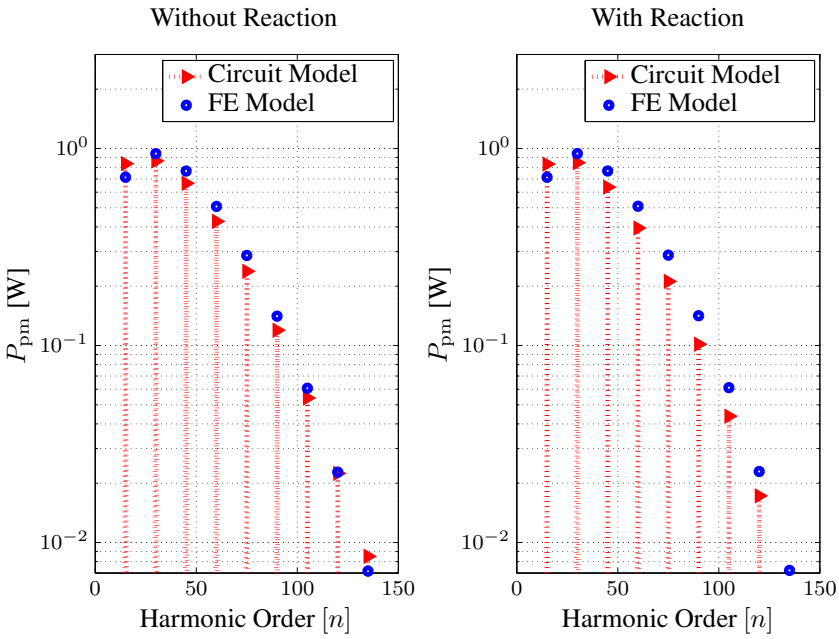

Figure 5.10: PM eddy power losses as a function of harmonic orders at no load at 2500 rpm.

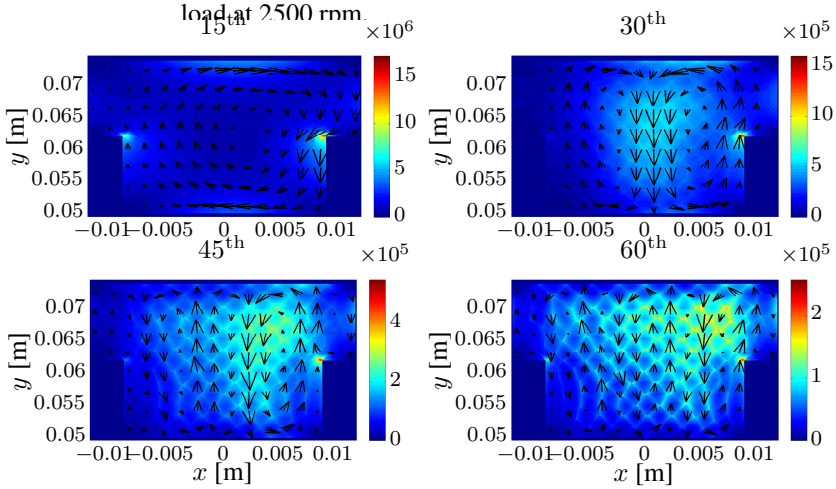

Figure 5.11: Eddy power losses per unit volume for different harmonic orders demonstrating the current path for each harmonic order at rated loading sinusoidal conditions using the model described in section 5.4.1.

Figure 5.11 shows that each harmonic order flows in a certain pattern. For example, for the 15^{th} harmonic, eddy currents in the PM flow only in one loop, while for the 30^{th} harmonic, the eddy currents flow in two loops. Regardless of

the direction of the current flow, the circuit model is capable to obtain the eddy currents precisely.

Figure 5.12 shows the difference at rated loading conditions for different harmonic orders. It is clear that additional harmonics exist due to the armature currents in the windings. Furthermore, the armature reaction of eddy currents in the PMs has no effect on the harmonic spectrum. Additionally, the circuit model shows a good correspondence with the FE models.

For the 150^{th} harmonic, the permanent magnet losses is less than 0.01W. Therefore, it is not necessary to make additional computations after this order.

Figure 5.13 shows the distribution of the power per unit volume for the two models. It is shown that the circuit model is capable of estimating the distribution of power loss in an accurate way compared to the results of the FE model. To obtain high quality figures of the circuit model, the nodes, shown in Fig. 5.4, are increased to obtain such a figure.

Figure 5.14 demonstrates the effect of the full 3D FE model at no load on the PM eddy current losses. The computation shows that the average losses of one PM multiplied by the number of PMs equals the total summation of the individual PM losses.

Table 5.1 summarizes the PM losses at no load and rated load conditions. It can be concluded that the circuit model is capable to obtain the total losses in an accurate way compared to the FE models based on slices. The error in the table is in percentage from the FE model.

The difference from Table 5.1 shows that the reaction field effect is not well dominant.

As a consequence, it is more effective in the pre-design state to use a non reaction field effect model (without inductances in the circuit model) for less CPU computation saving.

Compared to the full 3D FE model, the total PM losses compared to the FE and circuit models are capable to obtain the total losses in an accurate way.

Table 5.1: Eddy power losses for PM in [W] with and without reaction field effect.

	Without Reaction		With Reaction		3D Model
	FE Model	Circuit Model	FE Model	Circuit Model	
No Load	3.5 W	3.2 W	3.4 W	3.1 W	3.8 W
Err. (%)	-	5.8 (%)	-	8.8 (%)	
Rated Load	19.9 W	20.5 W	19.8 W	20.2 W	22.0 W
Err. (%)	-	3.0 (%)	-	2.0 (%)	

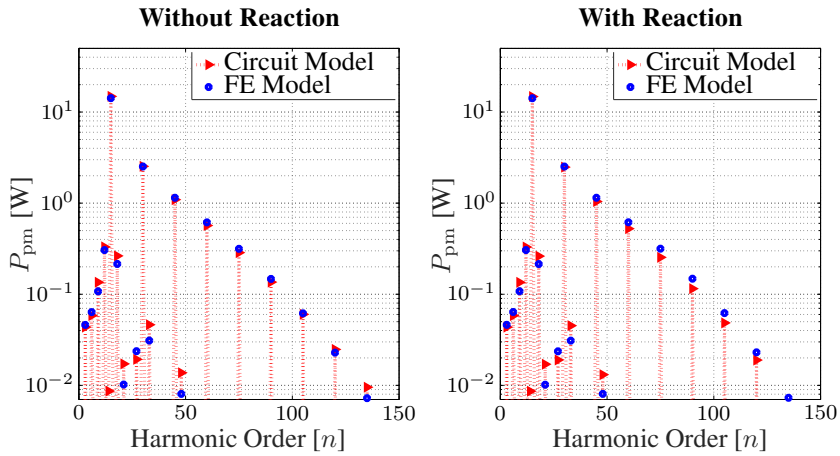

Figure 5.12: PM eddy power losses as a function of harmonic orders at rated load conditions at 2500 rpm.

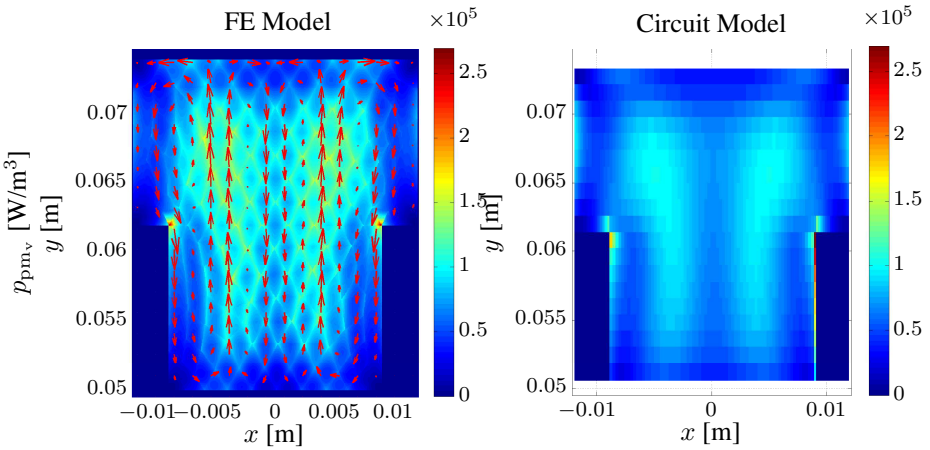

Figure 5.13: PM eddy power losses distribution $p_{\rm pm_v}$ [W/m^3] at a harmonic order of $45^{\rm th}$ from the fundamental at no loading conditions. (a) FE model. (b) Circuit model.

5.6.2 Pulse Width Modulation (PWM) Operating Conditions

In [96] a dynamic state space model based on FE is implemented for the AFPMSM for different carrier frequencies. The steps of the generation of the currents are based on creating a voltage waveform for a given input carrier frequency and imposing this voltage waveform to this state space space model. The parameters of this model are based on look up tables for the solution of the FE model taking into

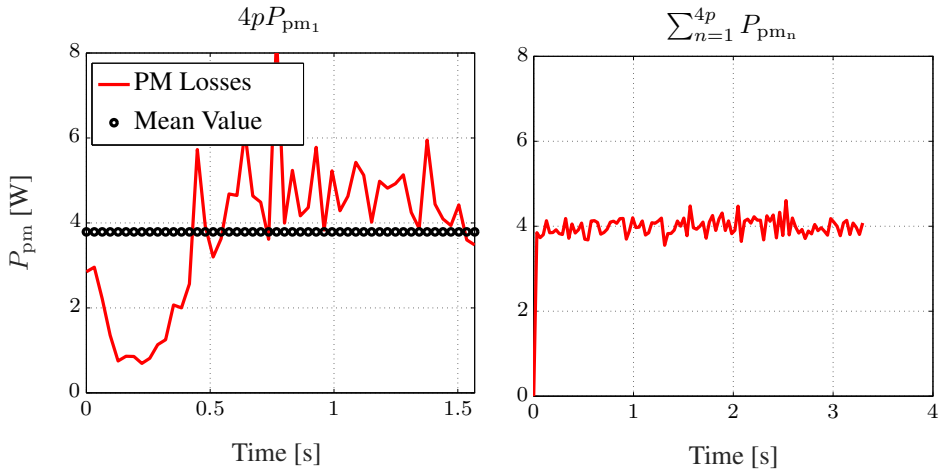

Figure 5.14: PM eddy power losses at no load for the full 3D time stepping model.

account the non-linearity of the magnetic materials. The outputs of these steps are the currents which will be the source to the PM eddy loss models.

Two different carrier frequencies (5kHz and 10kHz) are studied to model the losses. The currents for phase a for these two carrier frequencies are shown in Fig. 5.15. It shows also the harmonic spectrum for these two carrier frequencies. The total harmonic distortion (THD) is enhanced from 8.95% at 5kHz to 4.34% at 10kHz.

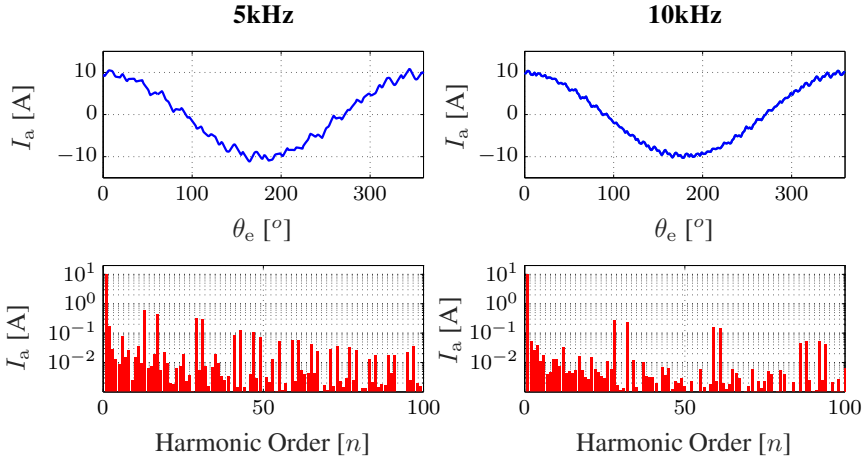

Figure 5.15: Current waveforms and their corresponding harmonic spectrum for 5kHz and 10kHz carrier frequency.

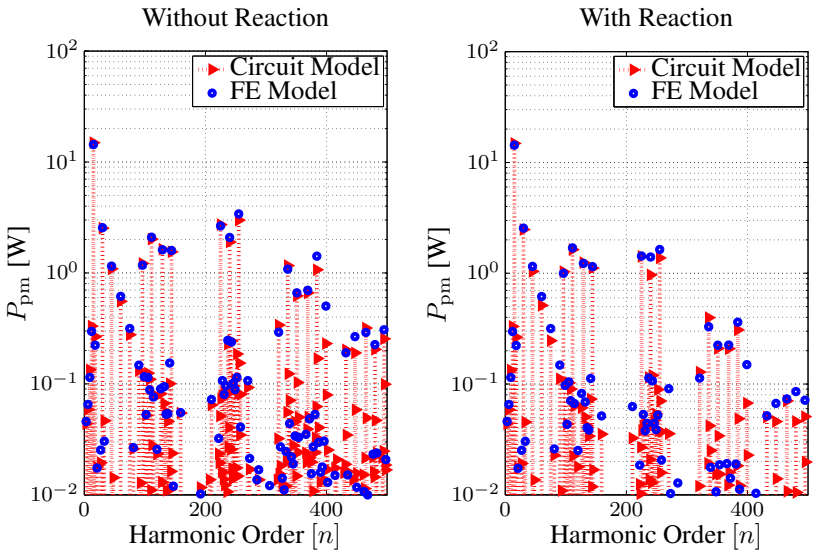

Figure 5.16: PM eddy power losses as a function of harmonic orders at carrier frequency of 5kHz at 2500 rpm.

The next step is to inject these currents on different eddy current loss models for different speeds and the losses with and without the reaction field could be observed.

Fig. 5.16 shows the power losses for the 5kHz case with and without the reaction field for the circuit and FE model. The maximum harmonic order in the sinusoidal case shown in Fig. 5.12 is observed to be 150 from the fundamental value. On the other hand, in the case of PWM shown in Fig. 5.16, other harmonics order appeared after this value and the amplitudes of these harmonic orders have increased too. It can be observed also that the effect of reaction field has increased at higher frequency orders.

Fig. 5.17 shows the effect of different rotational speeds on eddy power losses with and without reaction field effect for the FE model and circuit model. It could be pointed out that the effect of the reaction field is dominant at higher speeds while at low speeds this effect could be neglected. At higher speeds, the inductive component has a major effect. In addition, the circuit model can track the FE results in an effective way.

Table 5.2 proves that the circuit model is capable of obtaining accurate results in the case of PWM currents. It can also be observed that the losses have reduced by 10W when doubling the carrier frequency. The second observation is that the effect of taking into account the reaction field results in about 18% difference. This is a non-negligible value and should be taken into considerations for the study of PWM losses.

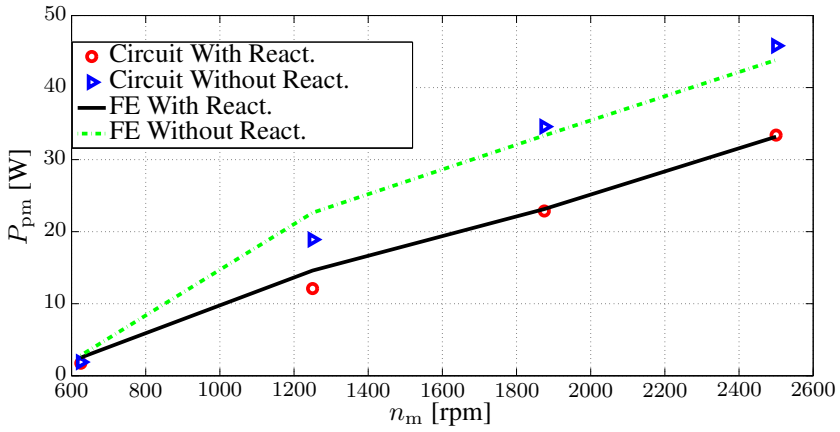

Figure 5.17: PM eddy power losses at carrier frequency of 5kHz at different speeds.

5.6.3 Skin Depth Effect

The reaction field effect has a strong relation with the skin depth in the PM. The skin depth δ in the PM equals:

$$\delta = \sqrt{\frac{2}{\omega_m \mu_{\mathrm{o}} \mu_{\mathrm{r}} \sigma}}, \tag{5.22}$$

where ω_m is the mechanical rotational speed in rad/s, μ_{o} is the permeability of free space, μ_{r} is the relative permeability of PM, and σ is the PM conductivity.

In normal design procedure with sinusoidal imposed currents, the maximum harmonic order is 150^{th} from the fundamental mechanical frequency as shown in Figs. 5.10 and 5.12. Fig. 5.18 shows the skin depth of the studied PM. At 150^{th} from the fundamental frequency, the skin depth is 16mm. The PM is a T-type PM. It has two widths of 18mm and 24mm. At this frequency, the skin depth is larger

Table 5.2: Eddy power losses for PM in [W] with and without reaction field effect for PWM cases.

	Without Reaction		With Reaction	
	FE Model	Circuit Model	FE Model	Circuit Model
5kHz	43.8 W	45.8 W	33.2 W	33.4 W
Err. (%)	-	4.6 (%)	-	0.6 (%)
React. Field effect (%)				31.1 (%)
10kHz	34 W	38 W	25.6 W	26.1 W
Err. (%)	-	11 (%)	-	1.56 (%)
React. Field effect (%)				32.8 (%)

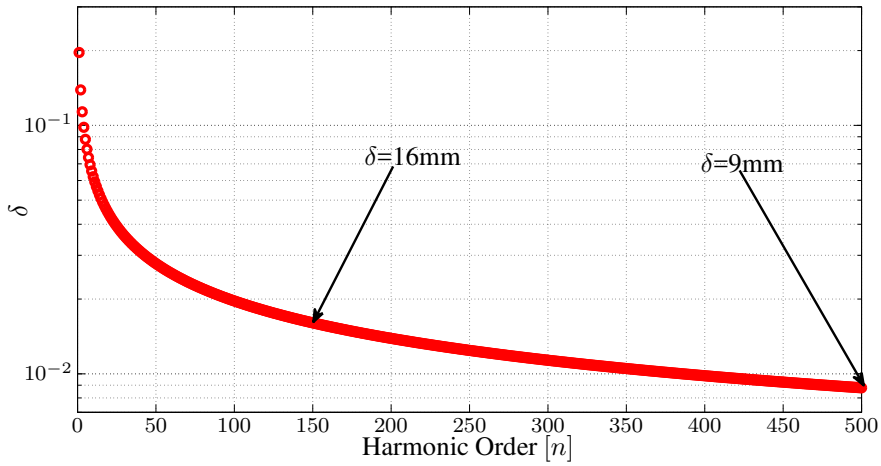

Figure 5.18: The skin depth in the PM with different frequencies.

than half of the PM width. Therefore, the skin depth will have minor effects on the results. As have been declared by the model with the reaction field effect, the reaction field has a minor effect with a sinusoidal operating condition as described in section 5.6.1.

While for PWM study, the maximum harmonic order is 500^{th} from the fundamental mechanical frequency as described by Fig. 5.16. The skin depth, shown in Fig. 5.18, is reduced to 9mm at 500^{th} from the fundamental frequency. This causes some effect in the PM losses as indicated in section 5.6.2.

5.6.4 PM Segmentation

In this part, PM segmentation is studied from the circuit and the FE models. The injected current will be the 5kHz case. No difference is observed between the circuit and the FE model for the distribution of power losses for one, two and four segments shown in Fig's 5.19, 5.20 and 5.21 respectively. The number of nodes is increased in these figures to prove the capability of the circuit model.

The average value of the power distribution is reduced. In addition, the total power losses caused by segmenting the magnets would be reduced as illustrated in Table 5.3.

It could be drawn from Table 5.3 that the total power is reduced as magnets are segmented. In addition, the effect of reaction field is reduced as the magnets are segmented too. Finally, the circuit model results are comparable with the FE results. All segments are simulated with a fixed number of nodes.

Table 5.3: Eddy power losses for PM in [W] with and without reaction field effect for the 5kHz case for different segmentations of the PMs.

	Without Reaction		With Reaction	
	FE. Model	Circuit Model	FE. Model	Circuit Model
One segment	43.8 W	45.8 W	33.2 W	33.4 W
Err. (%)	-	4.6 (%)	-	0.6 (%)
React. Field effect (%)				31.9 (%)
Two segments	21.7 W	21.3 W	17.7 W	17.9 W
Err. (%)	-	1.8 (%)	-	0.8 (%)
React. Field effect (%)				10.2 (%)
Four segments	13.4 W	13.5 W	12.84 W	13.3 W
Err. (%)	-	0.7 (%)	-	3.6 (%)
React. Field effect (%)				4.36 (%)

5.6.5 CPU Computation Time

The CPU time of the four models is compared. This is done on a core i7 processor, and 16 GB installed memory with 64 bit operating Windows 7 system.

Table 5.4 shows that the circuit model is very fast compared to the FE model. It is also observed that the circuit model with inductance takes more time than the model without reaction field. The 3D FE model takes less time than the 2D FE model because of the repetition of the 2D FE model for many slices (6 slices). The full transient 3D model takes about 5 days to obtain the solution. Therefore, less

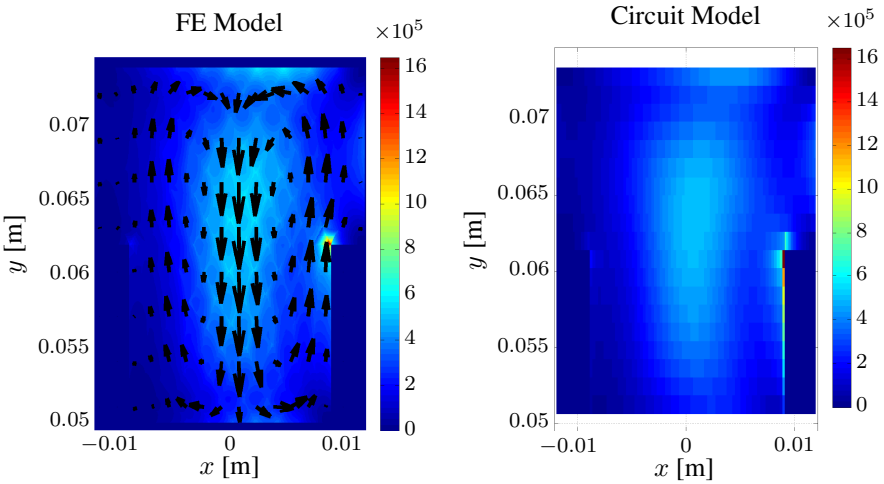

Figure 5.19: PM eddy power losses distribution $p_{\mathrm{pm_v}}$ [W/m^3] at a harmonic order of 30^{th} from the fundamental at rated loading conditions for one segment. (a) FE model. (b) Circuit model.

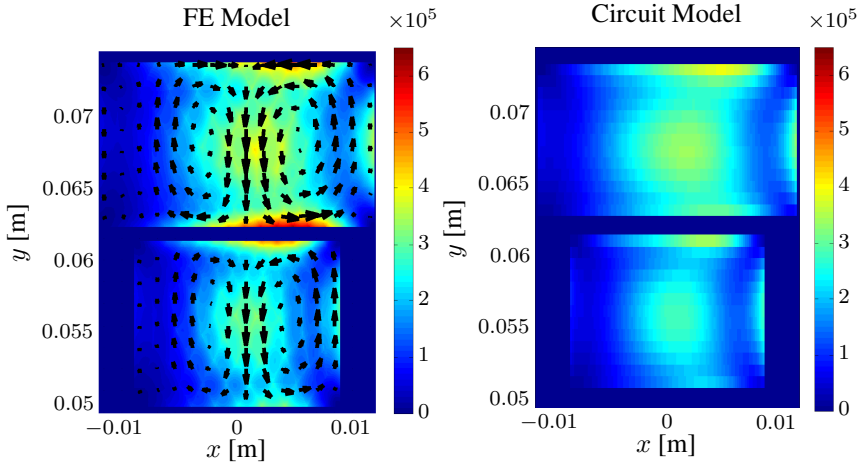

Figure 5.20: PM eddy power losses distribution $p_{\mathrm{pm_v}}$ [W/m^3] at a harmonic order of 30$^{\mathrm{th}}$ from the fundamental at rated loading conditions for two segments. (a) FE model. (b) Circuit model.

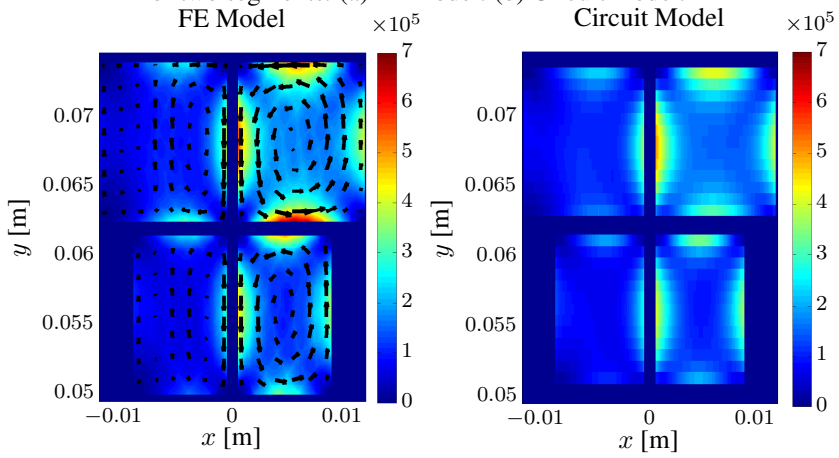

Figure 5.21: PM eddy power losses distribution $p_{\mathrm{pm_v}}$ [W/m^3] at a harmonic order of 30$^{\mathrm{th}}$ from the fundamental at rated loading conditions for four segments. (a) FE model. (b) Circuit model.

accurate models could be used for a primarily design instead of the full 3D model.

5.7 Conclusions

This chapter presents an electric circuit network that is capable to obtain the eddy currents in the permanent magnets (PMs) in the Axial Flux Permanent Magnet Synchronous Machines (AFPMSMs). This solution is based on a coupled solution

Table 5.4: CPU Time Comparison.

	Without Reaction		With Reaction		3D FE Model
	2D Multi-Slice FE Model sec. 5.4.1	Circuit Model sec. 5.2	3D FE Model sec. 5.4.2	Circuit Model sec. 5.2	sec. 5.5
Time (s)	70218 s	24 s	22842 s	110 s	518400 s

of Maxwell's equations and an electric circuit network. This is based on calculating the axial field in an accurate way on the surface of the PM and deep inside it. Afterwards, a Fourier series expansion is used to obtain the different frequency components of the magnetic field density. The eddy currents are then obtained by imposing the flux density distribution as a source term on the PM which is modeled by a simple electric network. The PM is divided into many slices in the axial direction. On each slice, the electric network is solved.

This network is composed of simple resistances and inductances. The inductances are used to model the reaction field effect of the eddy currents flowing through the PM. To show this effect, the machine is excited with different sources at different speeds. Also, a variant of the model is made that neglects the inductances, in order to show in which conditions this "low-frequency approximation" is acceptable. This method is able to take into account the effect of armature field and slots.

It is concluded from this chapter that inclusion of the reaction field is necessary when the machine is excited by a pulse width modulated (PWM) current, while for a sinusoidal excitation, the reaction field effect has minor contributions to the total eddy losses. In addition, the reaction field has a larger influence at higher speeds than at lower speeds for PWM injection. Also due to the spatial MMF distribution on the PM surface, one can't define a good resistance path for the eddy currents valid for all harmonic orders.

In conclusions, for a preliminary design, the circuit model with resistances only without the reaction field computation would be enough for the calculation of the PM losses. In this chapter, different PM segments are studied from the circuit model and FE model point of view.

Compared to the finite element (FE) models, the circuit model has the advantage of flexibility change in geometrical machine parameters, less CPU time, and accurate results for the PM losses up to 10%.

Chapter 6

An Electromagnetic Design Procedure for AFPMSMs

6.1 Introduction

In this chapter, a complete design toolbox is developed for AFPMSMs. A sensitivity analysis of the optimal parameters for the AFPMSMs working in the field weakening (FW) region is implemented.

Several authors have been developing different sizing equations that can be used for AFPMSM. A general sizing equation for AFPMSM was proposed in [97]. These equations could be used for a fast design procedure. These equations link the machine geometrical parameters to the required electromagnetic torque, depending on the magnetic material properties and the electric loading parameters.

In order to optimally design this machine for a wide speed range, fast models need to be utilized. Here, we use the efficient analytical models described in chapters 3, 4, and 5 [38, 44, 94]. These analytical models calculate the electromagnetic behavior, such as torque, iron losses, copper losses, and PM losses with a good agreement with the 3D finite element (FE) models. They are fully parameterized in terms of geometrical and electrical parameters.

The optimal design is obtained using the Pareto-front optimization technique [98] based on the results of the aforementioned analytical models. A comparison of different combinations of slots, poles and phases is done to determine the combination that achieves the optimal design. The results are verified by means of full 3D FE models.

6.2 Literature Review of Machines Working in the Field Weakening Region

AFPMSMs are widely used for electric vehicles application in many literatures [99, 100].

In practice, there are several types of machines working in the FW region [101]. Radial flux permanent magnet synchronous machines (RFPMSMs) are considered as one of the best candidates. Specifically, El-Refaie *et al.* in [101, 102] suggested an optimal flux weakening for the fractional slot winding surface RFPMSMs. In these articles, the authors proved that the surface PMSMs can operate in a wide speed range. The authors compared the fractional slot and distributed windings. The results showed the superiority of the fractional slot winding in terms of field weakening ability. On the other hand, the authors did not compare different combinations of fractional slot windings in terms of power density and inductance. Therefore, the objective of this study is to analyze the impact of different fractional slot winding configurations on the FW operation of the AFPMSM, focusing on the power density and the total inductance effects.

In addition, [103] has studied different winding schemes of concentrated and distributed windings, of three distinct machines of different q (number of slots per pole per phase), on the FW properties of surface PMSMs. A conclusion similar to El-Refaei that the concentrated winding has a better FW properties. Moreover, concentrated winding has a better thermal behaviour. In [104], loss assessment between distributed winding and concentrated winding was done. Due to the better FW band offered by the concentrated winding, the PM, rotor, and stator iron losses have increased. However, the copper losses have reduced due to the shorter end winding.

The use of AFPMSMs in the field weakening region is investigated in literature which is outlined briefly in this section.

In [105], a comparison between the performance of the interior AFPMSM and other types of machines was introduced. The results of that paper show the high power density of the interior AFPMSM compared to other machines. Due to the use of fractional slot concentrated windings in this type of machines, the eddy currents increase [104].

In [106], the authors showed that with less amount of PM material (therefore lower cost) in interior AFPMSM, the torque levels remained similar for surface AFPMSM. Since although the torque produced from the PM field is decreased, the reluctance torque increases. However, the surface mounted alternative has a better efficiency. Consequently, the surface AFPMSM is chosen for this study.

In [107], the authors designed a surface AFPMSM to achieve a CPSR of 3. The proposed design introduced additional C-shape double cores, which were made laminated to reduce the iron losses. However, the leakage inductance was appreciably increased as well as the size. More detailed mechanical enhancements for the AFPMSM to operate in the FW region was presented in [108].

6.3 AFPMSM Design Procedure

The machine design tool is shown in Fig. 6.1. It consists of five main parts:

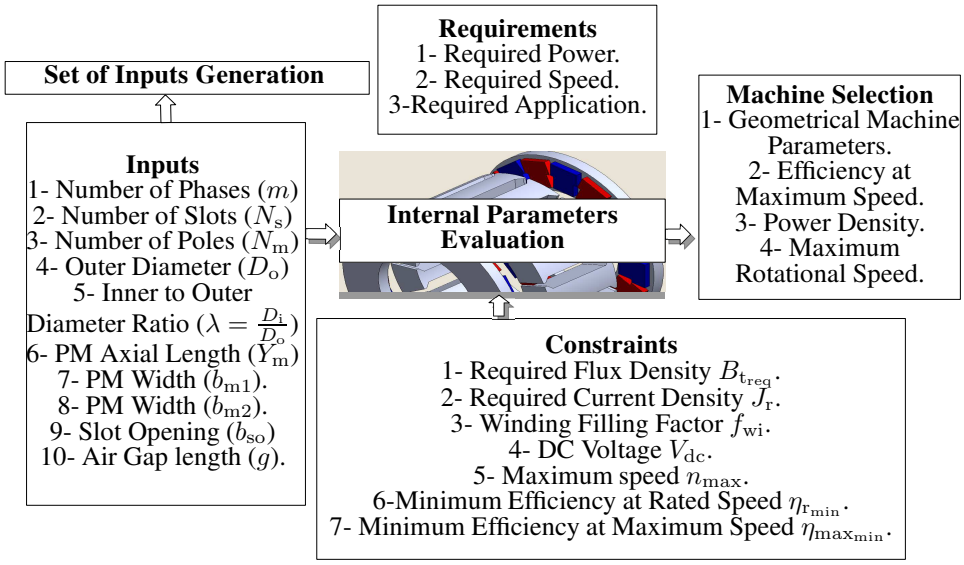

Figure 6.1: Design procedure for AFPMSM.

- **Requirements.** The required power and speed of the machine are the main objectives of the design. Moreover, the application plays an important role in the design phase. In this thesis, the AFPMSMs are designed to operate in the field weakening (FW) region.

  The important criterion while designing an electrical machine for the FW region is the constant power speed region (CPSR) shown in Fig. 6.2 [109]. As seen from Fig. 6.2, there are two modes of operations. Below the rated speed, the torque is kept at its rated value by injecting only a q-axis current (I_{q}) which equals the rated peak current (I_{peak}). This region is called the Maximum Torque Per Ampere (MTPA) region. Above the rated speed n_{rated} and till the maximum speed n_{max}, a field is produced by the armature currents to counter-act the field produced by the PMs. This field is obtained by a negative d-axis current ($-I_{\mathrm{d}}$) and an additional q-axis current to produce the torque. Therefore, this region is known as the FW region.

- **Set of Inputs Generation.** In this phase, the routine defines the following inputs: number of phases m, number of slots N_{s}, number of poles N_{m}, outer diameter D_{o}, inner to outer diameter ratio $\lambda = D_{\mathrm{i}}/D_{\mathrm{o}}$, PM axial length Y_{m},

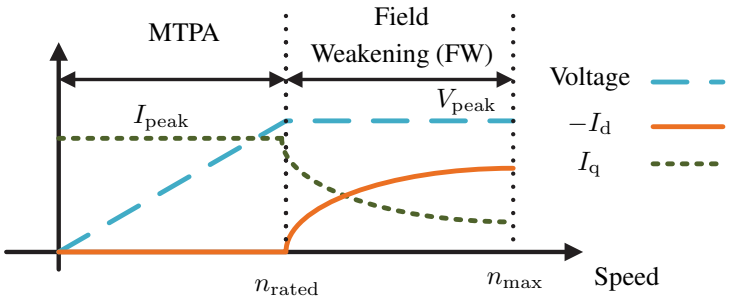

Figure 6.2: Operation modes for machines working in the field weakening region.

PM widths b_{m1} and b_{m2}, slot opening b_{so}, and air gap length g.[1] The PM consists of two rectangular stacks as shown in Fig. 5.1 (a) of widths b_{m1} and b_{m2}.

For different combinations of phases m, slots N_{s} and poles N_{m}. The algorithm generates many sets of inputs so that many different machines can be evaluated. For each set, each variables (λ, D_{o}, Y_{m}) have certain ranges (with minimum and maximum values) that are defined beforehand. Finally, there are some fixed inputs (g, b_{m1}, b_{m2}, b_{so}) that are chosen according to the geometry. One set of inputs represents one electrical machine.

The different variables in a set are chosen within the specified range, by Latin Hypercube sampling (LHS) [110].

- **Internal Parameters Evaluation.** For each set of inputs, the rest of the internal geometrical parameters are evaluated. These internal parameters are the number of turns N_{t}, the rated rms current I_{rated}, the slot width b_{s}, the axial length of the stator $Y_{\text{c1}}, Y_{\text{c2}}, Y_{\text{c3}}$, and the rotor Y_{r}.

- **Design Constraints.** The internal AFPMSM parameters are defined under certain constraints. These constraints are: the peak flux density of the considered material $B_{\text{t}_{\text{req}}}$, the maximum allowed current density J_{r}, the filling factor f_{wi}, the dc voltage limit V_{dc}, the maximum speed n_{max}, the minimum efficiency at rated speed $\eta_{r_{min}}$ and the minimum efficiency at maximum speed $\eta_{max_{min}}$.

- **Machine Selection.** The outputs are: the geometrical machine parameters, the efficiency at the maximum speed η_{max}, the power density P_{dens}, and

[1] These parameters are referred as to control design parameters in the rest of the chapter.

the total machine cost C_{tot}. The selection of the optimal machine is done manually by the user, as the desired trade-off between the power density and efficiency at the maximum speed.

The flow chart shown in Fig. 6.3, explains the design procedure for the AFPMSM. This design consists of three main routines.

- **Set of Inputs Generation.** The first routine determines the range of the inputs studied. These inputs are generated for different sets of machines. The generation of these sets is obtained by the Latin hypercube sampling (LHS) [110] to cover the entire studied region. More details can be found in section 6.3.1.
- **Internal Parameters Evaluation.** An internal design routine is used to obtain the rest of the internal parameters. This process is repeated for each set of machines. This procedure is done within predefined constraints. More details can be found in section 6.3.2.
- **Machine Selection.** Finally, to visualise the high number of computed set of machines in a clear way, a Pareto front is drawn between the efficiency at the maximum speed and the power density is generated for these sets. The selection of the optimum machine is done afterwards. Finally, all the output parameters are generated. More details can be found in section 6.3.3.

6.3.1 Set of Inputs Generation

In this study, various combinations of slots, poles, and phases are studied. The investigated number of phases is varied from 3 to 9 phases. The number of PMs are varied from 6 till 18 PMs. The number of the slots is chosen afterwards according to the following:

- The combinations are chosen according to the star of the slots for the double layer fractional slot concentrated winding [111].
- The combinations are chosen to avoid the unbalanced magnetic pull force [111].
- The combinations are chosen with a winding factor greater than 0.9. The winding factor for a specific winding expresses the ratio of flux linked by that winding compared to flux that would have been linked by a single-layer full-pitch non-skewed integer-slot winding with the same number of turns and one single slot per pole per phase. The torque of an electric motor is proportional to the fundamental winding factor [111].

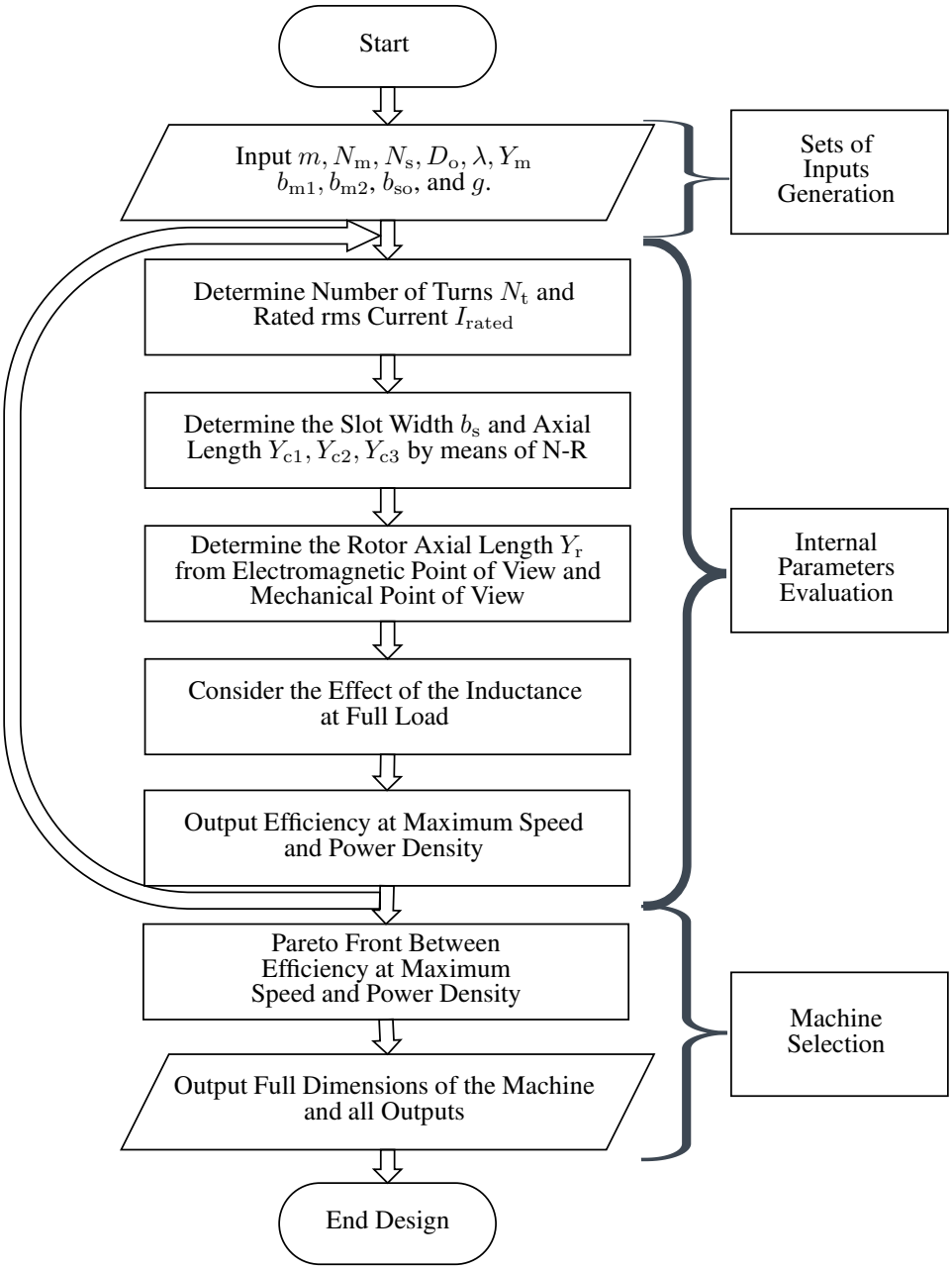

Figure 6.3: Flow chart of the complete design procedure of the AFPMSM.

This results in the combinations shown in Table 6.1. Table 6.1 shows the winding factor for each studied combination. Each column represents a certain phase number. For the same phase number, the number of PM values increases from top

to bottom in the table.

For each cell (a Slot/Pole/Phase combination) in Table 6.1, n sets of the control design parameters ($D_{\mathrm{o}}, \lambda, Y_{\mathrm{m}}, b_{\mathrm{m1}}, b_{\mathrm{m2}}, b_{\mathrm{so}}, g$), shown in Table 6.2, are generated to cover the entire permissible range of these parameters. Some of these parameters are fixed and some are variables. Here, $n = 100$. The range of the control design parameters is shown in Table 6.2.

Table 6.1: The studied combinations and their winding factors.

N_{m} inc.

	m						
	3	4	5	6	7	8	9
N_s/N_m	12/10	8/6	10/8	12/10	14/10	16/14	18/14
K_{w}	0.933	0.924	0.951	0.966	0.901	0.981	0.940
N_s/N_m	12/14	8/10	10/12	12/14	14/12	16/18	18/16
K_{w}	0.933	0.924	0.951	0.966	0.975	0.981	0.985
N_s/N_m	18/14	16/12	20/16		14/16		
K_{w}	0.902	0.924	0.951		0.975		
N_s/N_m	18/16	16/14	20/18		14/18		
K_{w}	0.945	0.962	0.976		0.901		
N_s/N_m		16/18					
K_{w}		0.962					
N_s/N_m		24/18					
K_{w}		0.924					

The PM consists of two blocks as shown in Fig. 5.1 (a). Each block has a fixed width of b_{m1} and b_{m2}. The width of each block is kept fixed at 95% of the pole pitch at minimum and average radius respectively. The air gap length g is fixed at 1mm. The slot opening b_{so} is kept as low as possible at 0.2 from the tooth pitch at the minimum radius $\tau_{\mathrm{s_{min}}}$. This was proven to be more efficient in the study for the FW [112].

The varying parameters, shown in Figs. 6.1 and 6.3, are the inner to outer diameter ratio $\lambda = \frac{D_{\mathrm{i}}}{D_{\mathrm{o}}}$, the PM axial length Y_{m}, and the outer diameter D_{o}. The outer diameter is a function of an initial outer diameter. This initial value is determined as follows;

$$D_{\mathrm{o_i}} = \left(\frac{T_{\mathrm{r}}}{\frac{2\pi}{8} K_{\mathrm{w}} K_{\mathrm{i}} K_{\mathrm{p}} B_{\mathrm{g}} A_{\mathrm{c}} (1-\lambda^2) \frac{1+\lambda}{2}} \right)^{1/3}, \tag{6.1}$$

where T_{r} is the required torque of the machine.

- K_{w} is the Electromotive Force (EMF) factor which, is the same as the winding factor.

Table 6.2: Range of control design parameters.

Type	Parameters	Symbol	Range
Variable	Outer diameter	D_{o}	(0.85-1.15)$D_{\mathrm{o_i}}$
	Inner to outer diameter ratio	$\lambda = \frac{D_{\mathrm{i}}}{D_{\mathrm{o}}}$	0.65-0.8
	PM axial length	Y_{m}	3mm-6mm
Fixed	PM width 1	b_{m1}	$0.95\tau_{\mathrm{m_{min}}}$
	PM width 2	b_{m2}	$0.95\tau_{\mathrm{m_{av}}}$
	Slot opening	b_{so}	$0.2\tau_{\mathrm{s_{min}}}$
	Air gap length	g	1mm

- K_{i} is the current waveform factor which, equals $\sqrt{2}$ for the sinusoidal supply.
- K_{p} is the electrical power waveform factor. Which, equals $\frac{1}{2}\cos\phi$, where $\cos\phi$ corresponds to the required power factor.
- B_{g} is the average air gap flux density. This value depends on the axial length of the permanent magnet and the air gap length. An average value of 0.8T is assumed.
- A_{c} is the electrical loading which depends on the cooling type [22]. A reasonable value for the natural air cooling is 30 kA/m and for a powerful forced coolant is 70 kA/m.
- $\lambda = D_{\mathrm{i}}/D_{\mathrm{o}}$ is the ratio of the inner to outer diameters.

6.3.2 Internal Parameters Evaluation

There are still some internal parameters that need to be evaluated for every set of machines, *i.e.* for every set of input variables. These parameters are the number of turns N_{t}, the rated current I_{rated}, the slot width b_{s}, the axial length of the stator $Y_{\mathrm{c1}}, Y_{\mathrm{c2}}, Y_{\mathrm{c3}}$, and the rotor Y_{r}.

To obtain these parameters, some design constraints exist in Table 6.3. The main constraints are summarized in the following points.

- **Required Flux Density.** The peak flux density required $B_{\mathrm{t_{req}}}$ is determined by the magnetic material properties. The chosen material is METGLAS 2605 alloy due to its advantages regarding thermal issues and lower losses [113, 114]. The fitted parameter values are $H_{\mathrm{o}} = 4.07$ A/m, $B_{\mathrm{o}} = 1.402$ T, and $\nu = 39.71$. The non-linear permeability μ_{r} with respect to the magnetic flux density of the measured $\mu_{\mathrm{r}} - B$ characteristics at 200Hz and equation (4.2) are shown in Fig. 6.4. Therefore, the The peak flux density is chosen to be 1.35T.

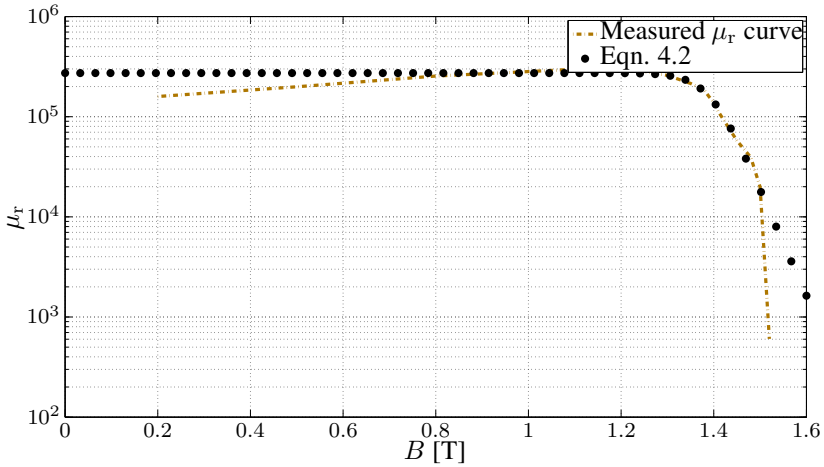

Figure 6.4: μ_r-B curve of the used stator material (METGLAS 2605) in the studied models [114].

- **Required Current Density.** The maximum allowed current density is determined according to the cooling type. The used value in this chapter requires a forced cooling technique as stated in [22]. For higher current density limits, the machine requires more powerful cooling.

- **The DC Voltage Limit.** The rated peak output voltage from the inverter V_{peak} is determined by the DC voltage value and the used modulation technique. The peak phase voltage for any number of phase m and a DC voltage V_{dc} with the space vector modulation technique is determined by [115]:

$$V_{\text{peak}} = m_i V_{\text{dc}}, \tag{6.2}$$

  where m_{i} is the modulation index:

$$m_{\text{i}} = \frac{1}{2\cos(\pi/(2m))}. \tag{6.3}$$

  This value is used in the design procedure to keep the machine's terminal voltage at its rated value depending on the number of phases.

- **The Maximum Speed** $n_{\max}$ is determined according to the modes of the design described in details in the appendices B and C.

  With respect to the maximum speed of the machine, two design modes are defined; the finite and the 'theoretical' infinite speed design. In [112], the authors demonstrated the difference between finite and theoretical infinite speed design of the AFPMSM.

Table 6.3: Constraints of the design.

Constraints	Symbol	Value
Required Flux Density	$B_{\mathrm{t_{req}}}$	1.35T
Required Current Density	J_{r}	5 A/mm^2
Winding Filling Factor	f_{wi}	0.5
DC Voltage Limit	V_{dc}	600V
Maximum Speed/Rated Speed	$n_{\mathrm{max}}/n_{\mathrm{rated}}$	5
Minimum efficiency at rated speed	$\eta_{\mathrm{r_{min}}}$	95%
Minimum efficiency at maximum speed	$\eta_{\mathrm{max_{min}}}$	90%

For a finite speed design, the machine is selected, if it can operate till a certain maximum speed defined by (6.4):

$$n_{\mathrm{max}} = 60\frac{V_{\mathrm{peak}}}{2\pi L_{\mathrm{s}} p(\frac{\psi_{\mathrm{pm}}}{L_{\mathrm{s}}} - I_{\mathrm{peak}})}, \tag{6.4}$$

where L_{s} is the machine inductance. The machine inductance L_{s} equals the d and q axis inductances L_{d} and L_{q} for surface AFPMSM. ψ_{pm} is the PM flux linkage.

For an infinite speed design, the machine can operate from the electromagnetic point of view till theoretically infinite speed. This means that the inductance of the machine becomes very large so that a small d-axis current can weaken the flux. This enhances the efficiency at the maximum speed.

With the predefined constraints described in Table 6.3, the procedure for the internal design to determine the rest of the machine parameters described below:

1. **The Number of Turns and Rated Current** N_{t} is determined according to the rated required peak phase voltage described in (B.1). The rated rms current I_{rated} is then determined according to the rated power of the machine P_{rated} [26].

$$N_{\mathrm{t}} = \frac{V_{\mathrm{peak}}}{K_{\mathrm{e}} N_{\mathrm{s}} B_{\mathrm{g}} \frac{f_{\mathrm{e}}}{p}(1-\lambda^2) D_{\mathrm{o}}^2}, \tag{6.5}$$

$$I_{\mathrm{rated}} = \frac{P_{\mathrm{rated}}}{m V_{\mathrm{peak}}/\sqrt{2}}. \tag{6.6}$$

After the initial design of these values, the number of turns and current are fine tuned by means of the combined solution of Maxwell's equations and the magnetic equivalent circuit (SC-MEC) described in chapter 4.

2. **The slot width b_{s} and axial length** Y_{c1}, shown in Fig. 4.8, are designed in such a way to keep the required flux density in the tooth $B_{t_{req}}$ at the required limit specified in Table 6.3. These limits depend on the application and material choice [116]. In this work, the flux density is set to 1.35 T as described in Table 6.3.

   While changing the slot width, the tooth axial length $2Y_{\mathrm{c1}}$ is changed to keep the current density within its predefined limit, i.e. J_{r} = 5 A/mm^2. Once the slot width is changed, the peak flux density varies.

   Therefore, an iterative algorithm, using e.g. the Newton-Raphson (N-R) technique, needs to be implemented to keep both the flux and current densities within the limits. This part is done at the rated speed and loading conditions. The SC-MEC model is used to find out the peak flux density inside the tooth.

   In the iterative procedure, the axial length is:

$$Y_{\mathrm{c1_n}} = Y_{\mathrm{c1_o}} \frac{J_{\mathrm{o}}}{J_{\mathrm{r}}}, \tag{6.7}$$

   where $Y_{\mathrm{c1_n}}$ and $Y_{\mathrm{c1_o}}$ are the new and old axial lengths, respectively. J_{o} is the old current density.

   The tooth-tips length Y_{c2} and Y_{c3} are calculated as follows [26]:

$$\begin{aligned} Y_{\mathrm{c2}} &= \frac{2}{3} \frac{B_{\mathrm{g}} b_{\mathrm{s}}}{B_{\mathrm{tip_{req}}}}, \\ Y_{\mathrm{c3}} &= \frac{1}{3} \frac{B_{\mathrm{g}} b_{\mathrm{s}}}{B_{\mathrm{tip_{req}}}}, \end{aligned} \tag{6.8}$$

   where B_{g} is the average air gap flux calculated from Maxwell's equations, and $B_{\mathrm{tip_{req}}}$ is the required flux density in tooth tips which equals 1.9T.

   The current density of the machine is calculated as:

$$J_{\mathrm{r}} = \frac{N_{\mathrm{t}} I_{\mathrm{rated}}}{\frac{b_{\mathrm{s}}}{2} f_{\mathrm{wi}} (2Y_{\mathrm{c1}})}, \tag{6.9}$$

   where Y_{c1} is half of the slot axial length of the copper area, f_{wi} is the winding filling factor. In this case f_{wi} is assumed to be 0.5 and is shown in Table 6.3.

3. **The rotor axial length** Y_{r} is an important design aspect from electromagnetic and mechanical points of view.

   Authors in [26, 117] developed mechanical analytical models for the YASA machine for a proper structural analysis of the rotor and stator for large scale applications. In addition, the authors in [118] developed mechanical FE models for a coreless AFPMSM in high speed application.

   - From the electromagnetic point of view, the rotor axial length Y_{r} equals [26]:
   $$Y_{\mathrm{r1}} = \frac{\pi D_{\mathrm{o}}}{4p} \frac{1+\lambda}{2} \frac{B_{\mathrm{g}}}{B_{\mathrm{t_r}}}, \tag{6.10}$$
   where $B_{\mathrm{t_r}}$ is the required flux density in the rotor side which equals 1.7 T, and B_{g} is the air gap flux density over one pole pitch.
   - From the mechanical point of view, the length of the rotor should be chosen to retain the maximum allowable deflection under the applied axial force. This axial force at the full load is deduced as follows:
   $$F_{\mathrm{a}} = \frac{1}{2\mu_{\mathrm{o}}} \sum_{i=1,2,..}^{n} \int_{0}^{2\pi R_{\mathrm{av}}^{i}} {B_{\mathrm{y}}}^2 t_{\mathrm{cp}} \mathrm{d}x \ , \tag{6.11}$$
   where B_{y} is the axial air gap flux density at the center of the air gap area calculated by Maxwell's equations described in section 3.4.2. t_{cp} is the radial length of each slice. A numerical integration is done over the radial length of the machine.
     - The maximum deflection y_{a} that can occur of the rotor shown in Fig. 6.5 in this section is set to be 10 $\%$ of the air gap thickness g, which is 1mm. This is illustrated in more details in [26]. The shaft is placed on 20 $\%$ of the outer radius, i.e. $b = 0.2\ R_{\mathrm{o}}$.
     The minimum rotor thickness during the design is:
     $$Y_{\mathrm{r2}} = \Big(\frac{12a^2(1-v^2)}{Ey^2} (M_{\mathrm{rb}} C_2 + Q_{\mathrm{b}} a C_3 - q a^2 L_{11}) \Big)^{1/3}, \tag{6.12}$$
     where v and E are the poisson ratio and the modulus of elasticity, respectively. Their values for the electrical steel are typically 0.3 and $2.1 \times 10^{11}\ N/m^2$, respectively. a is the outer radius. $M_{\mathrm{rb}}, C_2, Q_b, C_3, q, L_{11}$ are variables and can be found in [26, 117].
     - Considering also the dynamic stability of the machine during rotation, and due to the harmonics existing in the flux density waveform, an undesired vibration may arise in the rotor [22]. The natural frequency f_d has to be much higher than the frequency of the

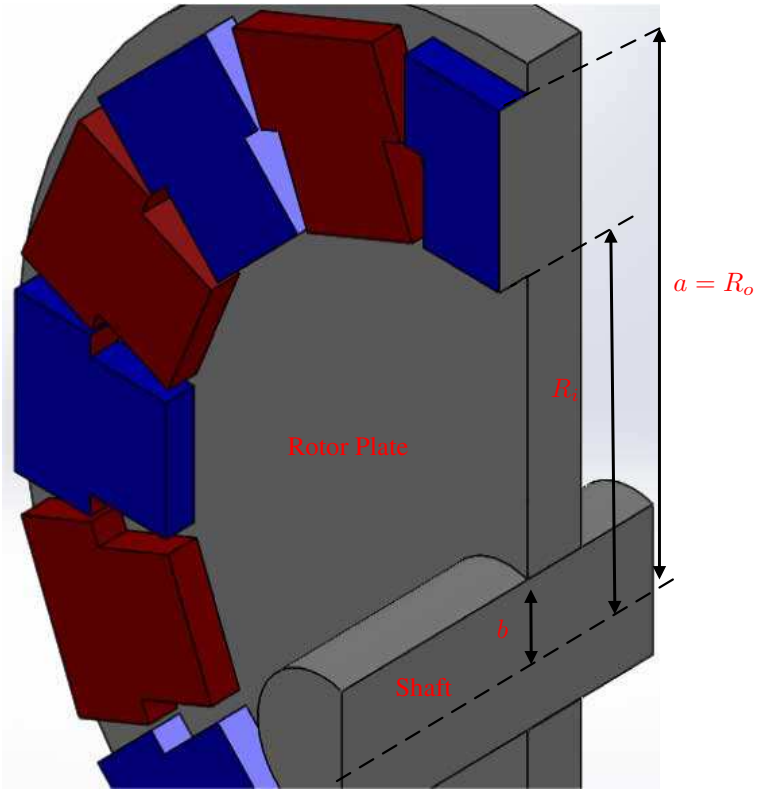

Figure 6.5: Structural analysis of AFPMSM rotor adapted from [117].

supply at the maximum required speed. In this case, an analytical formula is used to provide the minimum rotor thickness assuming a natural frequency equal to the frequency corresponding to the maximum speed [22]:

$$Y_{\mathrm{r3}} = \frac{2\pi f_{\mathrm{d}} R_{\mathrm{o}}^2}{K_{\mathrm{n}} \sqrt{E/\rho_{\mathrm{fe}}} / \sqrt{12(1-\nu^2)}}, \tag{6.13}$$

where ρ_{fe} is the mass density of the iron.

- The structural mass of the rotor is chosen to equal the maximum value of Y_{r1}, Y_{r2}, and Y_{r3}.

4. **The effect of inductance at full load** should be included. Usually, a high value of the machine inductance is needed for the operation in the FW region.

   The full load voltage is adjusted by varying the number of turns to keep the output voltage of the machine at rated loading conditions at the peak inverter voltage V_{peak} described in (6.2) and (6.3).

At rated operating condition, only q axis current is injected. Assuming the lossless equations described in Appendix B, the new value of number of turns $N_{\mathrm{t_n}}$ can be obtained as follows:

$$N_{\mathrm{t_n}} = \sqrt{\frac{(V_{\mathrm{peak}} N_{\mathrm{t_o}})^2}{(2\pi f L_{\mathrm{so}} I_{\mathrm{o}})^2 + E_{\mathrm{o}}^2}}, \tag{6.14}$$

where $N_{\mathrm{t_o}}$ is the old number of turns in (6.5), L_{so} is the machine synchronous inductance, I_{o} is the old rated current and E_{o} is the old peak no load voltage.

5. **Output Efficiency at Maximum Speed and Power Density.** For each set of input parameters, the efficiency at the maximum speed and the power density are generated. The details about the calculations of these parameters are found in section 6.3.3.

6.3.3 Machine Selection

Based on the designed machines, the Pareto front can be easily visualized to select the optimal machine topology among the n generated ones, see Fig. 6.6. Fig. 6.6 shows the 3-phase/14-poles/12-slots combination results. It demonstrates the options between finite and theoretical infinite speed designs. The Pareto front shows that there is only one particular theoretical infinite solution which is described by the red dot.

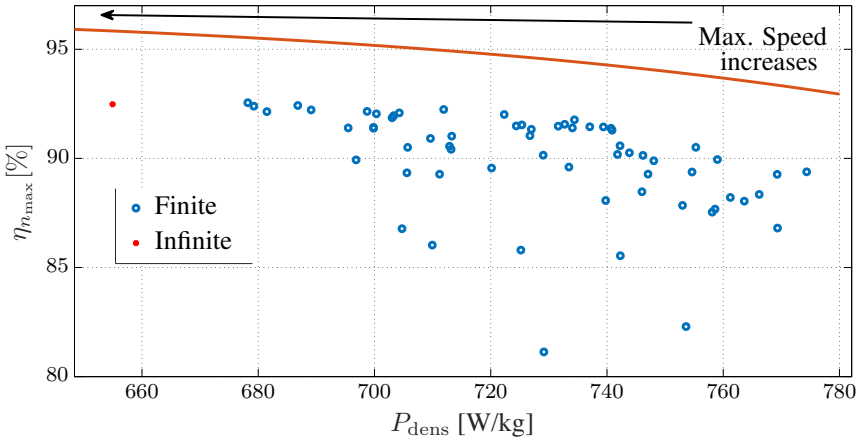

Figure 6.6: An example of Pareto front results to maximize the efficiency at the maximum speed and the power density.

After choosing the optimum solution from the set of the designed control input parameters, the machine is selected afterwards. The geometrical machine parameters are outputted afterwards. The list of these outputs are generated.

1. **The losses** (Copper, PM eddy losses, and stator iron losses).

   The copper losses are calculated including the end windings. There are two different end winding lengths at the inner and outer diameter as shown in Fig. 6.7 (b). The minimum and maximum length of the end winding at the inner and outer diameters equal:

$$\begin{aligned} l_{\mathrm{e_{min}}} &= L_{\mathrm{t_i}} + L_{\mathrm{t_o}}, \\ l_{\mathrm{e_{max}}} &= \frac{\pi}{2}(\tau_{\max} + \tau_{\min}), \\ l_{\mathrm{e}} &= \frac{l_{\mathrm{e_{max}}} + l_{\mathrm{e_{min}}}}{2}, \end{aligned} \tag{6.15}$$

   where $\tau_{\max}$ and $\tau_{\min}$ are the slot pitch at the outer and inner diameter, respectively. The maximum end winding length is calculated based on assuming a half circular winding. The total end winding is the average between both end windings. The total length and the area of one turn are calculated as:

$$\begin{aligned} l_{\mathrm{tot}} &= 2(R_{\mathrm{o}} - R_{\mathrm{i}}) + l_{\mathrm{e}}, \\ A_{\mathrm{t}} &= \frac{b_{\mathrm{s}}}{2}\frac{2Y_{\mathrm{c1}}}{N_{\mathrm{t}}} f_{\mathrm{wi}}. \end{aligned} \tag{6.16}$$

   The total resistance and copper losses are:

$$\begin{aligned} R_{\mathrm{s}} &= \frac{N_{\mathrm{s}}}{m}\frac{l_{\mathrm{tot}} N_{\mathrm{t}}}{\sigma_{\mathrm{e}} A_{\mathrm{t}}}, \\ P_{\mathrm{wi}} &= m I^2 R_{\mathrm{s}}, \end{aligned} \tag{6.17}$$

   where σ_{e} is the electric resistivity of copper.

   The PM and iron loss models, described in chapters 5 and 4 respectively, can accurately predict the loss values.

2. **The inductances** L_{d} and L_{q}.

   The inductances, as well as the voltage waveform, are calculated based on the SC-MEC model described in chapter 4, which takes into account the effect of magnetizing and leakage inductances.

3. **The maximum reachable speed** $n_{\max}$ can be obtained based on (6.4).

4. **The power density** P_{dens} of the machine based on the machine mass.

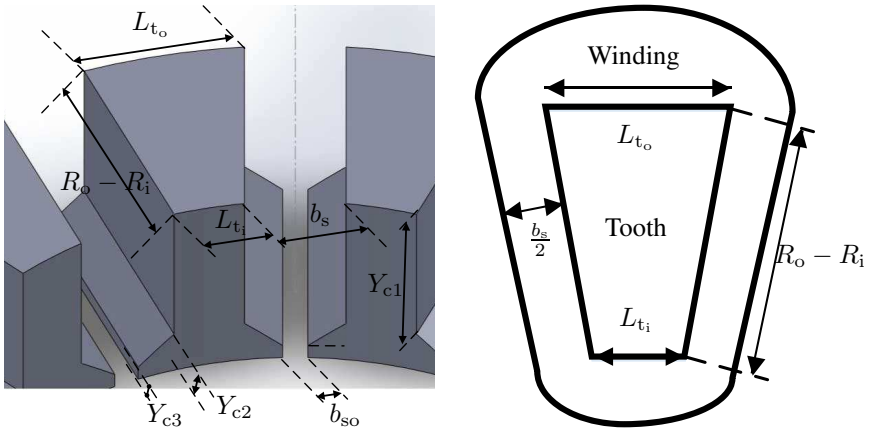

(a) 3D Model (b) 2D Model

Figure 6.7: Tooth model of the AFPMSM.

- The stator core mass M_s equals:

$$\begin{aligned} M_{\mathrm{s}} = \rho_{\mathrm{fe}} N_s \Bigg[& \frac{L_{\mathrm{t_i}} + L_{\mathrm{t_o}}}{2} (R_{\mathrm{o}} - R_{\mathrm{i}}) 2Y_{\mathrm{c1}} \\ & + \left(\frac{\pi(R_{\mathrm{o}} + R_{\mathrm{i}})}{N_{\mathrm{s}}} - b_{\mathrm{so}} \right) (R_{\mathrm{o}} - R_{\mathrm{i}}) 2Y_{\mathrm{c3}} \\ & + \left(\frac{\pi(R_{\mathrm{o}} + R_{\mathrm{i}})}{N_s} - \frac{b_{\mathrm{s}} - b_{\mathrm{so}}}{2} \right) (R_{\mathrm{o}} - R_{\mathrm{i}}) 2Y_{\mathrm{c2}} \Bigg]. \end{aligned} \tag{6.18}$$

- The rotor core mass M_r equals:

$$M_{\mathrm{r}} = \rho_{\mathrm{fe}} 2Y_{\mathrm{r1}} \frac{\pi D_{\mathrm{o}}^2}{4} (1 - \lambda^2). \tag{6.19}$$

- The PM mass equals:

$$\begin{aligned} M_{\mathrm{pm}} = 2\rho_{\mathrm{pm}} N_{\mathrm{m}} Y_{\mathrm{m}} \Big(& b_{\mathrm{m1}} \frac{(R_{\mathrm{o}} - R_{\mathrm{i}})}{2} + \\ & b_{\mathrm{m2}} \frac{(R_{\mathrm{o}} - R_{\mathrm{i}})}{2} \Big), \end{aligned} \tag{6.20}$$

  where ρ_{pm} is the mass density of PM.
- The winding mass equals:

$$M_{\mathrm{wi}} = \rho_{\mathrm{cu}} N_{\mathrm{s}} (l_{\mathrm{tot}} A_{\mathrm{t}} N_{\mathrm{t}}), \tag{6.21}$$

  where ρ_{co} is the mass density of copper.

- The structural mass M_{struct} depends on the selection of the axial rotor thickness for the three rotor thicknesses described in (6.10),(6.12), and (6.13):

$$M_{\mathrm{struct}} = 2\max(Y_{\mathrm{r1}}, Y_{\mathrm{r2}}, Y_{\mathrm{r3}})\pi(\frac{{D_{\mathrm{o}}}^2}{4} - b^2)\rho_{\mathrm{fe}} - M_{\mathrm{r}}. \qquad (6.22)$$

- The total mass M_{tot} at the end is the summation of the four mass values M_{s}, M_{r}, M_{struct} M_{pm}, and M_{wi}. This corresponds to a power density of $P_{\mathrm{den}} = P_r/M_{\mathrm{tot}}$.

5. **The cost of the machine.** The cost is predicted by the following equation knowing the mass of each part of the machine [119]:

$$C_{\mathrm{tot}} = C_{iron}(M_{\mathrm{s}} + M_{\mathrm{r}} + M_{\mathrm{struct}}) + C_{\mathrm{pm}}M_{\mathrm{pm}} + C_{\mathrm{co}}M_{\mathrm{wi}}, \qquad (6.23)$$

where C_{iron} is the cost per kilogram of iron. C_{pm} is the cost per kilogram of PM. C_{co} is the cost per kilogram of copper. In this thesis, we use C_{iron}, C_{pm}, C_{co} as 3, 40, and 15 €/kg, respectively.

In conclusions, the flow chart shown in Fig. 6.3 summarizes the complete design procedure.

6.4 Analytical Model Results and Discussions

In the following part, the results are subdivided into three main sections.

- Different slots, poles, phases combinations effects on the stator mass, different masses of the machine, the power density and inductance are studied in section 6.4.1.
- The design routine is applied afterwards to set up the complete design of the machine under two options of design. The finite speed design is studied in section 6.4.2. Then, infinite speed design is investigated in section 6.4.3. The difference between the two modes is discussed in section 6.4.4. The differences between two modes of design are discussed in appendix C. In summary, the machine is selected for finite speed design, when the maximum speed has a finite value. For an infinite speed, the machine is selected as it can operate till theoretically infinite speed.
- The influence of outer diameter and inner to outer diameter ratio is studied in section 6.4.5.

6.4.1 The Effect of Different Slots, Poles, Phases Combinations on Power Density and the Inductance

The Effect on Stator Mass

The torque to q-current ratio equals: [120]

$$T_{i_{\mathrm{q}}} = (m/2)p\psi_{\mathrm{pm}}. \tag{6.24}$$

To clearly identify the relation between the number of slots and poles on the stator mass, we consider two combinations with the same slot numbers like the three phase combination of 10poles-12slots and 14poles-12slots. Their winding functions are shown in Fig. 6.8.

The flux density is assumed sinusoidal with a peak value of $B_{\max}$.

1. **10-12 Combinations:** The flux density equals $B = B_{\max}\sin(5(\theta_{\mathrm{m}} + \theta_{\mathrm{s}}))$, where θ_{m} is the circumferential mechanical angle in radians, and θ_s is the shift of PM in radians.

   The flux linkage of phase (a) equals:

   $$\phi_{\mathrm{a}_1} = r_{\mathrm{g}} l_{\mathrm{eff}} \int_0^{2\pi} N_{\mathrm{a}}(\theta_{\mathrm{m}}) B(\theta_{\mathrm{m}}) \mathrm{d}\theta_{\mathrm{m}}. \tag{6.25}$$

   where r_{g} is the air gap radius, l_{eff} is the active length of the machine, N_{a} is the phase a winding function shown in Fig. 6.8. Assuming that both r_{g}, and l_{eff} equal one, the peak value of the flux linkage occurs at $\theta_{\mathrm{s}} = 0$ rad. The peak value ψ_{pm_1} of the flux linkage ϕ_{a_1}, the torque to q-axis current ratio $T_{\mathrm{i}_{\mathrm{q}_1}}$, and the peak flux per tooth $\phi_{\mathrm{t}_{\mathrm{p}_1}}$ equal respectively:

   $$\begin{aligned} \psi_{\mathrm{pm}_1} &= 1.49 B_{\max}, \\ T_{\mathrm{i}_{\mathrm{q}_1}} &= 11.2 B_{\max}, \\ \phi_{\mathrm{t}_{\mathrm{p}_1}} &= 0.39 B_{\max}. \end{aligned} \tag{6.26}$$

2. **14-12 Combination:** The flux density equals $B = B_{\max}\sin(7(\theta_{\mathrm{m}} + \theta_{\mathrm{s}}))$. The peak value of the flux linkage occurs at $\theta_{\mathrm{s}} = 0$ rad. The peak value of ϕ_{a_2}, the torque to q-axis current ratio, and the peak flux per tooth equal respectively:

   $$\begin{aligned} \psi_{\mathrm{pm}_2} &= 1.07 B_{\max}, \\ T_{i_{\mathrm{q}_2}} &= 11.2 B_{\max}, \\ \phi_{\mathrm{t}_{\mathrm{p}_2}} &= 0.28 B_{\max}. \end{aligned} \tag{6.27}$$

In conclusions from (6.26) and (6.27), it is clear that the torque to current ratio is the same for the two combinations. However, the peak flux per tooth is:

$$\phi_{\mathrm{t_{p_1}}} = 1.4\phi_{\mathrm{t_{p_2}}}, \tag{6.28}$$

In this case, the 14-12 combination gives 40% reduction in the total flux density on one tooth compared to the 10-12 combination. Therefore, during the design phase, the tooth can be thinner for the 14-12 combination. This allows more copper without any increase in the flux density. This is analogous with the $N_\mathrm{s}/N_\mathrm{m}$ value. As $N_\mathrm{s}/N_\mathrm{m}$ is lower, the flux density inside one tooth becomes less than a combination with high $N_\mathrm{s}/N_\mathrm{m}$.

Similar results are obtained for the seven phase system. The chosen combinations have the same N_s value. Table 6.4 shows that the tooth flux density increases as the $N_\mathrm{s}/N_\mathrm{m}$ increases. The small degradation in the torque to current ratio for $N_\mathrm{m} > (N_\mathrm{s} \pm 2)$ is due to the lower winding factor.

Table 6.4: Seven phase effect on torque to q current ratio and peak flux inside the tooth.

$N_\mathrm{s}/N_\mathrm{m}$ inc. ⇓

N_s	N_m	$N_\mathrm{s}/N_\mathrm{m}$	$T_{\mathrm{i_q}}$	$\phi_{\mathrm{t_p}}$
14	18	0.78	$12.6B_{\max}$	$0.2B_{\max}$
14	16	0.875	$13.64B_{\max}$	$0.24B_{\max}$
14	12	1.17	$13.64B_{\max}$	$0.32B_{\max}$
14	10	1.4	$12.6B_{\max}$	$0.36B_{\max}$

In conclusions from the above discussions, it is better to choose combinations with $N_\mathrm{s}/N_\mathrm{m} < 1$ in order to obtain low stator core mass.

However, other important aspects need to be considered such as the copper, rotor and rotor masses.

The Effect of Different Slots/Poles/Phases Combinations on Different Masses of the Machine

An analytical study is done to illustrate the effect of different combinations on the different mass components. The design is conducted for all combinations for the following constraints:

- Outer diameter of 0.18m.
- The inner to outer diameter ratio is fixed at 0.65.
- The air gap field is fixed at 0.8T.

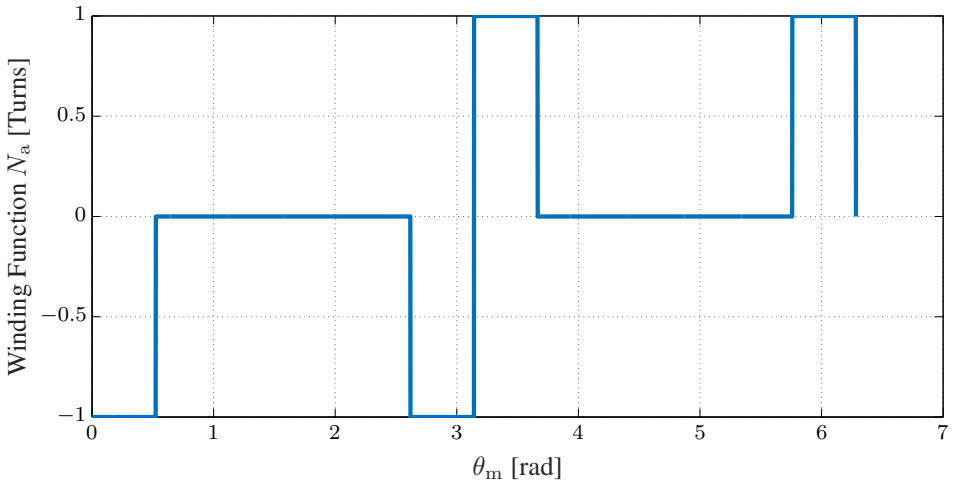

Figure 6.8: Winding function for the two different combinations of the 12slots/10poles and 12slots/14poles.

- Other constraints, shown in Table 6.3, are also valid.

The air gap field is kept constant by adjusting the PM axial length. The effect of different combinations on the different masses are illustrated below:

1. Table 6.5 shows the different studied combinations, their windings factor, and the N_s/N_m for each combination. It shows also the stator mass as an absolute number and as a percentage of the total mass of the machine (active and inactive mass). The percentage shows how important the stator mass with respect to the total mass is.

   It is clear from Table 6.5 and Fig. 6.9 that the stator mass increases as expected with the increase of the value of the N_s/N_m. Table 6.5 shows also the percentage of the stator iron core mass to the total active (rotor core, stator core, PM, and copper) and inactive mass (structural rotor mass).

2. The copper material has a general tendency of reduced copper mass with respect to the increase of number of stator slots. This is because of the reduced end winding when increasing the number of stator cores with the same copper filling factor. This is clearly shown in Fig. 6.10. The number of turns is variable to keep the voltage at full load at its rated volue.

3. The effect of different combinations on the rotor mass. The rotor mass is divided into electromagnetic and mechanical parts.

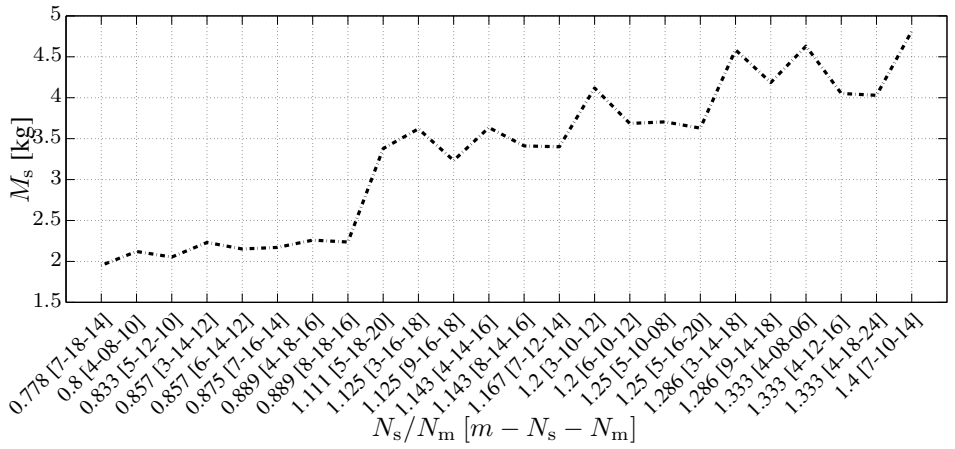

Figure 6.9: Effect of N_s/N_m on the stator core mass.

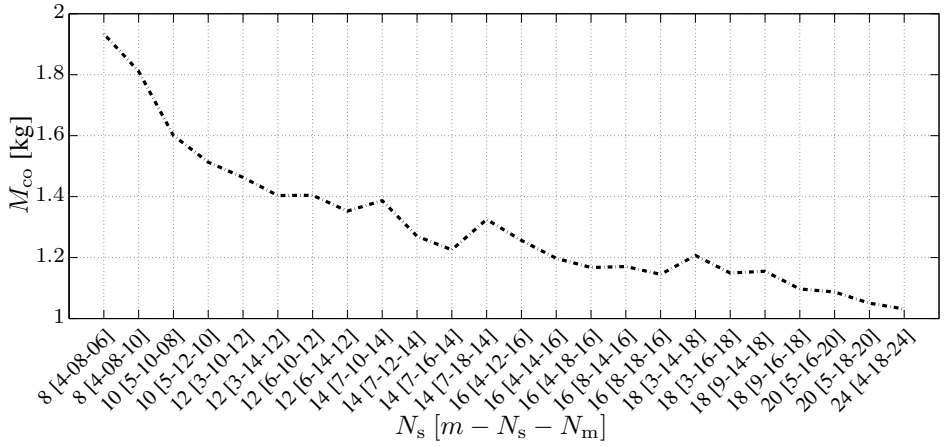

Figure 6.10: Effect of different combinations on the copper mass.

The rotor electromagnetic design is based on (6.10). It is clear that the rotor thickness Y_{r1} and mass M_r are inversely proportional to the number of pole pairs. Therefore, a general reduced tendency can be observed for the rotor mass with increased number of PMs. [22].

The rotor structural mass has a general tendency to increase with increasing the number of PMs. From (6.13), the required rotor thickness increases with the frequency as shown in Fig. 6.11. However, for low number of PMs, (6.10) becomes more dominant. Consequently, an increase of the rotor axial length is expected for a very low number of PMs.

It is clear that each mass has a general tendency against a certain parameter.

Table 6.5: The effect of $N_{\mathrm{s}}/N_{\mathrm{m}}$ ratio on the stator mass as an absolute number and as a function of the total mass.

$N_{\mathrm{s}}/N_{\mathrm{m}}$ inc.

m	N_s_N_m	N_s_N_m [frac]	K_w	M_s [kg]	M_s/M_{tot} %
7	14_18	0.777778	0.900969	1.951526	19.41297
4	8_10	0.8	0.92388	2.121354	25.67328
5	10_12	0.833333	0.951057	2.053662	24.89432
6	12_14	0.857143	0.965926	2.23155	24.75708
3	12_14	0.857143	0.933013	2.152099	24.22598
7	14_16	0.875	0.974928	2.171315	22.91472
8	16_18	0.888889	0.980785	2.260058	22.13259
4	16_18	0.888889	0.96194	2.237198	22.0062
5	20_18	1.111111	0.975528	3.379027	30.08891
9	18_16	1.125	0.984808	3.620481	33.32663
3	18_16	1.125	0.945214	3.233114	31.01637
8	16_14	1.142857	0.980785	3.635731	35.55281
4	16_14	1.142857	0.96194	3.411552	34.20066
7	14_12	1.166667	0.974928	3.400677	36.30427
6	12_10	1.2	0.965926	4.118438	41.45042
3	12_10	1.2	0.933013	3.685468	39.02903
5	10_8	1.25	0.951057	3.705046	35.04247
5	20_16	1.25	0.951057	3.628094	33.55169
9	18_14	1.285714	0.939693	4.585167	40.96879
3	18_14	1.285714	0.901912	4.185468	38.96954
4	8_6	1.333333	0.92388	4.630707	34.58425
4	24_18	1.333333	0.92388	4.052233	40.49544
4	16_12	1.333333	0.92388	4.02945	33.94525
7	14_10	1.4	0.900969	4.813046	45.53007

- The stator core mass has a general tendency with the number of slots per poles.
- The copper mass has a stronger relation with the number of slots.
- The rotor mass has a stronger tendency with the number of PMs.

Therefore, a complete electromagnetic design is executed for different combinations of phases/slots/poles to have complete guidelines for the designers for the AFPMSMs.

The Effect on FW Properties

From the field weakening point of view, it is important to have a large inductance to increase the field weakening capability. Inductances are divided into air gap and

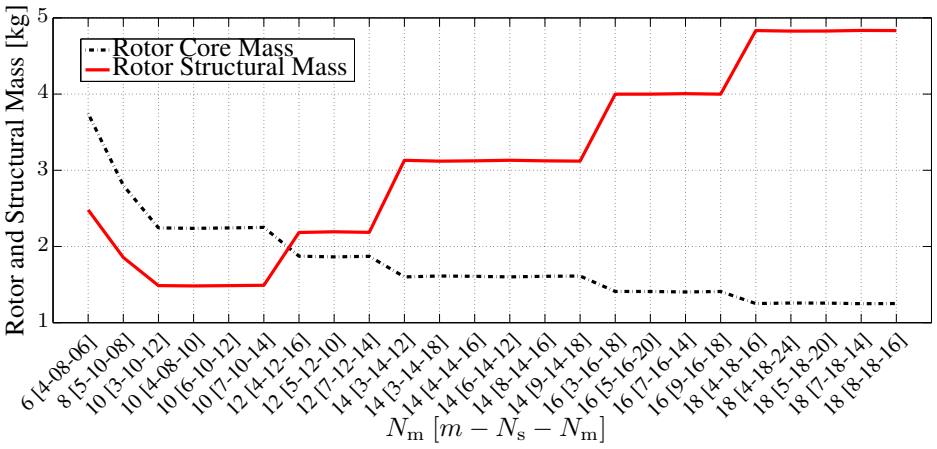

Figure 6.11: Effect of different combinations on rotor and structural mass.

slot leakage inductances.

1- To obtain a full insight on the performance of the AFPMSM for different combinations of slots, poles and phases, their inductances are investigated. A simple magnetizing inductance for an AFPMSM could be written as [121]:

$$L_{\mathrm{m_f}} = \frac{m\mu_{\mathrm{o}}}{4\pi} N_{\mathrm{ph}}^2 \Big(\frac{K_{\mathrm{w_p}}^2}{p^2}\Big) \frac{D_{\mathrm{out}}^2(1-\lambda^2)}{g'}, \tag{6.29}$$

where g' is the effective air gap area including the PM and effect of slots (Carter coefficient). $K_{\mathrm{w_p}} = K_{\mathrm{w}}$ is the fundamental winding factor, λ is the inner to outer diameter ratio ($D_{\mathrm{i}}/D_{\mathrm{o}}$), and N_{ph} is the number of turns per phase. (6.29) is only valid for the fundamental component. In order to take into account the harmonic effects, a leakage harmonic factor was introduced in [121]. This factor σ_δ describes the effect of the winding factor harmonics $K_{\mathrm{w_n}}$ on the total inductance caused by the fundamental values and harmonics. This value is described as:

$$\sigma_\delta = \sum_{n=1, n\neq p}^{\infty} p^2 \frac{K_{\mathrm{w_n}}^2}{n^2 K_{\mathrm{w_p}}^2}, \tag{6.30}$$

where n is the harmonic number.

The total magnetizing inductance including the harmonic effect is:

$$L_{\mathrm{m}} = L_{\mathrm{m_f}} + L_\delta = L_{\mathrm{m_f}}(1+\sigma_\delta), \tag{6.31}$$

$$L_{\mathrm{m}} = L_{\mathrm{m_f}} \sum_{n=1}^{\infty} p^2 \frac{K_{\mathrm{w_n}}^2}{n^2 K_{\mathrm{w_p}}^2}. \tag{6.32}$$

In [122], a complete study for machines working in FW showed that the best combination that results in the highest air gap inductance corresponds to the one that has the highest σ_δ.

Table 6.6 summarizes the effect of different combinations on the σ_δ factor. Each column represents a certain phase number. It is clear that for the same phase number, as the $N_\mathrm{s}/N_\mathrm{m}$ value increases from top to bottom in the table, the harmonic leakage factor of the selected combination decreases, the inductance decreases, and a worse FW capability is achieved. Therefore, it is better to design for a low value of $N_\mathrm{s}/N_\mathrm{m}$ to have a better FW capability.

2- The leakage inductance is an important factor in the design of the AFPMSMs for the FW region. The leakage inductance is mainly dependent on the slot width b_s, and the axial length of the tooth $2Y_\mathrm{c1}$. It is also dependent on the tooth tip heights $Y_\mathrm{c2} + Y_\mathrm{c3}$, and slot opening width b_so. The leakage inductance could be written as [121]:

$$L_\mathrm{l} = N_\mathrm{ph}^2 \mu_\mathrm{o} \frac{D_\mathrm{o}(1-\lambda)}{pq} \left(\frac{2Y_\mathrm{c1}}{3b_\mathrm{s}} + \frac{4Y_\mathrm{c2}}{b_\mathrm{s}+b_\mathrm{so}} + \frac{2Y_\mathrm{c3}}{b_\mathrm{so}}\right), \tag{6.33}$$

where q is the number of slots per pole per phase.

If the effect of tooth tips is neglected, a direct relation with the leakage inductance $L_\mathrm{l} \propto \frac{2Y_\mathrm{c1}}{b_\mathrm{s}}$ can be observed. Consequently, for a wider tooth and less axial length of the stator yoke, the inductance would be less.

To have a full insight on the leakage inductance performance of the machine, the analytical model is used. Two combinations are chosen with the same number of slots. The chosen combinations are N_m =14poles,N_s =12slots and N_m =10,N_s =12. The outer diameter is varied in the analytical model design procedure keeping all other parameters fixed. The no load voltage is kept also fixed. The air gap and leakage inductance are recorded for each outer diameter. This is shown in Fig. 6.12.

In conclusions from the above discussions, the slot width becomes smaller with the $N_\mathrm{m}/N_\mathrm{s} = 14/12$ rather than the $N_\mathrm{m}/N_\mathrm{s} = 10/12$ to keep the same flux density. This totaly reduces the leakage inductance for the $N_\mathrm{m}/N_\mathrm{s} = 14/12$ as shown in Fig. 6.12. The magnetizing inductance is higher for the $N_m/N_s = 14/12$ as expected.

Below an outer diameter of 147mm, the $N_\mathrm{m}/N_\mathrm{s} = 10/12$ combination can not achieve the required flux density shown in Table 6.3 inside the tooth because of the very large leakage inductance. Therefore, the $N_\mathrm{m}/N_\mathrm{s} = 14/12$ provides greater capabilities for FW below this outer diameter.

6.4.2 Finite Speed Design

In the finite speed design, the machines are selected to operate to a certain finite speed determined by (6.4). Therefore, the machine can not operate higher than this

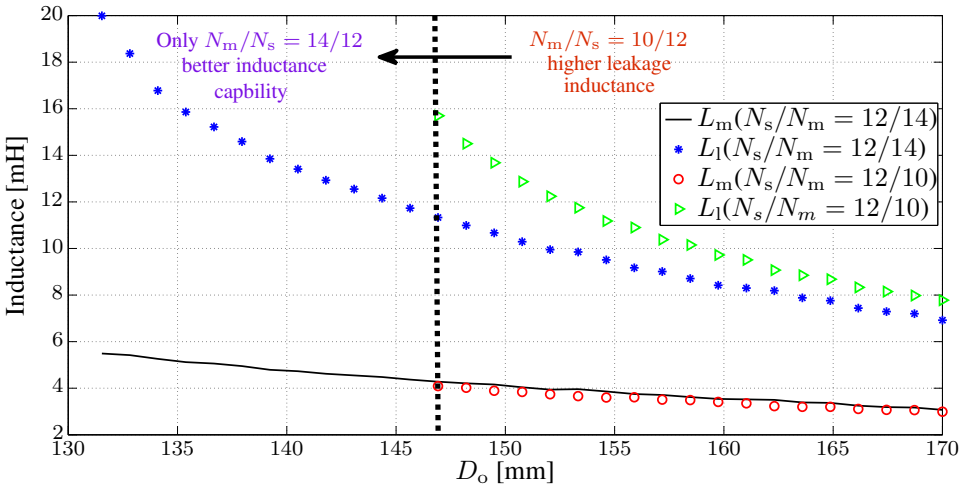

Figure 6.12: Effect of N_s/N_m on the magnetizing and leakage inductances.

speed under the voltages and currents limit.

Table 6.6 summarizes the effect of the design of different combinations on the power density, the maximum speed in (6.4), and the cost of the machine in the finite speed study. The N_s/N_m increases from up to down. Each column represents the result for a certain phase number m. For purposes of design, the maximum speed is kept the same.

Different conclusions are drawn from the table:

- Only combinations with $N_s/N_m < 1$ (in the upper part of the table) can operate in the FW region. This is explained by the high values of the harmonic leakage factor σ_δ associated with these combinations, see Table 6.6. The high σ_δ causes a high inductance according to (6.31).

- The highest power density is only associated with combinations of $N_s/N_m < 1$ and the high winding factor K_w.

For example, for the three phase system only the $N_s/N_m = 12/14$ combination results in the highest power density and maximum speed. Although other combinations in Table 6.6 like $N_s/N_m = 18/16$ have higher winding factors of 0.945 compared to 0.933, they neither reach the required speed nor the highest power density.

For the five phase system, only the $N_s/N_m = 10/12$ combination achieves the required speed with the highest power density. Although, other combinations have higher winding factors, they don't achieve larger power density.

For the seven phase system, despite the relatively low winding factor ($K_w = 0.9$) associated with the $N_s/N_m = 14/18$ combination, it achieves a very high

Table 6.6: The effect of different combinations on the winding factor, harmonic leakage factor, power density, maximum speed, and cost of the machine.

N_s/N_m inc.

	m						
	3	4	5	6	7	8	9
N_s/N_m[frac.]	0.86	0.8	0.833	0.86	0.78	0.89	1.13
N_s/N_m	12/14	8/10	10/12	12/14	14/18	16/18	18/16
K_{w}	0.933	0.924	0.951	0.966	0.9	0.981	0.985
σ_δ	4.78	8	6.85	9.79	16.598	11.96	7.04
P_{dens}[kW/kg]	0.74	0.67	0.756	0.763	0.78	0.74	0.65
$n_{\max}/n_{\mathrm{rated}}$	9.3	9.5	8.6	8.6	8.8	8.1	1.8
Cost (€)	58	66	60.7	56	53	54.7	55.7
N_s/N_m[frac.]	1.13	0.89	1.11	1.2	0.875	1.14	1.29
N_s/N_m	18/16	16/18	20/18	12/10	14/16	16/14	18/14
K_{w}	0.945	0.962	0.976	0.966	0.975	0.981	0.94
σ_δ	2.15	5.74	4.24	4	9.17	6.84	6.6
P_{dens}[kW/kg]	0.59	0.685	0.59	0.58	0.77	0.65	0.58
$n_{\max}/n_{\mathrm{rated}}$	1.8	8.2	1.6	1.8	8.3	1.6	1.7
Cost (€)	57	54.7	53	62	55	58.4	56
N_s/N_m[frac.]	1.2	1.14	1.25		1.17		
N_s/N_m	12/10	16/14	20/16		14/12		
K_{w}	0.933	0.962	0.951		0.975		
σ_δ	1.95	3.08	2.49		4.719		
P_{dens}[kW/kg]	0.504	0.6	0.604		0.67		
$n_{\max}/n_{\mathrm{rated}}$	1.6	1.5	1.8		1.7		
Cost (€)	70	56.5	58		56		
N_s/N_m[frac.]	1.29	1.33	1.25		1.4		
N_s/N_m	18/14	24/18	10/8		14/10		
K_{w}	0.902	0.924	0.951		0.901		
σ_δ	1.75	2.25	2.49		4.43		
P_{dens}[kW/kg]	0.53	0.53	0.53		0.53		
$n_{\max}/n_{\mathrm{rated}}$	1.7	1.5	1.8		1.7		
Cost (€)	60	58	67.5		64		
N_s/N_m[frac.]		1.33					
N_s/N_m		16/12					
K_{w}		0.924					
σ_δ		2.25					
P_{dens}[kW/kg]		0.61					
$n_{\max}/n_{\mathrm{rated}}$		1.8					
Cost (€)		59					
N_s/N_m[frac.]		1.33					
N_s/N_m		8/6					
K_{w}		0.924					
σ_δ		2.25					
P_{dens}[kW/kg]		0.44					
$n_{\max}/n_{\mathrm{rated}}$		1.8					
Cost (€)		76					

power density and the maximum speed. In addition, the $N_{\mathrm{s}}/N_{\mathrm{m}} = 14/16$ combination achieves a high power density with a high maximum speed due to its associated high winding factor $K_{\mathrm{w}} = 0.975$ but not as the $N_{\mathrm{s}}/N_{\mathrm{m}} = 14/18$, etc.

In spite of the very high winding factor of the nine phase system shown in Table 6.6, it can not achieve a high power density or the maximum speed as other combinations. This is due to the high value of $N_{\mathrm{s}}/N_{\mathrm{m}}$.

In conclusions, in the design procedure, it is important to select the combinations that have a high value of σ_δ in (6.30) to have optimal FW properties. In addition, combinations with $N_m > N_s$ as well as a high winding factor K_{w} result in a better performance than any other combinations in terms of the power density.

Fig. 6.13 (a) summarizes the effect of the number of phases on the power density. This result contains the combinations with the highest power density for each phase. It shows that the power density increases while utilizing a higher number of phases except for some phases. The four phase system (8 slots and 10 PMs) has a combination with a very low number of slots. This increases the end winding leading to higher copper mass. Moreover, the eight phase system (16 slots and 18 PMs), the $N_{\mathrm{s}}/N_{\mathrm{m}}$ is higher than the seven phase system of the first row in Table 6.6. This leads to larger stator mass. For the nine phase combinations, the $N_{\mathrm{s}}/N_{\mathrm{m}}$ is larger than unity leading to a very large stator mass compared to other combinations.

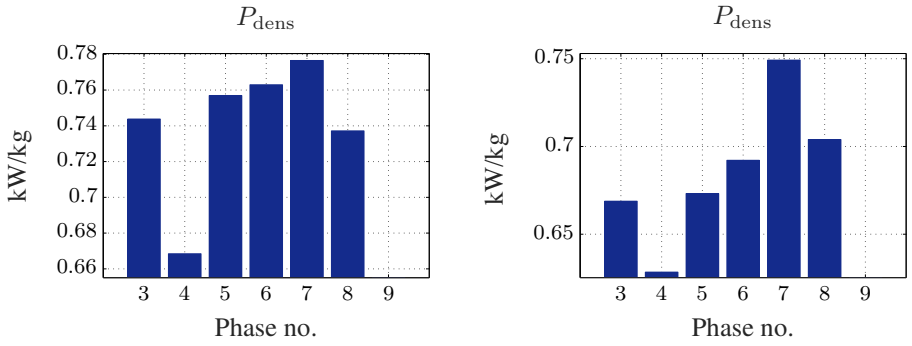

(a) Finite (b) Infinite

Figure 6.13: Power density results for finite and infinite speed design.

6.4.3 Infinite Speed Design

In the infinite speed design, the machines are selected to operate till theoretically infinite speed within the predefined constraints of the voltages and currents.

Table 6.7 summarizes the effect of the design of different combinations on power density, efficiency at rated speed, and cost of the machine in the infinite speed study. This is done for different numbers of phases, i.e. m in the Table.

It is clear that only combinations with the highest harmonic leakage factor, winding factor, and $N_{\mathrm{s}}/N_{\mathrm{m}} < 1$ result in the infinite speed design.

It is also clear that the power density compared to the finite speed design is reduced. This corresponds to the concept of the degradation of the power capability with the increase of the inductance value. To reach a 'theoretically' infinite speed, higher inductances are expected to occur. It is also clear that certain phases can not achieve the infinite speed design like the nine phase system because of the high $N_{\mathrm{s}}/N_{\mathrm{m}}$ value. Fig. 6.13 (b) shows only the combinations that succeed to achieve the infinite theoretical speed, and summarizes the effect of the number of phases on the power density. It is clear that the increase of the power density is related to the increase of the phase number and decrease of $N_{\mathrm{s}}/N_{\mathrm{m}}$.

Table 6.7: The power density, efficiency at the rated speed and cost of the machine for infinite speed results.

	m					
	3	4	5	6	7	8
$N_{\mathrm{s}}/N_{\mathrm{m}}$	0.86(12/14)	0.8(8/10)	0.833(10/12)	0.86(12/14)	0.78(14/18)	0.89(16/18)
P_{dens}[kW/kg]	0.67	0.63	0.673	0.69	0.75	0.703
η (%)	96	96	96.1	96.4	96.5	96.4
Cost (€)	62.3	69	64.1	59	55	54
$N_{\mathrm{s}}/N_{\mathrm{m}}$					0.875(14/16)	
P_{dens}[kW/kg]					0.675	
η (%)					96.3	
Cost (€)					55.4	

6.4.4 Comparison Between Finite and Infinite Speed Designs

The power density, efficiency at the maximum speed, and the cost of the machine are depicted in Fig. 6.14 for a finite and infinite speed design. The theoretical infinite speed design results in a better efficiency at the maximum speed. For the theoretical infinite speed design, less d-axis current is needed to mitigate the same flux. Therefore, the efficiency at the maximum speed is better. On the other hand, the theoretical infinite speed design results in a less power density. In addition, the cost of the infinite speed machine is higher than the finite speed design.

Torque is produced by the interaction between two fluxes of the PMs and the magnetomotive force produced by the copper windings. In order to obtain higher speeds, the inductance needs to be higher. Therefore, the amount of copper needed becomes more dominant than the PM flux. In consequence, the cost increases and the power density reduces.

Therefore, it is better to design a machine for a certain finite speed rather than designing it for a theoretical infinite speed. In the infinite speed design, the machine can operate in a wide range of speeds with a great efficiency over this range.

6.4.5 Results of a 14-12, 3-phase machine

Figure 6.15 shows the effect of outer diameter and inner to outer diameter ratio on the power density and maximum speed in per unit for the 3-phase, 14-12 combi-

nation. It is clear that the best power density occurs at certain outer diameter and inner to outer diameter ratios.

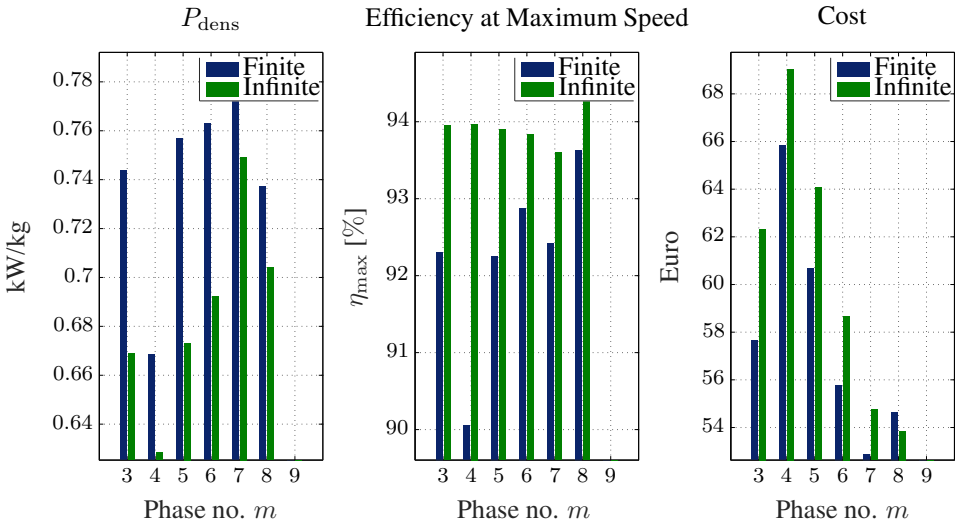

Figure 6.14: Comparison between finite and infinite speed results.

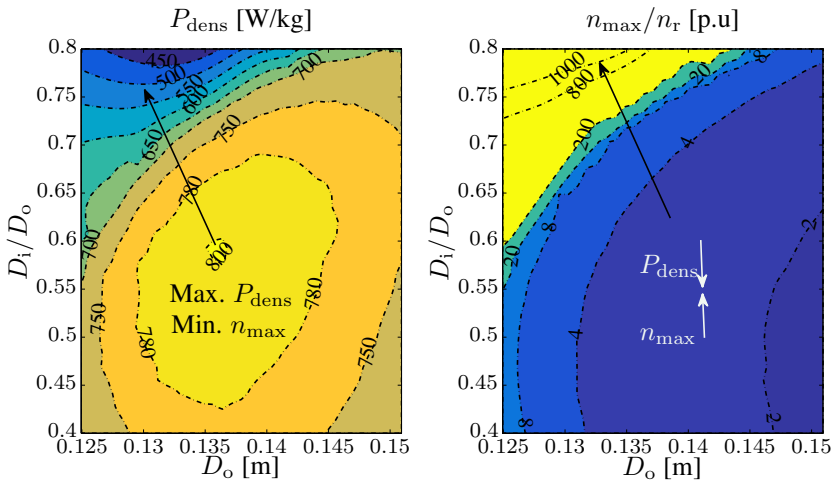

Figure 6.15: Effect of geometrical machine parameters change on the power density and maximum speed.

Figure 6.15 shows that the maximal speed is rather low in the point of optimal power density on the right. If a higher maximal speed is required, the chosen solution should be shifted as indicated by the arrow in the figure. Looking again at the power density plot (left figure), the same shift will lead to a lower power density. This corresponds to the results in Fig. 6.6. The solutions with a higher

power density have a lower maximal speed, as indicated by the arrow on top of Fig. 6.6.

6.5 Finite Element Validation

In this section, a 3D FE model is used to validate the obtained results using the analytical design tool. We have selected the three-phase machine topology, with design parameters outlined in Table 6.8. The star of the slot is is shown in Fig. 6.16.

Table 6.8: Geometrical parameters of the designed three phase machine.

Parameter	Symbol	Value
Number of pole pairs	p	7
Number of stator slots	N_s	12
Rated speed	n_{rated}	2500 rpm
Rated Torque	T_{em}	19.1 Nm
Remanent flux density permanent magnets	B_{rem}	1.26 T
Outer diameter	D_{o}	130 mm
Inner diameter	D_{i}	85 mm
Axial length core element	$2(Y_{\mathrm{c1}} + Y_{\mathrm{c2}} + Y_{\mathrm{c3}})$	81 mm
Axial length slot	$2Y_{\mathrm{c1}}$	68.8 mm
Slot width	b_{s}	10.2 mm

Figure 6.17 shows the flux density distribution of the selected three phase machine. A magnified version of the flux density distribution is shown in Fig. 6.18.

Both figures clearly show that the peak flux density inside the tooth corresponds to the targeted flux density value around the designed value of 1.35 T (The green color in the magnified version in Fig. 6.18). The 1.35T is chosen because the selected amorphous material grade has a saturation of 1.56T with a stacking factor of 0.9.

A good agreement between the analytical and FE based models of the voltage at no-load and full load conditions at the rated speed can be noticed in Fig. 6.19. The analytical model has succeeded to obtain the full load voltage as the desired value. Fig. 6.20 clarifies that at the maximum speed, the full load voltage does not exceed the voltage limit of the machine with the injection of the d-axis current. In addition, a good agreement between the analytical and FE model can be observed.

The losses difference of the 3D FE and analytical models is depicted in Table 6.9. It clearly shows that the model is capable of obtaining the iron loss values in an accurate way.

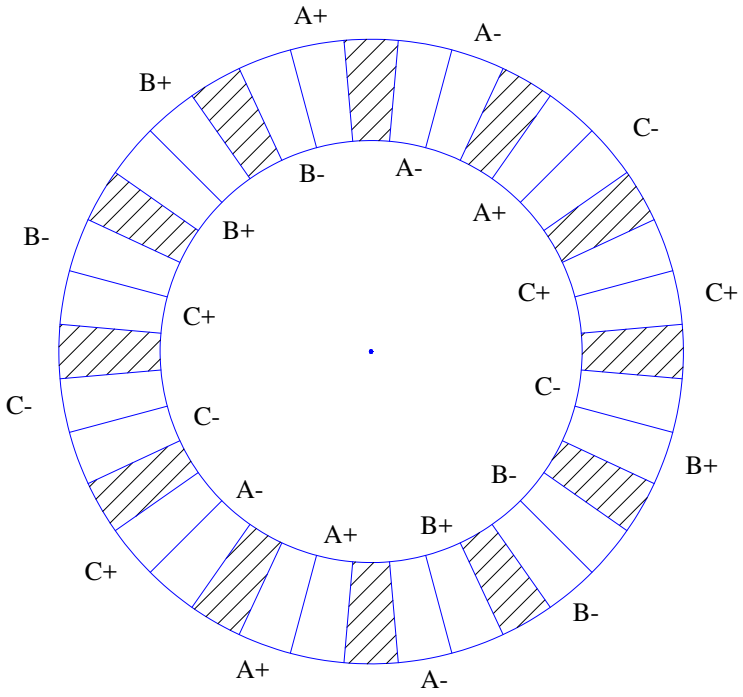

Figure 6.16: Phases distribution across the circumference for the 12 slot 14 pole combination.

Table 6.9: Iron losses difference between analytical and FE. models.

	Ana. Model	3D FE. Model	Err (%)
No Load	33.87 W	35.7 W	5 %
Full Load	52.86 W	55.3 W	4.4 %

The loss distribution over the entire working speed, based on the analytical model developed in [44], [94], can be observed in Fig. 6.21. The PM losses become more dominant at high speeds. These losses can be reduced by segmenting the PMs as shown in Fig. 6.22. The iron loss increases with a slow rate firstly by injecting the d-axis currents. This can be explained as the d-axis currents counter the main fields of the PMs. Afterwards, the rate increases again.

Figure 6.23 depicts the efficiency map of the 3-phase, 14-poles, and 12 slots machine up to the maximum speed of five times the rated speed. It proves that the designed machine has an efficiency greater than 90% at the maximum speed.

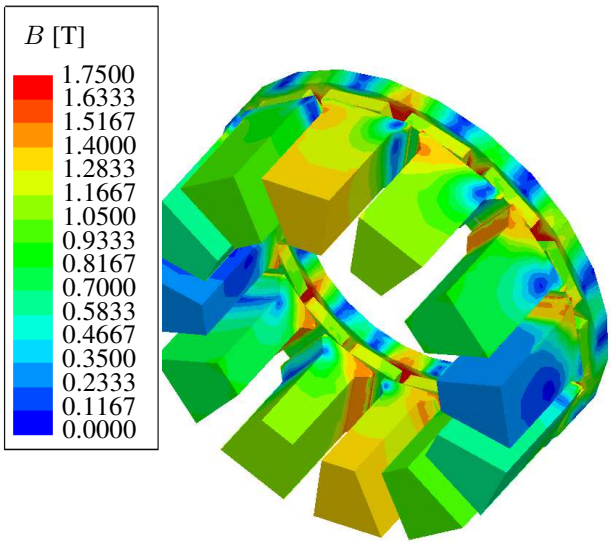

Figure 6.17: Tooth flux density of the AFPMSM.

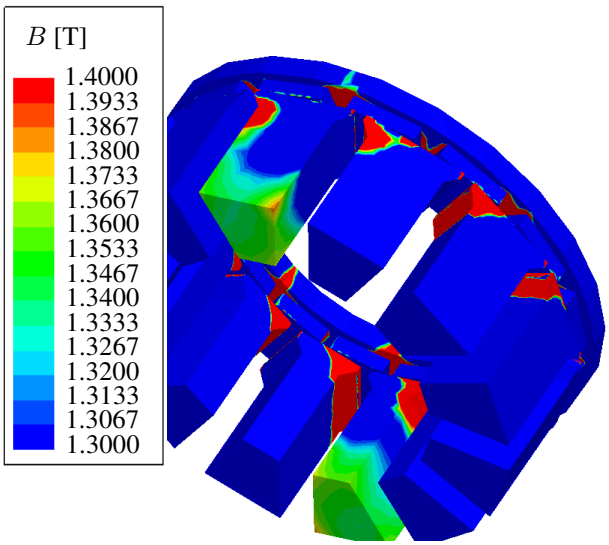

Figure 6.18: Tooth flux density of the AFPMSM (Magnified Version).

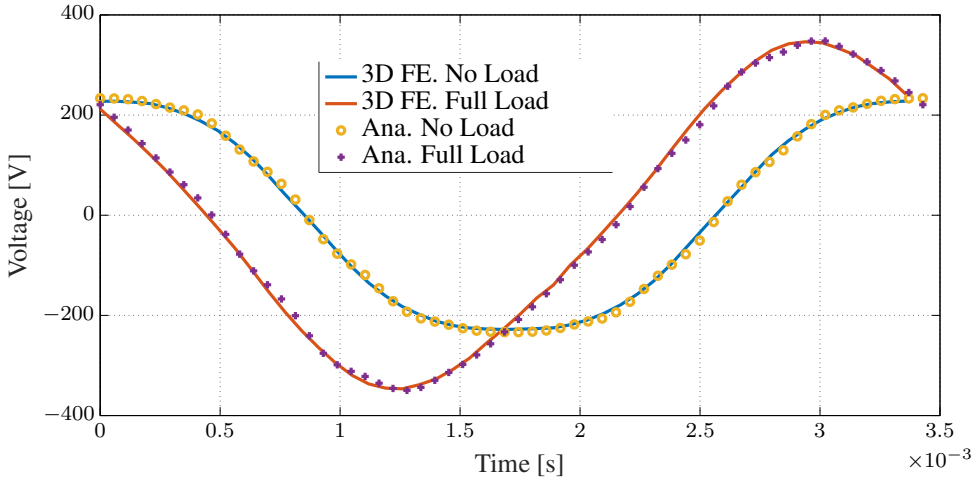

Figure 6.19: 3D FE and analytical voltage output of the machine at rated speed.

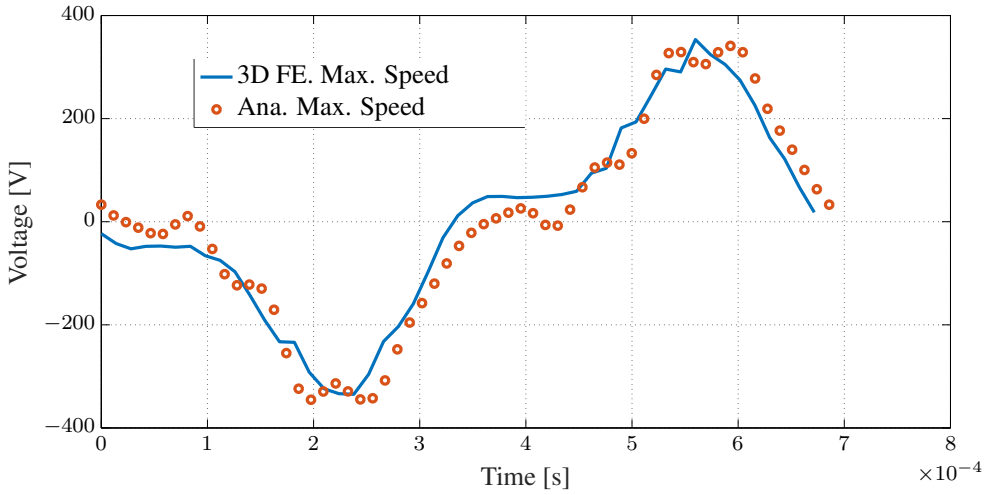

Figure 6.20: 3D FE and analytical voltage output of the machine at maximum speed.

6.6 d and q Current Effects on Torque Ripple

The torque ripple of the 12-14 machine is studied for different d and q axis currents in Fig. 6.24. Thanks to the developed accurate subdomain model discussed in section 3.4.3, it is possible to obtain accurately the torque ripple of the machine. It is clear that approaching the FW, which means more additional d-axis currents, leads to higher torque ripple.

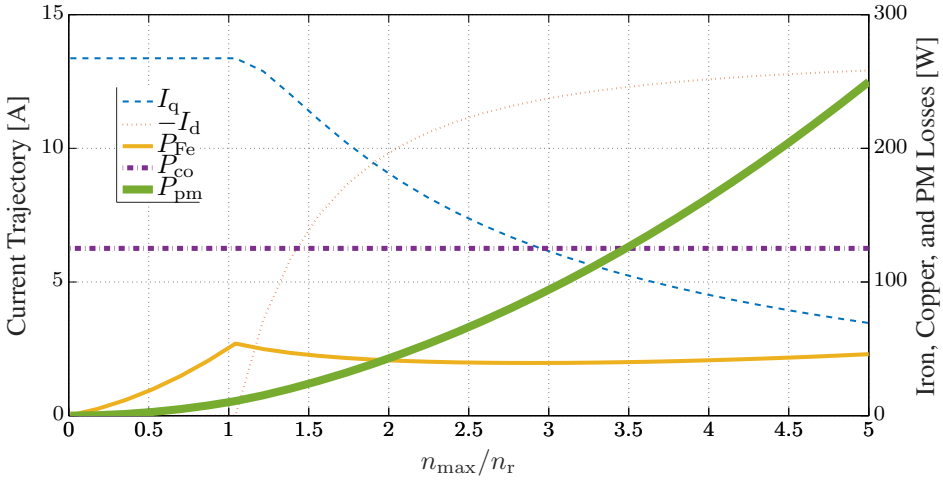

Figure 6.21: Losses distribution for I_d-I_q trajectory over the entire speed.

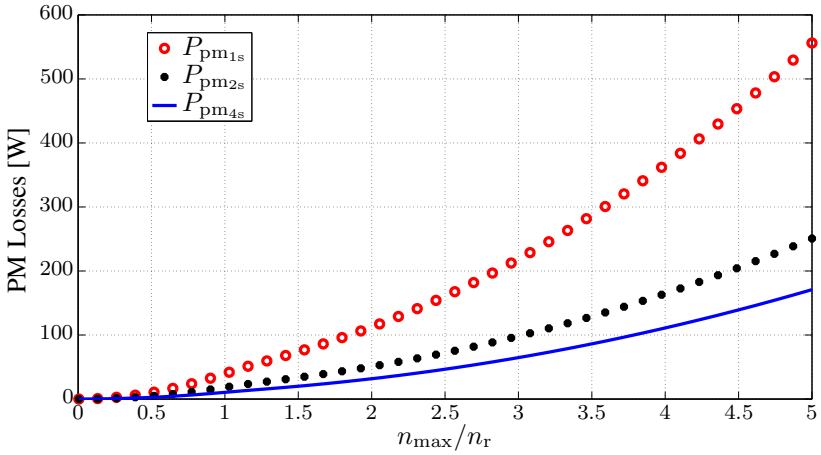

Figure 6.22: PM losses for different number of segments over the entire speed.

6.7 Conclusions

In this chapter, a complete electromagnetic design toolbox is developed for AFPMSMs. A sensitivity analysis of the optimal parameters for the axial flux permanent magnet synchronous machines working in the FW region is implemented.

Thanks to the presence of parameterized accurate analytical models discussed in chapters 3, 4, and 5, it is possible to obtain all the required parameters of the machine. A complete design toolbox is proposed in this chapter that allows a fast

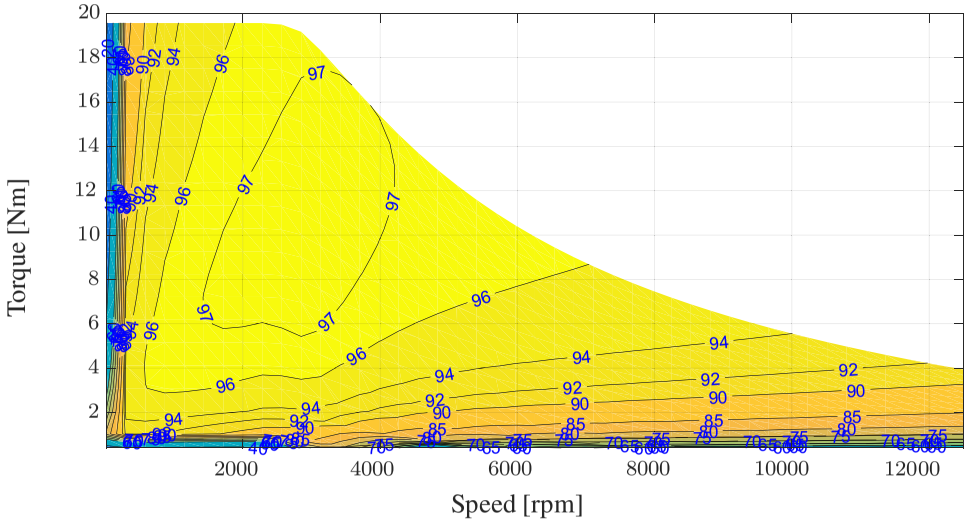

Figure 6.23: Efficiency map of the designed machine for several operating points.

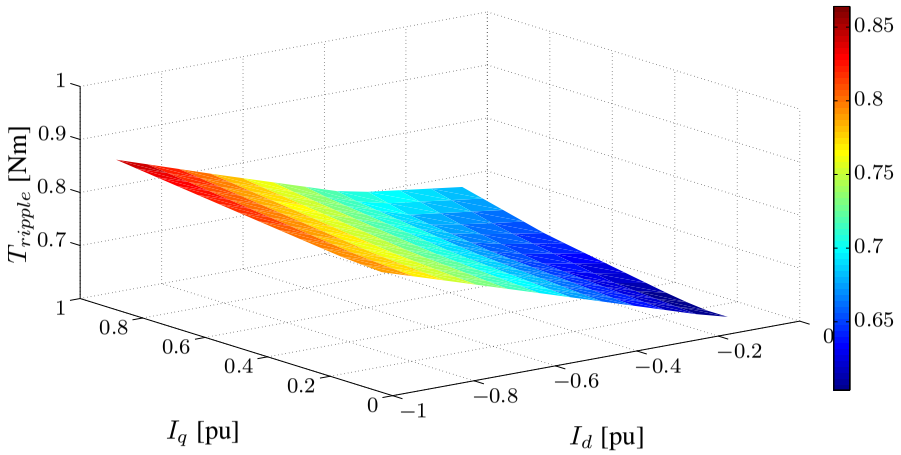

Figure 6.24: The effect of d and q axis current on the torque ripple for the 14 poles 12 slots machine.

and an accurate design for the AFPMSM.

The two goals of the ideal design for the FW region are to maximize the power density: P_{dens} and the ratio of maximal to rated speed: $n_{\max}/n_{\text{rated}}$ which is an inductance related parameter keeping the efficiency at the maximum speed above 90 %. Different slots/poles/phases combinations are studied to reveal the optimum combination for each phase. This chapter has studied the effect of the ratio of

number of stator slots to number of rotor poles on the P_{dens} and $n_{\max}/n_{\mathrm{rated}}$. It is found that for better FW capabilities *i.e.* high values of maximum speeds are required, low values of slots per poles ratio are needed. In terms of power density, it is not only important to use combinations with a high value of the winding factor K_{w}, but also to search for combinations with $N_m > N_s$.

The effect of the outer diameter, and the inner to outer diameter ratio are studied with respect to the two design goals. In addition, a comparison between the finite and the theoretical infinite speed designs is implemented. A complete 3D finite element (FE) validation has proven the robustness of the analytical model.

This chapter has clearly given complete guidelines for machine designers to have an efficient and robust performance of Axial Flux Permanent Magnet Synchronous Machine (AFPMSMs) working in the field weakening (FW) region. The analytical models developed by the authors made it possible to obtain all the required machine parameters (losses, inductances, voltages) in an accurate way and a fast way.

Chapter 7

Thermal Modeling of Air Cooled YASA Machine

7.1 Introduction

The torque density of electric machines strongly depends on the performance of the cooling system. In the YASA machine, cooling inherently occurs through self-ventilation by both rotor discs. Nevertheless, an independent cooling system remains necessary for most applications. In the YASA machine, the individual stator cores with concentrated windings are potted in the stator housing using an epoxy resin. These epoxy resins are relatively bad thermally conductive, and therefore, limit the heat transfer to the surface of the machine. Therefore, an introduction of new heat extraction fins that are placed behind the winding to provide new path for the heat flow. This cooling strategy is introduced and evaluated in this chapter.

An optimized design of the YASA machine requires accurate and fast models. These include electromagnetic, mechanical, and thermal models for the machine. Therefore, accurate and fast models have been under development. Electromagnetic fast and accurate analytical models were developed in chapters 3, 4 and 5 [44], [94], [37].

Thermal modeling of the YASA machine is an important aspect in the design procedure. There are mainly two types of models that are used. Coupled computational fluid dynamics (CFD) and thermal FE simulations in [123–126] are one solution to obtain the temperature distribution inside the machine. Another solution is to use effective solutions for the heat convective coefficients proposed in [127–130]. These coefficients can be the source inputs to a more detailed 3D FE thermal model in [131] or a lumped parameter thermal network (LPTN) [132, 133].

Coupled thermal and CFD analysis is highly needed with complex cooling systems. The authors in [123] studied the thermal effect of a forced air cooling using two different fan types mounted on the shaft in addition to the cooling fins mounted on the stator surface. The authors compared the cooling without fan and with the

fans. They proved great capability of the thermal model to describe the temperature behaviour of the system. In addition, the second fan type provided very great capabilities for cooling the system.

The authors in [124] proposed a hybrid cooling method of a water copper bars inserted in the teeth and a segment of potting material around the end winding. The stator frame is water cooled. The model used is based on a coupling between CFD and FE thermal model.

The authors in [125] developed an electromagnetic and thermal design toolbox based on a combined solution of CFD and thermal FE model.

The method of using a coupled solution of CFD and FE thermal model gives an accurate result in terms of detailed temperature distribution around the machine. However, it requires much calculation time. If an optimization of the system is required, this method can not be used to evaluate the thermal behaviour. The authors in [126] improved the FE thermal model by using a 2D model to improve the time consumption.

Many authors in [127, 128] investigated the heat flow for two solid discs, in which one disc is rotating at a certain speed. This was done throughout CFD. They developed analytical equations for the heat flow conditions that occur on the boundary surfaces of the rotor and stator. These equations are parameterized and function of the dimensions of the machine, rotor, and stator temperatures. The authors in [129] included the PMs on the rotor surface and developed analytical equations for the heat flow on the boundary surfaces taking into account the air flow inside the channels between the PMs. In [130], empirical equations are used for the convection coefficients in the air gap area. These coefficients are only valid for an enclosed rotor and stator system.

Authors in [132] developed LPTNs for the stator and the rotor. They used convection coefficients in the air gap area between the rotating rotor and fixed stator existing in [130]. The LPTN is modeled for both the rotor and the stator in 2D. In [133], the authors proposed a lumped parameter model (LPM). They have modeled a simplified version of the Torus machine by three heat pipes presenting the rotor and the two stators. The output of the LPM becomes an input to a detailed LPTN for the machine. However, the authors concluded that future research should be done to obtain the flow for more complex shapes of stators and rotors. In addition, PMs modeling is crucial as they create centrifugal air flow in the air gap area.

The convection equations in [129], allow decoupling of the rotor and stator models to be solved individually. This allows that the stator and the rotor by a one segment of slot pitch and pole pitch. Therefore, the conduction heat flux equations are solved separately. Accordingly, a thermal 3D FE model was developed in [131] based on the heat convective equations developed in [128].

In this chapter, the authors developed a LPTN based on the convective heat coefficients from [129]. The rotor is composed of a solid cylinder with holes under the channel between the PMs. These channels allow the air flow between PMs. They operate as fan type PMs. The main advantage of the model is the separation of

the stator and rotor LPTN. Thanks to analytical expressions of the convective heat transfer in the hollow type machine [129], it is possible to obtain the temperatures of both the rotor and the stator.

7.2 Heat Transfer

Heat transfer is the energy transfer that occurs due to the temperature gradient between two systems that come into thermal contact. It consists of three transfer mechanisms: conduction, convection and radiation. Each of the mechanisms is defined in the following sub-sections. [134]

7.2.1 Conduction

Thermal conduction occurs when there is a temperature gradient between two points from the high temperature point to the lower temperature point. The conduction heat transfer rate q_{h} is proportional to the cross sectional area S of the medium through which the heat is conducted and proportional to the temperature gradient ∇T in the direction of the heat flow:

$$\mathbf{q}_{\mathrm{h}} = -\int_S k_{\mathrm{h}} \nabla \mathbf{T} \cdot \mathbf{n} \mathrm{d}S, \tag{7.1}$$

where k_{h} is thermal conductivity of the material in [W/mK].

Equation (7.1) refers to the Fourier law of conduction. The negative sign indicates that the heat transfer flow goes in the direction from the high temperature to the low temperature.

The differential conduction equation is: [134]:

$$\rho C_{\mathrm{p}} \frac{\partial T}{\partial t} = Q_{\mathrm{h}} + \nabla \cdot (k_{\mathrm{h}} \nabla T), \tag{7.2}$$

where

- Q_{h} is the power generated per unit volume [W/m^3].
- ρ is the material density [kg/m^3].
- C_{p} is the specific heat capacity [J/kg K].

In the stationary situation the left hand side of (7.2) equals zero.

7.2.2 Convection

Convection of heat occurs due to the temperature difference between the body surface and the fluid (air, water, oil) that flows over the surface. Natural or forced convection can occur depending on the nature of the process. Natural convection is

due to the density differences in the fluid. The density differences are due to temperature differences caused by heat conduction or the body fluid interface. Forced convection requires an external source (fan, pumps,....) which causes a mechanical fluid transport.

Newton law of cooling gives the following expression for the convection description:

$$\mathbf{q}_{\mathrm{h}} = \int_S h_{\mathrm{c}} \nabla \left(\mathbf{T}_{\mathrm{s}} - T_{\mathrm{amb}} \right) \cdot \mathbf{n} \mathrm{d}S, \tag{7.3}$$

where

- q_{h} is the heat transfer rate [W].
- h_{c} is the heat transfer convection coefficient [W/m^{2}K].
- S_{c} is surface area exposed to fluid flow [m^2].
- T_{s} is surface temperature exposed to fluid flow [K].
- T_{amb} is the ambient temperature [K].

7.2.3 Radiation

Heat transfer through radiation takes place in form of electromagnetic waves mainly in the infrared region. Radiation emitted by a body is a consequence of thermal agitation of its composing molecules. With radiation, electromagnetic waves carry the energy. Electromagnetic radiation comes from accelerating electric charges. On a molecular level, that is what happens as objects warm up, their molecules vibrate harder and harder, causing acceleration of electric charges.

Finally the radiation heat transfer from a body surface (S) at temperature T_{s} to a body at temperature T_{rad} is proportional to:

$$q_{\mathrm{h}} \propto \varepsilon \sigma_{\mathrm{B}} ({T_{\mathrm{s}}}^4 - {T_{\mathrm{rad}}}^4), \tag{7.4}$$

where

- q_{h} is the heat flux [W/m^2].
- ε is the emissivity of the radiating surface.
- σ_{B} is s the Stefan-Boltzman constant, σ_{B}=5.67$\times 10^{-8}$W/m^{2}K.

Notice that, due to the relative low value for σ_{B}, radiation heat transfer can be neglected for relative small differences in temperature T_{s} and T_{rad}.

7.3 Description of the Stator Heat Extraction System

In this section, an introduction of the stator heat extraction system is introduced. Most electrical machines use the stator yoke as a mechanical interface between the electromagnetic active parts and the stator housing. The absence of the stator yoke in the YASA machines makes the construction challenging. A steel structure with fingers is proposed [135], but when mass and compactness become important, epoxy potting is very often proposed.

The use of epoxy resins as a potting material has also a major impact on the thermal design of the machine. These epoxy resins have a relatively low thermal conductivity [136]. In consequence, a high thermal resistivity between the heat source and the surface of the stator housing would limit the operation of the machine. In [137], epoxy materials are only used near both air gap regions and the coolant flows into a meander path through the individual stator cores. This technique works fine for liquid cooled automotive applications, but might become unsuitable for other applications. First, this technique is limited to liquid cooling which is for some applications undesired. The mechanical structure with only epoxy plates near both the air gaps might be mechanically insufficient to be used in direct drive wind generators.

Here, the individual stator cores with winding are arranged into the stator housing and the remaining space is potted using an epoxy resin. In Fig. 7.1 (a), the 15 stator cores with concentric winding, the stator (outer) housing and the (inner) central bearing block are clearly visible.

In order to avoid eddy currents in the massive parts stator housing and bearing block, a sufficiently high distance with the stator winding is maintained. As these empty spaces will be filled with epoxy resin during the potting process, a high thermal resistivity between the heat source in the winding and the surface of the stator housing will limit the cooling possibilities of the internal stator parts. In order to reduce this high thermal resistivity, an inward heat extraction fin will be integrated in the stator housing as illustrated in Fig. 7.1 (a). The fins reach up to the inner diameter of the stator winding to have a high contact surface with the stator winding.

For the sake of reducing eddy currents [138] due to leakage fluxes, the stator is made by a stack of coated aluminium profiles as can be seen in Fig. 7.1 (b). Despite the reduction of the thermal resistance, the winding thickness reduces and will result in an increase of the copper losses. The ratio between the fin thickness, i.e. better cooling, and the winding thickness, i.e. lower copper losses, needs to be optimised.

7.4 Thermal Properties of Electromagnetic Materials

The thermal properties of magnetic material are important in determining the thermal behaviour of the complete machine. The detailed parts of the stator and rotor

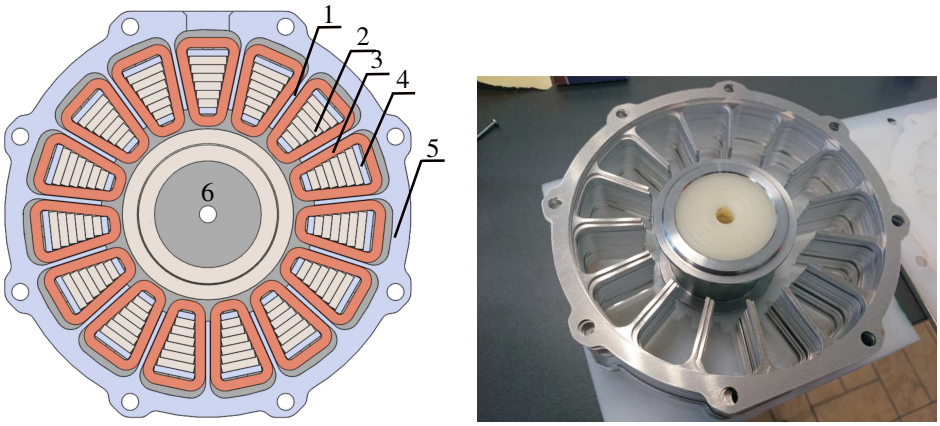

(a) (b)

Figure 7.1: (a) Stator heat extraction system. (1) Inward heat extraction fins. (2) Laminated core with 6 different stacks. (3) Concentrated winding. (4) Nylon contact between end winding and stator core. (5) Laminated stator housing. (6) Shaft. (b) Construction of the stator housing by stacking individual coated aluminium profiles of 2mm thickness.

components are shown in Figs. 7.2 and 7.3 respectively. The Thermal properties of each component of the machine is summarized in Table 7.1. The inward fins behind the winding is shown in Fig. 7.2 (b).

Table 7.1: Properties of the materials in the AFPMSM.

Machine part	Magnetic Material	k_{h} [W/mK]	C_{p} [J/kg K]	ρ [kg/m^3]
fins	aluminum	167	896	2712
bearing	steel	40	490	7650
epoxy Resin	epoxy	0.4	600	1540
Thermal contact between winding and core	nylon	0.25	1600	1140
Winding	copper	385	392	8890
rotor yoke	steel	40	490	7650
permanent magnet	Nd-Fe-B	9	500	7500

The boundaries shown in Figs. 7.2 and 7.3 are used to solve the 3D FE thermal model and LPTN model described in this chapter and chapter 7.

Crucial in the thermal FE model is the correct modelling of the anisotropic thermal properties of the materials and the correct dimensioning of the thin section spaces filled with epoxy resin.

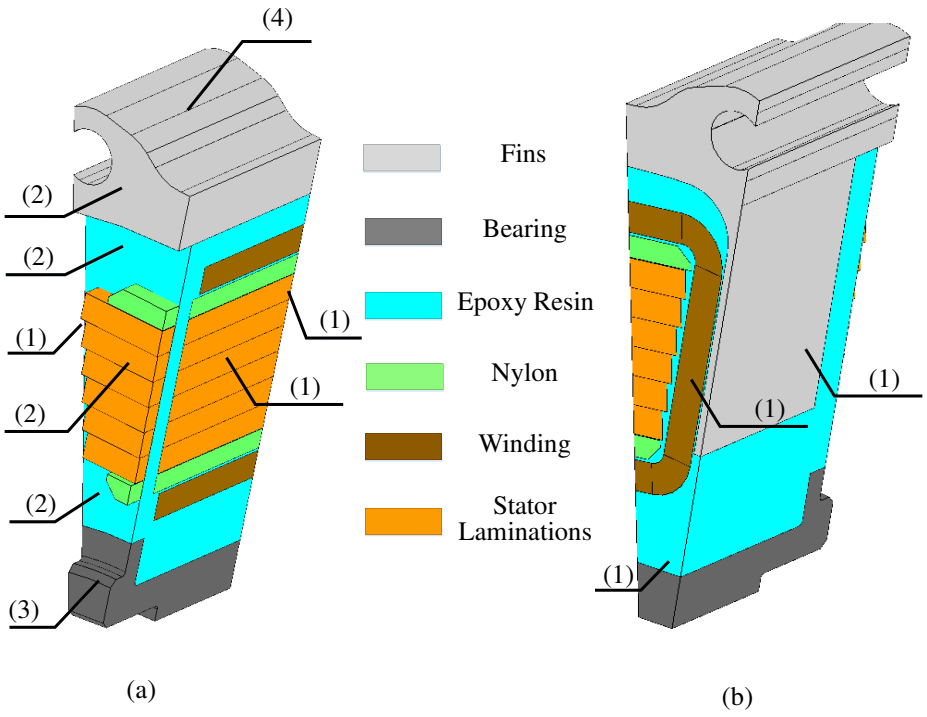

Figure 7.2: Thermal model of one quarter of the stator tooth. Boundary conditions, (1) Thermal insulation. (2) Stator facing rotor upper. (3) Stator facing rotor lower. (4) Stator sidewall. (a) Side view from front. (b) Side view from back.

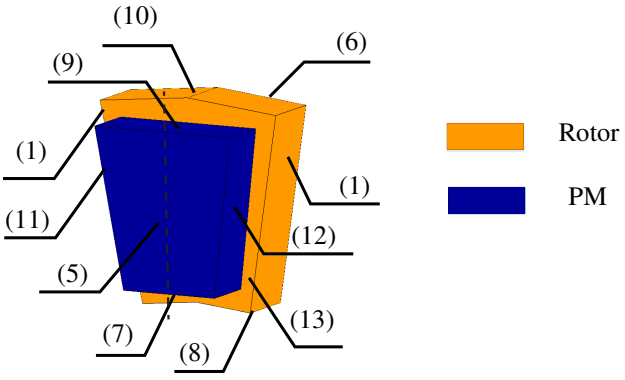

Figure 7.3: Thermal model of the rotor. Boundary conditions, (1) Thermal insulation. (5) Rotor facing stator upper. (6) Rotor left side. (7) PM lower. (8) Rotor lower. (9) PM upper. (10) Rotor upper. (11) PM left. (12) PM right. (13) Rotor facing stator.

For the stator cores made of thin laminated silicon steel, the laminated stator housing and the epoxy infiltrated winding, their thermal conductivities are mod-

elled using the Hasihn and Shtrikman approximation [139]. For the copper winding, the equivalent thermal conductivity value $K_{\mathrm{h_w}}$ in direction of lapping and perpendicular to lapping is calculated as:

$$K_{\mathrm{h_w}} = \begin{cases} f_{\mathrm{wi}} K_{\mathrm{h_{co}}} + (1 - f_{\mathrm{wi}}) K_{h_e}, & \text{In lapping direction} \\ K_{\mathrm{h_e}} \frac{(1+f_{\mathrm{wi}})K_{\mathrm{h_{co}}} + (1-(1-f_{\mathrm{wi}}))K_{\mathrm{h_e}}}{(1-f_{\mathrm{wi}})K_{\mathrm{h_{co}}} + (1+(1-f_{\mathrm{wi}}))K_{\mathrm{h_e}}}, & \text{In perpendicular direction} \end{cases} \tag{7.5}$$

where $K_{\mathrm{h_e}}$ is the thermal conductivity of the epoxy resin, $K_{\mathrm{h_{co}}}$ is the thermal conductivity of copper, and f_{wi} is the winding filling factor. The specific heat capacitance $C_{\mathrm{p_{wi}}}$ and mass density ρ_{wi} are also expressed as a function of the filling factor as shown below.

$$\begin{aligned} C_{\mathrm{p_{wi}}} &= f_{\mathrm{wi}} C_{\mathrm{p_{co}}} + (1 - f_{\mathrm{wi}}) C_{\mathrm{p_e}}, \\ \rho_{\mathrm{wi}} &= f_{\mathrm{wi}} \rho_{\mathrm{co}} + (1 - f_{\mathrm{wi}}) \rho_{\mathrm{e}}, \end{aligned} \tag{7.6}$$

where $C_{p_{co}}$, and ρ_{co} are the specific heat capacitance and mass density of copper. C_{p_e}, and ρ_e are the specific heat capacitance and mass density of epoxy.

In the experiments, the winding filling factor of the experimental setup equals 0.57.

The fins, shown in Fig. 7.2, are composed of stacking individual coated aluminium profiles of 2mm thickness. Between stacks, there is an insulating epoxy resin to reduce eddy currents in aluminum sheets. Therefore, the thermal conductivity in a perpendicular direction to the stacking (z-direction in Fig. 3.2 (a)) offers a lower thermal conductivity than the planar surface of the sheets (R and θ_m-direction in Fig. 3.2 (b)). The stacking factor f_{fins} is taken to be 0.96. The same equations of (7.5), and (7.6) can be used to obtain the thermal conductivity, heat capacitances and mass density.

The same criteria apply for the stator laminations. The stacking factor is calculated based on the thickness of each lamination and the number of laminations. The thickness of each lamination is 0.23 mm. The number of laminations is 17×6 laminations. The 6 determines six different widths of each lamination used. The value can be calculated based on the radial length of the machine ($R_o - R_i$). The thermal conductivities in the z and θ_m directions shown in Figs. 3.2 (a) and (b) are higher than the R direction.

The anisotropy of the laminated silicon steel stator cores and windings is included by specifying a tensor for the thermal conductivity rather than a scalar value [131].

7.5 AFPMSM Thermal Models

The most innovative part of the model is the separation of the LPTN models of the stator and rotor through the introduction of the convective heat transfer coefficient

in [129].

7.5.1 3D FE Thermal Model

The thermal FE model of the stator and the rotor are described in Figs. 7.2 and 7.3. Only one quarter of the FE model of the stator teeth in Fig. 7.2 is modeled. The boundary conditions of the stator and the rotor models are shown in Figs. 7.2 and 7.3 respectively. The heat flow transient equation in function of time t is described below for the stator and rotor FE models.

$$\rho_{\mathrm{j}} C_{\mathrm{p,j}} \frac{\partial T}{\partial t} + \nabla \cdot (-k_{\mathrm{j}} \nabla T) = q_{\mathrm{j}} \tag{7.7}$$

where ρ_{j} is the density of material j, $C_{\mathrm{p_j}}$ is the heat capacity of material j, k_{j} is the thermal conductivity of material j, and q_{j} is the heat source inside the machine.

In this model, the following assumptions have been made:

- The temperatures of the rotor surface, stator surface, and surrounding environment are isothermal.
- Air is considered as an incompressible ideal gas, so its density varies with temperature and the other properties are independent of temperature.
- Radiation effect between the rotor and the stator is considered to be negligible.

The studied rotor is shown in Fig. 7.4. It has holes in the rotor.

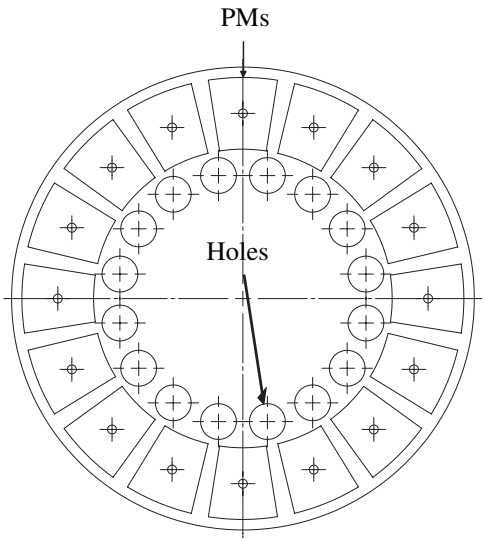

Figure 7.4: The rotor type studied.

The heat losses in the stator are caused by the copper and iron losses in the stator winding and core. They are assumed to be distributed over the volume of each element. The total iron losses P_{Fe} and copper losses P_{wi} are computed in chapters 4 and 6. Only one quarter of the tooth is modeled. Therefore, the total iron losses and winding losses are divided by $4N_{\mathrm{s}}$ as described below:

$$P_{\mathrm{Fe_1}} = P_{\mathrm{Fe}}/4/N_{\mathrm{s}}, P_{\mathrm{wi_1}} = P_{\mathrm{wi}}/4/N_s. \tag{7.8}$$

The heat losses in the rotor are caused by the losses in the PMs. One PM is modeled in the machine. The computation of PM losses can be found in chapter 5.

On each surface of the FE models shown in Figs. 7.2 and 7.3, there is a different boundary conditions that are applied on the surface. These boundary conditions are described below.

1. Thermal insulation is specified on the boundary number (1) shown in Figs. 7.2 and 7.3 for the stator and rotor respectively.

2. Boundaries with convective heat flux (2)-(13), shown in Figs. 7.2 and 7.3, can be obtained using the following procedure.

   The heat flux on each boundary surface i, shown in Fig. 7.2, is defined by [131]:

   $$\bar{q_{\mathrm{i}}} = \bar{h_{\mathrm{i}}}(\bar{T}_{\mathrm{surf_i}} - \bar{T}_{\mathrm{ref_i}}), \tag{7.9}$$

   where $\bar{h_{\mathrm{i}}}$ is the average convection coefficient at surface i, $\bar{T}_{\mathrm{surf_i}}$ is the surface temperature, and $\bar{T}_{\mathrm{ref_i}}$ is the reference temperature (average temperature of a nearby fluid contained with in an adjacent volume i).

   The heat flux h_{i} on a boundary surface i, shown in (7.7) depends on the surface temperature $T_{\mathrm{surf_i}}$ and a reference temperature $T_{\mathrm{ref_i}}$ (average temperature of a nearby fluid contained within an adjacent volume i). The reference temperature ($T_{\mathrm{ref_i}}$) is dependent on the parameters a_{i} and b_{i}. They can be found in [129].

   $$\bar{T}_{\mathrm{ref_i}} = a_{\mathrm{i}}T_{\mathrm{r}} + b_{\mathrm{i}}T_{\mathrm{s}} + (1 - (a_{\mathrm{i}} + b_{\mathrm{i}}))T_{\mathrm{a}}, \tag{7.10}$$

   where T_{r} is the rotor temperature, T_{s} is the stator temperature, and T_{a} is the ambient temperature.

   The convection coefficients $\bar{h_{\mathrm{i}}}$ are dependent on two dimensionless parameters: the Gap size ratio (G) and the rotational Reynolds number (Re) [129]:

   $$G = \frac{2g}{D_{\mathrm{o}}}, Re = \frac{\omega_{\mathrm{m}} D_{\mathrm{o}}^2}{4\nu}, \tag{7.11}$$

where ω_{m} is the mechanical rotational speed in rad/s, D_{o} is the outer diameter, ν is the kinematic viscosity of air, and g is the air gap thickness.

The convection coefficients are also function of the Nusselt number for each surface i.

$$\bar{h_{\mathrm{i}}} = \frac{\bar{Nu}_{\mathrm{i}} k}{l_{\mathrm{i}}}, \tag{7.12}$$

where k is the thermal conductivity of air, and l_{i} is characteristic length.

The $\bar{Nu}_{\mathrm{i}}$, a_{i}, and b_{i} are function of the gap size ratio, the Reynolds number, the PM span ratio α_{m} and the PM axial length Y_{m}.

$$\begin{aligned} a_{\mathrm{i}} &= F_i(G, Re, \alpha_{\mathrm{m}}, Y_{\mathrm{m}}), \\ b_{\mathrm{i}} &= G_i(G, Re, \alpha_{\mathrm{m}}, Y_{\mathrm{m}}), \\ \bar{Nu}_{\mathrm{i}} &= Y_i(G, Re, \alpha_{\mathrm{m}}, Y_{\mathrm{m}}), \end{aligned} \tag{7.13}$$

where the fitting of the coefficients for the different surfaces in the machine is done using CFD results.

Where the functions F_{i}, G_{i} and Y_{i} need to be defined. It is assumed that these functions with four variables can be rewritten as the product of four functions with one variable as [129],

$$\begin{aligned} a_{\mathrm{i}} &= a_{\mathrm{i}}^* f_{\mathrm{i},1}(G) \times f_{\mathrm{i},2}(Re) \times f_{\mathrm{i},3}(\alpha_{\mathrm{m}}) \times f_{\mathrm{i},4}(Y_{\mathrm{m}}) \\ b_{\mathrm{i}} &= b_{\mathrm{i}}^* g_{\mathrm{i},1}(G) \times g_{\mathrm{i},2}(Re) \times g_{\mathrm{i},3}(\alpha_{\mathrm{m}}) \times g_{\mathrm{i},4}(Y_{\mathrm{m}}) \\ \overline{Nu_{\mathrm{i}}} &= \overline{Nu_{\mathrm{i}}}^* y_{\mathrm{i},1}(G) \times y_{\mathrm{i},2}(Re) \times y_{\mathrm{i},3}(\alpha_{\mathrm{m}}) \times y_{\mathrm{i},4}(Y_{\mathrm{m}}) \end{aligned} \tag{7.14}$$

where the superscript $*$ represents the values of a_{i}, b_{i} and $\overline{Nu_{\mathrm{i}}}$ at the reference point. There are two categories of surfaces in the current system: the ones where the reference temperature is almost equal to the ambient temperature, and those where the reference temperature differs from the ambient temperature and should, therefore, be predicted. The details of the formulations for each surface are presented in Tables 7.2-7.4.

Table 7.2: Correlations to estimate the convective heat transfer for the surfaces with $T_{\mathrm{ref}} \cong T_{\mathrm{a}}$ [129].

Surface	Stator sidewall, $i = 4$	Rotor left side, $i = 6$	PM lower, $i = 7$	Rotor upper, $i = 8$
$\overline{Nu}_i^*$	105.76	216.52	492.10	239.56
$y_{\mathrm{i},1}$	$-4.476G^{-0.03846} - 6.795G + 6.373$	$1.785G + 0.9766$	$-3.29G + 1.024$	$1.645G + 0.976$
$y_{\mathrm{i},2}$	$3.91 \times 10^{-5} Re^{0.8773}$	$6.501 \times 10^{-6} Re + 0.3041$	$5.755 \times 10^{-6} Re - 0.3702$	$5.238 \times 10^{-6} Re + 0.425$
$y_{\mathrm{i},3}$	$0.8805\alpha_{\mathrm{m}}^{6.245} + 1.218$	$0.1325\alpha_{\mathrm{m}} + 0.8983$	$-1.20163\alpha_{\mathrm{m}}^{7.461} + 1.226$	$-0.7163\alpha_{\mathrm{m}} + 1.567$
$y_{\mathrm{i},4}$	$-1.246Y_{\mathrm{m}}^{-0.1443} + 2.899$	$1.751Y_{\mathrm{m}} + 0.9061$	$-0.03425Y_{\mathrm{m}}^{-0.5286} + 1.159$	$1.478Y_{\mathrm{m}} + 0.9211$

Table 7.3: Correlations to estimate the convective heat transfer for the surfaces with $T_{\mathrm{ref}} \cong T_{\mathrm{a}}$ [129].

Surface	PM upper, $i = 9$	Rotor upper, $i = 10$	PM left, $i = 11$	Rotor facing stator, $i = 13$
$\overline{Nu}_i^*$	202.28	181.40	285.20	235.85
$y_{\mathrm{i},1}$	$1.62G^{0.11}$	$2.322G + 0.9728$	$-0.002076G^{-1.193} + 1.345$	$1.647G^{0.1117}$
$y_{\mathrm{i},2}$	$8.669 \times 10^{-6} Re + 0.06863$	$4.737 \times 10^{-6} Re^{1.038} + 0.2024$	$9.1 \times 10^{-6} Re + 0.02189$	$7.975 \times 10^{-6} Re + 0.1496$
$y_{\mathrm{i},3}$	$-0.9382\alpha_{\mathrm{m}}^{8.902} + 1.132$	$-1.005\alpha_{\mathrm{m}} + 1.803$	$-7.126\alpha_{\mathrm{m}}^{29.8} + 0.9939$	$-2.903\alpha_{\mathrm{m}} + 3.29$
$y_{\mathrm{i},4}$	$-0.007892Y_{\mathrm{m}}^{-1.107} + 1.189$	$1.806Y_{\mathrm{m}}^{0.2031}$	$6.707Y_{\mathrm{m}}^{0.04971} - 4.8$	$3.917Y_{\mathrm{m}} + 0.7895$

Table 7.4: Correlations to estimate the convective heat transfer for the surfaces with $T_{\mathrm{ref}} \neq T_{\mathrm{a}}$ [129].

Surface	Stator facing rotor upper, $i = 2$	Stator facing rotor lower, $i = 3$	Rotor facing stator upper, $i = 5$	PM right, $i = 12$
a_{i}^*	0.4153	0.2317	0.00100	0.00100
b_{i}^*	0.0010	0.0010	0.1744	0.1739
$\overline{Nu}_{\mathrm{i}}^*$	374.53	243.90	304.84	606.37
$f_{\mathrm{i},1}$	$0.2824G^{-0.3381} - 0.2002$	$0.2033G^{-0.373}$	$1.71 \times 10^{-10} G^{5.386}$	$-0.01155G + 1$
$f_{\mathrm{i},2}$	$74.78Re^{-0.3734}$	$2.096 \times 10^{6} Re^{-1.422} + 0.9092$	1	$-1.967 \times 10^{-9} Re + 1$
$f_{\mathrm{i},3}$	$2.803\alpha_{\mathrm{m}}^{1.518} - 0.9881$	$26.23\alpha_{\mathrm{m}}^{2} - 40.02\alpha_{\mathrm{m}} + 16.23$	$9.892 \times 10^{-16} \alpha_{\mathrm{m}} + 0.9997$	$1.46 \times 10^{-14} \alpha_{\mathrm{m}}^{-102.4} + 0.9929$
$f_{\mathrm{i},4}$	$0.4205Y_{\mathrm{m}}^{-0.2972}$	$0.1982Y_{\mathrm{m}}^{-0.5497}$	$-3.205 \times 10^{-10} \mathrm{Y_m} + 0.9996$	$5.96 \times 10^{-11} \mathrm{Y_m} + 0.9999$
$g_{\mathrm{i},1}$	$3.386 \times 10^{-16} G^{-7.289} + 0.9843$	$0.009G + 1$	$0.005875G^{-1.206}$	$-15.73G + 1.135$
$g_{\mathrm{i},2}$	$7.556 \times 10^{13} Re^{-3.218} + 0.9953$	$1.824 \times 10^{-9} Re + 1$	$1.638 \times 10^{4} Re^{-0.8264} - 0.1472$	$31.79Re^{-0.1803} - 2.969$
$g_{\mathrm{f},3}$	$1.731 \times 10^{-15} \alpha_{\mathrm{m}} + 1$	$1.731 \times 10^{-15} \alpha_{\mathrm{m}} + 1$	$3.416\alpha_{\mathrm{m}}^{6.722} + 0.2816$	$-0.09794\alpha_{\mathrm{m}}^{-7.204} + 1.452$
$g_{\mathrm{i},4}$	$-7.017 \times 10^{-11} Y_{\mathrm{m}} + 0.9999$	$2.506 \times 10^{-10} Y_{\mathrm{m}} + 1$	$0.03617Y_{\mathrm{m}}^{-0.9332} + 0.4602$	$-4.089 \times 10^{5} Y_{\mathrm{m}}^{5.46} + 1.021$
$y_{\mathrm{i},1}$	$-2.967G^{0.6937} + 1.142$	$-0.6211G + 1.005$	$-0.0167G^{-0.6493} + 1.277$	$4.723G^{0.3274} - 14.47G$
$y_{\mathrm{i},2}$	$0.0001122Re^{0.7824} + 0.04018$	$0.0003289Re^{0.679} + 0.1569$	$3.552 \times 10^{-5} Re^{0.886}$	$0.001593Re^{0.5825} - 0.3542$
$y_{\mathrm{i},3}$	$-0.7732\alpha_{\mathrm{m}}^{5.583} + 1.224$	$-0.8183\alpha_{\mathrm{m}}^{6.34} + 1.21$	$-0.905\alpha_{\mathrm{m}}^{4.158} + 1.35$	$-15.86\alpha_{\mathrm{m}}^{35.42} + 0.998$
$y_{\mathrm{i},4}$	$13.86Y_{\mathrm{m}}^{1.709} + 0.9064$	$7.906Y_{\mathrm{m}}^{1.575} + 0.9243$	$3.607Y_{\mathrm{m}} + 0.8067$	$-113.7Y_{\mathrm{m}}^{2} + 12.51Y_{\mathrm{m}} + 0.6539$

As the analytical equations (7.10)−(7.13) are used to express the convective heat flux at different boundaries in the machine, the thermal model can be simplified as follows:

- The models for the stator and the rotor can be separated.
- Due to thermal periodicity, only one segment of each is modeled.

The heat flow transient equation, solved by the FEs, is described in (7.7) for both geometries of the stator and rotor are shown in Figs. 7.2 and 7.3. The boundary conditions are described on the figures. The boundaries with convective heat

transfer can be obtained by obtaining the reference temperatures in (7.10) and the convective heat coefficients in (7.10). According to the studied surface, the equations for the functions F_{i}, G_{i}, and $\bar{Nu}_{\mathrm{i}}$ can be obtained by (7.14) [129].

The resulting temperature distributions on the stator and the rotor surface are used to calculate the reference temperatures expressed by (7.10). In addition, the temperature dependence of the stator resistance is considered. This procedure is repeated until the temperature profile stabilizes.

7.5.2 Lumped Parameter Thermal Network (LPTN)

The lumped parameter thermal network (LPTN) is composed of small blocks of a 3D resistance network shown in Fig. 7.5 (a). The blocks with complex geometries are approximated by rectangular shapes. When there is a heat source in the block, it should be represented by an equivalent thermal resistance shown in 7.5 (b). The central node connected to the heat source (P_{losses}) and the thermal capacitance (c) gives the mean temperature of the block. The avarage temperature of the three dimensional axes (x, y, z) gives lower temperature than the central node. Therefore, a negative resistance equal to $-1/6$ of the total resistance in each direction is presented to take into account this effect. In addition, this resistance comes from the independent solution of the heat conduction solutions [140, 141].

Figure 7.5 (c) presents the equivalent resistance network for the block diagram without any heat source.

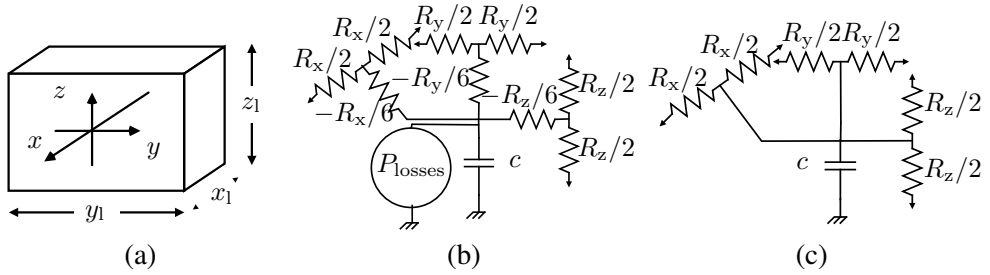

Figure 7.5: Thermal model of the resistance network. (a) Block orientation. (b) Resistance model with heat source. (c) Resistance model without heat source.

The equivalent resistances in each axis x, y, z are:

$$R_{\mathrm{x}} = \frac{x_{\mathrm{l}}}{S_{\mathrm{x}} K_{\mathrm{x}}}, R_{\mathrm{y}} = \frac{y_{\mathrm{l}}}{S_{\mathrm{y}} K_{\mathrm{y}}}, R_{\mathrm{z}} = \frac{z_{\mathrm{l}}}{S_{\mathrm{z}} K_{\mathrm{z}}}, \tag{7.15}$$

where $R_{\mathrm{x}}, R_{\mathrm{y}}, R_{\mathrm{z}}$ are the thermal resistance in the x, y, z directions. $x_{\mathrm{l}}, y_{\mathrm{l}}, z_{\mathrm{l}}$ are the lengths of the block. $S_{\mathrm{x}}, S_{\mathrm{y}}, S_{\mathrm{z}}$ are the areas perpendicular to the heat flow. $K_{\mathrm{x}}, K_{\mathrm{y}}, K_{\mathrm{z}}$ are the thermal conductivities of the isothermal material.

The thermal capacitance c equals:

$$c = \rho C_p V, \tag{7.16}$$

where V is the volume of the material studied.

For surface i with convection, the equivalent thermal resistance R_{ci} on this surface:

$$R_{\text{ci}} = \frac{1}{S_{\text{ci}} h_{\text{ci}}}, \tag{7.17}$$

where S_{ci} is the area exposed to the convection. h_{ci} are the convection coefficients computed in (7.12) according to the surface i.

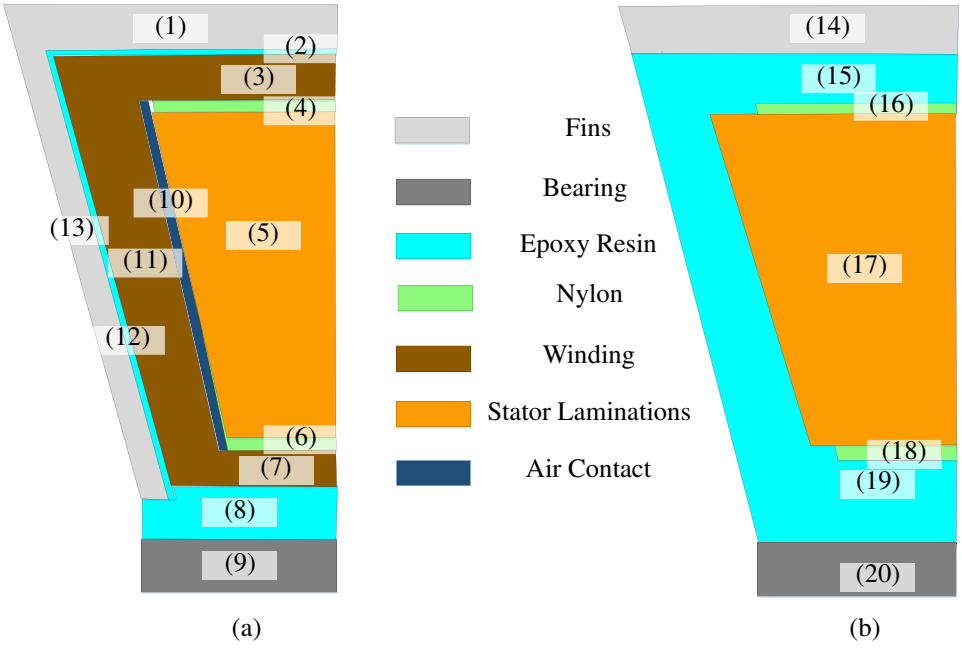

Figure 7.6: LPTN modeling principle. (a) Section I at the center of the tooth. (b) Section II at the center of the tooth tips.

The LPTNs of the stator and rotor are solved separately. The resulting temperatures on the stator and the rotor surface are used to calculate the reference temperatures expressed by (7.10). This procedure is again repeated similar to the 3D FE model until the temperature profile stabilizes. The LPTN of the stator and the rotor are described below.

- Only one-quarter of one stator tooth segment is modeled. The segment model, shown in Fig. 7.6, is divided into two regions in the axial direction.

They are at the center of the tooth-tips and at the center of the tooth in the axial direction. Both regions are shown in Figs. 7.6 (a) and (b) respectively.

The LPTN is dividing half the stator tooth into 20 regions, shown in Fig. 7.6. The equivalent LPTN is shown in Fig. 7.7. Each region of the 20 is made of a box that is the equivalent thermal resistance model shown in Figs. 7.5 (b) and (c). The selection of the scheme is determined according to the existence of sources. The considered loss sources are the winding and core losses. Additionally, each number shown in the LPTN network (Fig. 7.7) represents the equivalent model of the models described in Figs. 7.6 (a) and (b).

The total stator core losses and winding losses of the machine equal $P_{\mathrm{Fe}}, Q_{\mathrm{wi}}$. The stator core losses can be easily calculated using the model developed in chapter 4 [44].

The power losses in the stator segment are the source terms of heat. They are subdivided into the following parts;

- The stator iron losses are divided into two parts (Inside the tooth $P_{\mathrm{Fe}_{\mathrm{eff}}}$ and the tooth tips $P_{\mathrm{Fe}_{\mathrm{tip}}}$). The volume of each part determines the loss distribution. The temperature variations is almost equal inside the tooth axial length as well be shown later. Therefore, there is no need to discretize the stator tooth to more nodes. The total iron losses P_{Fe} can be easily calculated using the model described in chapter 4 using (4.4).

$$P_{\mathrm{Fe}_{\mathrm{eff}}} + P_{\mathrm{Fe}_{\mathrm{tip}}} = P_{\mathrm{Fe}}/4/N_{\mathrm{s}}, \tag{7.18}$$

  where N_{s} is the number of stator slots.

- The winding losses are divided into three main parts (The upper layer winding $P_{\mathrm{wi}_{\mathrm{up}}}$, the lower layer winding $P_{\mathrm{wi}_{\mathrm{down}}}$, and the radial effective part of the winding $P_{\mathrm{wi}_{\mathrm{eff}}}$.) Again the winding losses of each part are distributed according to the volumes of each part. The total copper losses can be calculated according to (6.17):

$$P_{\mathrm{wi}_{\mathrm{up}}} + P_{\mathrm{wi}_{\mathrm{down}}} + P_{\mathrm{wi}_{\mathrm{eff}}} = P_{\mathrm{wi}}/4/N_s. \tag{7.19}$$

The convection coefficient $(h_{\mathrm{c}1}, h_{\mathrm{c}2}, h_{\mathrm{c}3})$ and reference temperatures $(T_{\mathrm{ref}1}, T_{\mathrm{ref}2}, T_{\mathrm{ref}3})$, noted in Fig. 7.7, are described in Fig. 7.2 and can be easily calculated using (7.9)−(7.13). [129].

- The rotor is also composed of a resistance network that is depicted in Fig. 7.8. Only one PM and rotor segment are modeled in the machine.

  The power losses in the rotor core is mainly caused by the PMs. The total PM losses is P_{pm} in the machine can be calculated using the electric network

of the PM described in chapter 5 in (5.14). The PM losses in one PM P_{pm_1} equals:

$$P_{\mathrm{pm}_1} = P_{\mathrm{pm}}/2/N_{\mathrm{m}}, \tag{7.20}$$

where N_{m} is the number of PMs, and P_{pm} is the total PM losses computed using (5.14).

The convection coefficient ($h_{\mathrm{c4}} - h_{\mathrm{c16}}$) and reference temperatures ($T_{\mathrm{ref4}} - T_{\mathrm{ref16}}$), noted in Fig. 7.8, present the boundary surfaces described in the FE model of the rotor in Fig. 7.3. The position of these boundaries are described in Fig. 7.3 and can be easily calculated using (7.10)-(7.13) [129].

Figure 7.8 consists of four main elements. They are the PM, the rotor back to the PM area only, and two areas where the rotor is facing the air channel behind the PM.

The stator and rotor matrices are solved separately. The thermal conductance matrix G is constructed;

$$G = \begin{bmatrix} \sum\limits_{i=1,..}^{m} \frac{1}{R_{1,\mathrm{i}}} & -\frac{1}{R_{1,2}} & \cdots & -\frac{1}{R_{1,\mathrm{m}}} \\ -\frac{1}{R_{2,1}} & \sum\limits_{i=1,..}^{m} \frac{1}{R_{2,\mathrm{i}}} & \cdots & -\frac{1}{R_{2,\mathrm{m}}} \\ \vdots & \vdots & \ddots & \vdots \\ -\frac{1}{R_{\mathrm{m},1}} & -\frac{1}{R_{\mathrm{m},2}} & \cdots & \sum\limits_{i=1,..}^{m} \frac{1}{R_{\mathrm{m,i}}} \end{bmatrix}, \tag{7.21}$$

where m is the number of nodes in each matrix. $R_{1,\mathrm{n}}$ is the connecting resistance between each node n and node number one.

The heat capacity matrix equals:

$$C = \begin{bmatrix} c_1 & 0 & ... & 0 \\ 0 & c_2 & ... & 0 \\ \vdots & \vdots & \ddots & \vdots \\ 0 & 0 & ... & c_{\mathrm{m}} \end{bmatrix}. \tag{7.22}$$

The power losses matrix:

$$P_{\mathrm{loss}} = \begin{bmatrix} P_1 \\ P_2 \\ \vdots \\ P_{\mathrm{m}} \end{bmatrix}. \tag{7.23}$$

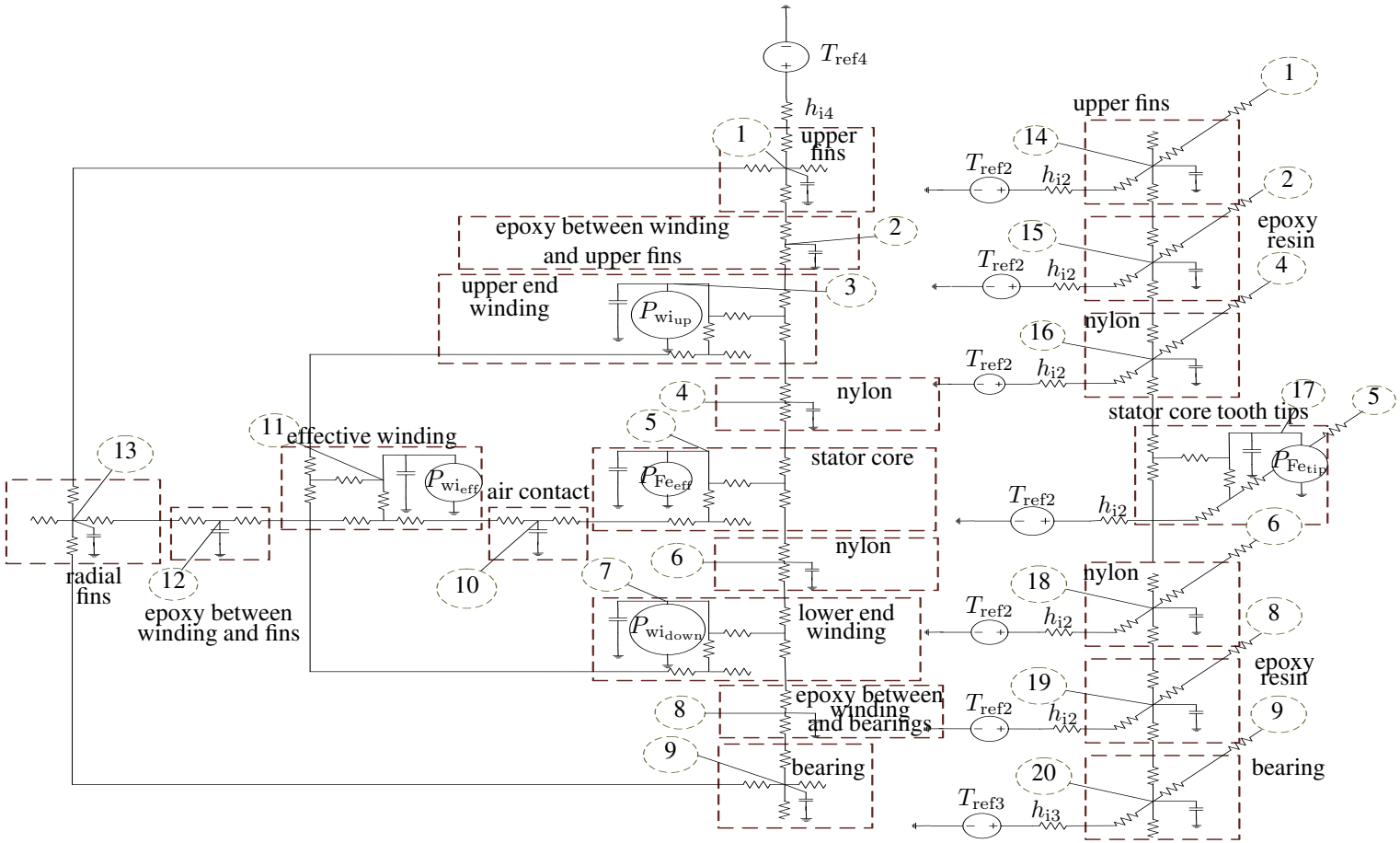

Figure 7.7: LPTN of the stator.

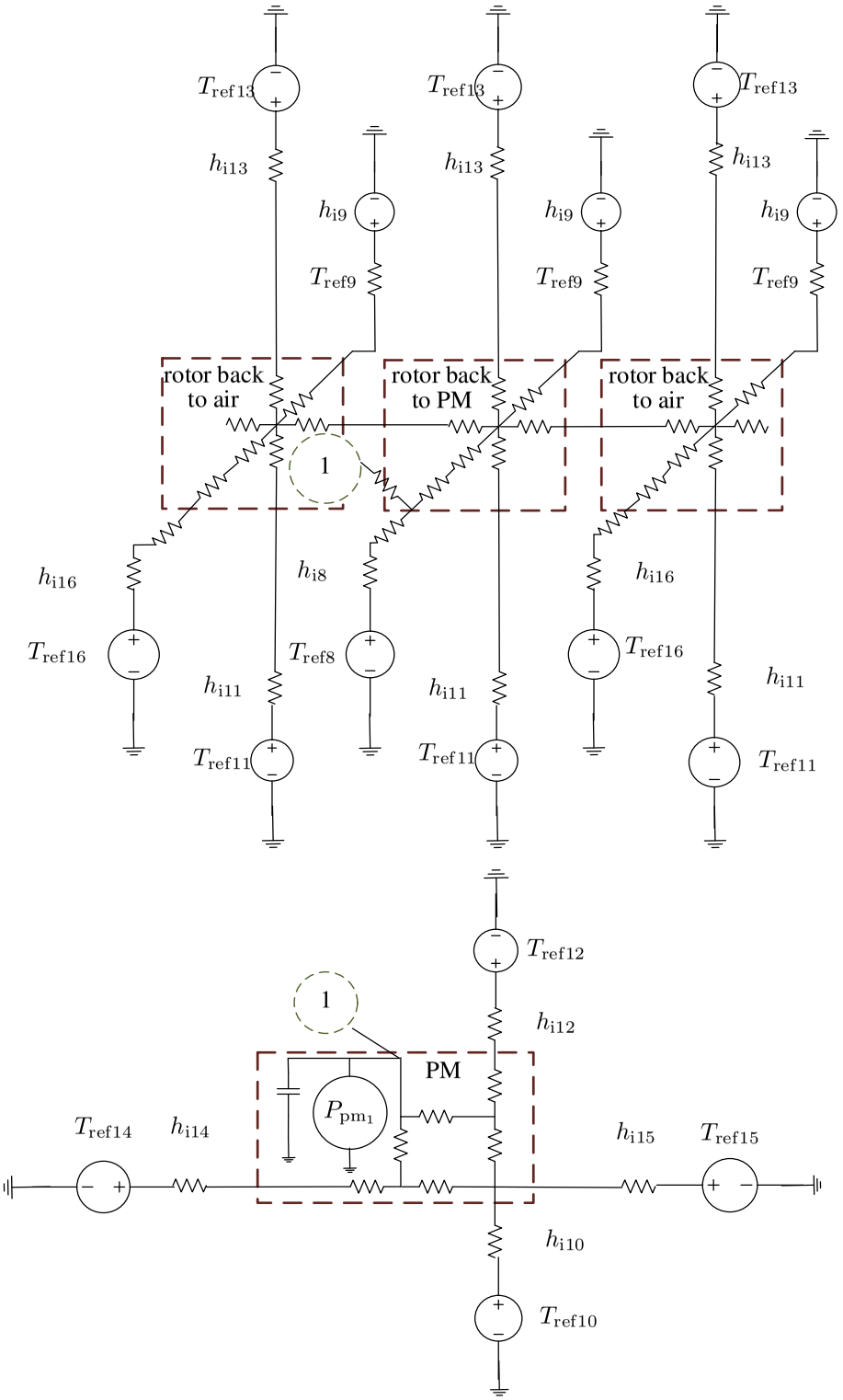

Figure 7.8: LPTN of the rotor.

The temperature of the machine equals:

$$T_{\mathrm{n}} = (G + \frac{C}{\Delta t})^{-1}(P_{\mathrm{loss}} + TR_{\mathrm{ref}}) + C\frac{T_{\mathrm{n-1}}}{\Delta t}, \tag{7.24}$$

where

- T_{n} is the temperature at a time instant n.
- Δt is the time interval between two subsequent times used in the calculation.
- TR_{ref} is the reference temperature imposed at each node $T_{\mathrm{ref_{d,m}}}$ divided by the connected resistance of this node $R_{\mathrm{d,m}}$.

$$TR_{\mathrm{ref}} = \begin{bmatrix} \sum\limits_{d=1,..} \frac{T_{\mathrm{ref_{d,1}}}}{R_{\mathrm{d,1}}} \\ \sum\limits_{d=1,..} \frac{T_{\mathrm{ref_{d,2}}}}{R_{\mathrm{d,2}}} \\ \vdots \\ \sum\limits_{d=1,..} \frac{T_{\mathrm{ref_{d,m}}}}{R_{\mathrm{d,m}}} \end{bmatrix}, \tag{7.25}$$

- $T_{\mathrm{n-1}}$ is the temperature rise at a time instant $n-1$.

The stator and rotor system of equations are solved for each time instant. However, the reference temperatures described in (7.10) are dependent on the rotor and stator temperature, therefore, an iterative solution is needed till the system converges for each time instant.

7.6 Inward Heat Extraction System Evaluation

Another model is also developed in [142] to model the effectiveness of the cooling inward fins behind the winding inside the machine. This model does not include these inward fins. This part is a result of co-operation with other colleagues.

In addition, to accurately measure the effectiveness of the inward fins, the boundaries of the model shown in Fig. 7.2 are all set to thermal insulation except the boundary number 4. This boundary is subjected to air. For this reason, a convection coefficient of h_4 =40 W/(m^{2}K) and a reference temperature of T_{ref4} =25$^o C$ are set.

To illustrate the need of a stator heat extraction system, a comparison is made between a 4kW, 2500rpm YASA without and with such a system using the 3D FE model. Only DC currents are imposed to the model. In this case, the same DC current is imposed to both models.

Total winding losses P_{wi} of 80W are imposed to the model with fins. In the example of the 4kW 2500rpm machine, 2mm thick fins are used. As a consequence,

the winding thickness decreases with a 20% when the inward fins exist. Therefore, only 64W is imposed to the model without fins.

The winding and core temperatures are shown in Figs. 7.9 and 7.10 respectively. They show that the inward fins greatly reduce the temperatures of the winding T_{wind} and cores T_{core}. They enhance the thermal behaviour of the stator heat extraction system. Table 7.5 shows the steady state temperature differences. It shows a 10 % reduction in the temperature because of the use of the fins.

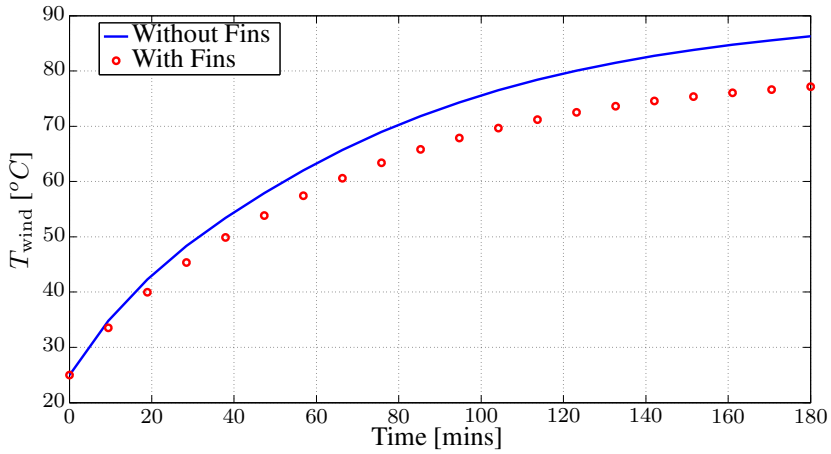

Figure 7.9: Comparison between the winding temperature without and with fins.

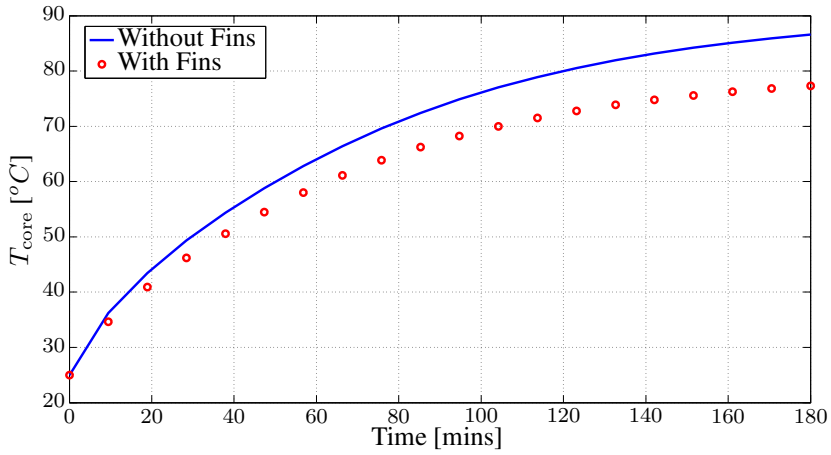

Figure 7.10: Comparison between the core temperature without and with fins.

Table 7.5: Steady state temperature differences and the effect of fins on the winding and core temperatures.

	Without fins	With fins	% enhancement of fins
$T_{\text{wind}} - 25\ [^oC]$	61	52	17 %
$T_{\text{core}} - 25\ [^oC]$	61	52	17 %

In Figs. 7.11 (a) and (b), the steady-state temperature are illustrated for a stator without and with stator heat extraction system. It is worth mentioning that with fins, a wining losses of 80W are imposed to the model, while without fins, only 64W are imposed.

Figure 7.11 (a) shows the temperature distribution without the inward fins. It is clear that the winding transports its copper losses in a radial direction towards the stator housing. Before reaching the stator housing, the heat flux has to travel trough an epoxy filled gap. The bad thermal conductivity results in a huge temperature gradient in the epoxy: the stator winding is at a high temperature while the stator housing remains relatively cool.

Figure 7.11 (b) shows the temperature distribution for the stator including the inward heat extraction system. The big contact surface between the winding and the heat extraction fin results in a better transfer of heat from the source in the winding to the stator housing. Fig. 7.11 (b) also indicates that the temperature difference over the thin heat extraction fin is very limited. Thanks to the inward heat extraction fins, the winding is thermally well coupled to the stator housing, and although the copper losses are increased due to the smaller winding thickness, the inside of the stator remains cooler in comparison with the machine without fins. Note that in Fig. 7.11 (b), a temperature gradient in the winding becomes visible due to the relative bad thermal conductance of the infiltrated winding in the direction perpendicular to the individual strands.

7.7 Conclusions

The cooling strategy in this PhD thesis is described, modeled and analyzed. The cooling of the stator is based on inward fins that are placed behind the stator windings. This cooling strategy provides a better cooling aspect for the losses in the stator winding and core laminations. To validate the effectiveness of the evacuation inward radial fins, a 3D thermal FE model is developed to validate the importance of these inward fins.

It is shown that the developed heat extraction system via the inward fins provides a great heat extraction system. The big contact surface between the winding and the heat extraction fin results in a better transfer of heat from the source in the

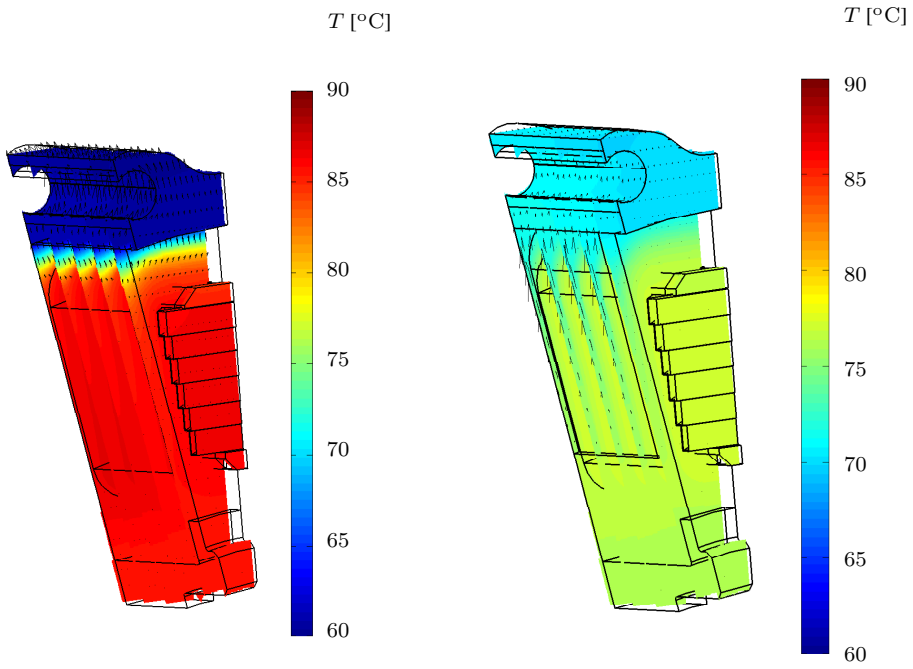

(a) Without fins (b) With fins

Figure 7.11: Cross section view on the steady state temperature distribution and heat flux in the stator of an AFPMSM without and with heat extraction fins. At the stator surface boundary, a convective heat coefficient of 40 W/(m^{2}K) and a reference temperature of 25^oC is set.

winding to the stator housing. Therefore, with the inward heat extraction system, the winding is thermally better cooled.

It is, therefore, recommended using these inward fins to provide excellent cooling for the machine. However, the dimensions of these fins should be chosen as a compromise between the copper losses and the optimum cooling of the machine.

In this chapter, a thermal analysis of an axial flux PM machine is discussed, and validated. Analytical equations for the convective heat transfer are used to decouple the model for the stator and the rotor finite element (FE) and lumped parameter thermal network (LPTN) models. As a consequence, thermal periodicity allowed to carry out the thermal simulations on a segment of the stator and the rotor only. This allows the separate computation of the stator and rotor segments. Therefore, the simulation time is strongly reduced compared with fully coupled transient 3-D simulations.

Chapter 8

YASA Experimental Setup

8.1 Introduction

In this chapter, the prototype construction of the machine is discussed. In addition, the electromagnetic properties of the analytical model of the combined SC-MEC model described in chapter 4 and 3D FE model are validated in this chapter. The lumped parameter thermal network and the thermal FE models described in chapter 7 are also validated.

8.2 Prototype Construction

In [35], the electromagnetic design of a 4kW, 2500rpm YASA-machine was optimised for energy-efficiency. This design optimisation has resulted in a set of parameters listed in Table 8.1.

Figure 8.1 shows the prototype of the YASA machine. It shows the stator and the rotor. The stator core consists of thin laminated grain oriented material. The windings are placed around the stator core. A plastic end plate is placed between the end-winding and the stator core. A stator housing is made of laminated aluminum sheets to reduce the eddy currents induced in them. Epoxy potting is used to get the different stator parts bonded into a single solid stator structure.

As this epoxy material has a high thermal resistivity, there will be a high thermal resistance between the winding and the stator housing. Therefore, radially inward heat extraction fins, are introduced in chapter 7 [142]. These fins provide an excellent thermal conduction path from the windings to the stator surface. This heat can be evacuated afterwards, by conventional cooling techniques such as forced air or water jacket cooling. In chapter 7, heat is radially evacuated from the stator surface by natural convection. These inward fins are shown in Fig. 8.1.

The construction of the stator and rotor is discussed in the following subsections. The experimental test setup was developed together with other colleagues.

Table 8.1: Axial flux PM machine prototype specifications.

Parameter	Value	Unit
Rated output power	4000	W
Rated speed	2500	rpm
Rated torque	15	Nm
Rated current	10	A
Pole number	16	-
Slot/tooth number	15	-
Outer diameter housing	195	mm
Outer diameter (active)	148	mm
Inner diameter (active)	100	mm
Axial length stator	61	mm
Total mass	9	kg
Magnet thickness	4	mm
Magnet width segments	18/21/24	mm
Magnets	NdFeB 40SH	-
Stator core material	M100-23r	-
Rotor back iron thickness	8	mm
Air gap length (adjustable)	$1 \leq 5$	mm
Slot width	11	mm

8.2.1 Construction of the rotors

The two rotor discs shown in Fig. 8.2 are made of 8mm thick steel, and combine two major functions. Firstly, they are a back-iron for the magnetic flux, and secondly they carry the high attraction forces from the permanent magnets to the stator cores. In general, the required thickness of these rotor discs is set by mechanical constraints rather than the electromagnetic ones.

On these rotor discs, the permanent magnets are glued. These magnets are 4mm thick in the axial direction, which is also the direction of the magnetisation. Adjacent magnets are magnetised in the opposite direction. In this prototype YASA-machine, each discs has 16 magnets, which results in a machine with eight pole pairs.

The permanent magnet material is NdFeB 40SH. This material grade combines a high remanent flux density, *i.e.* 1.300T at 20°C, with a sufficiently high operating temperature of 150°C. As this material has a relatively good electrical conductance, the eddy currents are induced in the permanent magnets by stator slotting and stator armature reaction. To limit the eddy currents and their corresponding power losses, segmentation of the permanent magnets [38] is introduced. In the prototype machine, the radial height (24mm) of the magnet is divided into three (3 times 8mm). The tangential lengths become 18, 21 and 24mm. The axial thickness *i.e.* the magnetisation direction is 4mm. This 4mm thickness results in an air gap flux density

of about 0.95T. To protect the permanent magnet material towards corrosion, each magnet segment is coated with a copper-nickel alloy.

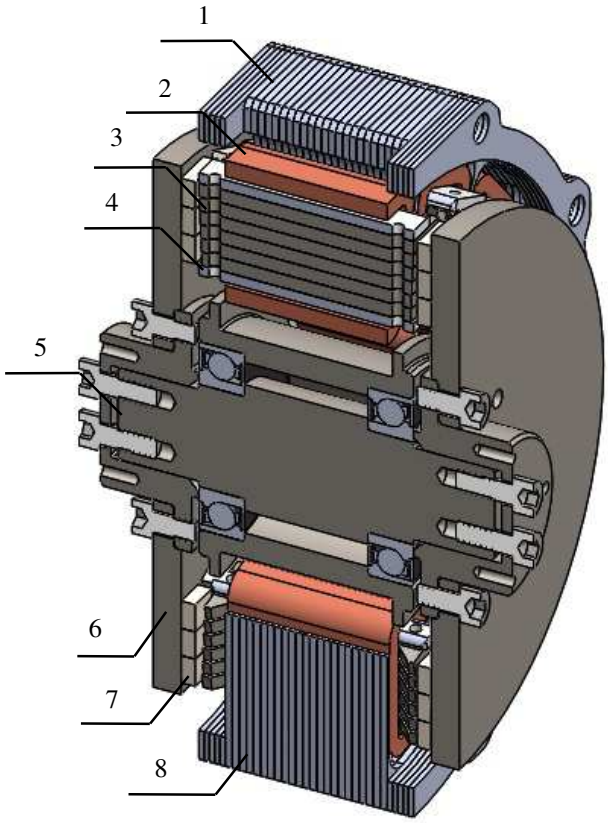

Figure 8.1: Cross section view on the prototype YASA-machine. (1) Laminated stator housing. (2) Concentrated winding. (3) Laminated core with 6 different stacks. (4) Nylon contact between end-winding and stator core. (5) Shaft. (6) Rotor disc back iron. (7) Permanent magnet (PM). (8) Inward heat extraction fin [142].

8.2.2 Construction of the modular stator element

Together with the rotor discs and the permanent magnets, the modular stator elements are the electromagnetic active components of the machine. Such a modular stator element includes a ferromagnetic core and a concentrated winding.

In the prototype YASA-machine, the ferromagnetic core is made of thin laminated silicon steel sheets. As the direction of the magnetic field in these cores

Figure 8.2: Rotor view for the YASA-machine.

is always in the axial direction, a grain-oriented material is used. In the YASA-machines, the use of such a grain-oriented material results in strong reduction of the core losses in comparison with the non-oriented ones [143]. In theory[1], the use of this grain-oriented material results in core losses less than 40W at rated load and speed. The core losses are measured at no load at the rated speed by the torque transducer.

After the stack of the stator core is made, it is impregnated in an epoxy resin to keep the individual steel laminates in place. This is shown in Fig. 8.3. Consequently, an electrical isolation foil is wound around the core. On this insulation foil, the winding is placed. This winding is composed of two parallel strands of 1.12mm diameter. The number of turns is equal to 57.

8.2.3 Experimental Test Set-Up

To perform measurements, the AFPMSM prototype is placed into a test set-up of which an overview is given in Fig. 8.4. In this test set-up, an asynchronous 7.5kW, 3000rpm motor is used as a prime-mover and is powered by a commercial drive. Set-points to this drive for the speed (or torque) are given by a dSPACE 1104 plat-

[1]Neglecting the degradation of the magnetic material properties due to cutting process, perpendicular fringing fluxes, *etc.*

form. The AFPMSM is used as a generator connected to the fully-programmable three-phase load.

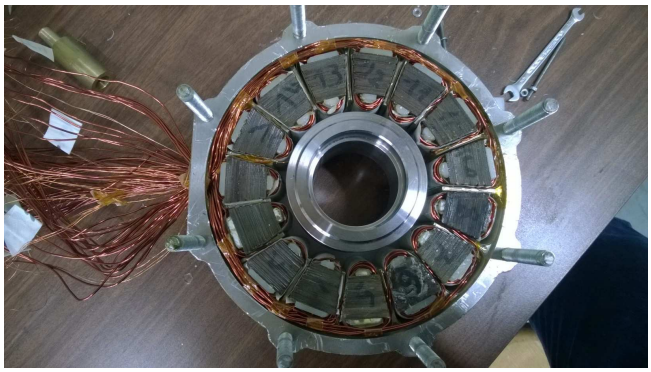

Figure 8.3: Stator view for the YASA-machine.

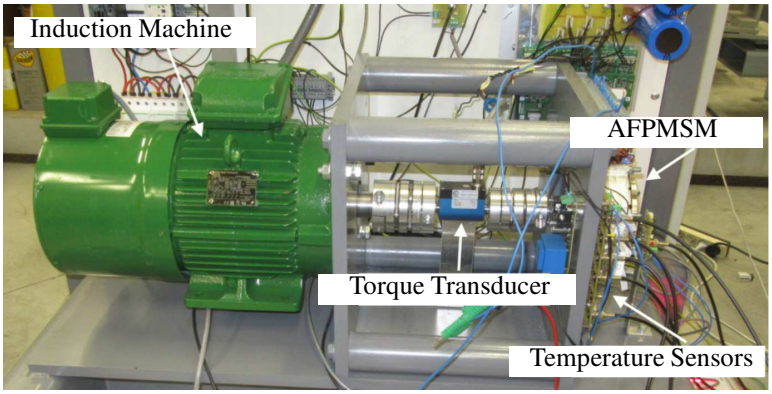

Figure 8.4: Axial-flux PM machine test set-up. From left to right: load (asynchronous) machine, torque sensor with couplings, axial flux PM prototype machine.

Feedback of the speed signal is realised by an incremental encoder attached to the asynchronous motor. Together with the torque value measured by the Lorenz DR2112 (nominal torque of 50Nm, accuracy of 0.1%) torque sensor, an accurate value of the mechanical power is achieved. Measurement on the electrical side of the prototype machine is done using a Tektronix PA4000 power analyzer. Interface boards are made to transfer the different sensors signals into the dSPACE platform.

The AFPMSMs can be operated using a dSPACE controlled custom-designed inverter and a Semikron SEMiX101GD12E4s IGBT-module, or can be connected to a fully-programmable three-phase load.

This load has the advantage of that it does not use a pulse-width modulation, which make the measurements less sensitive to the electromagnetic interference

(EMI).

Several temperature sensors, indicated in Fig. 8.4, are inserted in the test set-up to measure the temperature of the different parts of the machine. An infrared temperature sensor ZTP-135SR is used to measure the rotor temperature T_{pm}. For the winding T_{wind} and core temperatures T_{core}, platinum resistance thermometers of part number of PT100 are placed inside them. The room temperature where the measurement carried out is 25°C.

8.3 Experimental Validations

8.3.1 Electromagnetic Models Validations

In this part, the SC-MEC and the 3D FE model described in chapter 4 are compared with the experimental test setup shown in Fig. 8.4.

The experiment is done at a speed of 1000rpm. The load of the AFPMSM is a resistive load of 6Ω. The output rms current of the AFPMSM is 8 Amps which corresponds to an electromagnetic torque of 11.4Nm. The no load rms voltage is 58V. The output full load rms voltage is 48V.

Figures 8.5 and 8.6 show good agreements between the analytical, FE, and experimental results for no load and full load respectively. In addition, inductance comparison is made in Table 8.2. The comparison shows a good agreement between the two models with the experimental results.

Table 8.2: Inductance per phase between SC-MEC model, 3D FE model, and experimental results.

	Ana. Model	3D FE. Model	Exp. Results
Inductance (mH)	4.6	4.4	4

8.3.2 Thermal Models Validations

To distinguish between the different loss components of the machine, the NdFeB PMs in the rotor are replaced by aluminum trapezoidal dummy PMs. The span of the aluminum is set to 0.8 from the pole pitch. The rotor with the aluminum dummy PMs is shown in Fig. 8.7.

Moreover, to ensure that there are no eddy currents in the aluminum dummy PMs, DC currents are injected in the copper winding as shown in Fig. 8.8 in such a way that the flux lines cross the air gap in one direction only and returns via the bearings. Therefore, the losses in the rotor and PMs are assumed to be zero.

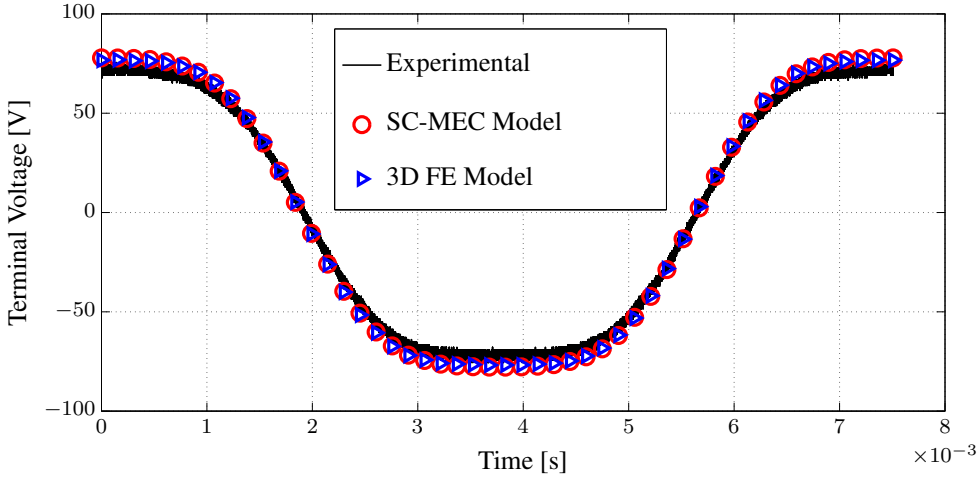

Figure 8.5: Voltage waveform of the studied machine under experiment at the no load.

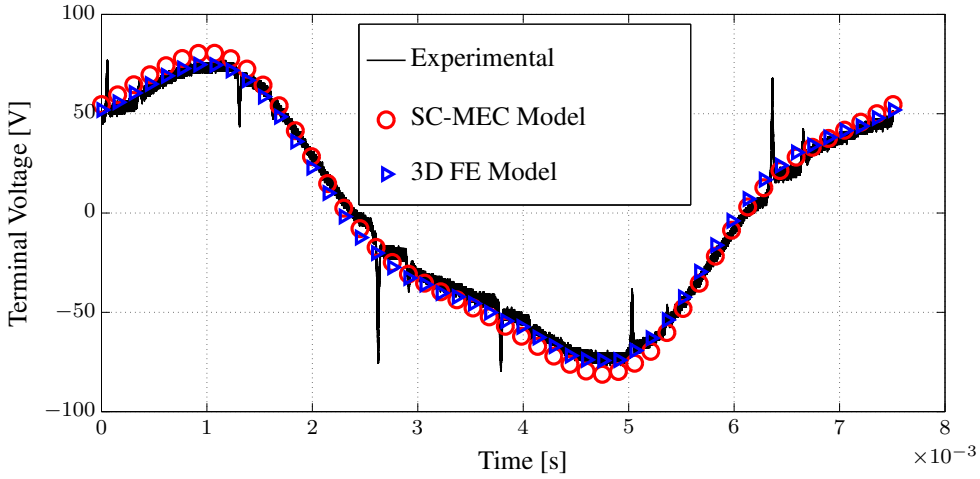

Figure 8.6: Voltage waveform of the studied machine under experiment at the full load.

Two cases of 1000 and 2000 rpm are studied. The DC current is kept constant during the experiments to keep the same winding losses of 100W for both cases.

In the experiment, there is a heat flux by conduction from the shaft and the bearing that is not taken into account in neither the 3D FE model nor the LPTN model.

The 3D FE model results of the rotor temperature distributions are shown in

Figure 8.7: The rotor with holes with the trapezoidal aluminum of the studied AFPMSM.

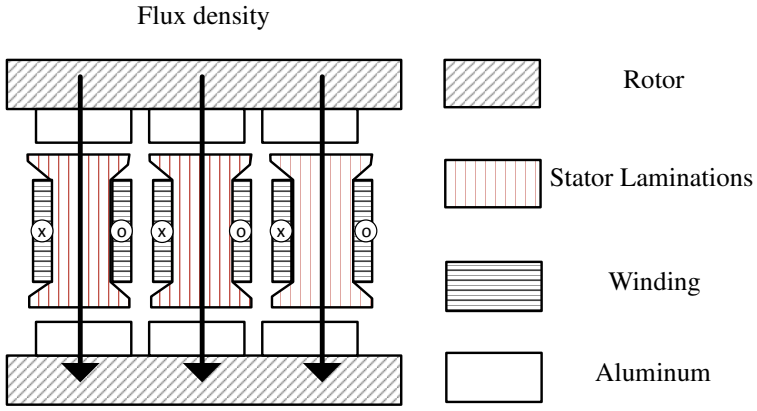

Figure 8.8: Stator and rotor configurations for the AFPMSM.

Figs. 8.9 (a) and (b) respectively for the two studied cases of 1000 rpm and 2000 rpm at steady state. As the rotor speed increases from 1000 to 2000 rpm, the rotor maximum temperature reduces from 30^{o}C to 27^oC. This is due to the higher convection coefficient in the air gap area.

The stator temperature distributions for the 3D FE model for the two studied cases are shown in Figs. 8.10 (a) and (b). The steady state average winding and core temperatures reduce about 14^{o}C at 2000rpm. This is due to the higher convection coefficient in the air gap area related with the higher speeds. This means that additional heat can be evacuated at higher speeds.

At 1000rpm, the temperatures for the winding $T_{\rm wind}$, core $T_{\rm core}$, and PM $T_{\rm pm}$

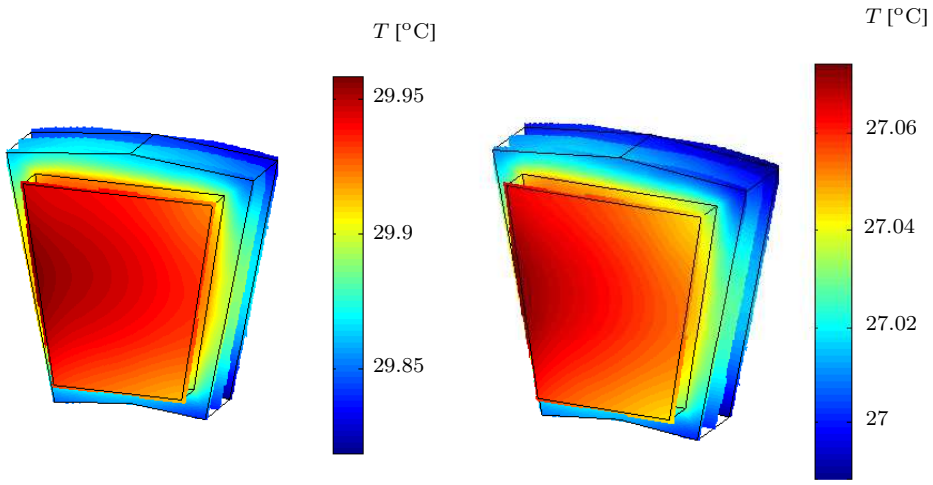

(a) 1000rpm (b) 2000rpm

Figure 8.9: Steady state rotor temperature distribution for the two studied cases of 1000 and 2000 rpm.

with respect to time are shown in Figs. 8.11, 8.12, and 8.13, respectively. In each figure, the experimental, 3D FE model, and LPTN results are presented.

The 3D FE model and the LPTN model winding and core temperatures result in larger temperature than the experimental result.

The rotor temperatures for the 3D FE model and the LPTN model are much lower than the experimental results. The main reason for this error is that the heat conduction from the shaft and the bearing to the rotor are not included in the 3D FE model and the LPTN model. This heat conduction raises the temperature of the rotor.

At 2000 rpm, the winding, core, and PM temperatures are shown in Figs. 8.14, 8.15, and 8.16 respectively.

The 3D FE model and the LPTN model give better results for the core and winding temperatures than at 1000rpm. This is due to the higher convection coefficient in the air gap area associated with higher speeds. The effect of the air gap convection coefficient becomes more significant at higher speeds.

The 3D FE model and the LPTN model under estimate the rotor temperatures. This is again due to that the heat transfer towards the bearings and the shaft is not included.

Additionally, Tables 8.3 and 8.4 show the steady state temperature differences between the different modeling techniques and the experimental setup at 1000 and 2000 rpm.

At 1000rpm, the maximum difference between the 3D FE model for the core

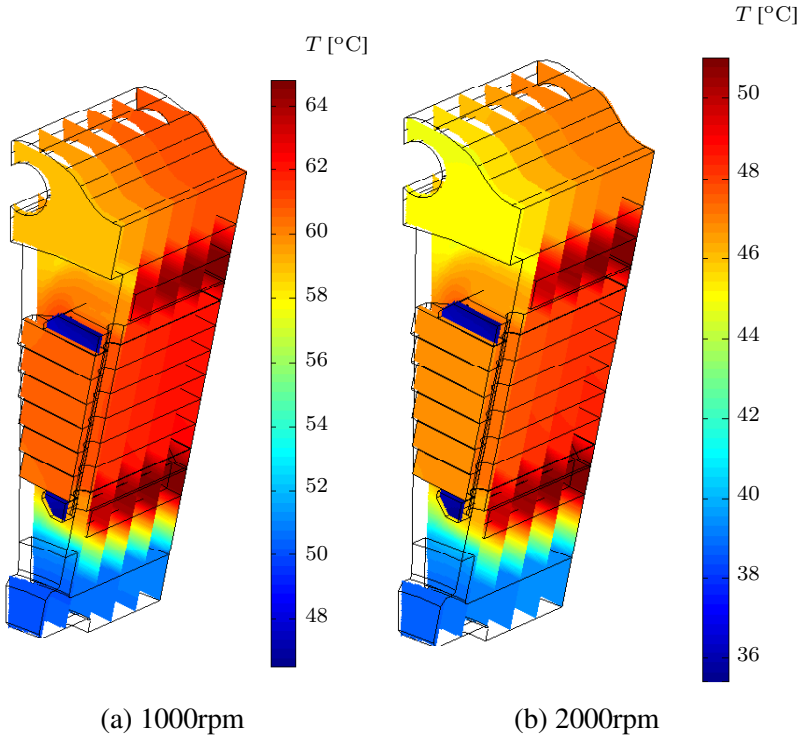

(a) 1000rpm (b) 2000rpm

Figure 8.10: Steady state stator temperature distribution for the two studied cases of 1000 and 2000 rpm.

and winding temperatures in percentage from the experimental result is 25.9%. The 3D FE model and the LPTN model underestimate the rotor temperature. As early mentioned, the main reason for this tendency is that the conduction heat transfer towards the shaft and the casing is not included in the 3D FE and the LPTN model.

The LPTN gives more accurate results with a percentage error of 17.8% for the winding temperature. The LPTN considers blocks with complex shapes as rectangles with area equal to the average area of the complex shape. This can cause a difference between the LPTN and the 3D FE model.

At 2000rpm, shown in Table 8.4, the maximum difference between the 3D FE model for the core and winding temperatures in percentage from the experimental setup is 9.1%.

The LPTN gives more accurate result than the 3D FE model with a percentage error of 4.4% for the winding temperature.

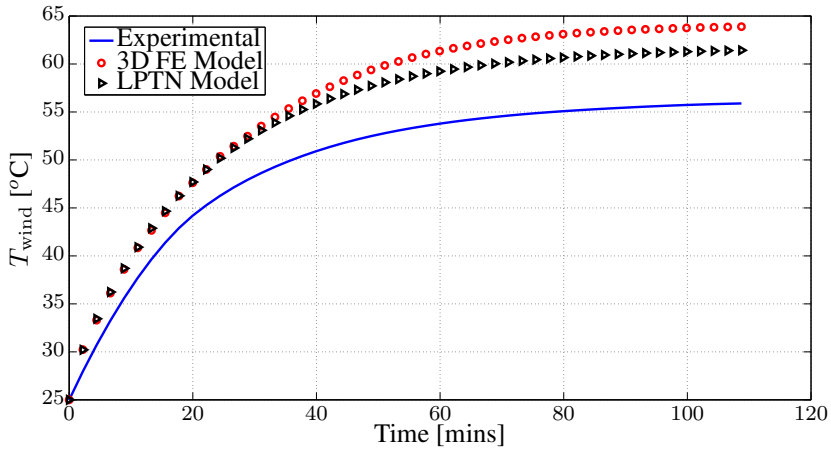

Figure 8.11: Winding temperature T_{wind} as a function of the time for the experimental, 3D FE model, and the LPTN at 1000rpm.

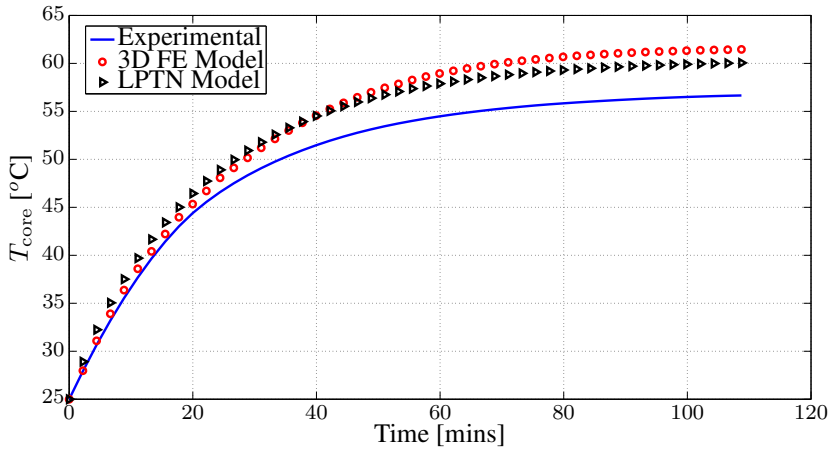

Figure 8.12: Core temperature T_{core} as a function of the time for the experimental, 3D FE model, and the LPTN at 1000rpm.

The CPU time of the LPTN model is compared with the 3D FE model. This was done on a core i5 processor, and 8 GB installed memory with 64 bit operating Windows 8 system.

Table 8.5 summarizes the CPU time between the FE model and the LPTN model. The LPTN model is very fast compared to the FE models. The LPTN model solves the complete problem in a 1s only.

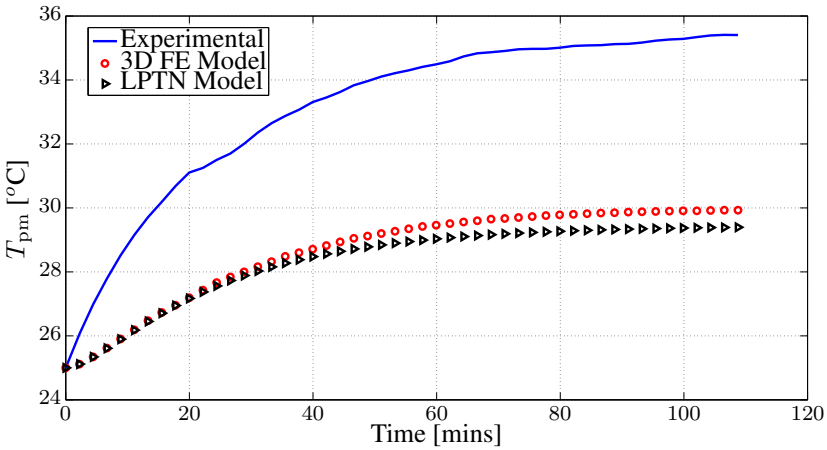

Figure 8.13: PM temperature $T_{\rm pm}$ as a function of the time for the experimental, 3D FE model, and the LPTN at 1000rpm.

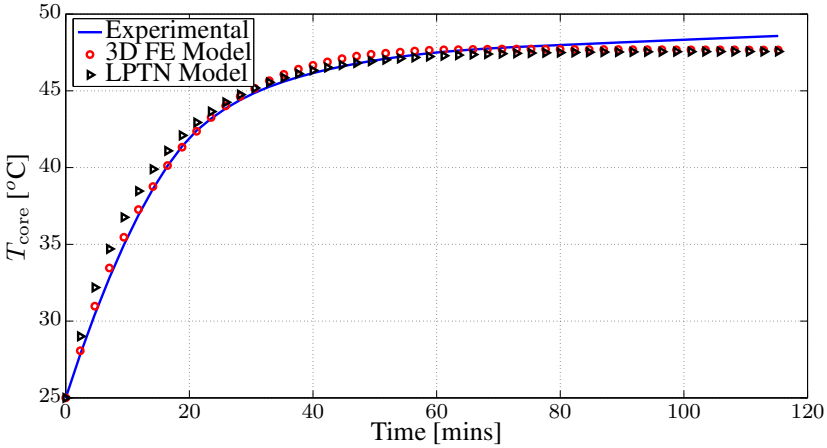

Figure 8.14: Winding temperature $T_{\rm wind}$ as a function of the time for the experimental, 3D FE model, and the LPTN at 2000rpm.

8.4 Machine Performance Over Entire Working Speed Range

In this section, the field weakening (FW) approach discussed in chapter 6 is used to obtain the performance of the machine over a wide speed range. In this approach, the operation is divided into two modes. These modes are shown in Fig. 6.2.

The first mode is when only q-axis current (MTPA region) is injected inside the machine. This mode ends when the voltage of the machine reaches the rated value. Afterwards, a negative d-axis current is injected through the machine (FW region)

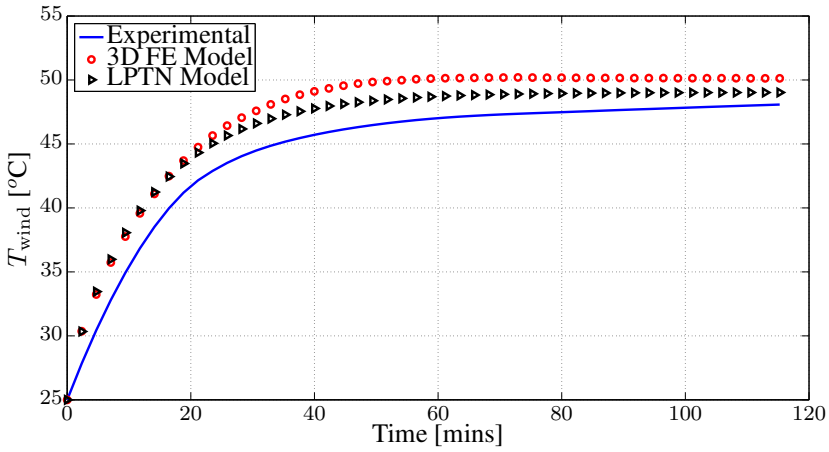

Figure 8.15: Core temperature T_{core} as a function of the time for the experimental, 3D FE model, and the LPTN at 2000rpm.

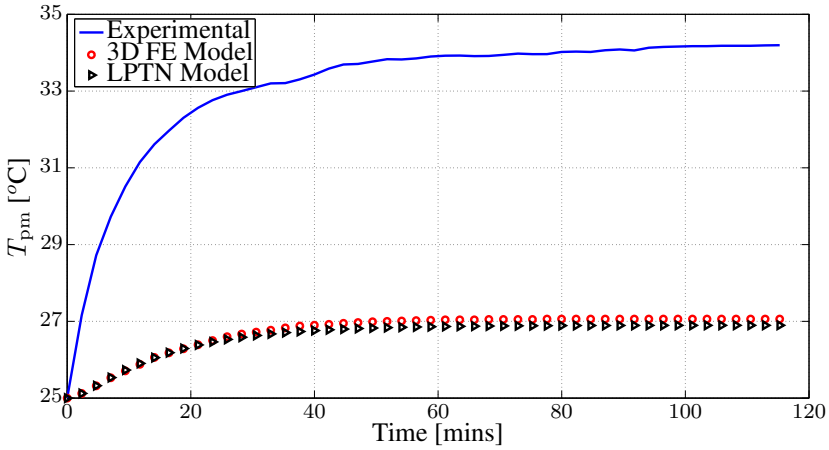

Figure 8.16: PM temperature T_{pm} as a function of the time for the experimental, 3D FE model, and the LPTN at 2000rpm.

by a value that keeps the terminal voltage and current with their rated values.

The distributions of the q and d axis currents inside the machine for different torque and speed values are shown in Figs. 8.17 and 8.18 respectively. The d-axis current is zero when the speed is below 3000rpm and negative above this speed.

The analytical model developed in chapter 4 is used to calculate the machine performance parameters in terms of the terminal voltage V_{t}, and iron losses P_{Fe}. In addition, the PM losses P_{pm} are calculated using the circuit model described in chapter 5.

The rms value of the terminal voltage V_t over a wide speed range is shown in

Table 8.3: Steady state temperature for the winding, core temperatures, and PM temperatures for 1000 rpm.

	Experimental	3D FE Model	LPTN
$T_{\text{wind}} - 25$	30.9	38.9	36.4
$T_{\text{wind}} - 25$ [%]	-	25.9	17.8
$T_{\text{core}} - 25$	31.7	36.46	35
$T_{\text{core}} - 25$ [%]	-	15.0	10.41
$T_{\text{pm}} - 25$	10.5	4.9	4.4
$T_{\text{pm}} - 25$ [%]	-	53.3	58.1

Table 8.4: Steady state temperature for the winding, core temperatures, and PM temperatures for 2000 rpm.

	Experimental	3D FE Model	LPTN
$T_{\text{wind}} - 25$	23	25.1	24
$T_{\text{wind}} - 25$ [%]	-	9.1	4.4
$T_{\text{core}} - 25$	23.6	22.7	22.6
$T_{\text{core}} - 25$ [%]	-	3.8	4.2
$T_{\text{pm}} - 25$	9.4	2	1.9
$T_{\text{pm}} - 25$ [%]	-	78.7	79.8

Table 8.5: Comparison of the CPU time between the LPTN and the FE model.

Model Type	CPU Time
3D FE Model	26 mins
LPTN	1s

Fig. 8.19. It is clear that below 3000rpm, the voltage increases till reaching the rated voltage. Afterwards, the voltage is kept almost constant because of injection of the negative d-axis currents.

The iron losses of the machine P_{Fe} over a wide speed range are shown in Fig. 8.20. The iron losses increase with the speed because of the high gradient of change of the flux density with respect to time.

When q-axis currents are only injected in the MTPA region, the iron losses remain almost the same at the same speed. This is nearly dependent on the machine design. This depends on how much amount of torque is produced by the PMs and how much amount amount is produced by the currents. As long as the PMs produce

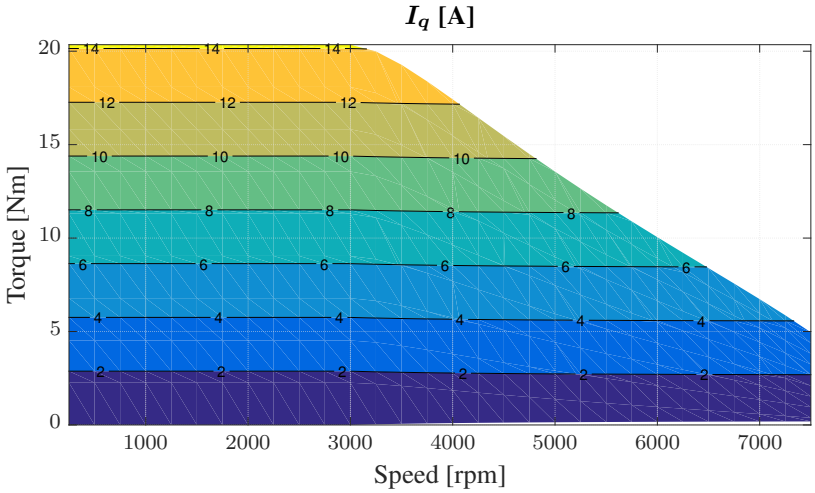

Figure 8.17: q-axis current distribution over a wide speed range for different torque and speed values.

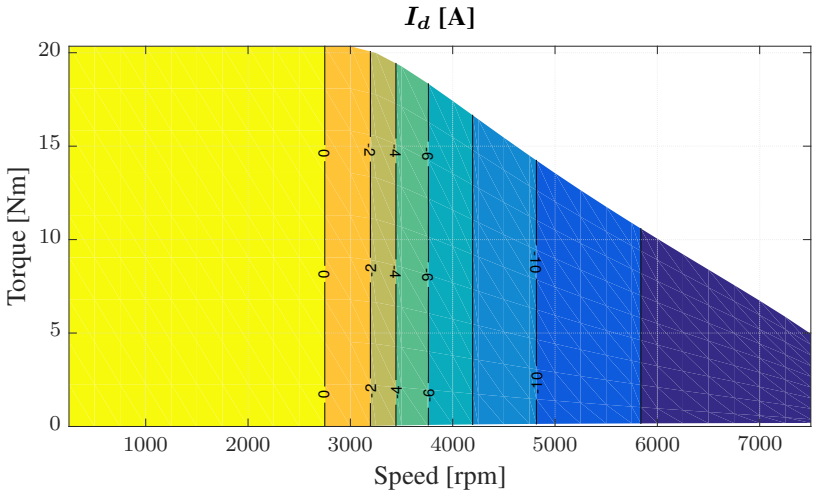

Figure 8.18: d-axis current distribution over a wide speed range for different torque and speed values.

much more torque, there will be no large gradient in the iron losses with respect to the q-axis current.

When d-axis currents start to be injected in the FW region, the flux density reduces inside the iron. Therefore, the iron losses reduce. However, because of the speed increase, the iron losses increases. Therefore, at the start of the operation of the FW region, the iron losses slightly increase with respect to the speed. As the speed increases more, the iron losses will eventually increase with a higher rate.

The PM losses of the machine P_{pm} over a wide speed range are shown in Fig.

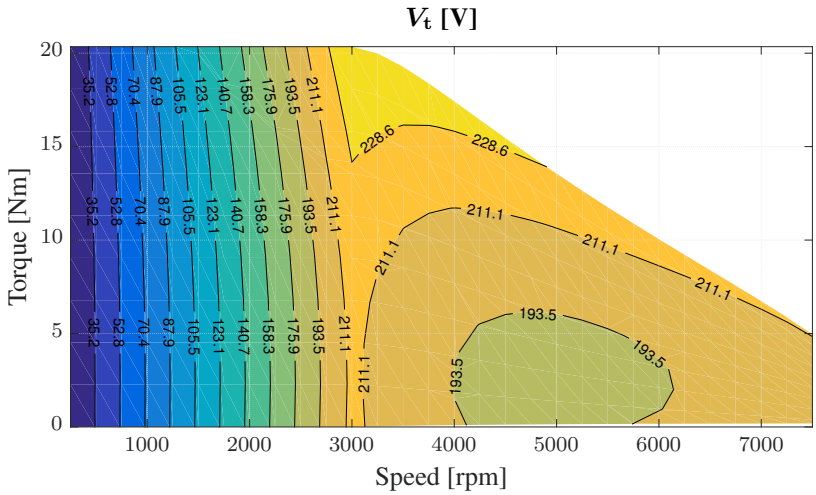

Figure 8.19: Terminal voltage distribution over a wide speed range for different torque and speed values for different d and q axis currents injected in the machine.

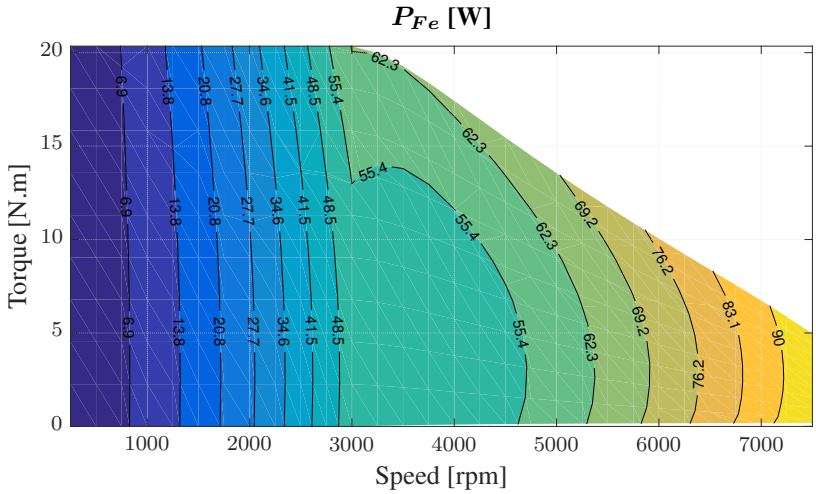

Figure 8.20: Iron losses distribution over a wide speed range for different torque and speed values for different d and q axis currents injected in the machine.

8.21. The PM losses are dependent on two components. They are the slotting effect which appears mostly at no load and the magnetomotive force (MMF) produced by the currents. The MMF produces higher losses as the speed increases. Therefore, as expected because of the MMF harmonics, when the speed increases the PM losses increases too as shown in Fig. 8.21.

In the MTPA region, where q-axis currents are only injected at the same speed,

the MMF harmonic components increase leading to much more PM losses.

Injecting the negative d-axis currents leads to additional PM losses. d-axis currents impose additional harmonics on the MMF distribution in space. Therefore, additional d-axis current would rise up the rate at which PM losses expands.

The copper losses in this performance analysis test include the temperature rise effect using (8.1):

$$R_{\mathrm{s}} = R_{\mathrm{so}} \left[1 + \alpha(T_{\mathrm{wind}} - T_o)\right], \tag{8.1}$$

where R_{so} is the stator resistance at the room temperature, α is the temperature coefficient at room temperature which equals $0.0040411/^oC$, and T_o is the room temperature of 20^oC.

The effect of temperature rise on the resistance is included during the computation of the LPTN.

Figure 8.22 shows the copper losses distribution over a wide speed range. The copper losses depends on the summation of the d and q axis currents.

Figures 8.23, 8.24 and 8.25 show the winding, core, and PM temperatures distribution respectively over a wide speed range. The temperature distribution of the winding and the core are almost the same.

In spite of the low losses at very low speeds, the temperatures at very low speeds are very high compared to the other speed ranges. However, due to the low convection coefficients in the air gap area, the cooling is done only via the stator surface. Therefore, all heat is evacuated through the stator surface. Consequently, the winding and core temperature are higher than at normal operation.

As the speed rises more than the rated speed, the temperatures should increase because of the additional losses appearing at higher speeds. However, due to the better convection coefficients in the air gap area at very high speeds, it allows better cooling for the rotor and stator.

However, at very high speeds, the PM losses increase rapidly reaching 115W leading to much higher temperatures shown in Fig. 8.25.

The complete efficiency map of the machine is depicted in Fig. 8.26. At rated load conditions, the efficiency of the machine equals 97%.

8.5 Conclusions

In this chapter, the experimental setup is illustrated, the electromagnetic 3D FE model and the SC-MEC developed in chapter 4 is validated via the developed experimental setup. The validation is done at a speed of 1000rpm. The validation is done for the terminal voltage at no load and full load conditions.

The thermal models are also validated by the experimental setup. The LPTN gives good results compared to the 3D FE model and with very fast appealing results of 1s compared to 26 minutes of the 3D FE model. More thermal inves-

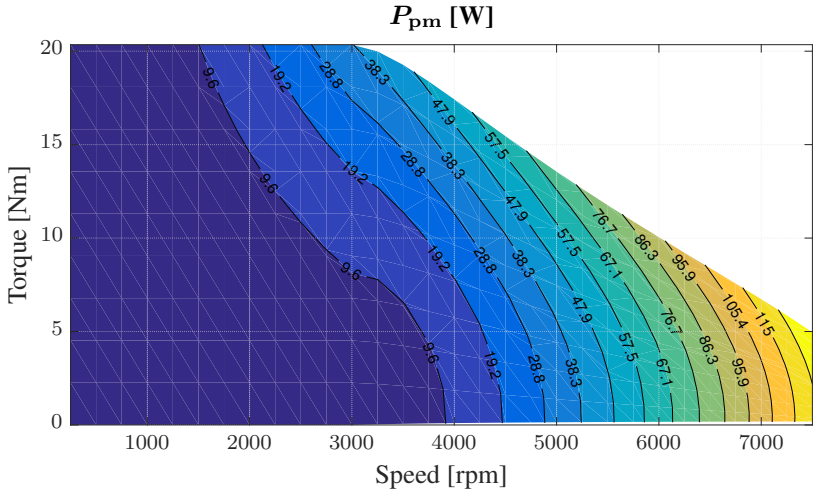

Figure 8.21: PM losses distribution over a wide speed range for different torque and speed values for different d and q axis currents injected in the machine.

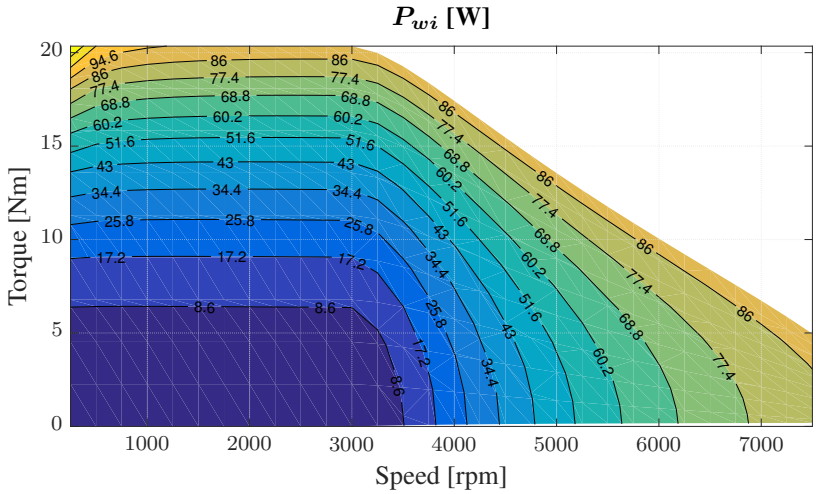

Figure 8.22: Copper losses distribution over a wide speed range for different torque and speed values for different d and q axis currents injected in the machine.

tigations are needed to model the heat conduction from the bearing and the shaft towards the rotor and the stator to have better results compared to the experiments.

The effect of operation over a wide speed range is studied in the chapter. Thanks to the developed electromagnetic and thermal models, the authors are capable to compute all the required parameters of the machine. These parameters include the losses, the terminal voltage, and the temperature distribution.

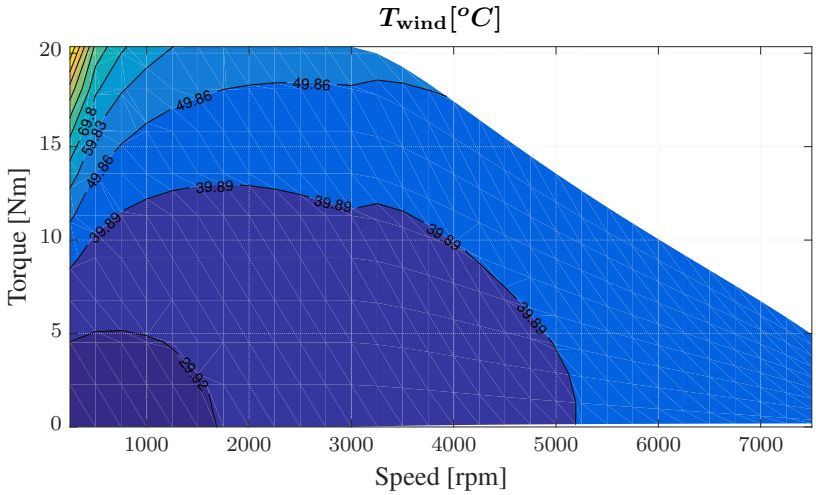

Figure 8.23: Winding temperature distribution over a wide speed range for different torque and speed values for different d and q axis currents injected in the machine.

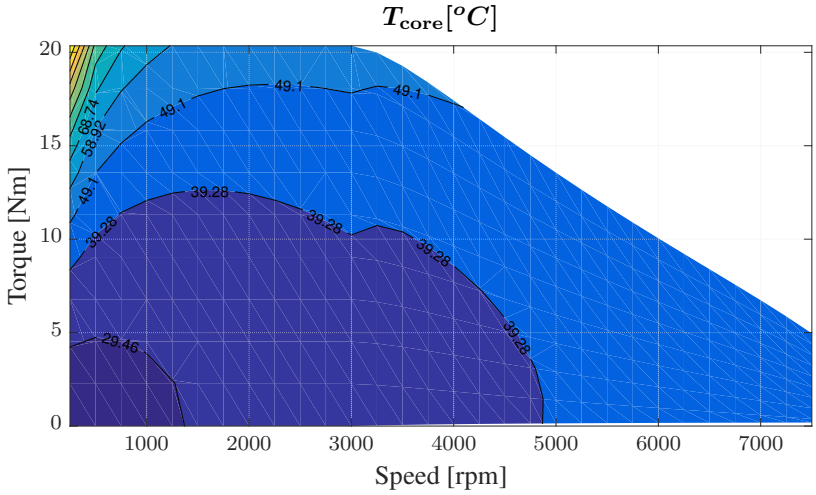

Figure 8.24: Core temperature distribution over a wide speed range for different torque and speed values for different d and q axis currents injected in the machine.

In spite of the higher losses at the maximum speed, the temperature of the machine remained within the limits similar to the rated condition. This is due to the better convection coefficient in the air gap area. This gives a better cooling opportunity at higher speeds.

In conclusion, the LPTN together with the design toolbox developed in this thesis can be used to design the AFPMSM for any power and speed.

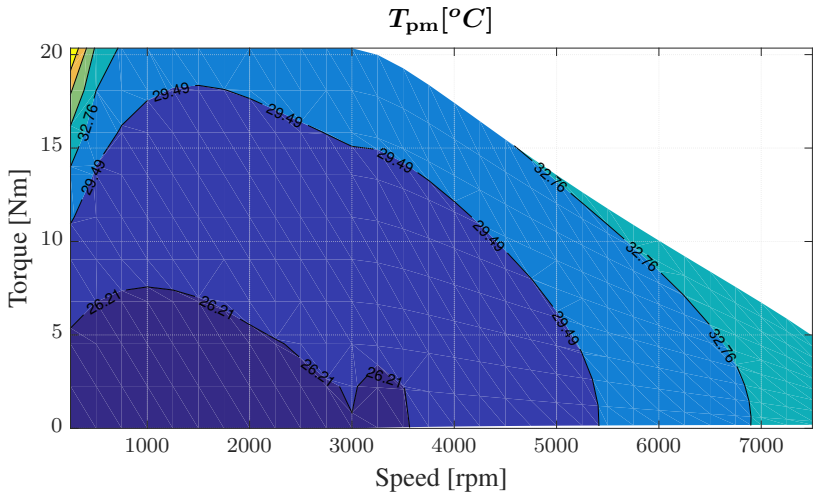

Figure 8.25: PM temperature distribution over a wide speed range for different torque and speed values for different d and q axis currents injected in the machine.

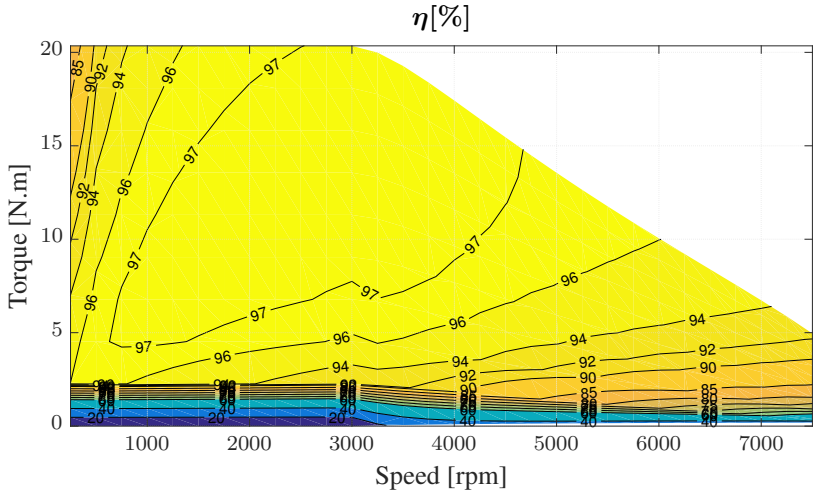

Figure 8.26: efficiency map distribution over a wide speed range for different torque and speed values for different d and q axis currents injected in the machine.

Chapter 9

Concluding Remarks

9.1 Conclusions

The research focusses on the electromagnetic design of the axial flux permanent magnet synchronous machine (AFPMSMs). In this context, the yokeless and segmented armature (YASA) machine is selected. Thanks to the absence of the stator yoke, the YASA machine can provide a great power density and a great efficiency compared to other topologies. The use of a double layer fractional slot concentrated winding in the YASA topology results in an easy and a modular construction of the stator windings and an easy assembly of the complete machine. During this work, the YASA machine is firstly introduced and compared to other axial and radial flux machines. This comparison has shown the superiority of the YASA machine.

An accurate electromagnetic and thermal modeling of the AFPMSMs is a mandatory task for an optimal design of the machine. During this research, a weak coupled thermal and electromagnetic analytical tool has been developed. This tool is capable of designing the machine for any input power and speed for any application. This tool is based upon validated electromagnetic and thermal analytical models.

Therefore, different electromagnetic modeling techniques have been developed in this work including finite element (FE) and analytical models. Although, the high accuracy obtained by the 3D FE and 2D multi-slice FE models, they are very time consuming and therefore not recommended to be used within iterative optimization routines. Fast analytical models have been developed to precisely calculate all the electromagnetic characterstics of the machine including the terminal voltage, iron losses, eddy current losses in the permanent magnets, copper losses, torque ripple, and cogging torque of the machine.

To precisely compute the cogging torque and torque ripple of the AFPMSMs, different concepts of analytical models have been developed accordingly. They are based on conformal mapping techniques and on subdomain modeling techniques. All these techniques neglect saturation of the stator magnetic material, like most

analytical techniques. A comparative study between these models and FE models is done. This comparison is conducted for different slot openings and pole arc ratios. It is found that the subdomain model is the only analytical model that can accurately compute the cogging torque and torque ripple of the machine. However, all models can accurately compute the induced voltage at no load. In addition, the models based on conformal mapping are much faster than the subdomain model.

Moreover, a novel analytical model (SC-MEC), based on a combined solution of Maxwell's equations and a magnetic equivalent circuit (MEC), is developed. This model overcomes the disadvantage of the models in the previous paragraph that takes into account the non-linear behavior of the magnetic material. This model can accurately compute the stator core iron losses and the terminal voltage of the machine. The SC-MEC model is validated through 2D and 3D finite element models. It is concluded that the SC-MEC model can accurately obtain the terminal voltage and the stator iron losses with a significantly lower CPU time compared to the FE models.

Rare earth permanent magnet (PM) materials, which are widely used in PM machines, have high electric conductivity. Therefore, eddy currents are induced in the permanent magnets when they are subjected to a time varying magnetic flux density. This leads to increased temperature of the PMs and to a demagnetization risk. Therefore, an electric circuit model is developed to compute these eddy currents produced in the PMs. This electric circuit is composed of resistances and inductances, and sources representing the time variant flux density in the magnets. A comparison is made between two variants: the first including the reaction field of the currents in the permanent magnets, and the second neglecting this reaction field. The electric circuit model is successfully verified amongst others through a complete 3D transient finite element model. In addition, it is found that during the design procedure, the reaction effect has a negligible effect on the total losses. Therefore, it is sufficient to use the model without the reaction field effect during the design phase.

An electromagnetic design toolbox has been developed for AFPMSMs. Thanks to the developed analytical models described before, the design toolbox gives the optimal geometrical machine parameters in a very short time and in an accurate way. This toolbox is developed to optimize the machine geometry based on the required input power and speed of the application. Since AFPMSMs are currently used in hybrid electric vehicles, it is important to check their applicability in the field weakening (FW) region. Consequently, a sensitivity analysis is done for different geometrical parameters and slots/poles/phases in order to select the optimum values for machines operating in the FW region. It is found that for better FW capabilities, which means that high ratios of maximum speed to rated speed are required, low values of the slots per poles ratio are needed. In terms of power density, it is not only important to use combinations with a high winding factor, but also to search for combinations with number of PMs larger than the number of slots. It is also worth mentioning that this toolbox has been used to design a 100kW YASA

machine for a low speed high torque (wind turbine) application. The prototype of this machine is still under construction.

An experimental 4kW research prototype has been developed in the Electrical Energy Laboratory of Ghent University together with several colleagues to validate the electromagnetic models. Furthermore, an overview of the cooling concept of the stator core and winding is evaluated. This cooling concept is based on inward fins that are placed between the windings to provide a new path for evacuating the heat. Moreover, a convective cooling concept is studied based on on a specific shape of the permanent magnets. The magnets are positioned on the rotor discs with air channels between them. During rotation, the magnets behave like ventilator fins, creating a radial air flow through the air gaps and providing excellent convective cooling.

Thermal models are developed to evaluate the complete performance of the YASA AFPMSMs. These models are based on a finite element and a lumped parameter thermal network (LPTN). The main advantage of these models is the use of convection coefficient equations developed by the department of Flow, Heat and Combustion Mechanics of Ghent University. These equations allow the separation of the stator and rotor thermal models. This separation allows fast results to be obtained. However, more research is still needed to model the rotor and the bearing in the FE and the LPTN models. Moreover, experimental verifications by the developed 4kW YASA machine are provided at the end. However, more research is still need to accurately include the shaft and the bearings in the LPTN and the FE models to obtain precise results for the rotor temperature.

9.2 Recommendations for Future Research

This work was focussing on the electromagnetic and thermal modeling of the axial flux permanent magnet machine. A design toolbox was developed to optimally design the machine. The following research topics are recommended to improve the performance of the YASA axial flux machines.

Parameterized magnetic equivalent circuit in the axial and circumferential direction with different number of nodes can be developed. This discretization allows the best selection for the number of nodes to optimally track the physical behavior of the fields.

From an electromagnetic point of view, a study for the effect of different permanent magnet shapes on the cogging torque, torque ripple, and the output quality of the induced voltage can be done. The developed subdomain model can be used to obtain such a study.

More thermal investigations are needed to model the shaft and the bearing within the 3D finite element model and the lumped parameter thermal network.

Multi-physics design of the axial flux machine is important to have a complete design toolbox of the machine. Therefore, it is important to investigate the scalability of the lumped parameter thermal network (LPTN). A validated scalable model

can be used for any geometry of the axial flux machine. The scalable LPTN should consider all possible geometries with the suggested cooling concept. Hot spot of the machine should be tracked to optimally design the machine.

Life time estimation of the machine using the coupled electromagnetic and thermal models can be done.

In addition, a detailed investigation on the mechanical design of the stator assembly is still missing. The stator is exposed to an electromagnetic axial force that causes stress on the stator housing. A minimum thickness of the stator core is required to attain this force. Analytical formulae for this mechanical thickness should be included in the final toolbox.

Using the developed optimization tool for the coupled electromagnetic and thermal model, scaling laws for the YASA machine for wind turbine applications from several kW to MW can be done. The objective at the end, is to provide the researchers and manufacturers by very simple equations that can be used directly to provide a good estimation of the final prototype.

Furthermore, the use of amorphous materials in the stator core elements can be considered. This involves the proper modeling of the material in the analytical model. Amorphous material has low iron losses up to high frequencies (several kHz), but a lower saturation flux density than the grain oriented silicon steel used in the prototype. Amorphous material may result in a “high-speed” axial flux machine, having a somewhat lower torque to weight ratio, but a much higher power-to-weight ratio at a high speed.

Appendices

Appendix A

Reluctance Evaluation of the MEC

Fig. 4.9 depicts different types of reluctance representation for different regions shown in Fig. 4.8. These are described in details below.

- In regions 1 and 2, the flux lines flow mainly in the axial direction and less lines flow in the circumferential direction. Therefore, it is only useful to use the T type reluctance described in Fig. 4.9 (a). The reluctances of these regions are derived according to the following set of equations.

  The maximum, minimum, and average tooth width equals:

$$\begin{aligned} T_{\mathrm{w_{max}}} &= \frac{2\pi R_{\mathrm{o}}}{N_{\mathrm{s}}} - b_{\mathrm{s}}, \\ T_{\mathrm{w_{min}}} &= \frac{2\pi R_{\mathrm{i}}}{N_{\mathrm{s}}} - b_{\mathrm{s}}, \\ T_{\mathrm{w_{av}}} &= \frac{T_{\mathrm{w_{max}}} + T_{\mathrm{w_{min}}}}{2}. \end{aligned} \tag{A.1}$$

  The reluctances of region 1 and 2, shown in Fig. 4.9 (a), equal:

$$\begin{aligned} R_{\mathrm{y1}} &= \frac{Y_{\mathrm{c1}}/6}{\mu_o \mu_r T_{w_{\mathrm{av}}} (R_{\mathrm{o}} - R_{\mathrm{i}})}, \\ R_{\mathrm{x1}} &= \frac{T_{\mathrm{w_{max}}} - T_{\mathrm{w_{min}}}/2}{\mu_{\mathrm{o}} \mu_{\mathrm{r}} \frac{Y_{\mathrm{c1}}}{3} (R_{\mathrm{o}} - R_{\mathrm{i}}) \log\left(\frac{T_{\mathrm{w_{max}}}}{T_{\mathrm{w_{min}}}}\right)}. \end{aligned} \tag{A.2}$$

- In region 3, where the flux starts to deviate and divide into more regions, the modeled flux lines are divided to three paths as shown in Fig. A.1. The variables shown in this figure are $X_{\min} = T_{\mathrm{w_{min}}}$, $X_{\max} = T_{\mathrm{w_{max}}}$, and

$Y = Y_{\mathrm{c1}}/3$. The variable (D) defines how much flux should flow into these paths. The shape of the reluctance is changed as shown in Fig. 4.9 (c). This reluctance representation shape was proven to be optimal by [75].

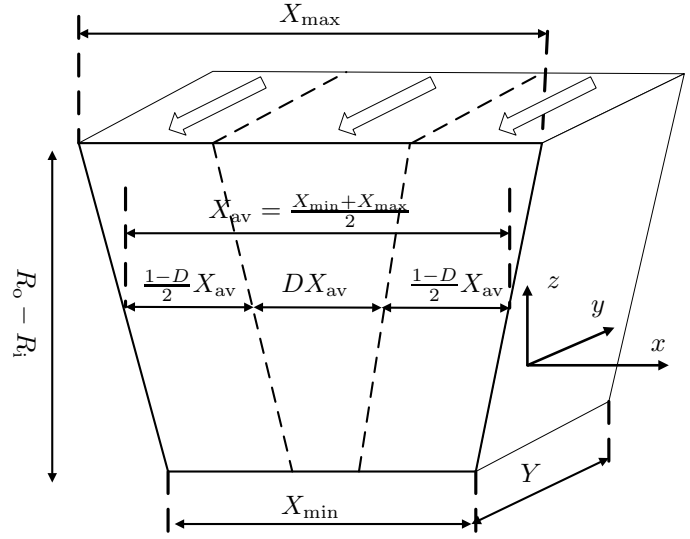

Figure A.1: A schematic front view of part of the tooth.

To obtain the value of the reluctances R_{y5} and R_{y6} shown in Fig. 4.9 (c), there are three parallel paths described in Fig. A.1. The distance at the average radius is equally distributed. Therefore, the value D equals $\frac{1}{3}$.

The reluctances of this region equals:

$$\begin{aligned}
R_{\mathrm{y4}} &= \frac{Y_{\mathrm{c1}}/12}{\mu_{\mathrm{o}}\mu_{\mathrm{r}} T_{\mathrm{w_{av}}} (R_{\mathrm{o}} - R_{\mathrm{i}})}, \\
R_{\mathrm{x4}} &= \frac{T_{\mathrm{w_{max}}} - T_{\mathrm{w_{min}}}/2}{\mu_{\mathrm{o}}\mu_{\mathrm{r}} \frac{Y_{\mathrm{c1}}}{6} (R_{\mathrm{o}} - R_{\mathrm{i}}) \log\left(\frac{T_{\mathrm{w_{max}}}}{T_{\mathrm{w_{min}}}}\right)}, \\
R_{\mathrm{y5}} &= \frac{Y_{\mathrm{c1}}/24}{\mu_{\mathrm{o}}\mu_{\mathrm{r}} \frac{1-D}{2} T_{\mathrm{w_{av}}} (R_{\mathrm{o}} - R_{\mathrm{i}})}, \\
R_{\mathrm{y6}} &= \frac{Y_{\mathrm{c1}}/24}{\mu_{\mathrm{o}}\mu_{\mathrm{r}} D T_{\mathrm{w_{av}}} (R_{\mathrm{o}} - R_{\mathrm{i}})}.
\end{aligned} \tag{A.3}$$

- Region 4, shown in Fig. 4.9 (b), is subdivided into three paths. In Fig. A.1, the value D equals $\frac{1}{3}$, hence, $X_{\mathrm{min}} = T_{\mathrm{w_{min}}} + \frac{b_{\mathrm{s}}-b_{\mathrm{so}}}{2}$, $X_{\mathrm{max}} = T_{\mathrm{w_{max}}} + \frac{b_{\mathrm{s}}-b_{\mathrm{so}}}{2}$, and $Y = Y_{\mathrm{c2}}/3$.

The reluctance equations are described below:

$$
\begin{aligned}
R_{\mathrm{y2}} &= \frac{Y_{\mathrm{c2}}/2}{\mu_{\mathrm{o}}\mu_{\mathrm{r}}\frac{1-D}{2}\left(\frac{b_{\mathrm{s}}-b_{\mathrm{so}}}{2}+T_{\mathrm{w_{av}}}\right)\left(R_{\mathrm{o}}-R_{\mathrm{i}}\right)},\\
R_{\mathrm{x2}} &= \frac{\frac{1-D}{4}\left(\frac{b_{\mathrm{s}}-b_{\mathrm{so}}}{2}+T_{\mathrm{w_{av}}}\right)}{\mu_{\mathrm{o}}\mu_{\mathrm{r}}Y_{\mathrm{c2}}\left(R_{\mathrm{o}}-R_{\mathrm{i}}\right)},\\
R_{\mathrm{y3}} &= \frac{Y_{\mathrm{c2}}/2}{\mu_{\mathrm{o}}\mu_{\mathrm{r}}D\left(\frac{b_{\mathrm{s}}-b_{\mathrm{so}}}{2}+T_{\mathrm{w_{av}}}\right)\left(R_{\mathrm{o}}-R_{\mathrm{i}}\right)},\\
R_{\mathrm{x3}} &= \frac{\frac{D}{2}\left(\frac{b_{\mathrm{s}}-b_{\mathrm{so}}}{2}+T_{\mathrm{w_{av}}}\right)}{\mu_{\mathrm{o}}\mu_{\mathrm{r}}Y_{\mathrm{c2}}\left(R_{\mathrm{o}}-R_{\mathrm{i}}\right)\log\left(\frac{\frac{b_{\mathrm{s}}-b_{\mathrm{so}}}{2}+T_{\mathrm{w_{max}}}}{\frac{b_{\mathrm{s}}-b_{\mathrm{so}}}{2}+T_{\mathrm{w_{min}}}}\right)}.
\end{aligned}
\tag{A.4}
$$

- Similar to region 4, region 5, shown in Fig. 4.9 (b), is subdivided into three nodes by the same ratio $D=\frac{1}{3}$, then, $X_{\mathrm{min}}=T_{\mathrm{w_{min}}}+b_{\mathrm{s}}-b_{\mathrm{so}}$, $X_{\mathrm{max}}=T_{\mathrm{w_{max}}}+b_{\mathrm{s}}-b_{\mathrm{so}}$, and $Y=Y_{\mathrm{c3}}/3$.

  The reluctance equations are described below:

$$
\begin{aligned}
R_{\mathrm{y2}} &= \frac{Y_{\mathrm{c2}}/2}{\mu_{\mathrm{o}}\mu_{\mathrm{r}}\frac{1-D}{2}\left(b_{\mathrm{s}}-b_{\mathrm{so}}+T_{\mathrm{w_{av}}}\right)\left(R_{\mathrm{o}}-R_{\mathrm{i}}\right)},\\
R_{\mathrm{x2}} &= \frac{\frac{1-D}{4}\left(b_{\mathrm{s}}-b_{\mathrm{so}}+T_{\mathrm{w_{av}}}\right)}{\mu_{\mathrm{o}}\mu_{\mathrm{r}}Y_{\mathrm{c2}}\left(R_{\mathrm{o}}-R_{\mathrm{i}}\right)},\\
R_{\mathrm{y3}} &= \frac{Y_{\mathrm{c2}}/2}{\mu_{\mathrm{o}}\mu_{\mathrm{r}}D\left(b_{\mathrm{s}}-b_{\mathrm{so}}+T_{\mathrm{w_{av}}}\right)\left(R_{\mathrm{o}}-R_{\mathrm{i}}\right)},\\
R_{\mathrm{x3}} &= \frac{\frac{D}{2}\left(b_{\mathrm{s}}-b_{\mathrm{so}}+T_{\mathrm{w_{av}}}\right)}{\mu_{\mathrm{o}}\mu_{\mathrm{r}}Y_{\mathrm{c2}}\left(R_{\mathrm{o}}-R_{\mathrm{i}}\right)\log\left(\frac{b_{\mathrm{s}}-b_{\mathrm{so}}+T_{\mathrm{w_{max}}}}{b_{\mathrm{s}}-b_{\mathrm{so}}+T_{\mathrm{w_{min}}}}\right)}.
\end{aligned}
\tag{A.5}
$$

Appendix B

AFPMSM Modes of Operation and Lossless Equations

Figure B.1 shows the operation under the maximum torque per ampere (MTPA) condition for speeds lower than the rated rotational speed n_{rated}. This applies only to surface PMSMs where the machine inductances ($L_{\mathrm{d}} = L_{\mathrm{q}}$) are equal. In this region, only q-axis (I_{q}) current as shown in Fig. B.1 is controlled to obtain the optimum torque per ampere. The terminal voltage V_{t} shown in Fig. B.1 is kept under the rated voltage in this region.

In the field weakening (FW) region, the machine operates with an injected d-axis current ($-I_{\mathrm{d}}$) as shown in Fig. B.1 with a value that keeps the voltage of the machine V_{t} at its rated value. The value of the total current in this case should not exceed the rated current value. Therefore, it is important that the machine inductance $L_{\mathrm{d}} = L_{\mathrm{q}}$ has a reasonable value to reduce the amount of the needed I_{d} to limit the full load voltage V_t to its rated value.

ψ_{pm} shown in Fig. B.1 represents the PM flux linkage in V.s. ω_{e} is the electrical speed in rad/sec. p is the number of pole pairs. The no load voltage E, at a speed of n_{m} in rpm corresponding to an electrical speed of $\omega_{\mathrm{e}} = p\frac{2\pi n_{\mathrm{m}}}{60}$, equals $\omega_{\mathrm{e}}\psi_{\mathrm{pm}}$.

In [144], the simplified lossless equations of the surface permanent magnet synchronous machines (SPMSMs) were presented, and they are given below:

$$V_{\mathrm{d}} = -\omega_{\mathrm{e}} L_{\mathrm{q}} I_{\mathrm{q}}, \tag{B.1}$$

$$V_{\mathrm{q}} = \omega_{\mathrm{e}} L_{\mathrm{d}} I_{\mathrm{d}} + \omega_{\mathrm{e}}\psi_{\mathrm{pm}}, \tag{B.2}$$

$$T_{\mathrm{e}} = (m/2)p(\psi_{\mathrm{pm}} I_{\mathrm{q}} + (L_{\mathrm{d}} - L_{\mathrm{q}}) I_{\mathrm{d}} I_{\mathrm{q}}). \tag{B.3}$$

In the surface AFPMSM $L_{\mathrm{d}} = L_{\mathrm{q}} = L_{\mathrm{s}}$. I_{d} and I_{q} are the d and q axis currents. T_{e} is the electromagnetic torque.

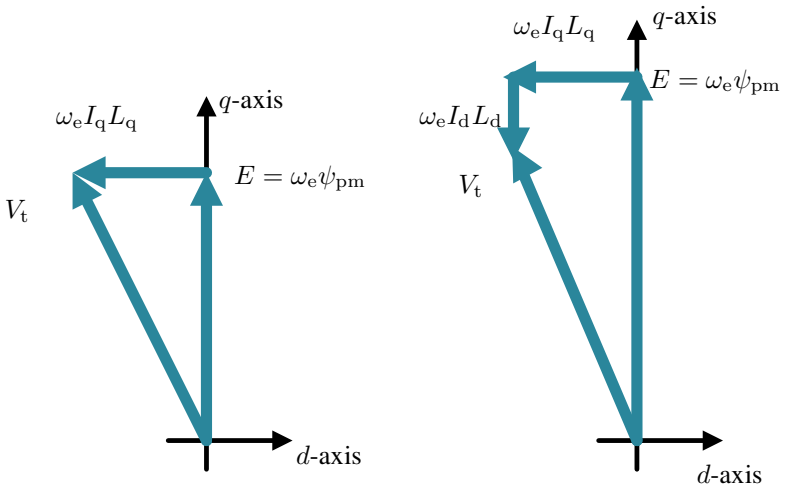

(a) MTPA (b) FW

Figure B.1: Operation in the MTPA and FW regions.

The machines voltage and current limits can be described by the following set of equations. The current/voltage limit equation describes the current/voltage limit circle shown in Fig. C.1. This limit is represented by the rated current I_{peak} and the rated voltage V_{peak}, respectively:

$$I_{\text{peak}}^2 = I_{\text{d}}^2 + {I_{\text{q}}}^2, \tag{B.4}$$

$$V_{\text{peak}}^2 = V_{\text{d}}^2 + {V_{\text{q}}}^2. \tag{B.5}$$

Combining the above equations together results in the following equations:

$$V_{\text{peak}}^2 = (\omega_{\text{e}} L_{\text{s}} I_{\text{q}})^2 + (\omega_{\text{e}} L_{\text{s}} I_{\text{d}} + \omega_{\text{e}} \psi_{\text{pm}})^2, \tag{B.6}$$

$$\frac{V_{\text{peak}}^2}{(\omega_{\text{e}} L_{\text{s}})^2} = (I_{\text{q}})^2 + (I_{\text{d}} + \frac{\psi_{\text{pm}}}{L_{\text{s}}})^2. \tag{B.7}$$

Appendix C

Finite and Infinite Speed Design

In this subsection, the modes of design are defined according to the voltage and current limits defined in the previous subsection

Figures C.1 (a) and (b) show the operation of surface PMSM under the FW mode. Two modes of operations are presented, one is the operation under the finite speed and the other one is under the infinite speed operation. Two circles are presented in these graphs. One corresponds to the rated current limit shown in (B.4), while the other one corresponds to the voltage limit shown in (B.7). The second circle is centered at $(-\frac{\psi_{\rm pm}}{L_{\rm s}})$ with a radius of $\frac{V_{\rm peak}}{(\omega_{\rm e} L_{\rm s})}$. It is obvious that increasing the speed will decrease the radius, i.e. the value, of the voltage circle.

Figure C.1 (a) shows the finite CPSR, where the $I_{\rm c} > I_{\rm peak}$, and Fig. C.1 (b) shows the finite CPSR where $I_{\rm c} < I_{\rm peak}$, with $I_{\rm c}$ being the characteristic current. In the case of the finite CPSR, the maximum speed ($n_{\rm max}$) that can be reached by the FW is shown in Fig. C.1, at which the voltage circle radius is $(\frac{\psi_{\rm pm}}{L_{\rm s}} - I_{\rm peak})$.

$$\frac{\psi_{\rm pm}}{L_{\rm s}} - I_{\rm peak} = \frac{V_{\rm peak}}{2\pi f_{\rm max} L_{\rm s}}, \tag{C.1}$$

where $f_{\rm max}$ corresponds to the frequency at the maximum speed $n_{\rm max} = 60 f_{\rm max}/p$. Then $n_{\rm max}$ could be defined as:

$$n_{\rm max} = 60 \frac{V_{\rm peak}}{2\pi L_{\rm s} p(\frac{\psi_{\rm pm}}{L_{\rm s}} - I_{\rm peak})}. \tag{C.2}$$

For an infinite speed design, the machine can operate from an electromagnetic point of view till theoretically infinite speed. This means that the inductances of the machine becomes very large so that a small *d*-axis current can weaken the flux. This enhances the efficiency at the maximum speed.

From the above discussion, it can be concluded that the characteristic current is the key parameter to determine the machine capability to work in the FW region. It is also advisable when working in the FW region to check the value of the maximum reachable speed.

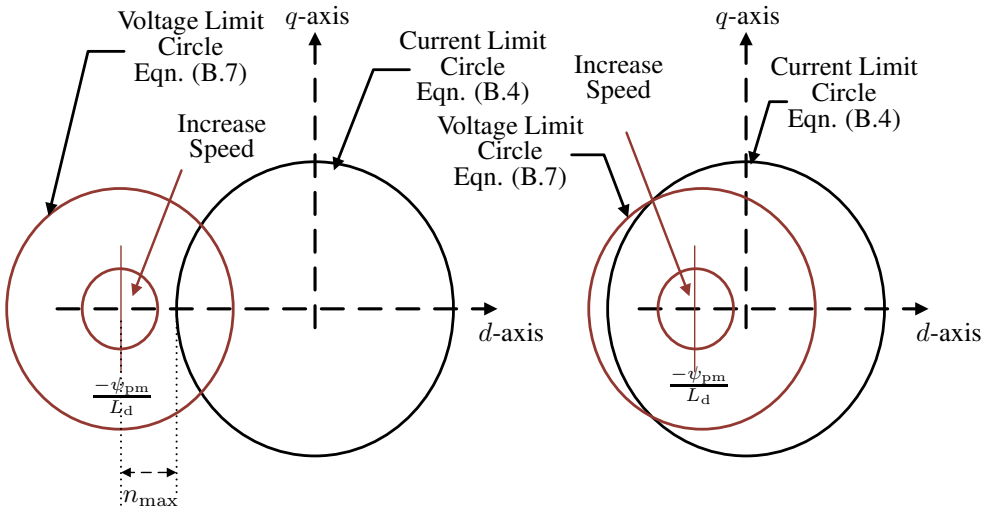

Figure C.1: Finite and infinite speed operation range.

Bibliography

[1] B. J. Chalmers, W. Wu, and E. Spooner, "An axial-flux permanent-magnet generator for a gearless wind energy system," *IEEE Transactions on Energy Conversion*, vol. 14, no. 2, pp. 251–256, 1999.

[2] A. Di Gerlando, G. Foglia, M. F. Iacchetti, and R. Perini, "Axial flux PM machines with concentrated armature windings: Design analysis and test validation of wind energy generators," *IEEE Transactions on Industrial Electronics*, vol. 58, no. 9, pp. 3795–3805, 2011.

[3] Y. Chen, P. Pillay, A. Khan, and S. Member, "PM Wind Generator Topologies," *IEEE Transactions on Industry Applications*, vol. 41, no. 6, pp. 1619–1626, 2005.

[4] T. F. Chan and L. L. Lai, "An axial-flux permanent-magnet synchronous generator for a direct-coupled wind-turbine system," *IEEE Transactions on Energy Conversion*, vol. 22, no. 1, pp. 86–94, Mar. 2007.

[5] G. F. Price, T. D. Batzel, M. Comanescu, and B. A. Muller, "Design and testing of a permanent magnet axial flux wind power generator," *the 2008 IAJC IJME International Conference*, 2008.

[6] A. Parviainen, M. Niemela, J. Pyrhonen, and J. Mantere, "Performance comparison between low-speed axial-flux and radial-flux permanent-magnet machines including mechanical constraints," in *IEEE International Conference on Electric Machines and Drives, 2005.*, 2005, pp. 1695–1702.

[7] T. J. Woolmer and M. D. McCulloch, "Analysis of the yokeless and segmented armature machine," *Proceedings of IEEE International Electric Machines and Drives Conference, IEMDC 2007*, vol. 1, pp. 704–708, 2007.

[8] F. Caricchi, F. G. Capponi, F. Crescimbini, and L. Solero, "Experimental study on reducing cogging torque and no-load power loss in axial-flux permanent-magnet machines with slotted winding," *IEEE Transactions on Industry Applications*, vol. 40, no. 4, pp. 1066–1075, 2004.

[9] W. Fei, P. C. K. Luk, and K. Jinupun, "A new axial flux permanent magnet Segmented-Armature-Torus machine for in-wheel direct drive applications," *PESC Record - IEEE Annual Power Electronics Specialists Conference*, pp. 2197–2202, 2008.

[10] H. Kierstead, R. J. Wang, and M. J. Kamper, "Design Optimization of a Single Sided Axial Flux Permanent Magnet In-Wheel Motor with Non-Overlap Concentrated Winding," Stellenbosch, South Africa, pp. 36–40, 2009.

[11] F. Giulii Capponi, G. De Donato, and F. Caricchi, "Recent advances in axial-flux permanent-magnet machine technology," *IEEE Transactions on Industry Applications*, vol. 48, no. 6, pp. 2190–2205, 2012.

[12] S. Kahourzade, A. Mahmoudi, H. W. Ping, and M. N. Uddin, "A comprehensive review of axial-flux permanent-magnet machines," *Canadian Journal of Electrical and Computer Engineering*, vol. 37, no. 1, pp. 19–33, 2014.

[13] C. C. Chan, "Axial-field electrical machines - design and applications," *IEEE Transactions on Energy Conversion*, vol. EC-2, no. 2, pp. 294–300, Jun. 1987.

[14] S. M. Mirimani, A. Vahedi, and F. Marignetti, "Effect of inclined static eccentricity fault in single stator-single rotor axial flux permanent magnet machines," *IEEE Transactions on Magnetics*, vol. 48, no. 1, pp. 143–149, 2012.

[15] M. Aydin, S. Huang, and T. A. Lipo, "Axial flux permanent magnet disc machines: a review," *Research Report*, pp. 61–71, 2004.

[16] ——, "Torque quality and comparison of internal and external rotor axial flux surface-magnet disc machines," *IEEE Transactions on Industrial Electronics*, vol. 53, no. 3, pp. 822–830, 2006.

[17] C. Du-Bar, "Design of an axial flux machine for an in-wheel motor application," *PhD dissertation, Chalmers University of Technology*, 2011.

[18] F. Profumo, Z. Zhang, and A. Tenconi, "Axial flux machines drives: A new viable solution for electric cars," *IEEE Transactions on Industrial Electronics*, vol. 44, no. 1, pp. 39–45, 1997.

[19] F. Caricchi, Crescimbini, F, and Honorati, O, "Performance of Coreless-Winding Axial-Flux Prmanent Magnet Generator with Power Output at 400 Hz, 300 r/m," *IEEE Transactions on Industry Applications*, vol. 34, no. 6, pp. 1263–1269, 1998.

[20] S. M. Hosseini, M. Agha-Mirsalim, and M. Mirzaei, "Design, prototyping, and analysis of a low cost axial-flux coreless permanent-magnet generator," *IEEE Transactions on Magnetics*, vol. 44, no. 1, pp. 75–80, 2008.

[21] M. J. Kamper, R. J. Wang, and F. G. Rossouw, "Analysis and performance of axial flux permanent-magnet machine with air-cored nonoverlapping concentrated stator windings," *IEEE Transactions on Industry Applications*, vol. 44, no. 5, pp. 1495–1504, 2008.

[22] A. Parviainen, "Design of axial-flux permanent-magnet low-speed machines and performance comparison between radial-flux and axial-flux machines," *PhD dissertation, Acta Universitatis Lappeenrantaensis*, 2005.

[23] A. M. EL-Refaie, "Fractional-slot concentrated-windings synchronous permanent magnet machines: Opportunities and challenges," *IEEE Transactions on Industrial Electronics*, vol. 57, no. 1, pp. 107–121, Jan. 2010.

[24] F. Caricchi, F. Crescimbini, F. Mezzetti, and E. Santini, "Multistage axial-flux pm machine for wheel direct drive," in *IEEE Transactions on Industry Applications*, vol. 32, no. 4. IEEE, 1996, pp. 882–888.

[25] S. Vun, M. McCulloch, and C. Leong, "The development of an electromagnetic analytical design tool for megawatt-scale YASA generators," *IET Conference on Renewable Power Generation (RPG 2011)*, pp. P44–P44, 2011.

[26] S. T. Vun and M. D. McCulloch, "Optimal Design Method for Large-Scale YASA Machines," *IEEE Transactions on Energy Conversion*, vol. 30, no. 3, pp. 900–907, 2015.

[27] K. Sitapati and R. Krishnan, "Performance comparisons of radial and axial field, permanent-magnet, brushless machines," *IEEE Transactions on Industry Applications*, vol. 37, no. 5, pp. 1219–1226, 2001.

[28] A. Cavagnino, M. Lazzari, F. Profumo, and A. Tenconi, "A comparison between the axial flux and the radial flux structures for PM synchronous motors," in *IEEE Transactions on Industry Applications*, vol. 38, no. 6. IEEE, Nov. 2002, pp. 1517–1524.

[29] Y. Chen, P. Pillay, and A. Khan, "PM wind generator comparison of different topologies," *Conference Record - IAS Annual Meeting (IEEE Industry Applications Society)*, vol. 3, pp. 1405–1412, 2004.

[30] M. Aydin and M. Gulec, "Reduction of cogging torque in double-rotor axial-flux permanent-magnet disk motors: A review of cost-effective magnet-skewing techniques with experimental verification," *IEEE Transactions on Industrial Electronics*, vol. 61, no. 9, pp. 5025–5034, Sep. 2014.

[31] P. Sergeant, H. Vansompel, and L. Dupré, "Influence of stator slot openings on losses and torque in axial flux permanent magnet machines," in *Mathematics and Computers in Simulation*, vol. 130, 2016, pp. 22–31.

[32] A. Hemeida, M. Taha, A. A. E. Abdallh, H. Vansompel, L. Dupré, and P. Sergeant, "Applicability of Fractional Slot Axial Flux Permanent Magnet Synchronous Machines in the Field Weakening Region," *IEEE Transactions on Energy Conversion*, vol. 32, no. 1, pp. 111–121, Mar. 2016.

[33] H. Tiegna, A. Bellara, Y. Amara, and G. Barakat, "Analytical modeling of the open-circuit magnetic field in axial flux permanent-magnet machines with semi-closed slots," *IEEE Transactions on Magnetics*, vol. 48, no. 3, pp. 1212–1226, 2012.

[34] H. Vansompel, P. Sergeant, and L. Dupré, "A multilayer 2-D-2-D coupled model for eddy current calculation in the rotor of an axial-flux PM machine," *IEEE Transactions on Energy Conversion*, vol. 27, no. 3, pp. 784–791, Sep. 2012.

[35] H. Vansompel, "Design of an energy efficient axial flux permanent magnet machine," *PhD dissertation, Ghent University*, 2013.

[36] H. Vansompel, P. Sergeant, and L. Dupré, "Optimized design considering the mass influence of an axial flux permanent-magnet synchronous generator with concentrated pole windings," *IEEE Transactions on Magnetics*, vol. 46, no. 12, pp. 4101–4107, Dec. 2010.

[37] A. Hemeida, B. Hannon, H. Vansompel, and P. Sergeant, "Comparison of three analytical methods for the precise calculation of cogging torque and torque ripple in axial flux PM machines," *Mathematical Problems in Engineering*, p. 2171547, 2016.

[38] A. Hemeida, P. Sergeant, and H. Vansompel, "Comparison of Methods for Permanent Magnet Eddy Current Loss Computations With and Without Reaction Field Considerations in Axial Flux PMSM," *IEEE Transactions on Magnetics*, vol. 51, no. 9, p. 8107511, 2015.

[39] H. Tiegna, Y. Amara, and G. Barakat, "Overview of analytical models of permanent magnet electrical machines for analysis and design purposes," *Mathematics and Computers in Simulation*, vol. 90, pp. 162–177, 2013.

[40] T. F. Chan, L. L. Lai, and S. Xie, "Field computation for an axial flux permanent-magnet synchronous generator," *IEEE Transactions on Energy Conversion*, vol. 24, no. 1, pp. 1–11, Mar. 2009.

[41] Z. Q. Zhu and D. Howe, "Instantaneous magnetic field distribution in brushless permanent magnet dc motors, Part III: Effect of stator slotting," *IEEE Transactions on Magnetics*, vol. 29, no. 1, pp. 143–151, 1993.

[42] D. Žarko, D. Ban, and T. A. Lipo, "Analytical calculation of magnetic field distribution in the slotted air gap of a surface permanent-magnet motor using complex relative air-gap permeance," *IEEE Transactions on Magnetics*, vol. 42, no. 7, pp. 1828–1837, Jul. 2006.

[43] M. Hafner, D. Franck, and K. Hameyer, "Static electromagnetic field computation by conformal mapping in permanent magnet synchronous machines," *IEEE Transactions on Magnetics*, vol. 46, no. 8, pp. 3105–3108, Aug. 2010.

[44] A. Hemeida and P. Sergeant, "Analytical modeling of surface PMSM using a combined solution of Maxwell's equations and magnetic equivalent circuit," *IEEE Transactions on Magnetics*, vol. 50, no. 12, p. 7027913, 2014.

[45] T. Lubin, S. Mezani, and A. Rezzoug, "2-D exact analytical model for surface-mounted permanent-magnet motors with semi-closed slots," *IEEE Transactions on Magnetics*, vol. 47, no. 2 PART 2, pp. 479–492, 2011.

[46] B. Hannon, P. Sergeant, and L. Dupré, "2-D Analytical Subdomain Model of a Slotted PMSM With Shielding Cylinder," *IEEE Transactions on Magnetics*, vol. 50, no. 7, p. 8101410, Jul. 2014.

[47] F. Dubas and C. Espanet, "Analytical solution of the magnetic field in permanent-magnet motors taking into account slotting effect: No-load vector potential and flux density calculation," *IEEE Transactions on Magnetics*, vol. 45, no. 5, pp. 2097–2109, May. 2009.

[48] Z. Q. Zhu, L. J. Wu, and Z. P. Xia, "An accurate subdomain model for magnetic field computation in slotted surface-mounted permanent-magnet machines," *IEEE Transactions on Magnetics*, vol. 46, no. 4, pp. 1100–1115, Apr. 2010.

[49] A. Rahideh and T. Korakianitis, "Analytical magnetic field calculation of slotted brushless permanent-magnet machines with surface inset magnets," *IEEE Transactions on Magnetics*, vol. 48, no. 10, pp. 2633–2649, 2012.

[50] O. De La Barriere, H. Ben Ahmed, M. Gabsi, and M. Lobue, "Two-dimensional analytical airgap field model of an inset permanent magnet synchronous machine, taking into account the slotting effect," *IEEE Transactions on Magnetics*, vol. 49, no. 4, pp. 1423–1435, 2013.

[51] A. Bellara, H. Tiegna, Y. Amara, and G. Barakat, "On load analytical modelling of the magnetic field for axial flux surface-inset permanent magnet machines with semi-closed slots," *Proceedings - 2012 20th International Conference on Electrical Machines, ICEM 2012*, pp. 2852–2858, 2012.

[52] Z. J. Liu and J. T. Li, "Analytical solution of air-gap field in permanent-magnet motors taking into account the effect of pole transition over slots," *IEEE Transactions on Magnetics*, vol. 43, no. 10, pp. 3872–3883, Oct. 2007.

[53] B. L. J. Gysen, K. J. Meessen, J. J. H. Paulides, and E. A. Lomonova, "General formulation of the electromagnetic field distribution in machines and devices using fourier analysis," *IEEE Transactions on Magnetics*, vol. 46, no. 1, pp. 39–52, Jan. 2010.

[54] Z. Q. Zhu, D. Howe, E. Bolte, and B. Ackermann, "Instantaneous Magnetic Field Distribution in Brushless Permanent Magnet DC Motors, Part I: Open-Circuit Field," *IEEE Transactions on Magnetics*, vol. 29, no. 1, pp. 124–135, 1993.

[55] A. M. EL-Refaie, "High Speed Operation of Permanent Magnet Machines," *PhD dissertation, Wisconsin Madison University*, 2012.

[56] L. J. Wu, Z. Q. Zhu, D. A. Staton, M. Popescu, and D. Hawkins, "Comparison of analytical models of cogging torque in surface-mounted PM machines," *IEEE Transactions on Industrial Electronics*, vol. 59, no. 6, pp. 2414–2425, Jun. 2012.

[57] A. Bellara, Y. Amara, G. Barakat, and B. Dakyo, "Two-Dimensional exact analytical solution of armature reaction field in slotted surface mounted PM radial flux synchronous machines," *IEEE Transactions on Magnetics*, vol. 45, no. 10, pp. 4534–4538, 2009.

[58] T. Lubin, S. Mezani, and A. Rezzoug, "Exact analytical method for magnetic field computation in the air gap of cylindrical electrical machines considering slotting effects," *IEEE Transactions on Magnetics*, vol. 46, no. 4, pp. 1092–1099, 2010.

[59] Y. Liu, F. Long, J. Yin, J. Lei, and Y. Gao, "Optimal design of a Halbach magnetized permanent magnet motor applied in electrical marine propulsion system," in *IEEE Transportation Electrification Conference and Expo, ITEC Asia-Pacific 2014 - Conference Proceedings*, Aug. 2014, pp. 1–5.

[60] S. Das, D. P. Arnold, I. Zana, J. W. Park, M. G. Allen, and J. H. Lang, "Microfabricated high-speed axial-flux multiwatt permanent-magnet generators - Part I: Modeling," *Journal of Microelectromechanical Systems*, vol. 15, no. 5, pp. 1330–1350, Oct. 2006.

[61] J. Tangudu, T. Jahns, and A. EL-Refaie, "Core loss prediction using magnetic circuit model for fractional-slot concentrated-winding interior permanent magnet machines," *Energy Conversion Congress and Exposition (ECCE), 2010 IEEE*, pp. 1004–1011, Sep. 2010.

[62] Y. Kano, T. Kosaka, and N. Matsui, "A simple nonlinear magnetic analysis for axial-flux permanent-magnet machines," *IEEE Transactions on Industrial Electronics*, vol. 57, no. 6, pp. 2124–2133, 2010.

[63] M. F. Hsieh and Y. C. Hsu, "A generalized magnetic circuit modeling approach for design of surface permanent-magnet machines," *IEEE Transactions on Industrial Electronics*, vol. 59, no. 2, pp. 779–792, Feb. 2012.

[64] T. Raminosoa, J. A. Farooq, A. Djerdir, and A. Miraoui, "Reluctance network modelling of surface permanent magnet motor considering iron nonlinearities," *Energy Conversion and Management*, vol. 50, no. 5, pp. 1356–1361, 2009.

[65] S. Ouagued, Y. Amara, and G. Barakat, "Comparison of hybrid analytical modelling and reluctance network modelling for pre-design purposes," *Mathematics and Computers in Simulation*, vol. 130, pp. 3–21, 2016.

[66] A. Adly and S. Abd-El-Hafiz, "Utilizing particle swarm optimization in the field computation of non-linear magnetic media," *Applied Computational Electromagnetics Society Journal*, vol. 18, no. 3, pp. 202–209, 2003.

[67] I. Alejandro and A. Trejo, *Numerical Modeling and Evaluation of the Small Magnetometer in Low-Mass Experiment*. School of Electrical Engineering, Royal Institute of Technology, 2007.

[68] D. A. Tziouvaras, P. McLaren, G. Alexander, D. Dawson, J. Esztergalyos, C. Fromen, M. Glinkowski, I. Hasenwinkle, M. Kezunovic, L. Kojovic, B. Kotheimer, R. Kuffel, J. Nordstrom, and S. Zocholl, "Mathematical models for current, voltage, and coupling capacitor voltage transformers," *IEEE Transactions on Power Delivery*, vol. 15, no. 1, pp. 62–72, 2000.

[69] A. Pulnikov, V. Permiakov, R. Petrov, J. Gyselinck, G. Langelaan, H. Wisselink, L. Dupre, Y. Houbaert, and J. Melkebeek, "Investigation of residual stresses by means of local magnetic measurement," *Journal of Magnetism and Magnetic Materials*, vol. 272-276, no. III, pp. 2303–2304, 2004.

[70] A. M. A. Abdallh, "An Inverse Problem Based Methodology with Uncertainty Analysis for the Identification of Magnetic Material Characteristics of Electromagnetic Devices," *PhD dissertation, Ghent University*, 2012.

[71] A. Abdallh, G. Crevecoeur, and L. Dupré, "Optimal needle placement for the accurate magnetic material quantification based on uncertainty analysis in the inverse approach," *Meas. Sci. Technol. Meas. Sci. Technol*, vol. 21, no. 21, pp. 115 703–16, 2010.

[72] G. Bertotti, "General Properties of Power Losses in Soft Ferromagnetic Materials." *IEEE Transactions on Magnetics*, vol. 24, no. 1, pp. 621–630, 1987.

[73] E. Barbisio, F. Fiorillo, and C. Ragusa, "Predicting loss in magnetic steels under arbitrary induction waveform and with minor hysteresis loops," *IEEE Transactions on Magnetics*, vol. 40, no. 4 I, pp. 1810–1819, 2004.

[74] M. N. O. Sadiku, "Magnetic Circuits," in *Elements of Electromagnetics*. New York, NY: Springer New York, 2001, pp. 347–354.

[75] J. Perho, "Reluctance network for analysing induction machines," *PhD dissertation, Aalto University*, 2002.

[76] B. Asghari, "Geometrical permeance network based real-time nonlinear induction machine model Open Access," *PhD dissertation, University of Alberta*, 2011.

[77] M. Barcaro, N. Bianchi, and F. Magnussen, "Six-phase supply feasibility using a PM fractional-slot dual winding machine," *IEEE Transactions on Industry Applications*, vol. 47, no. 5, pp. 2042–2050, 2011.

[78] H. Vansompel, P. Sergeant, L. Dupré, and A. Bossche, "A combined wye-delta connection to increase the performance of axial-flux PM machines with concentrated windings," *IEEE Transactions on Energy Conversion*, vol. 27, no. 2, pp. 403–410, 2012.

[79] H. Vansompel, P. Sergeant, and L. Dupré, "Effect of segmentation on eddy-current loss in permanent-magnets of axial-flux PM machines using a multilayer-2D 2D coupled model," in *Proceedings - 2012 20th International Conference on Electrical Machines, ICEM 2012*, Sep. 2012, pp. 228–232.

[80] N. Zhao, Z. Q. Zhu, and W. Liu, "Comparison of rotor eddy current losses in permanent magnet motor and generator," in *2011 International Conference on Electrical Machines and Systems, ICEMS 2011*, Aug. 2011, pp. 1–6.

[81] D. Stone, P. Mellor, D. Howe, and K. Atallah, "Rotor loss in permanent-magnet brushless AC machines," *IEEE Transactions on Industry Applications*, vol. 36, no. 6, pp. 1612–1618, 2000.

[82] H. Toda, Z. Xia, J. Wang, K. Atallah, and D. Howe, "Rotor eddy-current loss in permanent magnet brushless machines," *IEEE Transactions on Magnetics*, vol. 40, no. 4 II, pp. 2104–2106, Jul. 2004.

[83] H. Polinder and M. Hoeijmakers, "Eddy-current losses in the segmented surface-mounted magnets of a PM machine," *IEE Proceedings - Electric Power Applications*, vol. 146, no. 3, p. 261, 1999.

[84] M. Markovic and Y. Perriard, "A simplified determination of the permanent magnet (PM) eddy current losses due to slotting in a PM rotating motor," *International Conference on Electrical Machines and Systems (ICEMS)*, pp. 309–313, 2008.

[85] A. R. Tariq, C. E. Nino-Baron, and E. G. Strangas, "Iron and magnet losses and torque calculation of interior permanent magnet synchronous machines using magnetic equivalent circuit," *IEEE Transactions on Magnetics*, vol. 46, no. 12, pp. 4073–4080, 2010.

[86] J. Klötzl, M. Pyc, and D. Gerling, "Permanent Magnet Loss Reduction in PM- Machines using Analytical and FEM Calculation," in *Power Electronics Electrical Drives Automation and Motion (SPEEDAM), 2010 International Symposium on*, 2010, pp. 98–100.

[87] B. Aslan, E. Semail, and J. Legranger, "General analytical model of magnet average eddy-current volume losses for comparison of multiphase PM machines with concentrated winding," *IEEE Transactions on Energy Conversion*, vol. 29, no. 1, pp. 72–83, 2014.

[88] J. Pyrhonen, H. Jussila, Y. Alexandrova, P. Rafajdus, and J. Nerg, "Harmonic loss calculation in rotor surface permanent magnets-new analytic approach," *IEEE Transactions on Magnetics*, vol. 48, no. 8, pp. 2358–2366, 2012.

[89] W. Y. Huang, A. Bettayeb, R. Kaczmarek, and J. C. Vannier, "Optimization of magnet segmentation for reduction of eddy-current losses in permanent magnet synchronous machine," *IEEE Transactions on Energy Conversion*, vol. 25, no. 2, pp. 381–387, 2010.

[90] M. Mirzaei, A. Binder, B. Funieru, and M. Susic, "Analytical calculations of induced eddy currents losses in the magnets of surface mounted PM machines with consideration of circumferential and axial segmentation effects," *IEEE Transactions on Magnetics*, vol. 48, no. 12, pp. 4831–4841, 2012.

[91] L. J. Wu, Z. Q. Zhu, D. Staton, M. Popescu, and D. Hawkins, "Analytical model for predicting magnet loss of surface-mounted permanent magnet machines accounting for slotting effect and load," *IEEE Transactions on Magnetics*, vol. 48, no. 1, pp. 107–117, 2012.

[92] F. Dubas and A. Rahideh, "Two-dimensional analytical permanent-magnet eddy-current loss calculations in slotless PMSM equipped with surface-inset magnets," *IEEE Transactions on Magnetics*, vol. 50, no. 3, pp. 54–73, Mar. 2014.

[93] Y. Yoshida, K. Nakamura, and O. Ichinokura, "Basic examination of eddy current loss estimation in SPM motor based on electric and magnetic networks," *Proceedings - 2012 20th International Conference on Electrical Machines, ICEM 2012*, pp. 1586–1591, 2012.

[94] A. Hemeida and P. Sergeant, "Analytical modeling of eddy current losses in Axial Flux PMSM using resistance network," in *Proceedings - 2014 International Conference on Electrical Machines, ICEM 2014*. IEEE, Sep. 2014, pp. 2688–2694.

[95] C. Hoer and C. Love, "Exact inductance equations for rectangular conductors with applications to more complicated geometries," *Journal of Research of the National Bureau of Standards, Section C: Engineering and Instrumentation*, vol. 69C, no. 2, p. 127, 1965.

[96] P. Sergeant, H. Vansompel, A. Hemeida, and A. V. D. Bossche, "A Computationally Efficient Method to Determine Iron and Magnet Losses in VSI-PWM Fed Axial Flux Permanent Magnet Synchronous Machines," *IEEE Transactions on Magnetics*, vol. 50, no. 8, p. 8101710, 2014.

[97] S. Huang, J. Luo, F. Leonardi, and T. A. Lipo, "A comparison of power density for axial flux machines based on general purpose sizing equations," *IEEE Transactions on Energy Conversion*, vol. 14, no. 2, pp. 185–191, 1999.

[98] P. Di Barba, M. Farina, and A. Savini, "An improved technique for enhancing diversity in Pareto evolutionary optimization of electromagnetic devices," *COMPEL International Journal for Computation and Mathematics in Electrical and Electronic Engineering*, vol. 20, no. 2, pp. 482–496, Jun. 2001.

[99] J. Zhao, Y. Yan, Z. Gu, Z. Chen, and P. Zheng, "Research on an axial-axial flux compound-structure PMSM with varying air gap to fulfill field-weakening control," in *2014 17th International Conference on Electrical Machines and Systems (ICEMS)*, Oct. 2014, pp. 3345–3349.

[100] P. Upadhyay, K. Rajagopal, and B. Singh, "Design of a Compact Winding for an Axial-Flux Permanent-Magnet Brushless DC Motor Used in an Electric Two-Wheeler," *IEEE Transactions on Magnetics*, vol. 40, no. 4, pp. 2026–2028, Jul. 2004.

[101] A. EL-Refaie and T. Jahns, "Optimal Flux Weakening in Surface PM Machines Using Fractional-Slot Concentrated Windings," *IEEE Transactions on Industry Applications*, vol. 41, no. 3, pp. 790–800, May. 2005.

[102] A. M. El-Refaie, T. M. Jahns, and D. W. Novotny, "Analysis of surface permanent magnet machines with fractional-slot concentrated windings," *IEEE Transactions on Energy Conversion*, vol. 21, no. 1, pp. 34–43, 2006.

[103] F. Magnussen, P. Thelin, and C. Sadarangani, "Performance evaluation of permanent magnet synchronous machines with concentrated and distributed windings including the effect of field-weakening," in *Power Electronics,*

Machines and Drives, 2004. (PEMD 2004). Second International Conference on (Conf. Publ. No. 498), vol. 2, 2004, pp. 679–685 Vol.2.

[104] H. Cimen, E. Oguz, Y. Oguz, and H. Oguz, "Universities Power Engineering Conference (AUPEC), 2012 22nd Australasian," pp. 1–5, 2012.

[105] R. Benlamine, F. Dubas, C. Espanet, S. A. Randi, and D. Lhotellier, "Design of an axial-flux interior permanent-magnet synchronous motor for automotive application: Performance comparison with electric motors used in EVs and HEVs," in *2014 IEEE Vehicle Power and Propulsion Conference, VPPC 2014*. IEEE, Oct. 2015, pp. 1–6.

[106] Y. Okumura, M. Sanada, S. Morimoto, and Y. Inoue, "Study of characteristics of various structures in axial-gap PM motors," *Electrical Machines and Systems (ICEMS), 2012 15th International Conference on*, vol. 73, pp. 1–6, 2012.

[107] T. S. Kwon, S. K. Sul, L. Alberti, and N. Bianchi, "Design and control of an axial-flux machine for a wide flux-weakening operation region," *IEEE Transactions on Industry Applications*, vol. 45, no. 4, pp. 1258–1266, 2009.

[108] J. Zhao, D. Cheng, P. Zheng, X. Liu, C. Tong, Z. Song, and L. Zhang, "Field weakening capability investigation of an axial flux permanent-magnet synchronous machine with radially sliding permanent magnets used for electric vehicles," *Journal of Applied Physics*, vol. 111, no. 7, p. 07A719, Feb. 2012.

[109] M. T. Elsayed, O. A. Mahgoub, and S. A. Zaid, "Simulation Study of a New Approach for Field Weakening Control of PMSM," *Journal of Power Electronics*, vol. 12, no. 1, pp. 136–144, 2012.

[110] F. A. C. Viana, G. Venter, and V. Balabanov, "An algorithm for fast optimal latin hypercube design of experiments," *International Journal for Numerical Methods in Engineering*, vol. 82, no. 2, pp. 135–156, 2010.

[111] B. Aslan, E. Semail, J. Korecki, and J. Legranger, "Slot/pole combinations choice for concentrated multiphase machines dedicated to mild-hybrid applications," in *IECON Proceedings (Industrial Electronics Conference)*. IEEE, Nov. 2011, pp. 3698–3703.

[112] A. Hemeida, M. Taha, and P. Sergeant, "High speed operation design considerations for fractional slot axial flux PMSM," in *Proceedings - 2015 IEEE Workshop on Electrical Machines Design, Control and Diagnosis, WEMDCD 2015*. IEEE, 2015, pp. 97–103.

[113] H. Gavrila and V. Ionita, "Crystalline and amorphous soft magnetic materials and their applications - status of art and challenges," *J. Optoelectronics & Adv. Mater.*, vol. 4, no. 2, pp. 173–192, 2002.

[114] G. S. Liew, "Analysis and design of single-sided, slotted amm axial-field permanent magnet machines," *PhD dissertation, Adelaide University*, 2009.

[115] G. Grandi, G. Serra, and A. Tani, "Space vector modulation of a seven-phase voltage source inverter," in *International Symposium on Power Electronics, Electrical Drives, Automation and Motion, 2006. SPEEDAM 2006*, vol. 2006, 2006, pp. 1149–1156.

[116] S. Huang, J. Luo, F. Leonardi, and T. A. Lipo, "A general approach to sizing and power density equations for comparison of electrical machines," *IEEE Transactions on Industry Applications*, vol. 34, no. 1, pp. 92–97, 1998.

[117] N. Bianchi and M. Dai Pre, "Active power filter control using neural network technologies," *IEE Proceedings-Electric Power Applications*, vol. 150, no. 2, pp. 139–145, Mar. 2003.

[118] S. Kumar, T. A. Lipo, and B.-i. Kwon, "A 32,000 rev/min axial flux permanent magnet machine for energy storage with mechanical stress analysis," *IEEE Transactions on Magnetics*, vol. 52, no. 7, p. 8205004, Jul. 2016.

[119] H. Li, Z. Chen, and H. Polinder, "Optimization of multibrid permanent-magnet wind generator systems," *IEEE Transactions on Energy Conversion*, vol. 24, no. 1, pp. 82–92, Mar. 2009.

[120] P. Zhao and G. Yang, "Torque density improvement of five-phase PMSM drive for electric vehicles applications," *Journal of Power Electronics*, vol. 11, no. 4, pp. 401–407, 2011.

[121] P. Ponomarev, P. Lindh, and J. Pyrhonen, "Effect of slot-and-pole combination on the leakage inductance and the performance of tooth-coil permanent-magnet synchronous machines," *IEEE Transactions on Industrial Electronics*, vol. 60, no. 10, pp. 4310–4317, Oct. 2013.

[122] R. Ni, G. Wang, X. Gui, and D. Xu, "Investigation of d- and q-axis inductances influenced by slot-pole combinations based on axial flux permanent-magnet machines," *IEEE Transactions on Industrial Electronics*, vol. 61, no. 9, pp. 4539–4551, Sep. 2014.

[123] Z. Tan, X.-g. Song, B. Ji, Z. Liu, J.-e. Ma, and W.-p. Cao, "3D thermal analysis of a permanent magnet motor with cooling fans," *Journal of Zhejiang University SCIENCE A*, vol. 16, no. 8, pp. 616–621, Aug. 2015.

[124] M. Polikarpova, P. Ponomarev, P. Lindh, I. Petrov, W. Jara, V. Naumanen, J. A. Tapia, and J. Pyrhönen, "Hybrid cooling method of axial-flux permanent-magnet machines for vehicle applications," *IEEE Transactions on Industrial Electronics*, vol. 62, no. 12, pp. 7382–7390, Dec. 2015.

[125] F. Marignetti, V. Delli Colli, and Y. Coia, "Design of axial flux PM synchronous machines through 3-D coupled electromagnetic thermal and fluid-dynamical finite-element analysis," *IEEE Transactions on Industrial Electronics*, vol. 55, no. 10, pp. 3591–3601, 2008.

[126] F. Marignetti and V. Delli Colli, "Thermal analysis of an axial flux permanent-Magnet synchronous machine," *IEEE Transactions on Magnetics*, vol. 45, no. 7, pp. 2970–2975, Jul. 2009.

[127] D. A. Howey, A. S. Holmes, and K. R. Pullen, "Measurement and CFD prediction of heat transfer in air-cooled disc-type electrical machines," *IEEE Transactions on Industry Applications*, vol. 47, no. 4, pp. 1716–1723, Jul. 2011.

[128] A. Rasekh, P. Sergeant, and J. Vierendeels, "Convective heat transfer prediction in disk-type electrical machines," *Applied Thermal Engineering*, vol. 91, pp. 778–790, Dec. 2015.

[129] A. Rasekh, P. Sergeant, and v. J. Vierendeels, "Fully predictive heat transfer coefficient modeling of an axial flux permanent magnet synchronous machine with geometrical parameters of the magnets," *Applied Thermal Engineering*, vol. 110, pp. 1343–1357, 2017.

[130] F. Sahin, "Design and Development of a High-Speed Axial-Flux Permanent-Magnet Machine Design and Development of a High-Speed Axial-Flux Permanent-Magnet Machine," *PhD dissertation, Eindhoven University of Technology*, 2001.

[131] H. Vansompel, A. Rasekh, A. Hemeida, J. Vierendeels, and P. Sergeant, "Coupled Electromagnetic and Thermal Analysis of an Axial Flux PM Machine," *IEEE Transactions on Magnetics*, vol. 51, no. 11, p. 8108104, Nov. 2015.

[132] N. Rostami, M. R. Feyzi, J. Pyrhonen, A. Parviainen, and M. Niemela, "Lumped-parameter thermal model for axial flux permanent magnet machines," *IEEE Transactions on Magnetics*, vol. 49, no. 3, pp. 1178–1184, Mar. 2013.

[133] C. H. Lim, J. R. Bumby, R. G. Dominy, G. I. Ingram, K. Mahkamov, N. L. Brown, A. Mebarki, and M. Shanel, "2-D lumped-parameter thermal modelling of axial flux permanent magnet generators," in *Proceedings of the 2008 International Conference on Electrical Machines, ICEM'08*, Sep. 2008, pp. 1–6.

[134] D. Kowal, "Methodology to evaluate the influence of electrical steel properties on the design of wind turbine generators," *PhD dissertation, Ghent University*, 2013.

[135] A. Di Gerlando, G. M. Foglia, M. F. Iacchetti, and R. Perini, "Parasitic Currents in Structural Paths of YASA Axial Flux PM Machines: Estimation and Tests," *IEEE Transactions on Energy Conversion*, vol. 31, no. 2, pp. 750–758, jun 2016.

[136] S. Nategh, A. Krings, O. Wallmark, and M. Leksell, "Evaluation of impregnation materials for thermal management of liquid-cooled electric machines," *IEEE Transactions on Industrial Electronics*, vol. 61, no. 11, pp. 5956–5965, Nov. 2014.

[137] R. Camilleri, T. J. Woolmer, A. Court, and M. D. McCulloch, "Investigation into the temperature profile of a liquid cooled YASA© AFPM machine," in *6th IET International Conference on Power Electronics, Machines and Drives (PEMD 2012)*, 2012, pp. B93–B93.

[138] M. Galea, C. Gerada, T. Raminosoa, and P. Wheeler, "A thermal improvement technique for the phase windings of electrical machines," *IEEE Transactions on Industry Applications*, vol. 48, no. 1, pp. 79–87, Jan. 2012.

[139] L. Siesing, A. Reinap, and M. Andersson, "Thermal properties on high fill factor electrical windings: Infiltrated vs non infiltrated," in *Proceedings - 2014 International Conference on Electrical Machines, ICEM 2014*. IEEE, Sep. 2014, pp. 2218–2223.

[140] P. Mellor, D. Roberts, and D. Turner, "Lumped parameter thermal model for electrical machines of TEFC design," *IEE Proceedings B Electric Power Applications*, vol. 138, no. 5, p. 205, 1991.

[141] D. Kuehbacher, A. Kelleter, and D. Gerling, "An Improved Approach for Transient Thermal Modeling using Lumped Parameter Networks," in *Electric Machines & Drives Conference (IEMDC)*. IEEE, May. 2013, pp. 890 – 897.

[142] H. Vansompel, A. Hemeida, and P. Sergeant, "Stator Heat Extraction System for Axial Flux Yokeless and Segmented Armature Machines," in *IEMDC 2017 - IEEE International Electric Machines and Drives Conference*, Miami, 2017.

[143] D. Kowal, P. Sergeant, L. Dupré, and A. Van Den Bossche, "Comparison of nonoriented and grain-oriented material in an axial flux permanent-magnet machine," *IEEE Transactions on Magnetics*, vol. 46, no. 2, pp. 279–285, Feb. 2010.

[144] W. L. S. Miller and T. J. E, "Practical field weakening performance of the five classes of brushless synchronous AC motor drive," in *Electrical Machines and Drives, 1993. Sixth International Conference on (Conf. Publ. No. 376)*. IET, 1993, pp. 303–310.